Nanostructure and nanomechanics of stomatopod cuticle

Yi Zhang

A thesis submitted for the degree of Doctor of Philosophy

School of Engineering and Materials Science

Queen Mary University of London

October 2015

Declaration

I, Yi Zhang, confirm that the research included within this thesis is my own work or that where it has been carried out in collaboration with, or supported by others, that this is duly acknowledged below and my contribution indicated. Previously published material is also acknowledged below.

I attest that I have exercised reasonable care to ensure that the work is original, and does not to the best of my knowledge break any UK law, infringe any third party's copyright or other Intellectual Property Right, or contain any confidential material.

I accept that the College has the right to use plagiarism detection software to check the electronic version of the thesis.

I confirm that this thesis has not been previously submitted for the award of a degree by this or any other university.

The copyright of this thesis rests with the author and no quotation from it or information derived from it may be published without the prior written consent of the author.

Signature:

Date:

Abstract

Crustacean cuticle has attracted extensive attention for biomimetic purposes due to its outstanding mechanical properties including high toughness and stiffness. The mantis shrimp (stomatopod) telson is an extreme example, structurally optimized for dynamic loading at high impact forces.

Alpha-chitin fibrillar building blocks play a key role in determining the overall mechanical properties due to its hierarchical design across all length scales. Synchrotron X-ray diffraction combined with *in-situ* mechanical testing was employed to investigate the structural and mechanical responses in telson cuticle at different hierarchical levels. The stomatopod tergite was used as a reference to learn how the structural and mechanical design will be correlated to the morphological changes in telson. In the thesis, we developed a novel three dimensional fibre orientation reconstruction method using mathematical models. The method was used to determine the orientation and intensity distributions of both the in-plane and out-of-plane mineralised chitin fibres from the two dimensional synchrotron X-ray diffraction scans collected from telson and tergite samples. Subsequently, *in-situ* tensile tests were performed on tergite cuticle to study the deformation and reorientation mechanisms of chitin fibres in the Bouligand layers comprising the bulk of the tergite, by tracing the variation of lattice spacing of the (002) peaks (along fibril direction) and (110) peaks (perpendicular to the fibril) found in the X-ray diffraction spectrum of α-Chitin. Finally, *in-situ* four-point bending tests were conducted to study how morphological changes contribute to the nanomechanical properties of telson across the entire tissue

cross-section. Pre-strains were identified in the cuticle in static states, and vary according to the morphological position. Under loading, fibrils near physiological impact site deformed more than those in adjacent region, demonstrating different roles in energy dissipation in telson.

These above findings provide useful guidelines for designing synthetic composite materials that resist repetitive impact loading.

Acknowledgements

done such a good job in providing administrative support, so we could focus on our research.

I am also grateful to all my colleagues in the research group, including Li, Jingyi, Sheetal, Angelo, Liisa, and Yiran. Without their kind friendship and help I could not have achieved this goal.

My journey would not have been made so enjoyable without my friends, including Menglong, Chen, Mark, Shaz and Fabio; especially my roommate Simon, who has helped me so much during my time in London.

Last, but certainly not least, I must give tremendous and deep thanks to my family. They have always been there whenever I needed support and company. My achievement means nothing without them.

Publications, Poster presentations

Following papers were published or presented at scientific meetings based the work presented in this thesis:

Publications

- Y Zhang, O Paris, NJ Terrill, and HS Gupta. *The three-dimensional gradients in fibrillar orientation in an impact-resistant biological armour.* Scientific Reports. 2016, doi:10.1038/srep26249.

- Y Zhang, E Barbieri, O Paris, AH Barber, GB Sukhorukov, NJ Terrill, NM Pugno, and HS Gupta. *Angle dependent fibrillar strain and reorientation in the lamellae of a biological composite: the case of stomatopod cuticle.* 2016 (in preparation)

- Y Zhang, E Barbieri, O Paris, AH Barber, GB Sukhorukov, NJ Terrill, NM Pugno, and HS Gupta. *Morphologically correlated prestrain distribution optimized for high energy dissipation in the stomatopod telson.* 2016 (in preparation)

Poster presentation (including accepted abstracts)
- Y Zhang, O Paris, AH Barber, GB Sukhorukov, NJ Terrill, and HS Gupta. *Nanostructure of Biocomposites optimized for Dynamic Mechanical Loading: Mechanisms and Emulation.* Poster presented at the SEMS Research Graduate Poster Show/Industrial Liaison Forum. 14/11/2012, London,UK

- Y Zhang, E Barbieri, O Paris, AH Barber, GB Sukhorukov, NJ Terrill, NM Pugno, and HS Gupta. *Microscale fibre orientation and mechanics in a natural biological mechanical shield: synchrotron X-ray mapping of the mantis shrimp telson.* Poster presented at the 5th International Conference on the Mechanics of Biomaterials and Tissues, 08-13/December/2013, Sitges, Spain.

- Y Zhang, E Barbieri, O Paris, AH Barber, GB Sukhorukov, NJ Terrill, NM Pugno, and HS Gupta. *3D chitin fibre orientation reconstruction from 2D WAXD pattern.* Poster presented at Synchrotron User Meeting at Diamond Light Source, September 04-05/2013, Harwell, UK.

- Y Zhang, E Barbieri, O Paris, AH Barber, GB Sukhorukov, NJ Terrill, NM Pugno, and HS Gupta. *3D chitin fibre reconstruction from 2D WAXD pattern.* Poster will be presented at 2015 MRS Fall Meeting & Exhibit, December 01-06/2015, Boston, USA.

List of Abbreviations

SEM   Scanning electron microscopy

TEM   Transmission electron microscopy

Micro-CT   X-ray microtomography measurements

SAXS   Small Angle X-ray Scattering

WAXD   Wide Angle X-ray diffraction

FWHM   Full width at half maximum

IR   Infra-red spectroscopy

LINAC   Linear accelerator

FESEM   Field-emission scanning electron microscopy

IP   In-plane

OP   Out-of-plane

DIC   Digital image correlation

3D   Three dimensional

2D   Two dimensional

^{13}C NMR   Carbon-13 nuclear magnetic resonance

ACC   Amorphous calcium carbonate

ACP   Amorphous calcium phosphate

FAP   Fluoroapatite (FAP)

HAP   Hydroxyl apatite

CAS	Calcium sulphate
DOC	Dactyl club outer layer
DIC	Dactyl club inner layer
SEMS	School of Engineering and Materials Science
QMUL	Queen Mary University of London
BESSY	Berliner Elektronenspeicherring-Gesellschaft für Synchrotronstrahlung
ESRF	European Synchrotron Radiation Facility
XRF	X-ray fluorescence

List of figures

Figure 2.13. Synchrotron XRD analysis and mineral distributions in the dactyl club. (a): Example X-ray diffraction picture acquired from the impact region of the dactyl club. (b): 1D XRD profiles obtained from the impact (IR) and periodic

List of tables

Table of contents

Contents

Chapter 1: Motivation

In materials engineering, the need for composite materials to achieve extremely high fracture toughness, impact resistance and resilience while minimizing weight, in demanding aerospace, defence and structural applications is a pressing and ever evolving technological challenge [6]. While on the synthetic aspect, newer nanoscale structures like carbon nanotubes and graphene, combined with high performance polymers, are increasingly being used to attain these high performance goals[7-9]. biological composite materials like bone, tendon and arthropod cuticle provide numerous counter-examples where materials with high toughness or tailored stiffness are produced very efficiently from building blocks like proteins, polysaccharides and brittle minerals like apatite or calcium carbonate, which do not have outstanding mechanical properties on their own [10-13]. These optimizations, obtained after millennia of evolution, have provided numerous templates for materials with high stiffness and toughness (like bone and nacre from mollusc shells) [11, 14-17]. These structural designs have spurred materials engineers to investigate such systems as templates for synthetic materials, an area known as biomimetic or bioinspired materials science [6, 10, 13]. In this regard, while extensive attention[14, 18-20] has been paid to understanding toughening mechanisms in biocomposites like bone and tendon designed to resist relatively slow rates of loading (~ 1 Hz), much less is known about the few biological structural materials that are evolutionarily optimized for high loading rates. At the same time, the understanding of dynamic deformation at the nanoscale in synthetic composite materials is also relatively limited, when compared to the wealth of information on static mechanical properties of such systems

[14, 18-20]. In this thesis, we consider a remarkable natural composite designed to resist fast loading without damage (the telson of mantis shrimp).

Figure 1. 1. *Image of mantis shrimp from website.*
(https://mantisshrimp.wordpress.com/tag/mantis-shrimp-evolution/, 18/01/2016)

Mantis shrimp (**Figure 1.1**) (also known as stomatopod) is a naturally aggressive predatory form of shrimp, whose smashing or spearing appendages (dactyl) and a protective shield (telson), exhibit remarkable resistance to withstand repetitive and powerful impacts from the environment, either during preying (e.g. on shells)[1, 21, 22] or in ritualized intraspecific fights [23]. Indeed, as the stomatopod can destroy the mollusc shells, which contains the high toughness nacre material, we can say the cuticle (the tough exoskeletal covering of stomatopods) surpasses the already high impact-resistance of the much studied and more well-known abalone nacre. Therefore, the stomatopod cuticle is naturally an ideal biological model for understanding the optimization secrets against dynamic loading in multiscale composites. While recent work has uncovered remarkable structural design features in the offensive (smashing) dactyl club [1, 24-26], the corresponding multiscale structure-function relations in the defensive organ (telson [22, 23, 27]) have been much less studied. The

telson exhibits a ribbed shape; also outperformed the regular shaped tergite cuticle even though is built with similar chemical components. **Our overall hypothesis** in this PhD thesis is that the structural gradients and deformation mechanisms at the nano- and microscale in the cuticle of telson are crucial for its overall impact resistance. **Our aim**, in this regard, is to determine the structure-function relations enabling these mechanisms at multiple structural levels in the telson.

The understanding of these structure-function relations in telson (and cuticle more broadly) is facing multiple technological challenges due to the complex hierarchical structures (as most biological materials are). The cuticle of arthropods, in general, exhibits complicated hierarchical structures from atomic and molecular levels to the highest level of morphological shape of the entire shell, segment or animal [6]. To determine the mechanical responses and functionalities from all those levels requires structural characterization techniques corresponding to multiple length scales. More importantly, those techniques need to be adapted to mechanical testing requirements. The conventional methods including scanning electron microscopy (SEM), transmission electron microscopy (TEM), require sample preparation procedure which usually changes their native physiological condition (dehydration). While for Raman spectroscopy, confocal microscopy and micro-computed tomography are either not capable of quantitative analysis or cannot be combined with mechanical tests. Further, the samples of the above methods are usually considerably changed from due to the preparation process. In this regard *in situ* and microprobe X-ray scattering and diffraction, using high brilliance synchrotron radiation, can overcome those drawbacks, providing both time-resolved imaging of mechanics at the nanoscale as well as micro-

spatially resolved X-ray imaging maps of the spatially graded microstructure. On more common tissues like vertebrate bone, dentin and tendon, synchrotron techniques have been applied extensively over the last decade or more on selected relatively simple tissue types [28-31].

However, the application of these advanced synchrotron micro- and nanoscale imaging and *in situ* techniques to arthropod cuticle poses special challenges in terms of technique and interpretation, which need to be resolved. **Firstly**, due to the 3D textured helicoidal arrangement of mineralised chitin fibres in cuticle, interpreting the 3D fibre orientation from the 2D X-ray diffraction pattern requires more advanced models than currently published [3, 32]. Though many mathematical models have been developed to predict crystalline fibre orientation, some important orientation distribution parameters (like the fibre plane tilt angles in 3D) are still missing. Therefore a more advanced model needed to be developed to predict and reconstruct the 3D fibre which will be the first goal of this thesis (**Chapter 4** and **Objective 1**, **Figure 1.2**). **Secondly**, the cuticle matrix is, at the molecular level, a chitin/protein/mineral composite with strains and stresses likely different in each phase, and these small scale deformation mechanics are largely undetermined *in situ* in cuticle, except in some artificially treated, special cases of unidirectional oriented chitin tendons (this gap is considerably more than the comparable case in bone[14, 19, 20, 33] and tendon [34, 35]. Hence, specialized *in situ* deformation mechanical experiments, in simple loading modes like tension, need to be done on cuticle to determine nanoscale deformation mechanisms, which will be the second objective of the thesis (**Chapter 4** and **Objective 2**, **Figure 1.2**).

Thirdly, as the telson has structural modulations at the micro- $(1 - 10$ μm) and mesostructural level (100 μm – 1 mm) as well as at the smallest nanometre scale, a full description of telson mechanics would need to determine spatial variation of nanoscale mechanics across the macroscopic dimensions of the organ. These necessitate development of both more realistic mechanical test modes like bending, as well as combining *in situ* mechanics with microfocus mapping [36], which will be the third objective of this thesis (**Chapter 5** and **Objective 3**, **Figure 1.2**).

Our ultimate goal is to examine the correlations between the structural design of stomatopod telson cuticle with its high impact resistance mechanical properties, therefore ideally we would like to apply impact load to the telson sample with a velocity (30 m/s) and acceleration (1.5 x 10^5 m/s^2) close to what the mantis shrimp will come across in the natural environment. However, the designing of high load rate mechanical tester for in-situ test is challenging. The required ultrafast motor is usually very expensive. On the other hand, the experiments also require the high brilliance X-ray source, fast beam shutter, advanced detector and data analysis. Hence, it is important to characterise the structural properties and quasi-static mechanical properties before we move to the higher budget and technically challenging high strain rate impact test.

In **Figure 1.2**, an overview of the structure of the thesis and timeline is presented, together with an approximate timeline over which the preparation, experimentation, modelling, analysis and writing were completed.
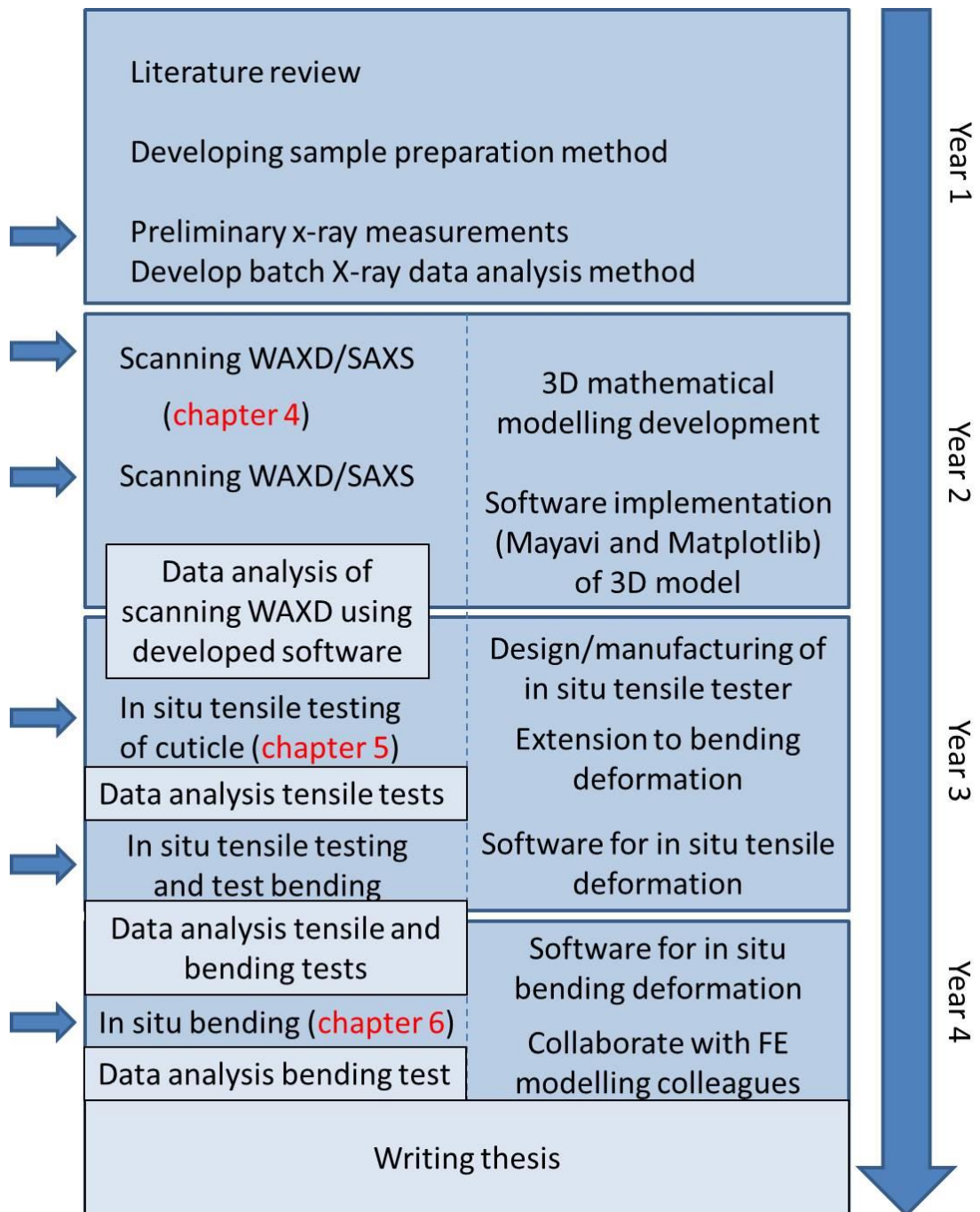
Figure 1. 2. *An overview of thesis structure and timeline of the PhD project. The blue arrows in the left indicate synchrotron beam times.*

Chapter 2: Structure and Mechanics of Cuticle

2.1 Arthropod cuticle

Arthropoda represent one of the most diverse groups of invertebrates in the animal kingdom [37]. Examples include insects, crustaceans, and chelicerates (including horseshoe crabs, sea spider) and these species have successfully adapted to virtually every habitat on earth, in a range of environmental conditions [38]. Anatomically, arthropods are usually characterized by having an exoskeleton, jointed appendages and segmented body. The evolutionary success of arthropods can partly be attributed to the protection offered by their characteristically tough exoskeleton to their internal organs [39, 40]. In order to adapt to different habitats and ecological niches, arthropod cuticles exhibit a broad range of mechanical properties, although – as common for other biological materials – the basic material building blocks are similar. These include the polysaccharide chitin, proteins and an inorganic phase consisting of biomineral polymorphs of calcium carbonate [41-43]. The basic material component of a stiff chitin fibrils surrounded by amorphous cross-linked protein matrix, together with water and a calcium carbonate/phosphate biomineral phase has evolved into a range of functionally different structures via structural differentiation at meso- and microscopic length scales. The variation of the properties, anisotropy and architecture at these higher levels between cuticle types, when combined with the intrinsic material performance of the mineralized chitin fibrils, is critical in obtaining the impressive diversity of specialized functions achieved in arthropod cuticle [44, 45].

The Young's modulus of arthropod cuticle can vary in a wide range within a small range in density (1–1.3 Mg/m^3) [46]: from 1 kPa for the intersegmental membrane, through the MPa range for wet and unsclerotized cuticle of larva and puparium, to 20 GPa for tanned, dry cuticle of the adult in wing, tibia and elytron [47]. The material origins of these wide variations in mechanical performance have drawn a great deal attention from material scientists, in order to find inspiration from such biological models to replicate high performance synthetic materials [12, 48-50]. The main subject of investigation in this study, the crustacean cuticle, is in contrast to other unsclerotized Arthropoda cuticle (soft cuticle of maggots for example) – usually calcified, which increases stiffness up to 100 GPa, albeit not at the cost of decreased toughness [51-54]. Arthropod cuticle holds several lessons for materials scientists attempting to replicate the high mechanical efficiency, low metabolic costs and facile synthesis conditions of natural biological composites like cellulose[47], mineralized collagen [51] and chitin [52, 53]. Through a combination of a stiff phase of alpha-chitin fibrils with a more extensible but tough protein matrix, a variable degree of water content, and a stiff mineral phase, the nanoscale structure achieves both stiffness and high toughness, a feature common to other natural composites (**Figure 2.1**) [55].

Crustaceans are a largely marine subphylum of arthropods, including s uch familiar animals as crabs, lobsters, crayfish, shrimp, krill and barn acles. The exoskeleton of crustaceans and insects is formed by cells of the hypodermis (an epithelial layer located beneath the cuticle) during both the pre- and post-moult stages when the animal sheds and regro ws the exoskeleton [55]. The crustacean moult cycle is divided into fo

ur discrete stages; pre-moult, ecdysis, post-moult, and intermoult [56]. In Crustacea (as in other Arthropoda), the cuticle serves as a support for organs and provides sites for muscle attachment. It protects the animal from internal and external mechanical stress and environmental hazards like desiccation and predation. Multiscale experimental and modelling studies have found that the crustacean cuticle possesses excellent mechanical properties in terms of stiffness that strongly depend on the overall mineral content and the specific microstructure of the mineral–protein matrix [52].

Structurally, the most distinctive feature for crustacean cuticle is the exquisite hierarchical structural design, built around a set of molecular building blocks including chitin, protein and various minerals[1, 44, 50, 57]. Such a hierarchical design is ubiquitous in natural materials, including bone, wood and shells [12]. Prior work – largely on these other materials – has shown that the mechanical properties of such biological materials are highly dependent on the structural design at all length scales in the hierarchy [12], necessitating an understanding of the structural properties at each of these scales, starting from the lowest level [47]. As a material composite, crustacean cuticle is both renewable and regenerated, with moulting cycles achieved over weeks [58]. Further, cuticle (particularly crustacean cuticle) achieves very high toughness and impact resistance [59, 60], as it is the functional barrier to the harsh external environment experienced by such crustaceans. Finally, mineralized cuticle is built in a layer-wise/scaffold manner to enable progressive deposition of layers of a chitin/protein/mineral matrix away from the interior soft tissue [61], together with a network of pore canals running perpendicular to the

surface which transport the components of the stiff reinforcing mineral phase [62].

In the following, we summarize the different hierarchical levels, followed by a more detailed discussion of the existing knowledge of the properties of the structural elements at each length scale.

2.2 Hierarchical structural of arthropod cuticle

The basic building blocks in crustacean cuticle are combined (via cell-directed self-assembly) into elements at multiple hierarchical levels. The lowest level of hierarchy in the general arthropod cuticle is β-1, 4-linked N-acetylglucosamine molecules (of the order of Angstroms in size) (a) (**Figure 2.1**) which polymerize to form chains of chitin (of the order of 1-10 nm) (b) (**Figure 2.1**). At the next hierarchical level [63], 18–25 chitin molecules arrange anti-parallel to form crystalline α-chitin nanofibrils (c) (**Figure 2.1**) with a diameter of around 3 nm. Each nanofibril then is wrapped with proteins to form so-called chitin–protein fibres (d) (**Figure 2.1**) with diameters 50~350 nm[63]. With the combination of mineral-protein matrix, these nanofibres are then assembled into horizontal fibre plane with fibres orientated parallel to each other. Those mineralised individual chitin–protein fibre planes are further stacked over each other, with a gradual rotation between adjacent layers around a direction normal to the planes. Such a helicoidal arrangement is referred to as a twisted plywood or known as Bouligand structures (the latter referring to the principal investigator of these motifs in the 1960s and 1970s) [13, 49, 64-67] (f). Such a structure is also found in other connective tissues, most notably in bone where it is combined with a rotation of the fibres around their axis to form a rotated plywood structure [49, 68].

However, another key structural feature in the micro level is that the plywood style arranged fibre planes are interrupted by voids originating from the pore canal system. The biological function for these pore canals is to transport minerals after moulting stage, the process where arthropods replace their old exoskeleton with a new, larger one in order to grow. Hence, the resulting tissue appears like a honeycomb-like structure (e) (**Figure 2.1**) which was first described as such in the research investigations of D. Raabe and co-workers [63, 69]. These plywood layers show structural differentiation and gradients in properties at the mesoscopic scale of a few millimetres (f) (**Figure 2.1**). Specifically, the entire cuticle consists of three layers: endocuticle, exocuticle, and an outer thin waxy layer, the epicuticle, and the exo- and endocuticle exhibit significant structural and morphological differences in the lamellar packing [70, 71]. Beyond all the above hierarchical levels, for some animals like stomatopod, the cuticle also exhibits morphological changes depending on the body parts of animal. For example, the telson cuticle of stomatopod exhibits a more complicated 3D curvature compared to the regular shaped tergite cuticle, which will be described in detail in later sections.

2.2.1 Molecular components and description

Second only to cellulose, chitin is the next most abundant natural polymer on earth and the most abundant nitrogen-bearing organic compound in nature. Similar to cellulose, in the native state it occurs as crystalline microfibrils that are a few nanometres across. Chitin is a common constituent in the cell walls of fungi and arthropod exoskeletons which includes insects, crustacean and various other organisms [58]. Structurally the chitin molecule is a linear polysaccharide of β-1,4-linked N- acetylglucosamine residues (shown

in **Figure 2.1**). It differs from cellulose by replacing one hydroxyl group on each monomer with an acetyl amine group. The absence of hydroxyl ions in chitin made it insoluble in aqueous solutions. However, its derivative chitosan can be water soluble due to the deacetylation process from chitin through chemical treatments [61, 72, 73].
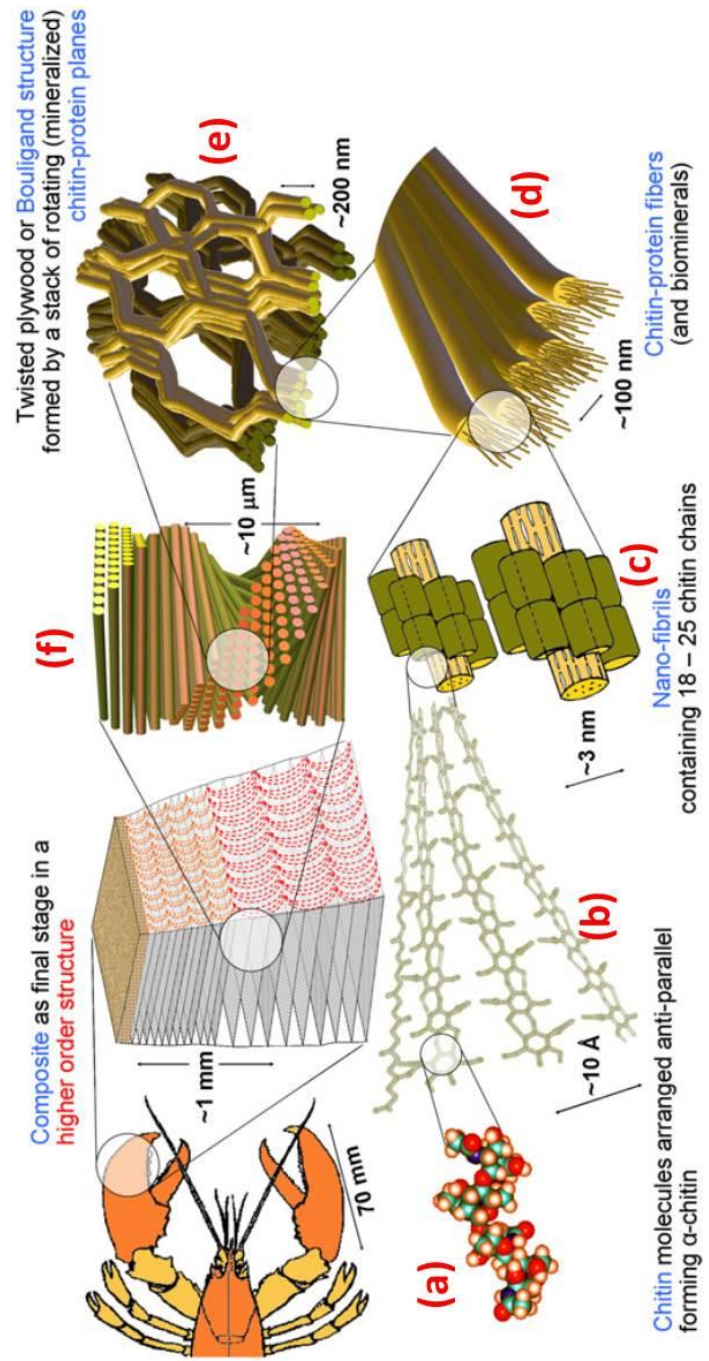
Figure 2.1. *Hierarchical microstructure of the cuticle of the lobster H. americanus [63]*
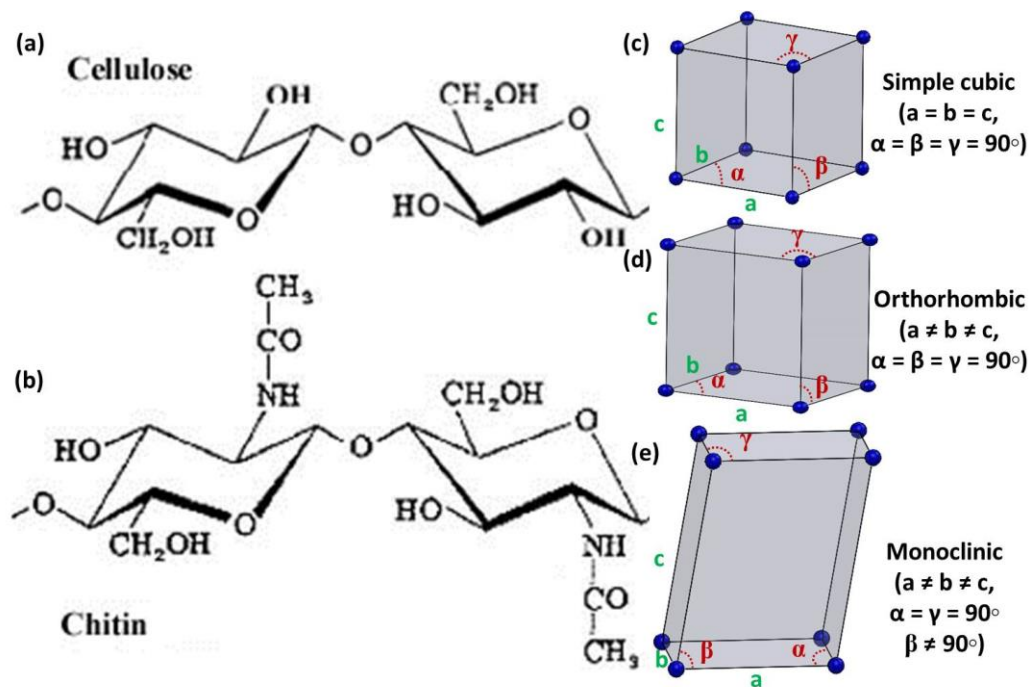
Figure 2.2. Chemical structures of chitin (a) and cellulose (b). Examples for cubic(c), orthorhombic (d) and monoclinic (e) crystal system. Image (a) is obtained from website (http://www.ispm.ru/lab5/epolisakharid.html, 22/10/2015).

Chitin occurs in three different polymorphic forms due to different packing and arrangement style of the molecular chains in the crystal cell. The α-Chitin consists of tightly packed anti-parallel molecular chains with $P2_12_12_1$ symmetry which forms a crystalline orthorhombic unit cell [59, 60]. In α-chitin, inter-sheet hydrogen bonds prevent diffusion of small molecules such as water into the crystalline phase[61]. In contrast the less crystalline β-chitin exhibits a parallel style of chain arrangement, forming a monoclinic unit cell [62]. The rarer β-chitin is found for example in squid [61, 74], where water can penetrate into the crystalline phase due to a lesser number of inter-sheet hydrogen bonds. γ-Chitin, which can be found in fungi, is formed of alternating parallel chains in one direction and antiparallel

one in the opposite direction. The crystalline α-chitin usually predominates within the exoskeleton of large crustaceans.

Experimental methods to determine the molecular structure of chitin include X-ray diffraction [44], Infra-red (IR) spectroscopy as well as Carbon-13 nuclear magnetic resonance (^{13}C-NMR) [45, 61]. The IR spectroscopy and solid-state ^{13}C-NMR methods are convenient to determine the difference between different polymorphic forms of chitin, the deacetylation degree as well the variation of the intermolecular and intramolecular hydrogen bonding of chitin[75]. Due to the highly homogenous structure the α-chitin consisting of eight major resonances peaks in the ^{13}C-NMR spectra in the solid state, while it is difficult to differentiate the C-3 and C-5 signals which merged together in the spectrum of β-chitin. In addition, under IR spectroscopy the Amide I band of α-chitin is split whereas a merged single band dominates for the β-chitin. X-ray diffraction is well suited to understand the orientation and variation of the crystalline structure of chitin [59, 76, 77], but especially when probing microscale gradients in chitin structure across different tissue regions in cuticle, synchrotron microfocus X-ray sources are needed[44, 63, 78, 79]. Pioneering work by Blackwell and co-workers [59, 80] has identified the orthorhombic dimensions of the α-chitin unit cell as $a = 0.475$ nm, $b = 1.885$ nm, and $c = 1.032$ nm [59] (**Figure 2.3**). As an example of the X-ray diffraction from such a structure, **Figure 2.4** shows a diffraction spectrum collected from the tendons of snow crab *C. opilio*. Among all the different diffraction indexes, we note specially the strong reflections at (002) and (004), as they indicate the direction and lattice spacing of the c-axis of the orthorhombic lattice cell, as well as the strong (110) reflection which is oriented perpendicular to the c-

axis direction [81, 82]. As will be described later, these two sets of reflections will prove to be important markers of fibrillar orientation and also mechanical deformation at the molecular level.

2.2.1.1 Mineral

The arthropods cuticle usually harden their fresh cuticle through a sclerotization process, which is acquired by the cross-linking between protein-polysaccharide and protein-protein using quinonoid-sclerotizing agents [53]. In addition, most crustaceans reach even higher hardness by a biologically regulated calcification process of the chitin/protein matrix. We describe the protein phase in the next section, while here we focus on the nature of the mineral phase. The biominerals such as hydroxyapatite $(Ca_{10}(PO_4)_6(OH)_2)$[83], calcium carbonate $(CaCO_3)$, magnetite (Fe_3O_4) and amorphous silica $(SiO2)$ in bones, teeth, nacre and crustacean cuticle have been recognised as essential components for the mechanical support of the animals[84, 85].

α-chitin: orthorhombic crystal structure
(a=4.74 Å, b=18.86 Å, c=10.32 Å)
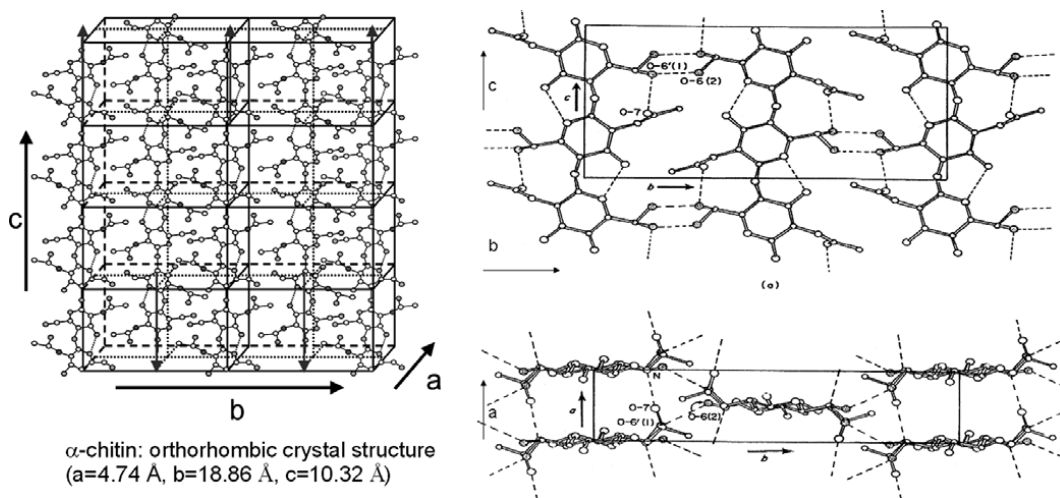
Figure 2.3. *Crystal structure and unit cell of α-chitin viewed normal to the bc-plane (top) and the ab-plane (bottom). The hydrogen bonds were indicated by dotted lines[63].*

Experimental probes to determine the distribution of mineral distribution in the cuticle include thermo gravimetric analysis (TGA) [86], energy-dispersive spectroscopy (EDS) measurements [1], Raman and Infrared spectroscopy[87] as well as X-ray diffraction [44].
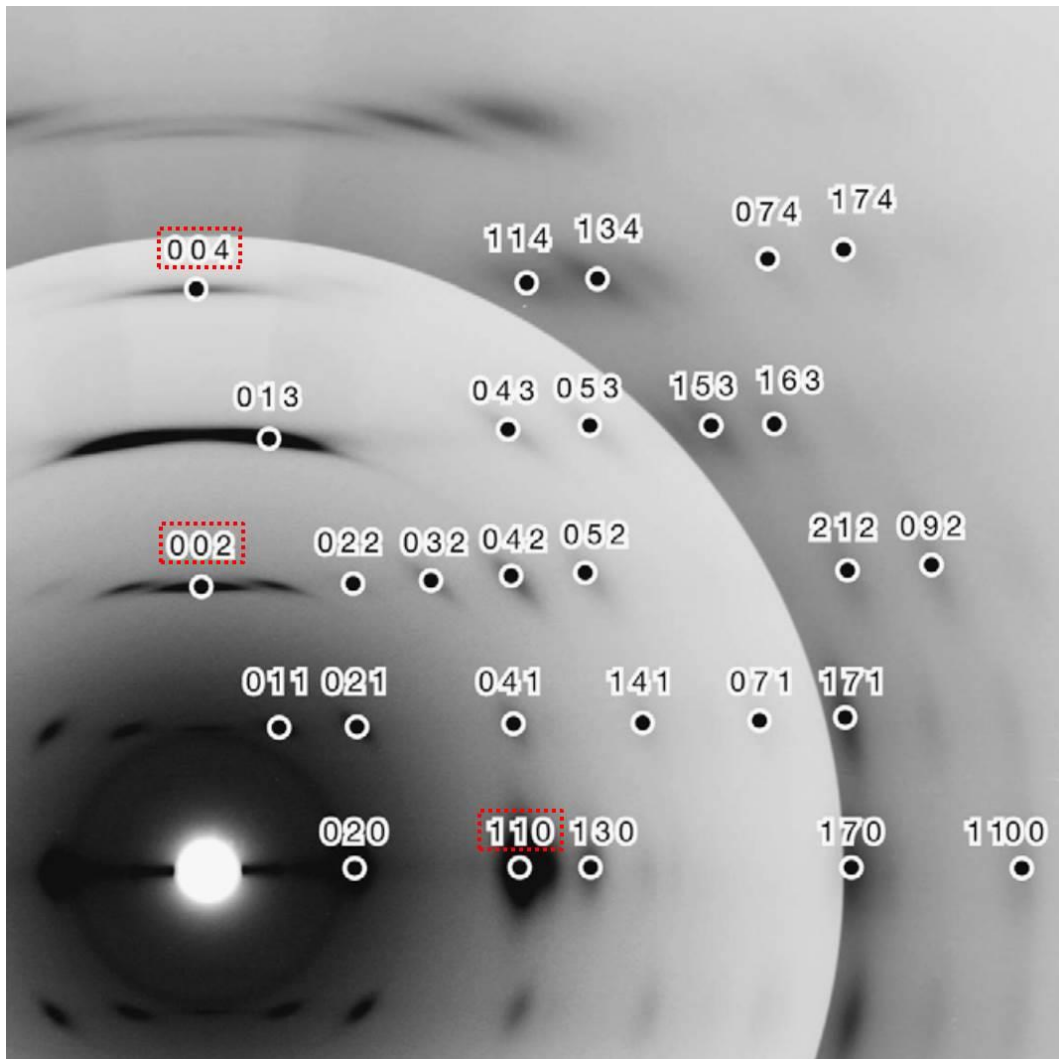
Figure 2.4. *Synchrotron X-ray fibre diffraction diagram of the tendon of C. opilio recorded [81].The reflections which are usually used to measure the deformation of crystal lattice were indicated by red dashed rectangles.*

Previous studies on crab, lobster, and mantis shrimp [44, 58] show that calcium carbonate is the main mineral phase component within crustacean cuticle, including both crystalline (calcite) and amorphous (ACC) polymorphs. Calcium carbonate based biominerals are

prevalent in the organic matrices of marine or aquatic organisms, including the abalone nacre of shells [11, 16]. ACC is a polymorph of low stability which tends to transform into more stable crystalline phases. In addition to calcium carbonate, other prevalent biominerals, including amorphous calcium phosphate (ACP), hydroxyl-apatite (HAP) [1], fluoroapatite (FAP) and calcium sulphate (CAS) [24], can also be found in different regions of certain crustacean cuticles [47].

Though the characterization of the mineral phase in the crustacean has drawn great attention and the distribution of various minerals in different species have been reported, there is still limited knowledge of the biomineralization process. It is well established [88, 89] that in a wide variety of biomineralized composites the formation of the majority of biominerals is under biological control, which means that the nature of the mineral phase is controlled precisely by proteins and other biological factors secreted by cells in the organic precursor scaffolds. The details of the mechanisms of biomineralization in cuticle remain in many aspects unknown. Even though it was reported that magnesium and phosphate ions, proteinaceous macromolecules and low-molecular weight phosphorylated components of the organic matrix could be responsible for the stabilization of ACC[12, 90], but the exact role of those molecules during the nucleation and precipitation processes of mineral phase still need to be further studied. From the viewpoint of a material scientist, the interaction between mineral phases with other organic constituents will be even more interesting because it may offer knowledge for making the synthetic composites much stronger by strengthen the bonding between the mineral and organic components.

In common to other biomineralized tissues like bone, the amount and distribution of the various mineral phases is considered as a key factor in controlling the mechanical properties of arthropod cuticle. The generic motif of a stiff mineral phase (~ 100 GPa) embedded or forming a composite arrangement with a more extensible, tough phase like chitin or collagen is a common one in biomineralized composite, accounting for their high strength and toughness [12, 18]. Broadly, it is known that stiffness increases with increasing mineralization, but the precise structural laws and constitutive models are surprisingly complex and are only now being elucidated for tissues like bone [91]. Functionally, there is a trade-off between increasing the stiffness through mineralization versus the increased weight this entails. For the animals which mainly use the cuticle as an armour against intensive predatory attack, like crabs, a hard, stiff and highly mineralized shell will be needed, while for animals where fast movement to prey and escape from enemy like lobsters a lighter, less mineralized cuticle will be needed [92].

Even for the same animal, the mineralization degree of the exoskeletons may differ considerably at different anatomical locations of the body, in order to adapt to multiple functions [24, 53]. Indeed, this specialization of cuticle to different functions is one of the reasons for the interest in chitin based composites from materials scientists. Furthermore, no homogeneity can be assumed even though for the cuticle collected from the same part of the animal body. Generally, in crustacean, the outermost cuticle layers need to be effective at resisting against impact and wear, hence these regions are usually more calcified with the minerals in more stable crystalline polymorphs like calcite. On the contrary, in the rest of the exocuticle as well as the

endocuticle, the less stable ACC and, in a lesser extent, amorphous calcium phosphate (ACP) abounds. Another important factor is the necessity to recycle the minerals during moulting, since ACC can be extracted much more easily from the old cuticle and stored in the endocuticle in order to be used for mineralizing the new cuticle. Most interestingly, in the species like mantis shrimp the mineral phases of its cuticle exhibit not only varied chemical composition but also different structure: Chemically, crystalline hydroxyapatite and fluoroapatite were found replacing calcite in the outer layer of both the smashing and spearing dactyl clubs. Structurally, those apatite crystals are highly preferentially oriented with their c-axis perpendicular to the impact surface [1, 24, 79], which are believed to enhance the mechanical properties in ways to increase functionality, and these will be described later in **section 4**.

2.2.1.2 Protein and water

The mechanical properties of cuticle are influenced by the chitin architecture and the degree of mineralisation, but also the precise combination of proteins in the cuticular matrix and the hydration states also play important roles in determining its properties [93, 94]. The relative percentages of chitin, protein, and mineral matter in crustacean shell vary between different species within very broad range of each component: chitin 10 – 20%, protein 13 – 50%, and mineral 15 – 70% [19]. The proteins in crustacean cuticle which are synthesised by epidermis usually have relative molecular mass smaller than 31 kDa [95, 96]. The elastic modulus and Poisson's ratio of protein are considered to be 4 MPa and 0.49 [97], according to the tensile experiments on wet membrane samples which contain chitin but no minerals, whereas the elastic modulus and Poisson's ratio of

the protein within the mineral protein matrix which surrounds the chitin fibres in crustacean cuticle are considered to be 1 MPa and 0.46. In addition, the protein contributes to the overall mechanical properties of cuticle by intimate bonding with chitin fibrils which make it an indispensable part of the whole hierarchical structural design in cuticle. Though early X-ray diffraction research indicated that protein is ordered, its relation to the chitin fibrils was unclear. Blackwell and Weih proposed a three-dimensional model with crystalline chitin in the core and surrounded with a protein sheath, using X-ray diffraction data from the ovipositor (a cuticle-based egg-laying appendage) of the ichneumon fly (*Megarhyssa*) (**Figure 2.5**) [98]. Later, the molecular level interaction between chitin and protein was detected from molecular modelling and X-ray diffraction study. The chain folded sheet of protein β-sheet is attached to the (010) face of the chitin nanofibres [99]. Recent biochemical studies reveal the types of chitin-binding proteins (CBPs) which further proved the covalent bonding of chitin and protein using protein expression methods [100, 101].

6_1 protein helix
7·25 nm

3·06 nm

Chitin microfibril
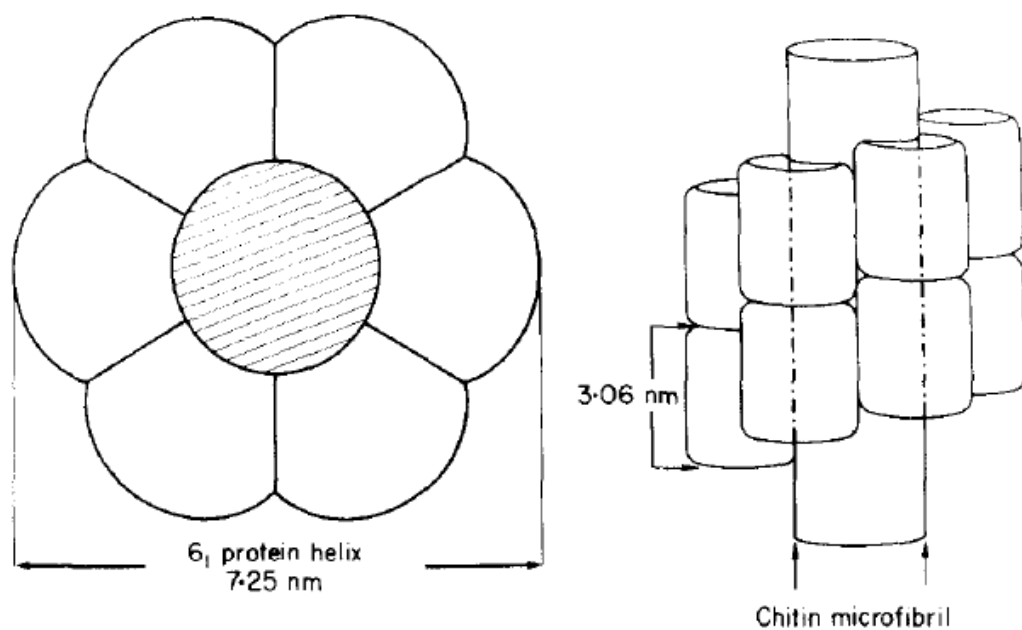
Figure 2.5. *Arrangement of the protein subunits around the chitin core from two viewing angle: (left) perpendicular to the fibre axis, (right) along the chitin fibre axis)[98].*

Cuticular proteins are essentially structural proteins, and they are usually bonded to chitin or other components of cuticle. Proteins take part in the hardening and darkening, that is, sclerotization or tanning of cuticles when the protein chains are stabilized by aromatic crosslinks and so made water insoluble. The properties of various regions of cuticle are functionally optimised and are, to a large extent, determined by the proteins present in the cuticular matrix. Both soft pliable cuticles and stiff solid cuticles contain their own characteristic proteins which differ from the resilin in several respects, although some similarities are present. It may be of interest to compare the various types of cuticular proteins to see whether some of the differences in protein structure can be related to differences in the mechanical properties.

Mechanically, the cuticle can be extremely sensitive to the water content. When the water content increases, the cuticle becomes softer and the stiffness decreases correspondingly. Many arthropod insects can change their stiffness by up to 10-fold increase by variation of the water content only by a few percent. And these processes are biologically controlled by changing pH value, hormonal content and other unknown mechanisms [47, 102, 103].

2.2.2 Chitin nanofibrils and nanofibres

As shown in **Figure 2.1,** the chitin molecule chains are arranged in an anti-parallel style which forms crystalline chitin fibrils, further, with the combination of cuticular proteins, the chitin fibrils then cluster

together to form chitin fibres (100 nm in diameter) which can be examined under scanning electron microscope.

In most of the cases, the orientations of chitin fibres are parallel to the cuticle surface of arthropods. However, another set of chitin fibres were found running through the pore canals (**Figure 2.6d**) which are perpendicular to the cuticle surface of crustaceans including crab, lobster and mantis shrimp. The fibres which are parallel to the cuticle surface usually were denoted as in-plane (IP) fibres (**Figure 2.6f**); correspondingly the fibres running in the perpendicular direction of cuticle surface are called out-of-plane fibres (OP) (**Figure 2.1e**).

The in-plane chitin fibres are well-known as the main structural components for the building of plywood styled fibre planes. The exquisite plywood architecture design is considered as a key feature constituent to the overall mechanical properties and has drawn great attention among material scientists. In the following section we will talk about this in more detail. The out-of-plane fibres are considered to be correlated to the transport of the nutrients during the moulting stage. However, the mechanical properties of the out-of-plane fibre were still unknown.

The other important feature for crustacean cuticle is that the crystallographic texture of chitin is identical to the topological textures of the chitin fibres, with the c-axis of the chitin lattice cell being identical to the longitudinal axis of the chitin fibres [63]. The coincidence of fibre orientation to the crystal orientation allows us to deduce the orientation of chitin fibres from X-ray diffraction studies.
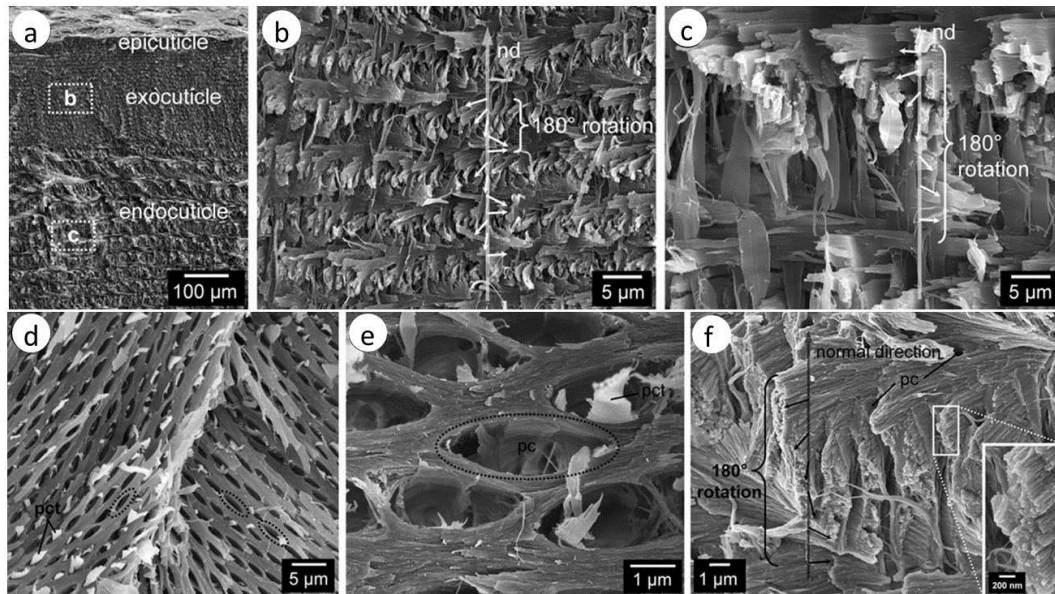
Figure 2.6. SEM image showing the microstructure of lobster cuticle. a) The cross section of lobster cuticle shows the epicuticle, exocuticle and endocuticle layer. b) Plywood structure in exocuticle c) Plywood structure in endocuticle. d) The pore canal system viewing perpendicular from the cuticle surface. e) High magnification image shows the pore canals and the out-of-plane fibres. f) The in-plane fibre rotation forms plywood structure [104].

Chitin nanofibre has been extensively used in biomedical applications due to its good mechanical properties and biological degradability. The chitin nanofibres have already been found in (i) stem cell and tissue engineering [105], (ii) wound dressing [106], (iii) cosmetic and skin health [107], (iv) drug delivery and bioimaging and biosensing [108]. Also, due to the abundance in nature, the chitin based materials are also low in cost which makes them competitive in package industry. Vast raw chitin fibres can be obtained from the waste of crustacean shells from food production [58, 109]. The isolation of chitin from crustaceans requires the removing of the two major constituents of the tissue: proteins by deproteinization and inorganic calcium carbonate by demineralization, together with small amounts of pigments and lipids which are generally eliminated during the two

previous steps [110]. In some cases, an additional step of decolorization is applied to get rid of the residual pigments.

2.2.3 Lamellar structure

The in-plane mineralised chitin fibres are arranged parallel to each other within a single layer. However, unlike most synthetic lamellar composites where the fibre orientations change abruptly, these fibre layers are then stacked on top each other in successive layers and rotate gradually around the direction perpendicular to the cuticle surface, which results in a twisted plywood (Bouligand) structure (**Figure 2.1f**). The plywood structure design can be widely found among crustaceans and other biological tissues [49]. The plywood lamellar design ensures high stiffness in all directions to help the cuticle survive impacts from different orientations. The helicoidal arrangement of mineralised chitin fibres layers are believed to largely increase surface area per unit crack length in the crack propagation direction hence amplifying the total energy dissipated during impact and crack propagation, which have been confirmed in engineered helicoidal composites[111]. When a crack propagates straight into neighbouring layers though the helicoidal path, it encounters an elastic modulus oscillation due to their anisotropic stiffness. As a result, the crack propagation is hampered by the modulus oscillation, which improves the damage tolerance with an efficiency that depends on the crack propagation direction relative to the chitin fibre orientation [26]. Also, the Bouligand-type structure allows the lamellae to reorient in response to the loading environment; In the scale of arapaima gigas, most lamellae reorient towards the tensile axis and deform in tension through stretching/sliding mechanisms thereby enhancing the scale's ductility and toughness to prevent fracture [10].

The SEM images also indicate that there is a pore canal (with diameters about 1-3 μm) structure across the cuticle. The parallel in-plane fibre layers are interrupted by canal running across of the cuticle (**Figure 2.6 d-e**). The chitin fibres close to the canals continuously round the holes to form a honey comb like structure. The pore canals are vital for the crustacean due to its important role in biomineralization by acting as a transport route for nutrients. However, its mechanical role is still needs to be further investigated. Chen et al[112] reported that the maximum pull out force of the fibre from the fibre-round-hole distribution is significantly larger than that of the non-fibre-round-hole distribution based on experimental results. On the other side, the compress and fracture of pore canals further toughening the cuticle. The formation of regular honeycombs with thick walls (i.e., with in-plane area fraction of the pores < 0.3) guarantees the largest possible in-plane stiffness compared to other planar microstructures with the same porosity fraction. This specific geometrical design ensures that the canal-pore-area fraction can be as large as possible while ensures optimal cuticle stiffness and fluid transport capacity for fast mineralization.

2.2.4 Mesoscale structure

Generally, the fully developed arthropod cuticle can be divided into four distinctive layers: The thin outermost epicuticle layer, exocuticle, endocuticle and inner membrane layer. The epicuticle is mainly composed of lipids, proteins as well as minerals. Usually there is no chitin fibre existing in the epicuticle region. The epicuticle layer acts as an environmental barrier for the animals to protect water lose. Beneath the thin epicuticle layer lays the exocuticle which consists of chitin as well as proteins and minerals. The epicuticle and exocuticle

are both secreted prior to ecdysis [113]. The endocuticle is the principle layer which accounts for more than 50% of volume fraction for the whole tissue. The endocuticle is also consisting of proteins, chitin and minerals. The exocuticle and endocuticle are both featured by the layers of mineralized chitin fibres immersed in collagen protein matrix and the pore canal systems running perpendicular to the surface. But the mineral content in the exocuticle is higher, the size of pore canals are smaller, the lamella thickness is smaller compared to the endocuticle [110]. The membrane layer which lies under the endocuticle layer remains un-calcified.

2.3 Mechanics of cuticle

Though one of the most important functions of cuticle is structural, the cuticle has also to be mechanically strong to withstand the external loadings from environment. As we mentioned before, the mechanical anisotropy occurs on different hierarchical levels due to the structure and chemical composition duel variation. Therefore, to understand the macroscopic mechanical properties of the tissue, one should take into account its structure–property relations at all length scales down to the molecular level. On the macro level, the young's modulus, hardness and toughness of cuticle can be measured by traditional material mechanical characterisation methods. And the overall cuticle properties changed when there are significant variations in the properties of the constituents (chitin, amorphous calcium carbonate (ACC), proteins). On the micro level, nanoindentation test can offer us mechanics values down to lamella scale. However, the most challenging part lies in the study of the mechanics on the nanoscale where the basic building materials start to form into intimate bonded nanocomposites with various structures. Of all the constituents,

mineral is the easier phase to be studied due to the fact that large content of minerals are amorphous which can be assumed as uniformly distributed. Generally, the dynamic mechanical behaviour is considered more correlated with the inorganic components than the biological components. The mechanics of chitins and proteins are less known due to its wide varieties but somehow it is not the priority because it is less in content within cuticle. Below we will report the main mechanical features of cuticle from macro to meso, micro and nanoscale:

2.3.1 Macroscopic mechanical properties of cuticle

Tensile and compression tests have been performed to examine the macroscopic mechanical properties of cuticle samples. As shown in the **Figure 2.7 (I-II)**, the stress-strain curves of lobster cuticle were considerably affected by the hydration conditions [104]. In the dry state, the lobster cuticle exhibits linear elastic behaviour and with a strain to brittle fracture of 0.7%, whereas the wet cuticle show plastic deformation, with a strain to yield of 0.5% and extends to a strain to fracture of about 1.8%. The structural stiffness of the dry samples lies between 5.8 and 7.0 GPa, which are higher than those collected from wet samples (about 4.8GPa) [104].

Despite the twisted plywood arrangement of the fibres which leads to anisotropic stiffness for different directions, the well-developed pore canal systems for transporting minerals to harden the new exoskeleton after the moult stage has been found also exhibit mechanical functions in the lobster's exoskeleton. As shown in **Figure 2.7III**, under compression tests the samples tested in normal direction exhibit a large linear elastic region, and a subsequent onset of plasticity,

whereas the samples tested in transverse direction show an extended plateau region after a relatively small elastic region, and at the end a steeply rising portion of the stress-strain curve. Also, the strains to fracture are much lower in normal direction compared to the transverse direction. The different mechanical responses against compression can be related to the pore canal systems. The anisotropic mechanical properties in different orientations can be correlated to the mechanical functions in different structure levels.
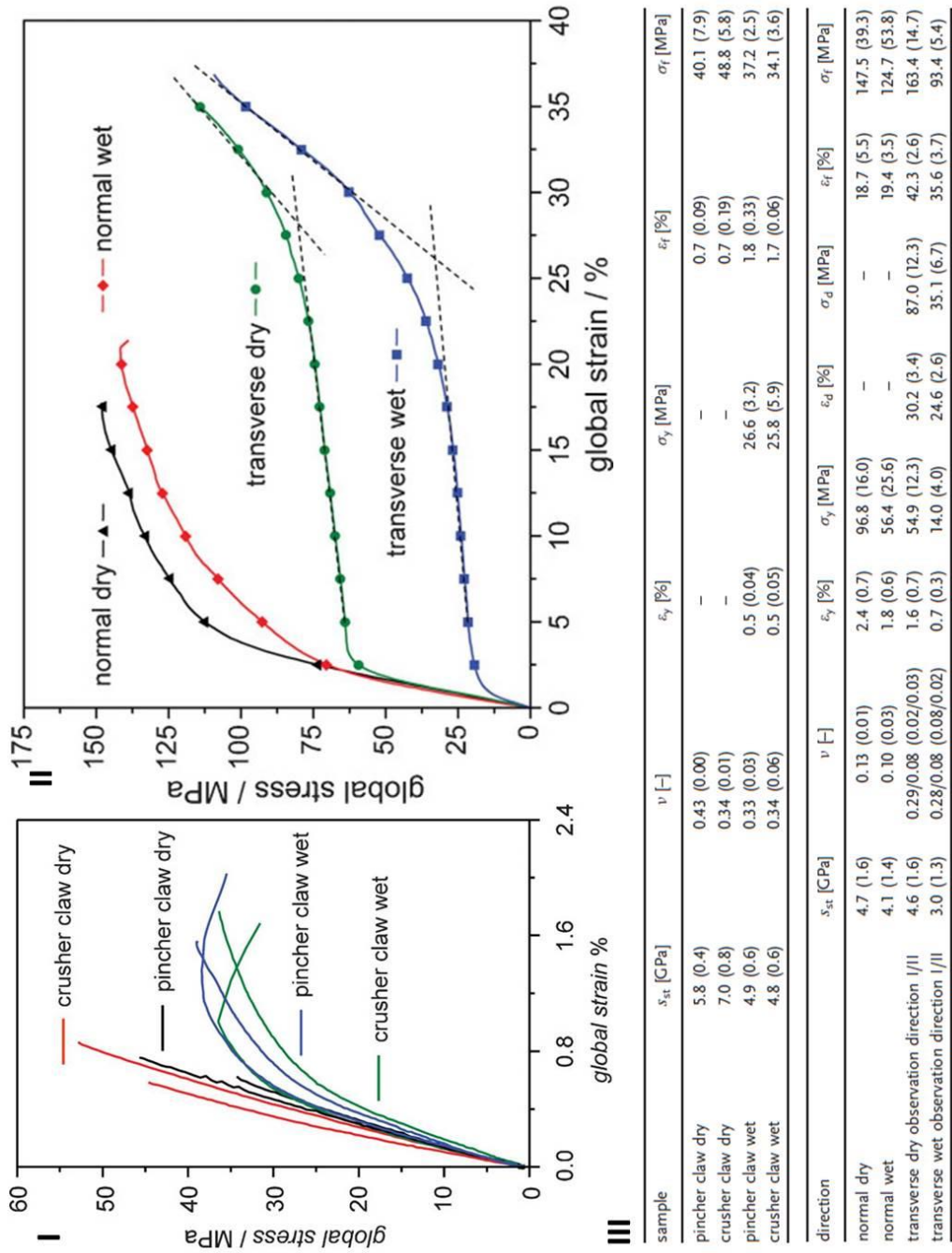
Figure 2.7. *Mechanical tests on lobster cuticle. I-II): Global stress-strain behaviour of lobster endocuticle from the pincher and crusher claw from tensile (I) and compression (II) test. III): The mechanical values of tensile and compression tests for lobster cuticle [104].*
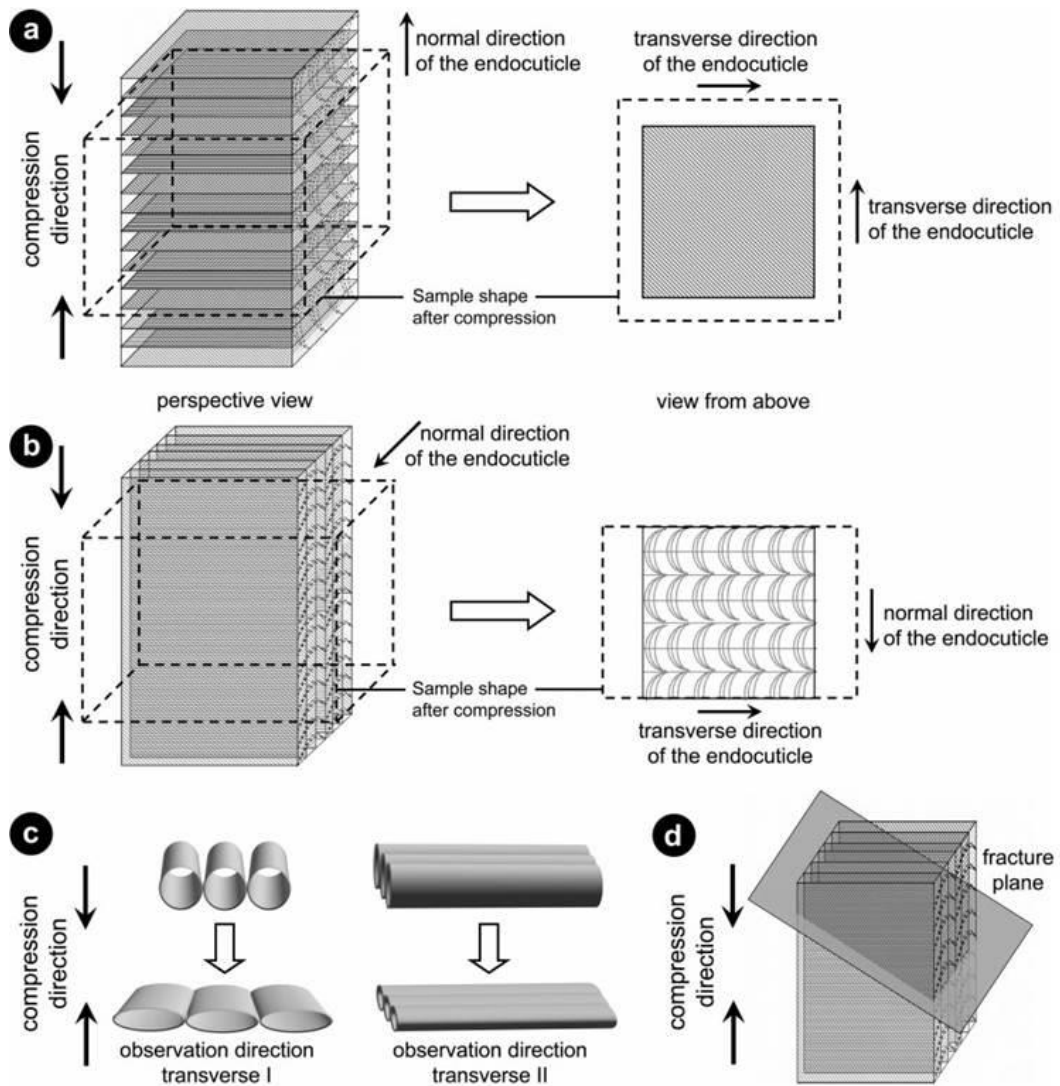
Figure 2.8. *Schematic illustration of how the pore canals of the honeycomb structure affect the mechanical properties from normal and transverse direction[104].*

Two different failure types of cuticle can be found due to the compression and collapse of the pore canals. When the cuticle is under compression transversely, the pore canals are compressed and broaden in transverse direction, while in the normal direction the length increase along the axis of the pore canal is negligible. **Figure 2.8** illustrates the deformation behaviour of the pore canals schematically. The samples under compression from normal direction failed by cleavage in the compression direction, while the samples under

transverse compression load showed a distinct fracture plane, oriented perpendicular to the cuticle surface and 45° to the compression direction, where the maximum shear stress was located [104]. This is because of structural failure along the long axes of the pore canals, resulting in the propagation of the crack from one pore canal to the next. The steeply increased stresses after the plateau region are caused by the fracture of pore canal structures, which then followed by progressive failure of the adjacent structure. However, the above toughening mechanisms result from the broadening and collapse of pore canals have neglected the existence of the mineralised chitin-protein fibres which has been found in previous literature in the crustacean cuticle [63, 69]. Unlike the continuous helicoidal layered structure of in-plane fibres, the mechanics of fibres running through the pore canals are very difficult to be tested by traditional Nanoindentation mappings. Therefore, new methods need to be developed to structurally and mechanically characterise the out-of-plane fibres.

The physiological state of the organism plays a particularly important role for the material, such as, for example, the actual stage of the moulting cycle, or the general environmental and living conditions, like pH, salt content, temperature, nutrition, or diseases. The water can affect the mechanical properties of cuticle by breaking the hydrogen bonds between proteins themselves and between protein and chitin [103]. Nanoindentation test on the impact region of the stomatopod dactyl club shows no significant differences in measured values between dry and hydrated conditions, however the stiffness of the periodic region is three times higher in dry state (10 and 25 GPa) then in hydrated conditions (3 to 8 GPa). Hydration also seems to be able

to impede the formation of micro cracks in the structure during compression, which supports the role of water as a plasticizer [47].

2.3.2 Microscopic mechanical properties of cuticle

In the microscopic level, Nanoindentation testing serves as a powerful method for revealing gradients and anisotropy in the hardness and the elastic properties of cuticle materials [71, 79, 114]. Thus, Nanoindentation has been used to study the orientation dependence of the elastic properties and the hardness and the influence of the grade of mineralization of fibres in stomatopod dactyl cuticle combined with post-indentation high-magnification field-emission scanning electron microscopy (FESEM) observations. As expected, the yield stress drops gradually from outer region (3.5 GPa) to inner region (less than 0.5 GPa) of the club and exhibits a clear elastic-plastic transition (**Figure 2.9 a-c**). The FESEM images collected on the cuticle planes under the contact points from outer region and inner region after indentation tests show different toughening mechanisms. The outer region of dactyl club (**Figure 2.9a**) demonstrated a graded, quasi-plastic compressive response. Regional interfacial sliding, gradual rotation of apatite nanorods and generation of a process zone with a major radial crack surrounded by multiple micro cracks(**Figure 2.9g**) can be found in the FESEM images collected in this region, leading to vast energy dissipation by localized yielding prior to the nucleation of shear-induced circumferential cracks. Those toughening mechanisms can also be demonstrated by the pop-in events from the stress-strain curves. Due to the incorporation of soft materials including chitin and cuticle proteins, the outer layer of the dactyl club managed to dissipate much more contact energy by yielding before cracking than the pure geologic fluoroapatite (FAP) crystal [25].
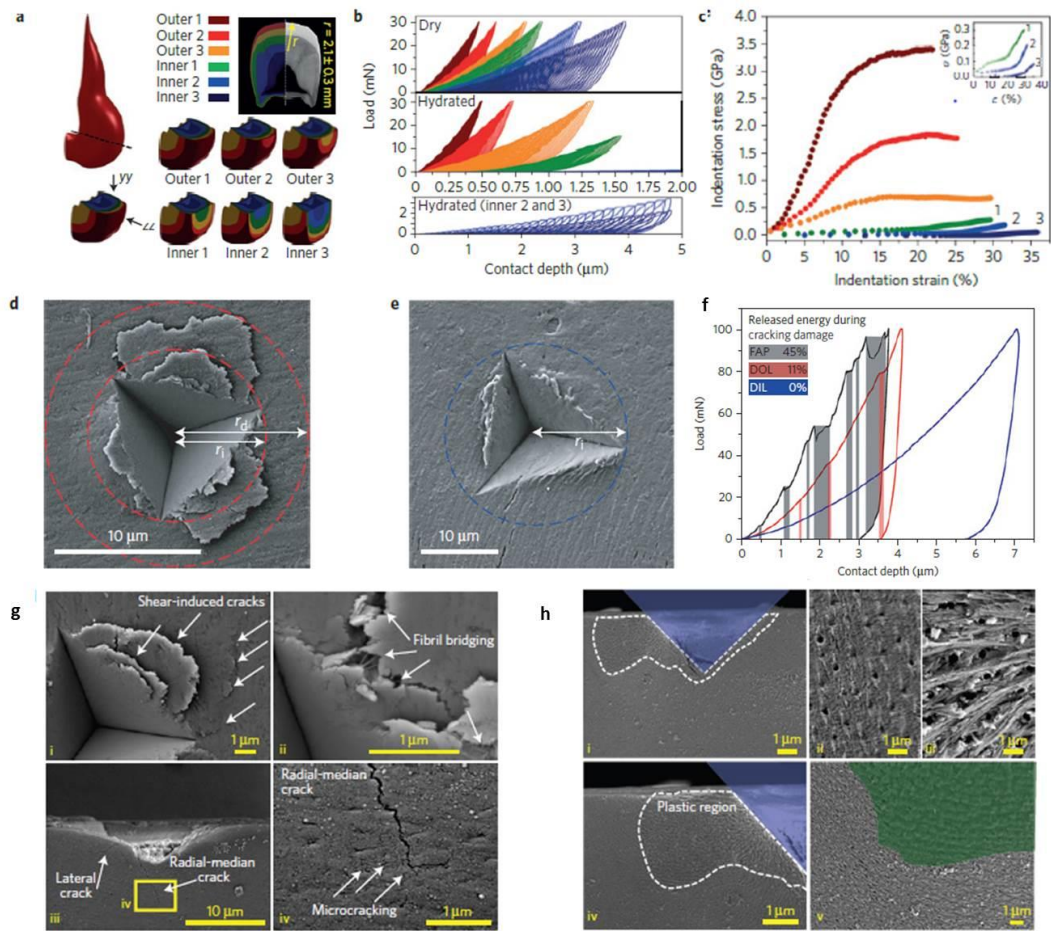
Figure 2.9. *Nanoindentation tests on stomatopod dactyl. a): Schematic defining different regions in the cross-section of the club. The different regions were indicated using different colours. b): Partial loading–unloading curves collected from indentation tests in dry (top) and hydrated (middle and bottom) conditions. c): Indentation stress as a function of strain (%) curves in dry conditions derived from the partial loading–unloading curves obtained in b. d-e): FESEM images collected from outer dactyl (d) and inner dactyl after indentation test. (e). f): The load and displacement curves of FAP, the dactyl club outer layer (DOL) and the dactyl club inner layer (DIL) under indentation. h-g): post-indentation FESEM images collected from the planes under the contact points for outer dactyl (g) and inner dactyl (h) reveal different deformation and damage mechanisms[25].*

On the other hand, the inner layers where the club was mainly built by chitin and amorphous minerals. As shown in **Figure 2.9h**, clear evidence of microchannel densification can be observed, which

resulting in a strain hardening behaviour in the stress-strain curve (inset image of **Figure 2.9c**) with lower compressive yield strengths but much higher yield strains. In total, the incorporation of a residual soft phase in the outer region of cuticle promotes localized interfacial sliding and rotation of the FAP crystals which results in a quasi-plastic response under impact, whereas, the inner cuticle region of dactyl exhibits strain-hardening behaviour associates with microchannel densification. Both mechanisms are beneficial for the toughness of the stomatopod dactyl cuticle [25]. Similar results were obtained from Nanoindentation mapping on the stomatopod dactyl [1]. The elastic modulus decreases from 70 GPa in the outer impact region to 10-25 GPa in the inner periodic region. The modulus mismatch across the whole dactyl acts as a deflector to prevent catastrophic crack propagation. As shown before, the Nanoindentation test was useful in determining the mechanical response variations on the cuticle. However, the mechanical properties of plywood lamella structure considerably dependent on the orientation of fibrous components in the lamella plane. Considering the hardness and Young's modulus value acquired from nanoindentation test is an average from multiple layers in the cuticle, the mechanical properties achieved from nanoindentation test sacrifices the information of the influence of fibre orientation. In addition, because of the complicated macrostructure, the dissected cuticle samples usually need to be embedded in Resin, the inclusion of resin molecules in the sample will inevitably affect the accuracy of the final mechanical values of tested cuticle sample.

2.3.3 Nanoscale mechanics of chitin

Relatively little is known experimentally about the mechanics of cuticle at nanoscale, owing to the experimental challenges involved in

small-scale mechanical testing of biocomposites. At the scale of the chitin molecule, the elastic modulus of the crystalline region in the direction parallel to the chain axis (E_l) is a parameter of interest. The E_l value of chitin is depending on the molecular conformation and the intramolecular hydrogen bonding system in the crystalline lattice. Synchrotron X-ray diffraction can be employed to determine the E_l value of chitin by tracing the lattice parameters change in the crystals formed by chitin molecules. However, the chitin nanofibres within cuticle usually exhibit a complicated 3D orientation distribution which induces great challenge to analyse the data, therefore selected arthropod tissues with simple parallel chitin fibril orientation or extracted chitin fibrils were initially used to characterise the elastic modulus of chitin at the smallest hierarchical level. Using X-ray diffraction on the tendon of snow crab, Nishino et al [77] has reported E_l value of α-chitin as 41 GPa. Annealing at 160°C was performed before tensile tests to enhance the crystallinity of the samples collected from snow crab. Later, a slightly higher E_l value (59.3 GPa) was reported by Ogawa et al [115] by X-ray diffraction test on purified crab tendon (with parallel fibred chitin fibrils) by repetitive treatment with 5% KOH and 0.3% $NaClO_2$ solutions to remove the minerals and proteins. We note that these molecular-scale elastic moduli (40-60 GPa) are much higher than values obtained from macroscopic mechanical tests (1-10 GPa) on similar oriented tissues. Elastic moduli measured parallel to the chitin orientation in the tibial flexor apodeme of the locust gave ~20 GPa [116] and 8.47 GPa from chitin tendon [117]. The much smaller values acquired from macroscopic measurements are likely because they represent the net structure modulus of the entire microstructure rather than the elastic modulus of one single chitin fibre [63], and additional mechanisms

like interfibrillar shear and lamellar level strains are included, thereby increasing total strain and thus reducing the effective modulus. A drawback with the molecular level effective moduli values reported above are that they were either acquired from chemically extracted fibres from biological tissue with no guarantee of the purity of chitin fibre and structural integrity of chitin molecules, or tested *in situ* but assuming a single chitin fibre orientation inside the tissues (or selecting the tissues where this fairly stringent restriction holds). There is thus an unmet need to measure the molecular level stresses and strains in the complex three-dimensional arrangement of typical cuticle tissue *in situ*, as well as to study intra-tissue variations of these nanoscale deformation mechanisms,

2.3.4 Modelling of the multiscale mechanics of cuticle

Due to the limitation of the current material characterisation techniques and complexity in the hierarchical design of cuticle, there is still not enough knowledge available on the structural and mechanical properties in different hierarchical levels of cuticle. This gap is especially true for the intimate interactions between the different components in the micro and molecular level. Therefore, multiscale computing simulation approaches are employed to help identifying the relevant key ingredients with respect to a certain mechanical property (e.g. modulus or toughness) and the tolerance of this property at the overall macroscopic scale against chemical and structural variations. Most multiscale models use fixed averaged values for the properties and volume fractions of the constituents (structural polymers, proteins, minerals) to predict the overall tissue properties [1]. But those models have large drawbacks when applied to the cuticle by neglecting the presence of considerable structural

variation in different hierarchical scales, including the morphological changes from different parts of cuticle (like the regular shaped tergite and complicated shaped telson in stomatopod). A more integrated model needs to be employed to analyse the relationship between the structural design and mechanical properties from all length scales.

Nikolov et al.[52, 97] proposed a hierarchical multiscale modelling approach for the elastic properties of mineralized lobster cuticle using *ab initio* calculations for chitin molecular properties and homogenization performed in a bottom-up order through all hierarchical levels. The term *ab initio* calculations is a computational chemistry method based on quantum chemistry, firstly used in quantum chemistry by Parr and co-workers, including David Craig when studying on the excited benzene states[118], In the case of Nikolov's work, a hierarchical computational approach is employed, which combines valence force field molecular dynamics (VFFMD) with tight binding (TB) calculations to predict the location of hydrogen atoms and hydrogen bonds in α-chitin and then predict the mechanical properties on the molecular level. The summarization of the structural design, experimental methods as well as the simulation methods and predicted Young's modulus value for different length scale of cuticle are listed in **Figure 2.10** [52].

From the modelling results of Nikolov and co-workers [52, 97], it was found that the mechanical properties of cuticle is more dependent on the higher structural levels (larger than the molecular level), through variations of design parameters such as the volume fraction of minerals and chitin-protein fibres, as well the microscale plywood and pore canal structural design. The variations in the elastic property of its chitin and proteins at the lower hierarchical level were found to

have less effect, an three times increase of the elastic modulus of chitin fibrils will only result in less than 30% percent increase for whole in-plane cuticle elastic modulus change, and for protein an increase of elastic modulus will barely change the whole elastic modulus of cuticle [97]. By comparison of the results from multiscale predictions with the experimental data from macro scale tensile and compression tests, micro scale nanoindentation tests as well as molecular deformation data from X-ray diffraction study, it is possible to identify at least the most probable order of magnitude of some of their properties.
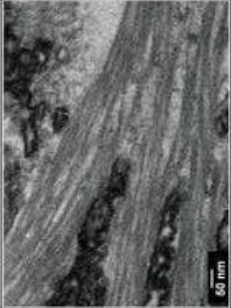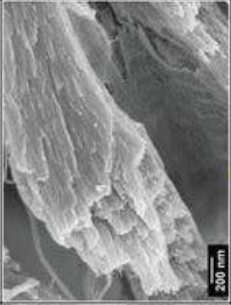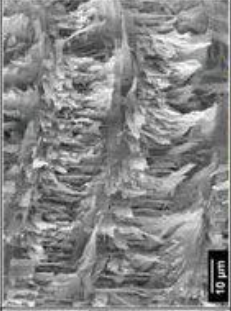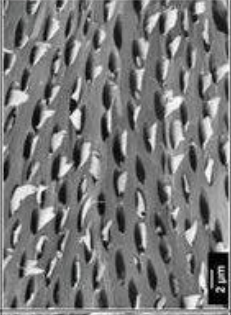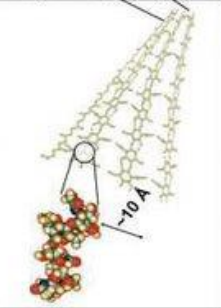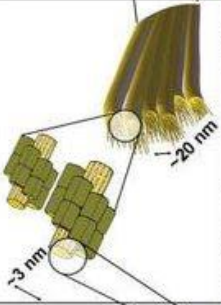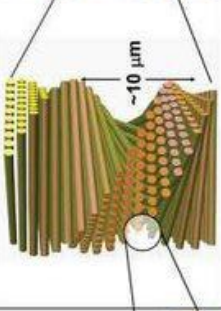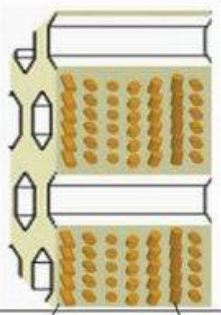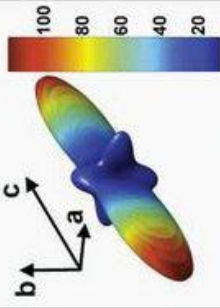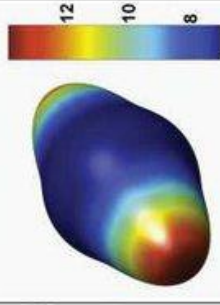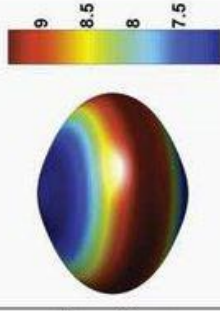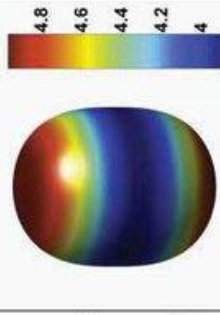
Scale	0.1 nm – 10 nm	10 nm – 100 nm	100 nm – 10 μm	10 μm – 1 mm
Hierarchical structure unit	α-chitin (H-bonded anti-parallel N-acetyl-glucosamine molecular chains)	Mineralized chitin-protein nanofibrils in a planar array	Twisted plywood stack of mineralized chitin-protein planes without pore canals	Twisted plywood stack of mineralized chitin-protein planes with pore canals
Experimental method	Transmission electron microscope	Field emission scanning electron microscope	Field emission scanning electron microscope	Field emission scanning electron microscope
Microstructure				
Schematic				
Simulation method	Ab initio; density functional theory	Mori-Tanaka scheme (chitin-protein fiber); Torquato 3-point scheme (mineral-protein matrix)	Dilute approximation, tensor rotation	Torquato 3-point homogenization
Elastic behavior, 3D maps of Young's modulus [GPa] a,b-axes: basal directions of the chitin unit cell c-axis: longitudinal (chain) axis of the chitin molecule				

Figure 2.10. Overview picture showing the hierarchical structures for cuticle at different length scales. In addition, the modelling methods and corresponding anisotropy prediction for a typical mineral content of 70 wt.% [52].

2.4 Structural specialization of mantis shrimp

2.4.1 Organ and animal level studies

Increasing demand for new, sophisticated multifunctional materials has brought natural structural composites into focus, since these have been optimized in their functions in a long selection and adaptation process during evolution. As a biomaterial scientist, we are interested in finding a biological model with high dynamic mechanic properties which allow it tolerate time dependant loadings. Thereby, stomatopod which is famous for its remarkable dynamic mechanical properties has attracted our attention. The lacking of knowledge of about the structural properties and energy dissipation mechanism make the studying of stomatopod even more attractive for us.

Stomatopods, also known as "mantis shrimp," are an order of marine crustaceans whose fossil record can be dated back 300 million years. The mantis shrimp is a remarkable animal that nearly all parts of its body are optimally designed to fulfil their function (**Figure. 2.11 a-b**). These include both the stomatopod eyes, which allow them to see polarized light and are the most complex visual organs in the animal kingdom, as well as the stomatopod exoskeleton structures which include the fastest appendicular strikers in the animal kingdom. The stomatopod can hurl its raptorial appendages at speeds up to 23ms^{-1} and generate extreme accelerations up to $102{,}000 \text{ m/s}^2$ from a standing start. Indeed, the power of the strikes is so large that stomatopods need to be kept in a specially strengthened aquarium so as to avoid breakage. With an acceleration of close to a .22 calibre bullet and forces up to 1500 N (thousands of times its own body weight ~ 100 g), the greatly enlarged second thoracic raptorial appendages of stomatopods can inflict serious damage on the prey and make them

successful predators in the reef communities where they live. The victims including mollusc shells, crab exoskeletons, the skulls of small fish, which are heavily mineralized biological structures [1]. Note many of these prey items are so-called tough and damage-tolerant biological materials, which make the structural performance of the stomatopod club even more impressive, in context.

Among the large number of species of stomatopods, *Odontodactylus scyllarus* is one of the larger (ranging in size from 3 to 18 cm), more colourful mantis shrimps commonly seen in the Indo-Pacific from Guam to East Africa (**Figure. 2.11b**). At the body level, the second thoracic appendage of *Odontodactylus scyllarus* can be divided into several parts (**Figure. 2.11c**) including the saddle, carpus and meral-V which works together to form an energy amplification mechanism[21, 27], while the club of the appendage which consists of the propodus and the dactyl parts (the terminal segments) are the direct force and energy loaded region when the stomatopod spear or smash on prey, especially the dactyl part [22, 27].

In order to generate extreme acceleration in water, a large amount of energy must be stored and released over a short period. Stomatopods increase their power output using an elastic energy storage and force transmission system consisting of elastic springs, latches and lever arms [22, 27]. While these speed and force amplification mechanisms are of great importance in delivering the high impact speeds necessary for the smashing appendages to fulfil their function, from a material science perspective, the most interesting feature is the structural design of the smashing (Dactyl) and defensive (telson) appendages, at the microstructural and nanoscale.
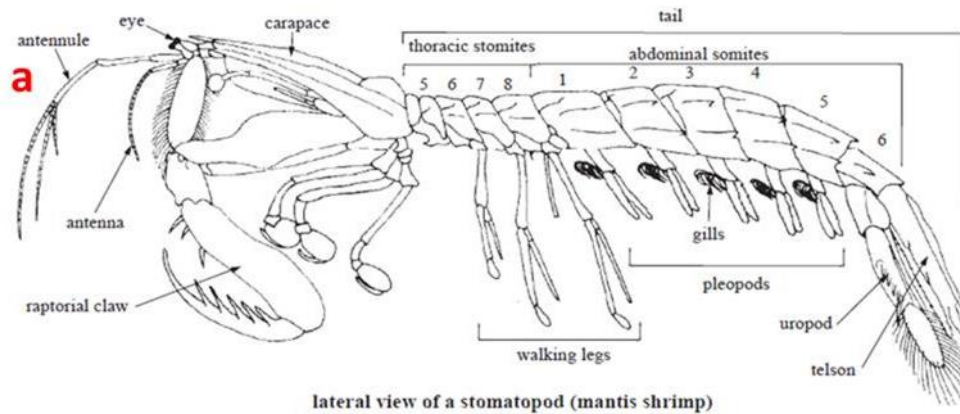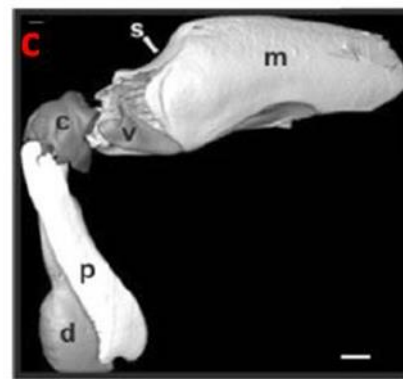
Figure. 2.11. (a): A lateral view of stomatopod [119], (b): Light microscope image of Odontodactylus scyllarus. (c): 3D structural components of the mantis shrimp (m, merus; s, saddle; c, carpus; p, propodus; d, dactyl. v, meral-V; Scale bars, 4mm.). The different colours demonstrate different mineralisation degrees (lighter colours indicates greater mineralization and darker means more poorly mineralized areas) [1].

2.4.2 Structural and Mechanical Properties of Stomatopod Dactyl

The dactyl part has been evolved into two forms depending on species to adapt different functions: a hammer-like dactyl (*Odontodactylus*) which can be used to smash the hard shell of their prey with powerful blow, or a spear-like dactyl (*lysiosquilla*) to impale and grasp the prey. Both types of stomatopod dactyl can deliver fast and powerful strike to destroy their prey but at the same time their own dactyls can survive from the instantaneous reaction forces and the high stresses

generated from the collapse of cavitation bubbles between their appendage and the striking surface [1]. From view of the materials scientist, the stomatopod dactyl serves as a high performance natural composite to be extremely damage tolerant to withstand thousands of highly energetic blows per year before being replaced during periodic moulting events. The micro and nano scale structural information and micromechanics of both the hammer-like [1] and spear-like dactyls [24] have been investigated using Energy-dispersive spectroscopy (EDS), X-ray diffraction, Raman spectroscopy and imaging as well as nanoindentation measurements.

The hammer-like *Odontodactylus* dactyl can be divided into three distinct regions (**Figure 2.12a**) that work together to create a structure harder than many engineered ceramics: the impact region (IR), the periodic region (PR), and the striated region, where the striated region is weak in mechanical properties which act poorly in protect the club from catastrophic fracture. The impact region (50-70 μm thick), located at the impacting surface of the club, is the stiffest region (modulus values from 65 to 70 GPa in both try and wet condition) of the club due to large extent of mineralization (**Figure 2.12b**). Previous literature showed the hardness of the stomatopod cuticle increase with the P:Ca ratio, which indicates calcium phosphate is better for increased hardness compare to the more common calcium carbonate [120]. X-ray diffraction measurements also demonstrated that most minerals in this region are in the form of crystalline hydroxyapatite, which is very rare in the exoskeletons of marine invertebrates. In addition, From synchrotron X-ray diffraction mapping study the hydroxyapatite crystallites within impact region were found exhibiting highly preferred orientation (**Figure 2.12c**) with the (002) lattice

planes oriented parallel to the impact surface[1], while the apatite mineral phase found in bovine bone [121] showed a smaller degree of crystallinity. Due to the higher mineralisation degree and crystalline texture, the dactyl club exhibits a high hydrostatic compressive strength up to 4 GPa, which is even higher than most engineering ceramics such as zirconia or silicon carbide whose compressive strengths are on the order of 2 to 3.5 GPa [1].
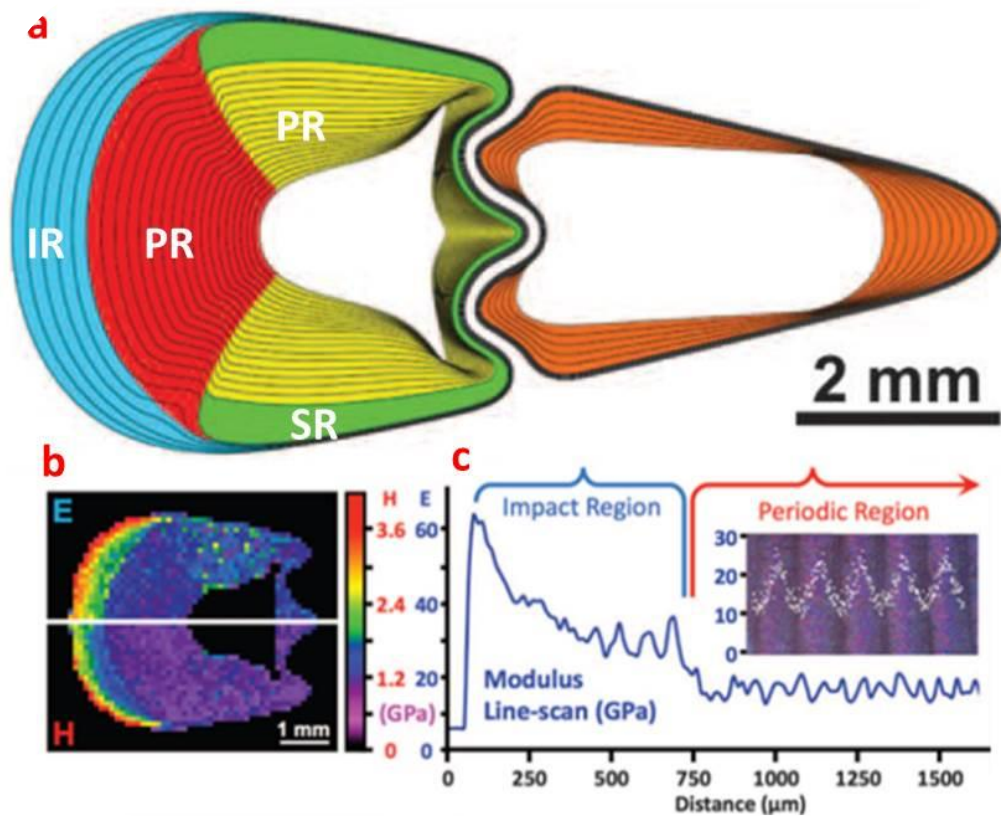
Figure 2.12. (a): Three distinct structural domains within the cross-section of the dactyl club: (i) impact region (IR), (ii) periodic region and (PR) striated region (SR). (b): Nanoindentation map on the dactyl club. (c): Line scan across five layers [1].
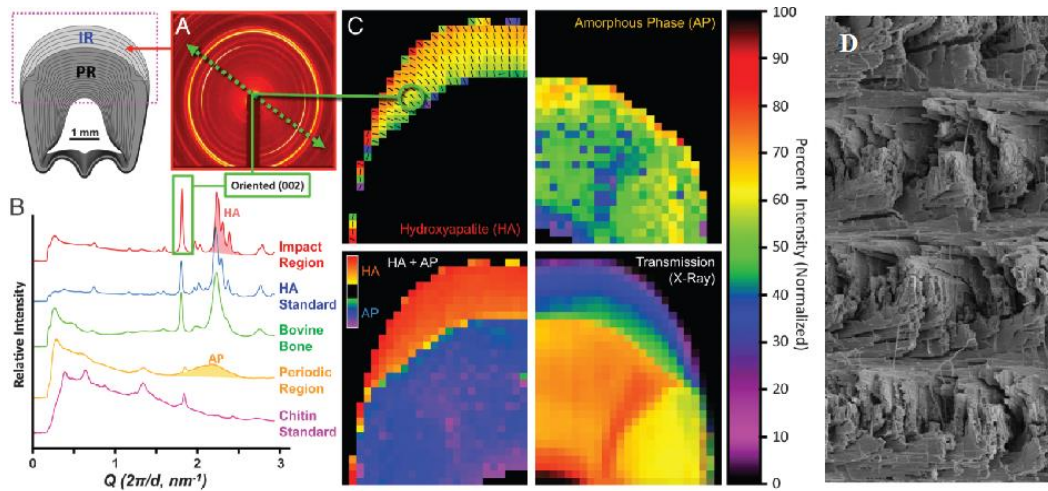
Figure 2.13. Synchrotron XRD analysis and mineral distributions in the dactyl club. (a): Example X-ray diffraction picture acquired from the impact region of the dactyl club. (b): 1D XRD profiles obtained from the impact (IR) and periodic regions (PR) compared with profiles from standard HA and chitin. (c): Mineral concentration maps for the crystalline HA and the amorphous phases. (d):The SEM image collected from the periodic region of dactyl club showing plywood structural of chitin fibril (with periodicity: ~75 μm)[1].

The periodic region is located underlying the impact region (**Figure 2.13**). The structural design in this region is similar with other crustacean cuticles, which is mainly constituted by mineralized chitin fibres which form into Plywood style (**Figure 2.13d**). As we mentioned before, the helicoidal architecture of the chitin fibres can help prevent crack propagation and dissipate energy which make the whole periodic region a second-line defence under attack. Finally, the sharp modulus oscillation between the impact surface and the bulk of impact (stiffer) region can further hinder the propagation of crack [1].

2.4.3 Structural and mechanical properties of stomatopod telson

In order to seize burrows in their natural reef habitats, ritualized duels are ubiquitous among mantis shrimps. However, these behaviours are highly ritualized, and mantis shrimps will only smash on the tails of

each other without injury until one of the contestants backs down (**Figure 2.14**). More specifically, it is the telson at the tail act as a shield protecting the animal in the intraspecific dominance fight. As we know, the smash of the appendages of mantis shrimp is very powerful that the impact will cause destructive damage to a series of so-called tough and damage-tolerant biological structures (mollusc shells, crab exoskeletons); the telson itself must be very robust to resist the powerful punches from other mantis shrimps.
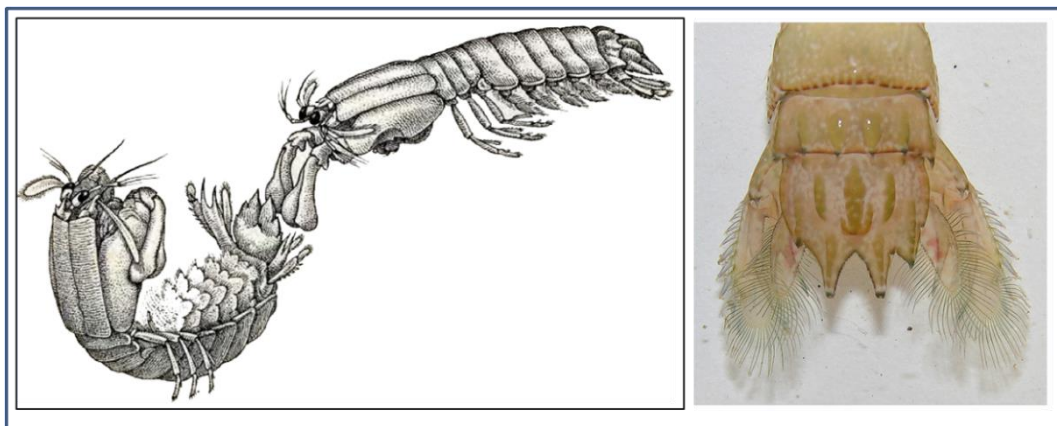
Figure 2.14. The ritualised fights between mantis shrimps [23] (left) and images of its telson (right). Image collected from the internet (http://blogs.thatpetplace.com/thatfishblog/2011/08/11/mysterious-mantis-shrimp-a-look-at-distictive-anatomy-for-species-identification/#.VqivkfmLTIU, 27/01/2016).

Computed Tomography was used to study the structure and mineralization distribution of stomatopod telson [122]. The two images in the left of **Figure 2.16** show macro morphological differences between the surfaces of telson and tergite cuticle. The telson cuticle is about twice the thickness of tergite cuticle as shown in the two right images in **Figure 2.15**. The locations where cuticle thickness was measured were indicated by arrows in **Figure 2.15**. Also compared to the regular shaped tergite cuticle, the telson cuticle has three

distinctive ridges which run along the whole telson which called carina. These carinae do not deform under impacting, but the overall dome of the telson does. Also, the two images in the centre of **Figure 2.15** demonstrated that the carinae part is more intensively mineralized than the surrounding areas, especially in the central carinae. The combination of this mixture of rigid and compliant structures may impart enhanced absorptive capabilities of the telson. Indeed, similar structural strategies are employed in the design of synthetic armour.
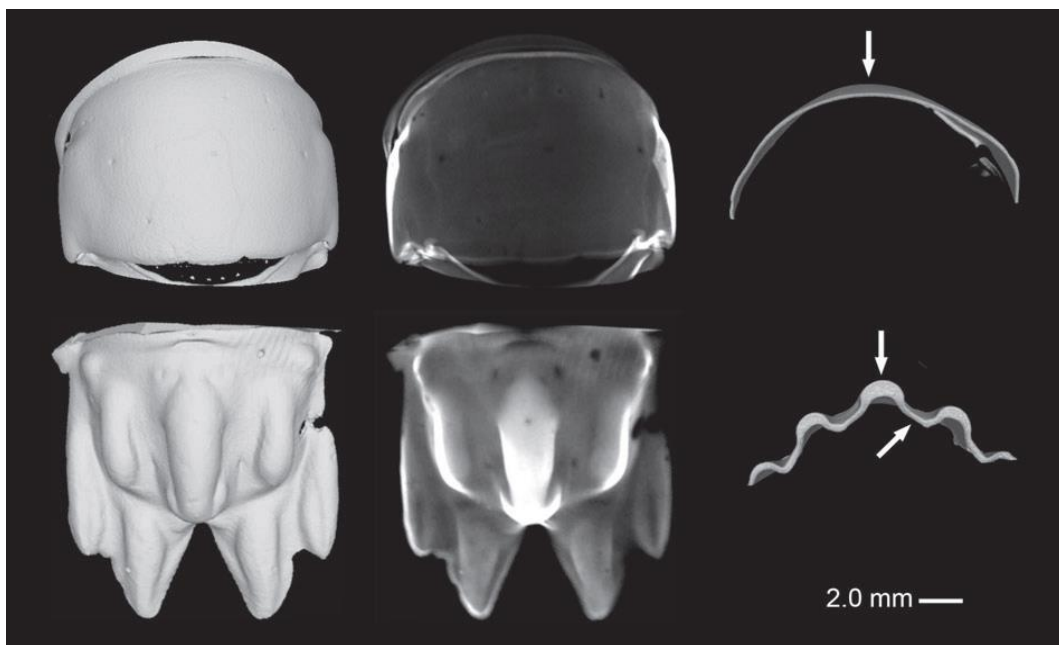
Figure 2.15. Micro-CT images of the fifth abdominal tergite (upper row) and the telson (lower row) cuticle[122].

The coefficient of restitution is a fractional value representing the ratio of speeds after and before an impact between two objects and is widely used to determine whether the impact is elastic or inelastic. In order to examine the features of the punching among mantis shrimps, Patek et al used performed coefficient of restitution by dropping steel balls onto mantis shrimp telsons and recorded the impacts with high

speed video cameras. The results shown that the average coefficient of restitution for the telson (0.56) was significantly lower than that of the tergite (0.67), the telson therefore dissipates 69% of the energy during impact, while the abdomen loses about 55% [122]. This result indicated that the stomatopod telson absorbs impacts in an inelastic way, similar with a punching bag than a trampoline.

However, at the present time, though some significant progress has been made on studying the microstructure and the mechanism(s) of energy dissipation in the stomatopod dactyl and telson, literature on the micro and nano structural properties of these complex organs, as well as how these structures influence the mechanical properties under dynamic loading remains quite limited. quantitative investigation of the nano-scale structural characteristics and how it leads to the extreme impact resistant mechanisms, will provide crucial inspiration in the fabrication of tough ceramic/organic composites like body and vehicle armour, as well as the high impact resistant materials utilized in the aerospace industry [123] as well as high speed projectiles [50].

Chapter 3: Introduction to methodology and design of in-situ mechanical tester

3.1 Theoretical background of X-ray scattering

Different imaging techniques spanning multiple orders of magnitude in length scale have been employed to study the hierarchical design of biological tissues and how the different structure level related to their whole mechanical properties [52, 97]. These include, but are not limited to, synchrotron X-ray microfocus diffraction and scattering [14, 19, 81], transmission electron microscopy (TEM) [124] and scanning probe microscopy [17, 125] at the atomic scale, and confocal microscopy [126, 127] and microcomputed tomography [122, 128] at the micron-scale. Among all these, X-ray diffraction and scattering techniques are capable of providing quantitative information about molecular lattice spacing (wide-angle X-ray diffraction or WAXD)[60, 81], as well as morphology or periodicities at the next-larger nanometre length scale (small-angle X-ray scattering or SAXS) [14, 18, 19]. The specific benefits of WAXD or SAXS structural information is that highly quantitative information can be obtained from samples usually imaged in close-to-native state, and complex sample preparation techniques (with their potential to induce sample damage), such as found in transmission electron microscopy, are not necessary. While laboratory sources for SAXS or WAXD utilize beams of the order of ~100-500 microns [e.g. the Bruker Nanostar], microfocus X-ray beams, using advanced synchrotron X-ray optics, are currently able to combine the molecular level resolution of WAXD or SAXS with micron-scale spatial gradients in nanoscale texture, by means of mapping the spatial variation of WAXD or SAXD patterns

over the scale of microns [44]. SAXS is usually utilized to obtain information at the nanometre (0.1-100 nm) length scale (obtained from a relatively narrow range of diffracting angle ($2\theta < 5°$ for a Cu-Kα source, corresponding to a length scale of 0.154 nm), such as fibril orientation in wood cellulose [129, 130] or mineral shape and orientation in bone [14, 28, 131], while WAXD can acquire information down to atomic and molecular level by using a wider-range of diffracting angles (**Figure 3.1**). In synchrotron microfocus setups, it is in several cases possible to obtain SAXS and WAXD spectra either simultaneously or sequentially by changing the measured Bragg angle when move the sample closer, or further, from the detector.
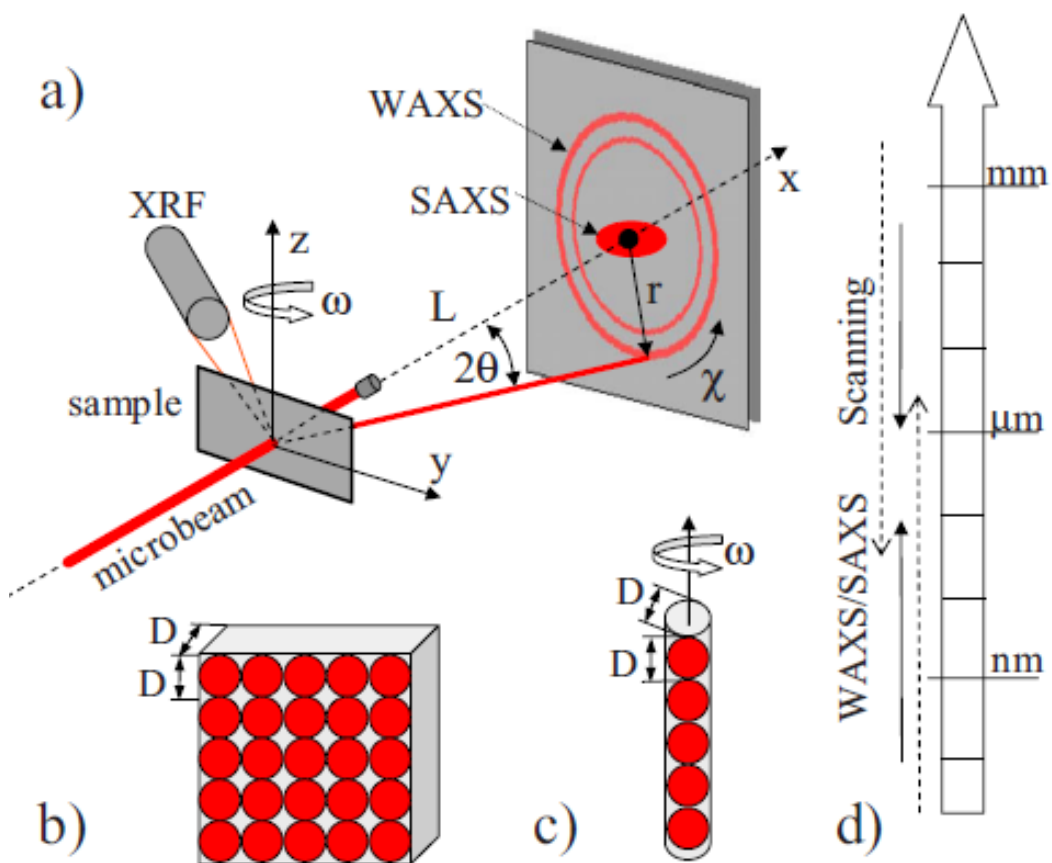
Figure 3.1. *The difference between SAXS and WAXS (WAXD)[36].*

Here, we briefly review the theoretical background of elastic X-ray diffraction and scattering, as found in numerous textbooks [132, 133]. X-rays are electromagnetic radiation whose wavelengths range from 0.01 nm to 10 nm (corresponding to energies in the range of 100 keV to 100 eV). X-rays were discovered by the German physicist Wilhelm Roentgen in 1895; therefore "X-ray" is also referred as ""Roentgen rays". At the beginning X-rays were used mainly in the medical field due to the penetrating power of X-ray radiation. The different degrees of absorption in materials of different densities were used to image skeletal damage or bullets in the human body. However, the use of X-rays to investigate molecular structure (crystallography) was initiated after the discovery of X-ray diffraction by Max von Laue and the Braggs (W. H. Bragg and W. L. Bragg) [134]. In particular, the Bragg's Law relating the manner in which an X-ray beam undergoes constructive (**Figure 3.2**) and destructive diffraction from a lattice was a very significant step forward in X-ray diffraction studies. The Bragg's law refers to the following equation:

$$2d_{hkl}.\sin\theta = n\lambda \quad \text{equation 3.1}$$
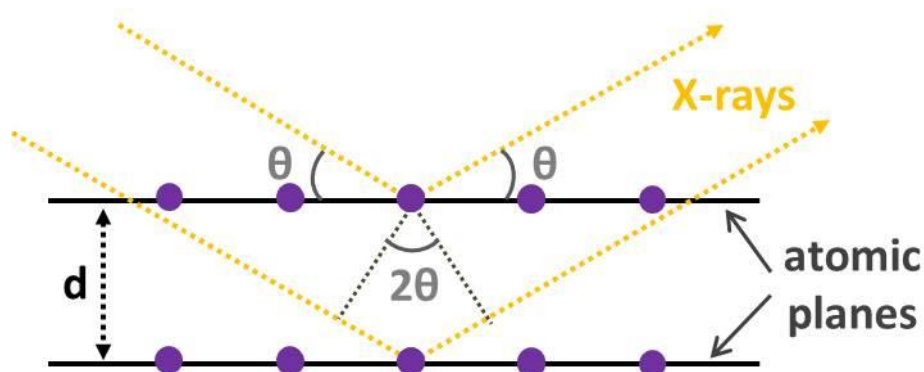
Figure 3.2 Schematic of the Bragg Law.
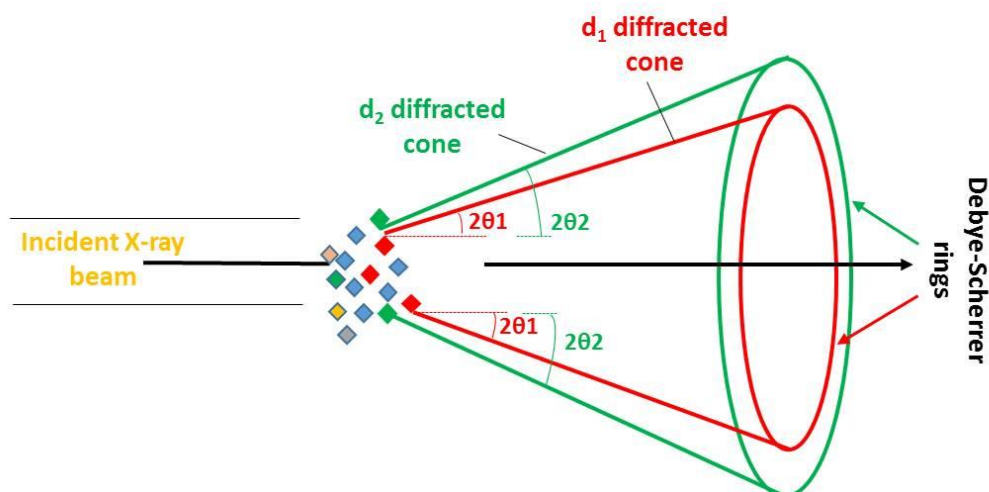
Figure 3.3. Powder diffraction. Image was modified based on the image from internet (http://pd.chem.ucl.ac.uk/pdnn/diff2/kinemat2.htm,28/10/2015) .

In Bragg's Law, the crystal is considered as a set of discrete parallel atomic planes with interplanar distance of $d_{(hkl)}$, where the (*hkl*) are the Miller indices of the crystallographic plane. When the X-ray is incident onto the atomic plane at an angle of θ, at the atomic level the electromagnetic field of the incident radiation interacts with the negative electron charge density associated with the atom. As a result, to first approximation, there is scattered electromagnetic radiation emitted by the atoms, and each atom can be considered a point source of radiation. Bragg's law quantifies the fact that due to emission of X-rays from adjacent atoms, only X-rays at specific (diffracting) angles will undergo constructive interference, specifically when the path length between scattered beams from adjacent atoms is an integral multiple of the wave length λ. In other words, for the wave from a specific atomic plane to be in phase with the wave from the adjacent plane, the wave needs to travel a whole number (*n*) of wavelengths inside the material. Bragg's law allows us to calculate the spacing between neighbouring planes of atoms provided we know the

wavelength of the X–rays, and the angular positions of the diffraction peaks. Generalizing beyond the simple 1D example given above, using the angles of the diffracted peak positions, it is in principle possible to predict the 3D crystalline structure [133]. Conventionally, powder X-ray diffraction, carried out on a powdered (spatially homogenized) sample of a specific material, is used to obtain a 2D diffraction pattern, where a series of Debye-Scherrer rings are visible (**Figure 3.3**) at different integral orders of the different lattice planes present in the sample.

3.1.1 Reciprocal lattice, Ewald sphere construction and diffraction intensity

The Ewald sphere construction is basically a geometric construction that allows one to visualize the properties of Bragg's law (**equation 3.1**), and in particular to show how the geometrical orientation of the sample influences the diffraction pattern. The relationship between the Ewald sphere and Bragg's law is shown schematically in **Figure 3.4**. Consider the centre of the circle as the (real space) origin of diffraction and the point where the horizontal beam exits the circle as the origin of reciprocal space. The construction in **Figure 3.4** shows that for any reciprocal space vector q, only those that fall on the circle will obey Bragg's law and therefore lead to diffraction. For a given crystallographic lattice, diffraction will only happen when those reciprocal lattice points intersecting the circle. In X-ray diffraction, the reciprocal lattice is 3-dimensional and the **Figure 3.4** can be considered as a 2D section in 3D space.
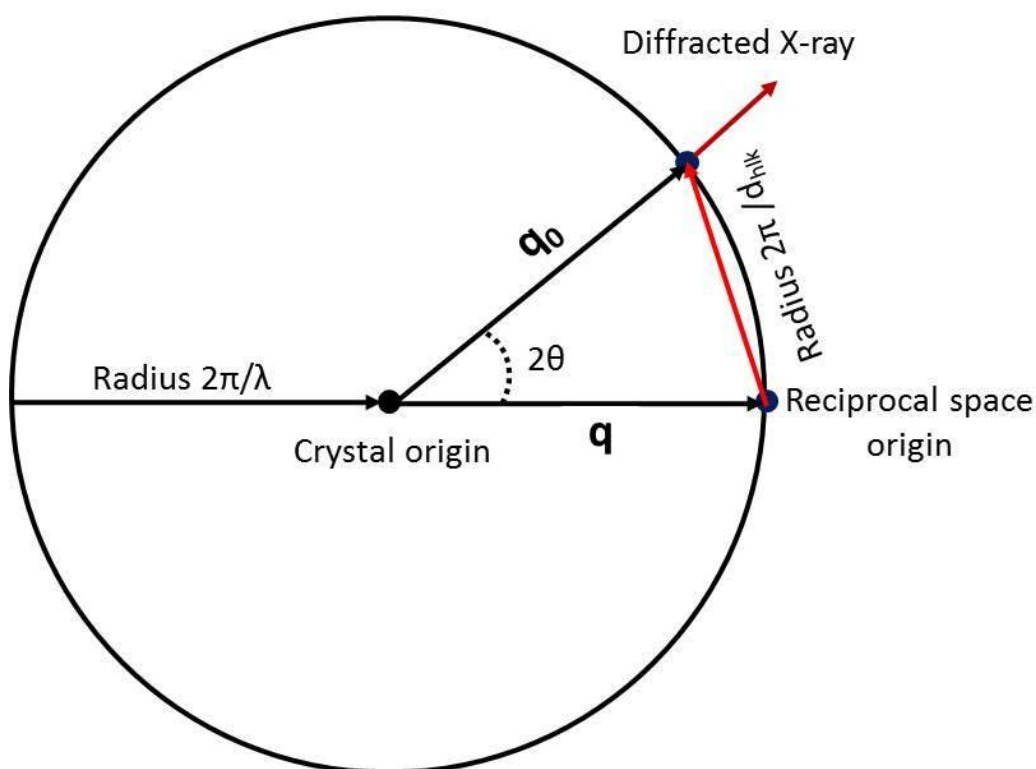
Figure 3.4 Ewald sphere construction.

3.1.2 X-ray diffraction from chitin

As the majority of this thesis will be concerned with the diffraction from the chitin phase of arthropods, we summarize some basic information about the use of WAXD for understanding chitin structure here. Chitin is an ordered polysaccharide, and will generate a diffraction pattern in WAXD. The molecular structure of chitin, as found in arthropods, was addressed by the work of Blackwell and co-workers [59, 98]. Using the oriented locust ovipositor tissue as a model system, the crystalline structure of α-chitin was determined. A representative image of the X-ray diffraction [80]spectrum is shown in **Figure 2.4**. Based on this pattern, an orthorhombic structure of chitin was deduced, as shown schematically in **Figure 2.3** where the lattice spacing is also indicated. Due to the fibre symmetry of the samples used, the diffraction peaks are the intersection of diffraction rings with

the Ewald sphere. It is observed that the orthorhombic lattice is largest in the b-direction. Blackwell and co-workers also proposed a nanoscale model for the chitin fibril/protein sheath structure based on the X-ray fibre diagrams of ichneumon fly ovipositor, except the diffraction peak from chitin, the existence of diffraction peaks for protein indicated the protein in the chitin fibres are ordered which forms subunits arranging around the chitin core in in 6_1 helical array with an axial repeat of approximately 3.06 nm[98].

3.1.3 X-ray diffraction from complex textured biocomposites

In materials science, texture refers to the distribution of crystallographic orientations for a polycrystalline sample. If most of its crystalline components are orientated in a preferred direction, the sample is considered to have a strong texture. On the other hand, when the crystalline components are all randomly orientated, then the sample has no or a weak texture. As discussed earlier, the properties of polycrystalline material depend on the intrinsic properties of components and on the texture of the composites. The anisotropic material properties of single crystals will affect the total properties of the composites to a large extent if the orientation of the crystals are not randomly distributed but are arranged in a preferred direction or form a certain texture. The texture of the materials which occurs naturally or introduced by the manufacturing process therefore becomes an important parameter to be determined in material science.

The texture of polycrystalline material is usually measured with Electron backscatter diffraction (EBSD), tomography and X-ray diffraction[135]. Equipped with modern field emission SEMs (FS-SEMs), EBSD can reach nanometre spatial resolution which makes it

popular for determining texture on a microscopic scale. However, Due to a relatively small penetration depth the EBSD is mainly used on surface characterization. Besides, the sample preparation process of EBSD also may induce considerable physiochemical status changes of the materials which also limited its application for examining biological materials of which material property needed to be determined in its natural environment.

The non-destructive x-ray tomographic techniques are also widely applied in the three dimensional imaging of the texture of the biological materials [136, 137]. The short-wavelength synchrotron radiation has high penetration ability through biological which allows structural examinations for large sample size up to millimetre thickness. Among all the tomographic methods, the conventional transmission tomography or fluorescence tomography are limited on the spatial resolution and not able to detect the individual nanofibres and nanocrystals within the biological composts. The newly developed ptychographic tomography has the potential to reach an isotropic 3D resolution of subnanometer volume but its application are confined to small samples like cells[138] and catalyst particles[139, 140].

For textured and fibril-based biocomposites like bone, wood and cuticle, SAXS and WAXD are the most common methods for obtaining the phase and orientation distribution of the different components. However, unlike the analysis of the powder diffraction pattern, the interpretation of the scattering and diffraction pattern collected from these biocomposites can be challenging. This complexity arises due to the fact that in micro-scale volumes of tissue, all orientations of the diffracting crystallite unit are not equally likely

to be present. For example, in bone lamellae, a sublamellae is characterized by a typical fibril direction [29, 141]. As the mineral apatite phase in bone aligns with the fibril direction [14, 18, 19, 142], it is clear that the mineral crystallites are also preferentially aligned along a main direction in space. Besides, the tilting of lamellae plane in 3D will result in 3D diffraction intensity distribution in reciprocal space. Owing to the fact that most SAXS and WAXD signals are obtained by area detector, only a 2D SAXS and WAXD pattern can be obtained per acquisition while to understand the full orientation distribution the full 3D SAXS and WAXD intensity information is needed. In order to extract the full orientation distribution information, the sample need to be rotated in multiple angular directions relative to the incident beam, whence, by the well-known Ewald construction[133, 143, 144], crystallites oriented at different directions in the sample will successively satisfy the Bragg diffraction condition. The crystallographic texture is then determined by calculating the diffraction data into pole figures as polar maps of the 3D orientation distribution of a specific reciprocal lattice direction in space [44].

One other important approach is to combine the scanning SAXS and WAXD imaging with computed tomography to obtain the full 3D scattering distribution in each voxel of the 3D space. Florian et al. managed to demonstrate that this combined method can be used to extract the orientation distribution of a sample from the nanometre to the millimetre scale by a successful experiment on the human tooth[145]. However, reconstruction for the SAXS and WAXD tomography requires the signals to be rotationally invariant, or at specific conditions when the momentum transfer vectors q of the crystalline components is parallel to the rotation axis. The rotationally

invariant restriction therefore excludes the application of this method on a wide range of biomaterials of which the crystallographic axes are textured in 3D, especially when WAXD signals is needed.

To sum up, the conventional x-ray texture measurements described above are capable to analyse crystallographic orientation in micro textured, spatially graded biomaterials like bone and cuticle in theory. However, they also have some severe drawbacks. Firstly, as tomography measurements usually require long times for large samples like bone and cuticle, it is not easy to test the sample at the synchrotron x-ray source where the beam time is highly limited. If the X-ray diffraction is carried out using a lab-source, the beam size (~100-500 μm) is typically much larger than the scale of the fibrillar or molecular gradients in the tissue: which are, for bone lamellae ~5 μm [146] and for cuticle ~10-30 μm [1]. Hence gradients within this structure cannot be visualized as an average over multiple units of the same structure is obtained. Secondly, even if the microfocus beams available at synchrotrons are used, the thickness of the sample in the direction along the beam direction, together with lateral spatial inhomogeneity perpendicular to the beam, introduces a cross-talk between structurally distinct sample volumes upon sample rotation. Indeed, only in specially prepared sample orientations, as shown for bone lamellae in **Figure 3.5 a-c**, is it possible to carry out sample rotation even along a single axis without inducing cross-talk. Generally, the conditions are that the sample sections have to be of the same thickness as the diameter of the beam (to avoid a tunnel effect) and that the sample must be laterally homogenous in texture perpendicular to the axis of rotation, as shown in **Figure 3.5d**. Last but not least, the long acquisition time needed for the conventional

texture measurements and combined tomography and x-ray diffraction method due to the multiple rotation process makes it difficult to be used in *in-situ* mechanical testing.

Model-based approaches (as opposed to standard texture measurements) [97, 98], which do not require sample rotation, have an important role in obtaining 3D nanostructure intensity distribution information in graded biocomposites. By model based approaches, we mean analyses where a structural form (for instance an array of fibrils with fibre symmetry around the main axis) is for the basic scattering unit, but the three-dimensional angular direction, and distribution around this direction, is a parameter to be adjusted to bring the model predictions in line with experiments.

An example of such a model-based approach is the work of Fratzl and Lichtenegger on WAXD and SAXS scattering from cellulose [129, 130, 147-149]. Here, fibre symmetry was assumed for a cellulose fibre, which led to the reciprocal lattice wave-vectors for the cellulose lattice to be smeared out into rings instead of single points in reciprocal space. The measured diffraction signal can be visualized as the projection of the intersection of the reciprocal space scattering object with the Ewald sphere. For an arbitrarily oriented fibril, these rings will intersect with the Ewald sphere (**Figure 3.6**) at two points. In the limit of SAXS (**Figure 3.6a**), the radius of the Ewald sphere is much larger than the dimensions of the reciprocal sphere, and the intersection points will be separated by 180° on the detector plane. In general, however, this will not be true for WAXD (**Figure 3.6b**), and the peak separation can be less than 180°. The cellulose fibre directions can be deduced by the peak positions of WAXD spectrum [32].
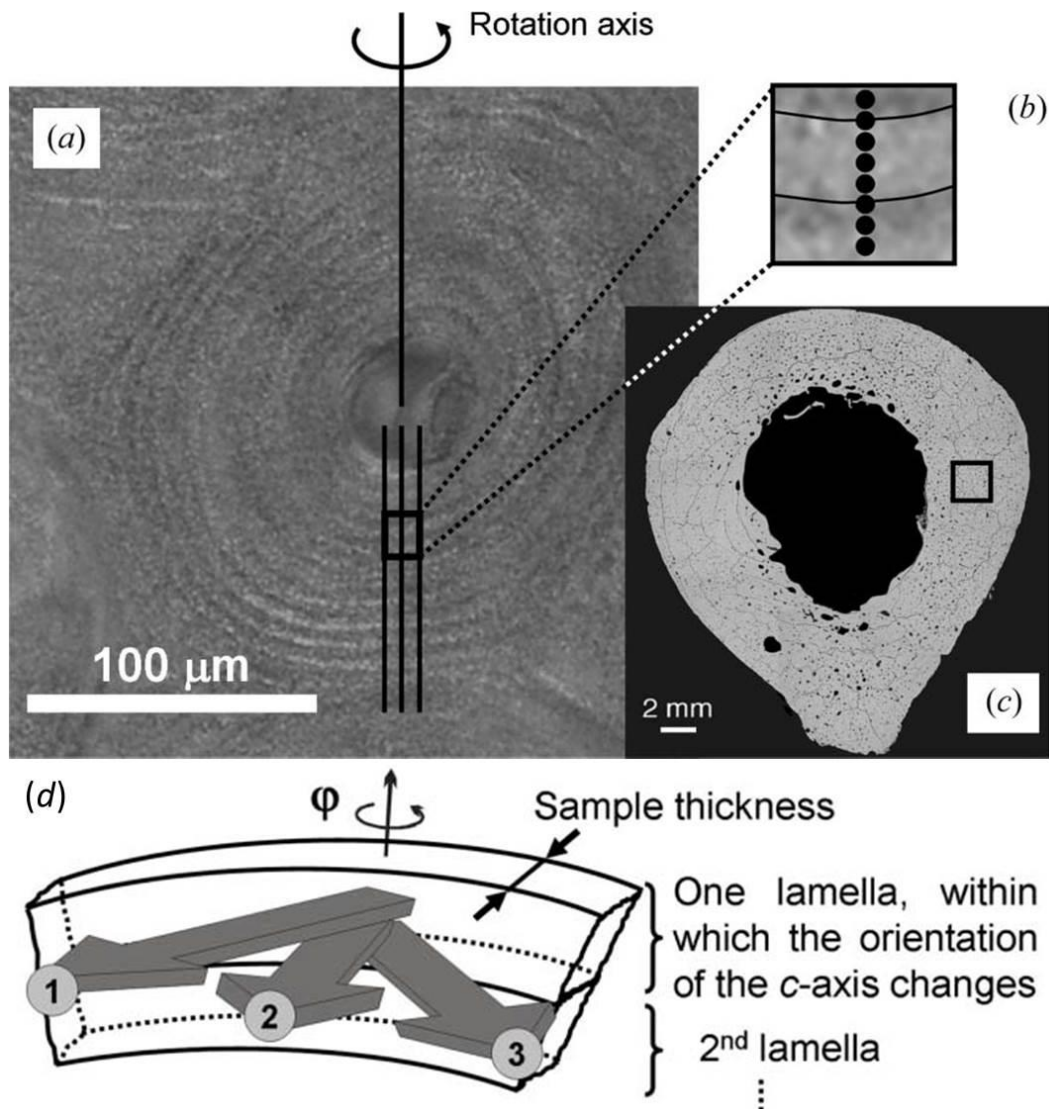
Figure 3.5. *Bone sample used in X-ray texture measurement. (a): The polarizing light microscope image collected from thin human bone sample showing alternating brightness due to the lamellae changes. (b): High-magnification zoom image of five alternating lamellae. (c): Cross section of the femoral midshaft from where samples originate. (d): Schematic showing the direction of c-axis orientation from three different measuring points relative to sample orientation. Images collected from [29]*

Paris and Mueller described the relationship between X-ray diffraction patterns with the 3D fibre orientation distribution of the

cellulose fibrils in more detail [3]. An analytical expression (**equation 3.2**) was which relates the azimuthal intensity distribution measured
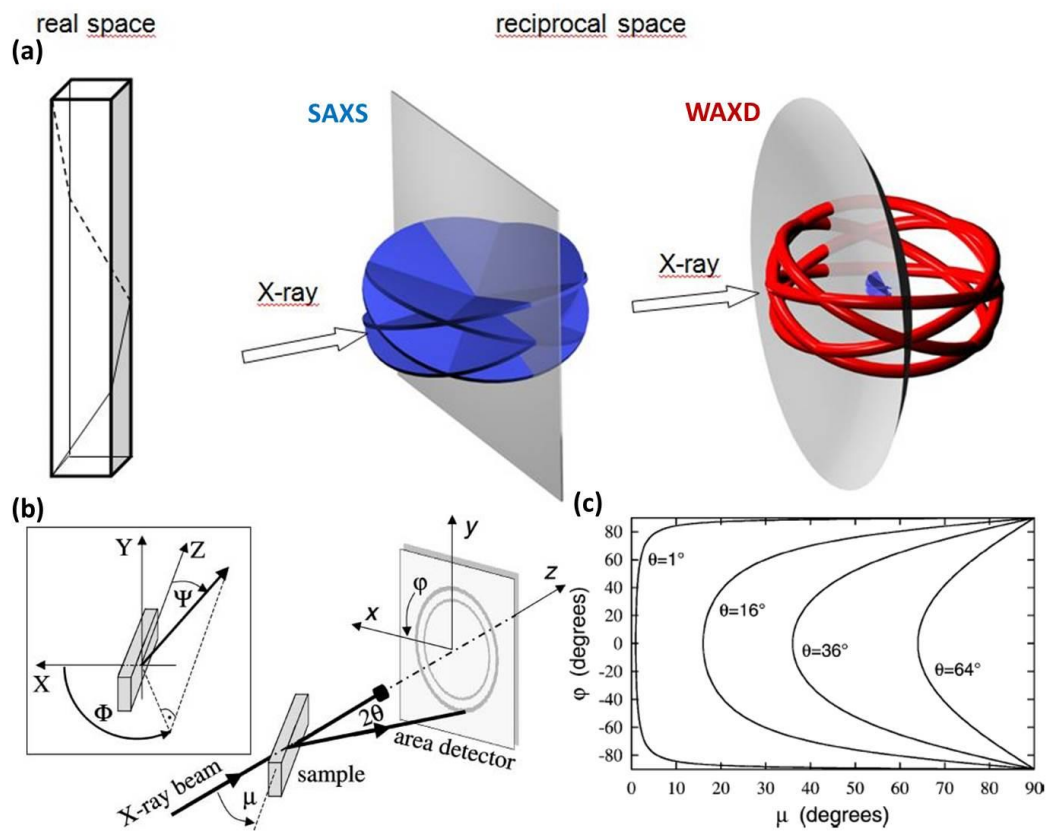
Figure 3.6 (a): Intersection of the reciprocal planes of discs (SAXS) and (002) reflection rings (WAXD) with Ewald sphere, image collected from [2] (b): Sample coordinate system (box) and diffraction coordinate system as described in [3]. Where Φ and Ψ are the angles in the sphere coordinates in the sample coordinate system. The angle μ indicates the fibre axis tilt angle from the main beam direction. The angle φ denotes the azimuthal angle in the detector plane. (C): Azimuthal detector angle φ of Bragg spots as a function of the fibre tilt angle (μ) for selected Bragg angle (2θ).

with an area detector to the orientation distribution of the fibres within the specimen (**Figure 3.6b**) from the microfocus X-ray diffraction test. Note all the symbols including μ, θ, φ and Ψ were define at **Figure 3.6b**.

$$\cos \varphi = \frac{\cos \Psi + \sin \theta \cos \mu}{\cos \theta \sin \mu} \ equation \ 3.2$$

However, little information exists on the general case encountered in experiments, which is a distribution of fibre orientations (for example in a lamella) with a certain body-fixed frame, rotated into the general laboratory measurement frame via Euler angles. In the course of this thesis, a general relation will be derived for the case of diffraction from chitin lamellae, and here we note only the need for such a treatment.
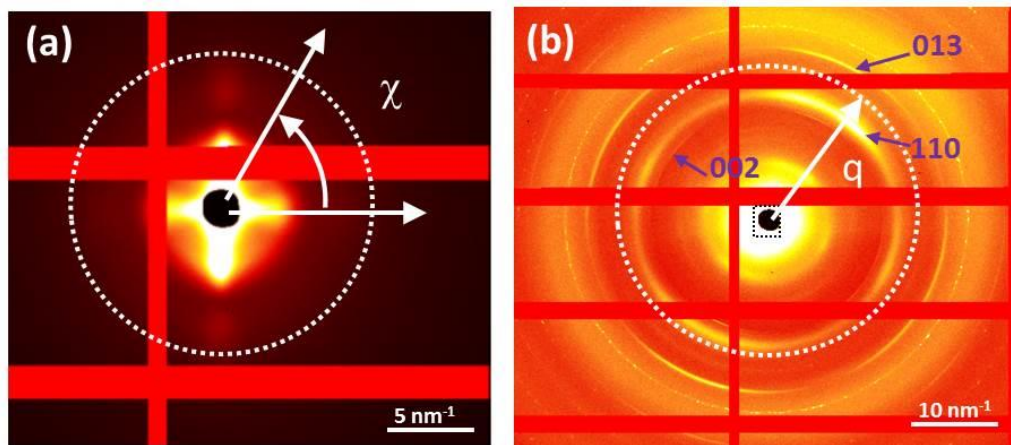
Figure 3.7. *SAXS (a) and WAXD (b) pattern example from chitin. (The red lines in both the patterns indicated the masked region in Fit2D).*

3.1.4 Two-dimensional and one-dimensional data reduction

The scattered diffraction (or scattering) intensity on the detector is denoted by I (q,χ), where q is the reciprocal wave vector (along the radial direction) and χ the azimuthal angle on the detector plane (**Figure 3.7**). To reduce the two-dimensional diffraction intensity to azimuthally or radially averaged intensity profiles, software processing packages like Fit2D [150, 151] can be used. The CAKE command in Fit2D can rebin the diffraction intensity into a (q,χ) coordinate system, whence an averaging across rows or columns in

the rebinned data leads directly to the azimuthal or radial profile. The mask region in Fit2D indicated that the pixels in the selected region are subsequently excluded from any data reduction process.

Azimuthal intensity profiles I (χ): In the case of anisotropic scattering, the azimuthal angular intensity dependence of a diffraction ring arising from a specific lattice plane *d* (e.g. (110) or (002) in chitin) is of interest. In order to obtain this angular dependence, the intensity at the equivalent wave vector $q_d = 2\pi/d$ is averaged over a narrow radial sector, and corrected for the contribution of the diffuse background scattering using ring subtraction method. A thin upper ring and inner ring were selected whose radius is larger (q_{upper}) and smaller (q_{inner}) by an equal amount than the radial sector where (110) reflection (q_{110}) located. The corrected intensity distribution for (110) reflections then (I_{cor}) will be the raw (I_{raw}) minus the average value from the integrated intensity distribution from outer (I_{outer}) and inner ring (I_{inner}) as shown in **equation 3.3**.

$$I_{cor} = I_{raw} - \frac{I_{outer} + I_{inner}}{2} \quad equation\ 3.3$$

An example WAXD spectrum from an oriented section of chitin is shown in **Figure 3.8a**, where the corrected azimuthal intensity profiles I (χ) for (110) reflection of chitin is also plotted (**Figure 3.8b**). It is observed that there is a strong azimuthal dependence of the intensity around the detector plane. Further, the height of the two main peaks in the (110) profile are asymmetric. The origin of these phenomena in terms of a structural model (following the discussion in the earlier section 3.1.2) will be discussed in more detail in **Chapter 4**.
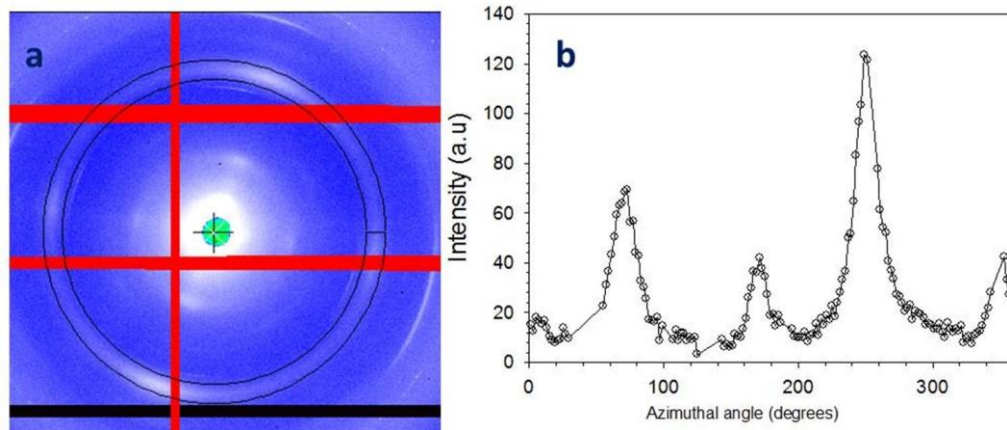
Figure 3.8. *Example WAXD pattern from chitin (a) and the corresponding I (χ)*
curve plotted for the (110) reflection.

Radial intensity profiles I(q): X-ray diffraction has been widely used
to measure the strains of polycrystalline materials[33, 152-154]. When
a material is under tensile or compressive strain, the crystal lattice will
be elongated or contracted correspondingly and induce changes for the
spacing of the {hkl} lattice planes. By tracking the changes of lattice
spacing of one or multiple special lattice planes one can evaluate the
strain and stress for the crystalline components inside the
polycrystalline materials. Furthermore, by precise measurement of
shift of lattice spacing from initial value while the specimen is under
external load or environmental variation the material properties of the
specimen can be characterized *in-situ*. In order to measure the lattice
spacing of the different crystallographic axes, azimuthally averaged
profiles of intensity are needed, where the peaks of intensity are at
multiples of $2\pi/d$ where d is the lattice spacing of interest. However,
the definition of the azimuthal averaging sector requires special care.
For perfectly oriented crystallites along the vertical direction, the (002)
peak of 0.512 ~ 0.520 nm (in the case of α-chitin) will be a single
diffraction spot along the vertical direction. Hence, a narrow
azimuthal angular sector centred on 90° is required, rather than an

average from 0 to 360°. Further, as will be explored in more detail in **Chapters 5** and **6** on tensile and bending deformation of cuticle.

3.2 Synchrotron radiation sources

From the review of the hierarchical structure of cuticle in **Chapter 1**, it is clear that in order to determine the molecular- and supramolecular architecture of cuticle, it is necessary to obtain X-ray diffraction spectra from micro-scale resolved volumes and (in order to study *in situ* mechanics) with sub second level time resolution. In order to obtain such X-ray diffraction spectra with high spatial resolution (~microscale) and time resolution (~ms to seconds), special X-ray sources known as synchrotrons are essential [36]. Synchrotrons are sources for generating very high brilliance X-ray radiation, with controllable energy, monochromaticity and other parameters, depending on the experimental technique to be utilized. Here, we briefly review the working principles of synchrotrons. Electrons are generated in an electron gun, very like the cathode ray tubes found in older TV sets. They are then accelerated up to very high speeds, close to that of light, through a series of three particle accelerators. These accelerators are the linear accelerator (LINAC), the booster synchrotron and the storage ring. The kinetic energy of electrons (200 million electron-volts in ESRF, France) was largely increased by a series of oscillating electric potentials along the LINAC. The electrons then been injected into the booster ring where the electrons were further accelerated up to 6 billion electron-volts (ESRF, France) before being injected into the storage ring. The storage ring is polygon tube consists of straight sections angled together with bending magnets. These bending magnets generate uniform, vertical magnetic fields (also called dipole fields) within the beam pipe which guide the

electron beam around the ring. Ideally, each bending magnet would produce a uniform, vertical magnetic field through the beam pipe. This field is also called the dipole field.

As the accelerated electrons pass through each magnet they lose energy, which is emitted in the form of electromagnetic radiation. In the third generation synchrotrons insertion devices such as wigglers or undulators are incorporated into the straight sections of the storage ring to change the direction of the beam and hence increase the brightness of the beam before entering the Beamline [155]. From the storage ring the radiation is then be channelled out into different beamlines (**Figure 3.9**). For some beamlines, additional insertion devices were used to tune the energy of the beam.

In the beamlines, different experiments are carried out using further optimised radiation beam. Usually a beamline is divided into an optics hutch, an experimental hutch and a user control room. The radiation beam coming out from the storage ring is filtered and focused in the optics hutch and then pass through the experimental hutch where the sample is placed. However, to avoid the radiation damage, the users will be controlling the sample stage or other experimental conditions in the user control room. Various techniques have been developed to generate micro and nanofocus X-ray beams including Fresnel zone plates, compound refractive lenses, Kirkpatric-Baez mirrors and Bragg-Fresnel optics. The wide range wavelengths choice and high brilliance of the synchrotron X-ray provides incisive probes for a wide range of applications from materials science, advanced chemistry and physics, food engineering, environmental sciences, structural biology and pharmaceutical sciences. During my PhD period, synchrotron experiments were performed in various synchrotron beamlines such as

I22 in Diamond Light Source (UK), mySpot in BESSY II (Germany) and ID02 in ESRF (France). The energy of electrons for the I22 beamline where we collected most of the WAXD patterns are ranging from 12 - 15 keV and the flux level can reach 1.2×10^{13} photon/s. For some biological samples, some radiation-absorbing materials like molybdenum and lead are used to lower the flux level for radiation concern.
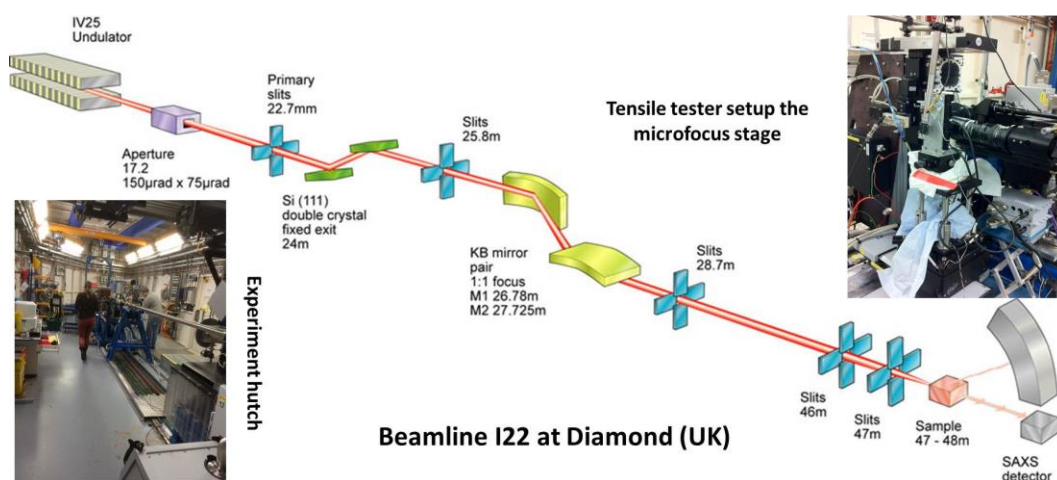
Figure 3.9. *Layout of I22 beamline in Diamond Light Source. The schematic picture from website for Diamond. The images for the experimental hutch as well as the tensile tester setup were taken during the synchrotron experiment.*

3.3 Design of tensile tester

In order to perform tensile and bending test to investigate the overall mechanical material properties, a new tensile tester and bending tester have been designed by us and manufactured with the help of technicians in the school.

Since the mechanical testing need to be applied in-situ in the synchrotron beam line, the testers need to be able to fit in the whole synchrotron setup. However, the conventional mechanical testing rigs (Instron™ etc.) usually are not designed for synchrotron setup

requirement. Therefore, two custom made micro- mechanical testers were made to be able to adapt to the beam line setup. A tensile tester (**Figure 3.10**) and a four-point bending tester (**Figure 3.12**) were designed and both equipped with fluid chamber in order to keep sample in dehydrated state during stretching or bending.

The tensile tester is an updated design based on the previous synchrotron tensile tester which was mainly used for bone samples. The new tensile tester is designed to accommodate the longer cuticle specimens (10-15mm) and other biological samples like sea cucumber and sea urchin. Due to the variation of sample length for different samples, we discard the old design of using two M110.1DG motors (Physik Instrumente, United Kingdom, 5mm travel range each) system and replace it into one motor system to get a larger travel range of 25 mm. The high-resolution M126.DG1 motor (Physik Instrumente, United Kingdom) can sustain a maximum load of 200N and with minimum incremental motion down to 0.1μm. All the important parts for the tensile tester are indicated with numbers and in the list (**Table 3.1**) explained the source of those different parts.

A load cell is a transducer that is used to create an electrical signal whose magnitude is directly proportional to the force being measured. The various types of load cells include hydraulic load cells, pneumatic load cells and strain gauge load cells. The strain gauge load cell contains four resistors in a Wheatstone bridge configuration. When a strain applied to the specimen due to a mechanical force, the resistance of the sensing resistors in the Wheatstone bridge will change accordingly. The unbalanced resistance inside the Wheatstone bridge result in an electrical signal (voltage) output which will then amplified by an amplifier.

Comparing to original tensile tester, the fluid chamber is made wider so it is easier to assemble, which is crucial for the in-situ test in synchrotron where time is precious. The chamber door was made of transparent cast acrylic so the deformation of specimen under loading can be recorded by camera during lab testing. However, during the synchrotron test, the window area of chamber door will be replaced by Kapton film to reduce X-ray absorption by acrylic window. In addition, the original 22N load cell (RDP Electronics Ltd, UK) was replaced by 110N load cell (RDP Electronics Ltd, UK) to make the tester versatile for different sample types.

The sample holder design was kept almost the same, only the M2 thread was replaced by M3 to make the sample change process easier and time saving. The front side of the sample holders were designed with a circular shaped hole (6 mm in diameter and 3 mm in depth) to place the dental cement (Filtek TM Supreme XT, 3M ESPE, USA) which was used to embed cuticle samples. This sample gripping design avoids any additional forces applied on the fragile cuticle specimens by conventional tightening gripping systems, which may introduce stress concentrations at the grip ends. While the back side of the sample holders were designed to be flat to fit thin and flat samples which do not need to be embedded in advance. Both sides were equipped with M3 screw holes and clamps to further fix samples during testing. The whole sample preparation process will be explained later in **chapter 5**.

Number	Name	Source
1	M126 motor	Purchased
2	Load cell holder	Made in lab
3	Load cell (100N)	Purchased
4	Sample holder	Made in lab
5	Sample clamp	Made in lab
6	Specimen	Prepared in lab
7	Dental material	Purchased
8	Fluid chamber	Made in lab
9	Base	Made in lab
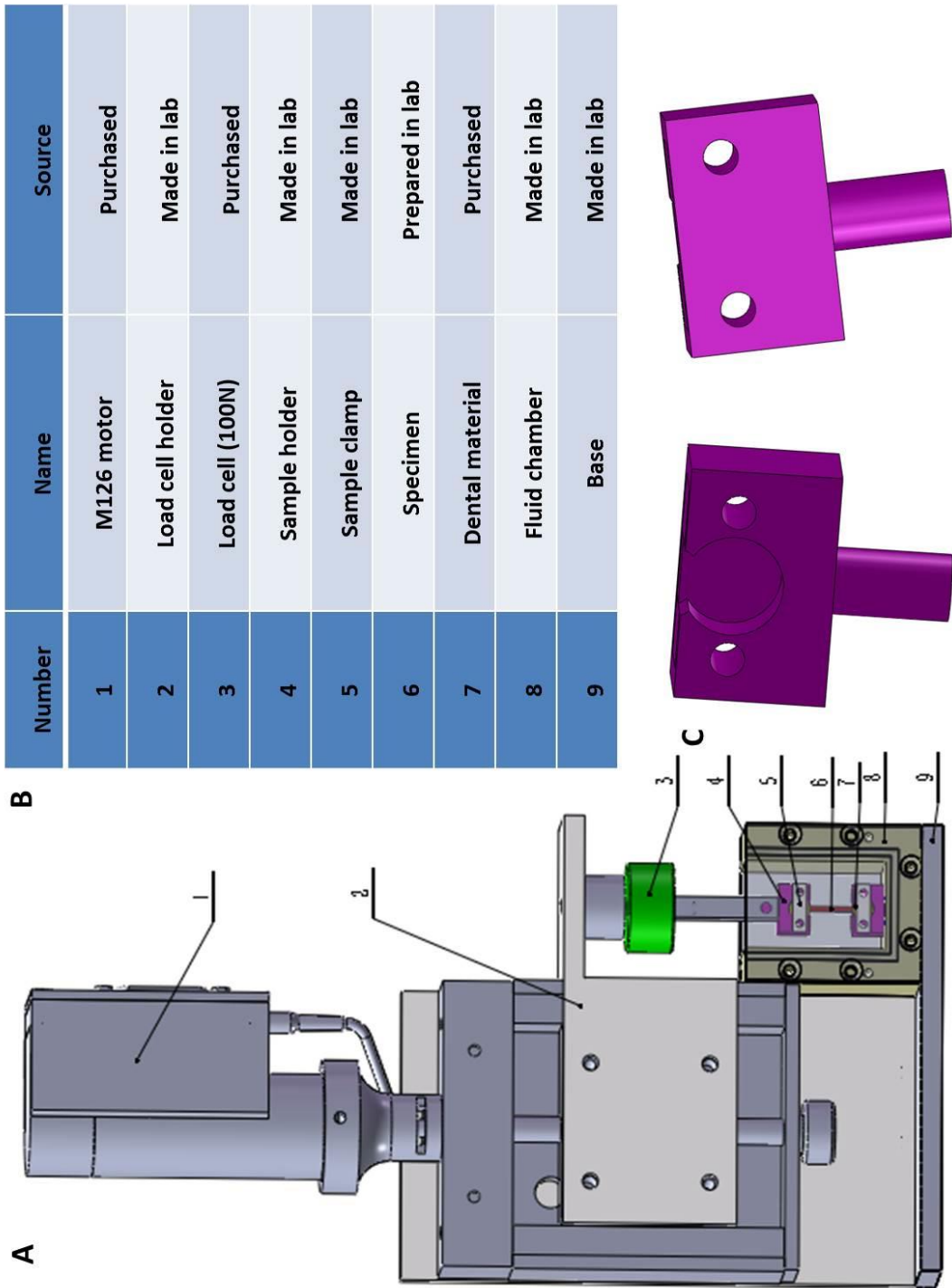
Figure 3.10. Tensile tester. (A): Sketch for the tensile tester. (B): List of the important parts in the tensile tester. (C): Detail image of the both sides of the sample holder.

3.4 Design of four-point bending tester

In order to study how the entire stomatopod cuticle responds against external loadings, a four-point bending tester was designed and manufactured to accommodate the telson and tergite samples with complex shapes.
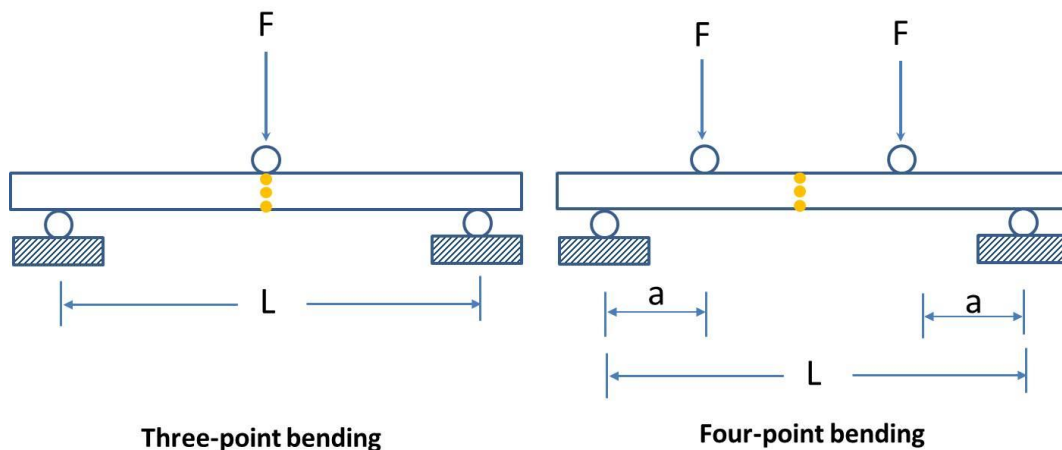
Figure 3.11. *Schematic diagrams of the three-point bending test and four-point bending. The yellow solid points indicate the beam hit locations during the synchrotron tests.*

Usually, three-point and four-point test are the two most common configurations which are used to obtain mechanical properties like flexural strength and flexural modulus [156]. The peak stress introduced by three point bending locates at the middle point of the specimen mid-point (or contact point) with reduced stress elsewhere, while the peak stresses produced by four-point bending are over an extended region on the specimen. Hence, the four-point bending test avoids stress localization and premature failure. Therefore, four-point bending test is more beneficial for investigating the mechanical responses variations across large areas of the telson cuticle. Also, the loading pin in the three point bending system will block the outlet X-

ray under the load pin where the most important regions usually locate thereby will affect the scattering and diffraction patterns we acquired from synchrotron tests, especially in the WAXD condition where the diffraction signal are widely spreading after hitting the sample (**Figure 3.11**). For the above reasons, a four-point bending configuration was used when designing the bending test. The tester was manufactured by the technicians in SEMS according to the 2D Solidworks drawings offered by us.

As shown in **Figure 3.12**, the four-point bending tester includes two motors with a travel range of 5mm each (M110.1DG, Physik Instrumente, United Kingdom) which give a 10 mm displacement range. **Figure 3.13** shows the detail designs for the upper loading pin system and the sample holders inside the fluid chamber. The motors are also controlled LabVIEW programme which developed by technicians in our department. A 22N load cell (RDP Electronics Ltd, UK) and matched amplifier (RDP Electronics Ltd, UK) were incorporated to record the loads during bending test.

In order to facilitate the process of sample exchange, a double lip seal was used to connect the fluid chamber with the bottom holder which connects to the motors. Therefore, the fluid chamber can move up and down freely without leaking of fluid. During the bending test, the fluid chamber will be moved up enable the samples being immersed in the fluids while after the test the fluid chamber will be moved down to leave room for mounting and dismounting samples.

Number	Name	Source
1	M110 motor	Purchased
2	Top holder	Made in lab
3	Load cell (22N)	Purchased
4	Loading pin system	Made in lab
5	Sample	Prepared in lab
6	Fluid chamber	Made in lab
7	Sample holder	Made in lab
8	Double lip seal	Made in lab
9	Bottom holder	Made in lab
10	Tester fixter	Made in Lab

Table 3.2. list of important parts for bending tester.
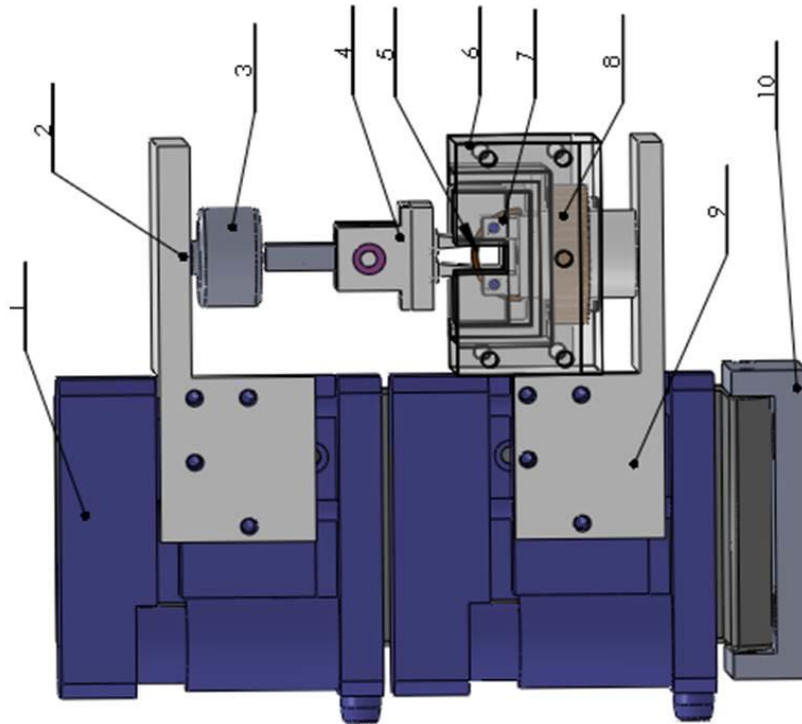
Figure 3.12. Sketch for bending tester.
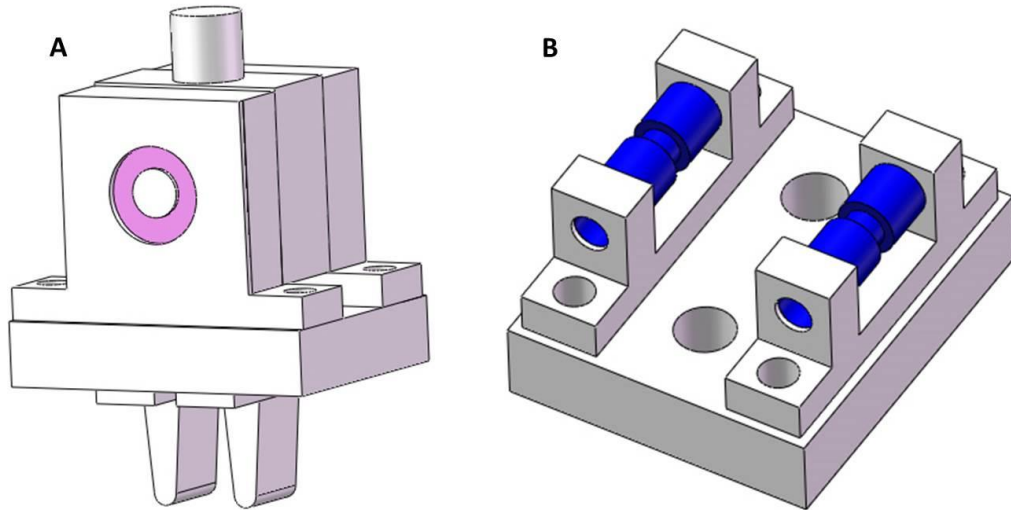
Figure 3.13. *Detail designs of the upper loading pin system (A) and the bottom sample holder (B) in the four-point bending tester.*

3.5 Digital image correlation

The digital image correlation (DIC) method is 3D, full-field image technique to measure contour and deformation of specimens under mechanical testing. Due to the rapid developments in high resolution digital cameras and computational methods, the DIC technique has been incorporated into the static and dynamic mechanical testing to increase the accuracy of strain measurements. The DIC method has already been successfully employed to measure the heterogeneity of elastic–plastic displacement and strain fields in metallic materials with heterogeneous microstructure [157, 158]. For biological composites the DIC technique is extremely useful because they are comparably small in volume and sensitive the traditional grip methods. The biological samples for mechanical testing usually need to be embedded in dental materials which result in large difference between the real tissue strain and strains from the motor position change due to the sample sliding inside dental materials under loading. Previous

tensile testing experience for embedded bone samples show the motor strain can be several times of the tissue strains acquired from DIC analysis. Therefore, in this thesis the technique was developed to measure the deformation of the cuticle sample on tensile and bending tests.

The whole method is based on the recognition of geometrical changes in the grey scale distribution of digital images before and after deformation. As shown in **Figure 3.14a,** the initial unstrained image is mapped by a grid of square facets which is defined by the facet size and the step size (a). The number and size of facet can be determined according to different mechanical test types and resolution requirements. For the tensile test on the cuticle samples, only two squares which represent the places of interests located on both end of samples. The facets are characterized by the grey scale distribution and the corresponding dimensional coordinates are assigned to the facet centres[159]. After straining, the new grey scale pattern is again analysed and the new coordinates which contains the same grey scale distribution with the initial facets are determined **(Figure 3.14b)**. The strains then can be determined by the facet centre coordinates changes before and after straining. The spatial resolution of the method, therefore, depends only on the resolution of the images collected during the mechanical tests and the quality of the selected facets for the place of interests.
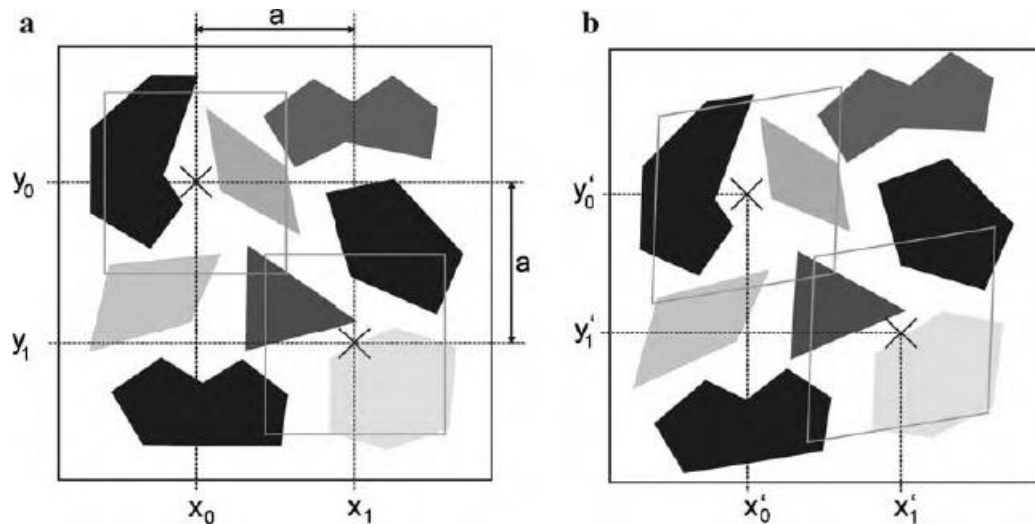
Figure 3.14. Pattern recognition of the facets with the centre coordinates x0/y0 and x1/y1 before (a) and after deformation (b)[160].

The images used for the DIC analysis were collected using a Basler scA1600-14gm GigE camera (Germany) with a resolution of 1626 pixels * 1236 pixels as well as a fast frame rate (14 fps). The image correlation software programme was updated based on the in-house LabVIEW/NI Vision-based digital image correlation package which running at Windows XP system [161] with the help of technicians in SEMS. Currently it can run in Windows 7 system.

Figure 3.15 shows the user interface of the software. The images acquired during the tensile tests will be loaded together with the file where the corresponding motor strains were saved. Two red rectangles (shown in **Figure 3.15**) will be placed on each end of the sample to select regions of interest. The positions of the two rectangles can be easily changed by control panel under the image window. The image strains which were considered as the tissue strain will be captured automatically once the programme went through all the images which corresponding to different motor strains. After that, the motor strains and tissue strains were plotted together in SigmaPlot and the ratio

between motor strains and tissue strains was obtained by fitting the curve using linear function.
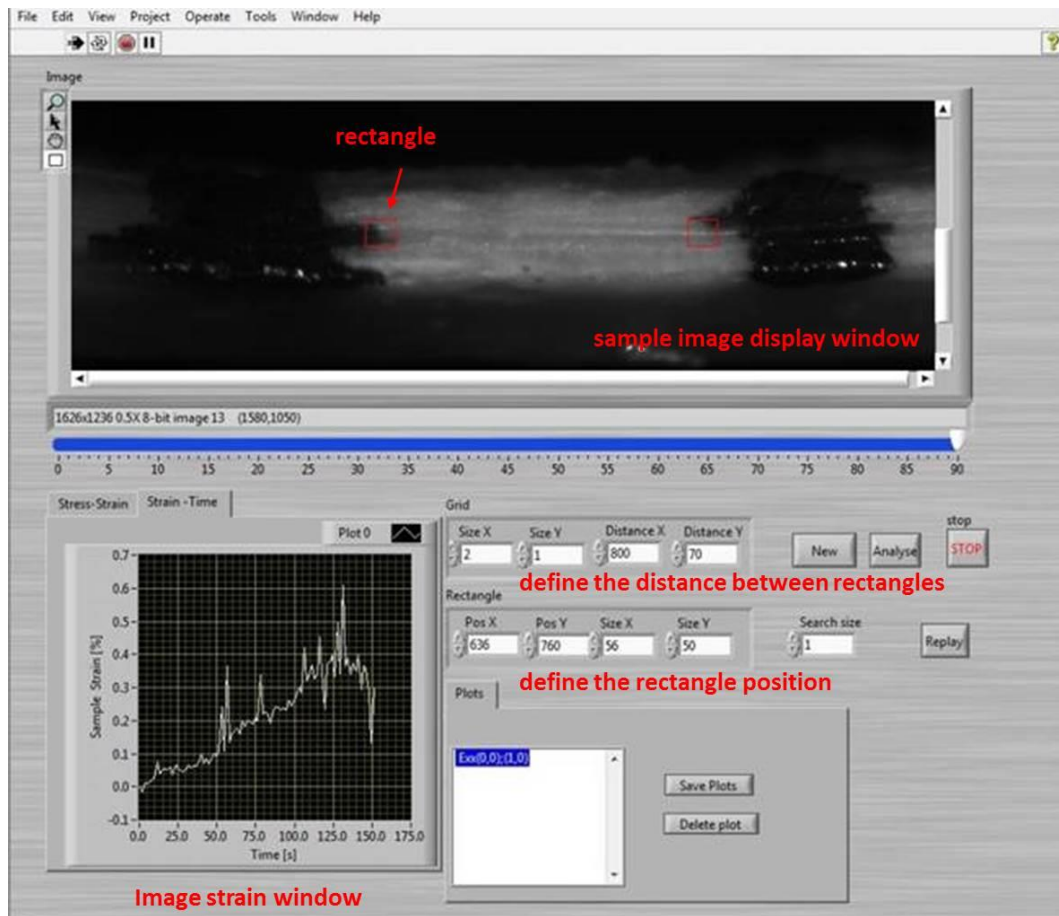
Figure 3.15. *The interface of digital correlation programme developed to measure the tissue strain.*

Chapter 4: The graded three-dimensional chitin fibril orientation in an impact-resistant biological armour (stomatopod telson)

4.1 Synopsis

As discussed in Chapter 2, the stomatopod telson is a specialized exoskeleton cuticular segment, designed to resist loading without damage [4, 21-23]. A schematic Figure showing the multiple levels of structural hierarchy is shown in **Figure 4.1**. The basic material component of a stiff chitin fibrils surrounded by amorphous cross-linked protein matrix, together with water and a calcium carbonate/phosphate biomineral phase has evolved into a range of functionally different structures via structural differentiation at meso- and microscopic length scales. These functions include flexibility [92] or ability to pierce prey [59]) and are achieved by finely-tuned spatial gradients [81, 86], and compositional [1] and ultra structural [87] variations. Biological examples include the biting pincers of lobster for localized application of crushing and tearing forces [44], the hyper-extensible locust ovipositor designed deposit eggs deep into sandy ground [58], the vibration sensing pads of spider sensilia [44], and the controlled iridescence of certain beetle cuticles [1]. Considering the material-performance indices of high toughness and impact resistance, a remarkable example of this type of functional specialization is observed in the armoured exoskeleton of stomatopod (mantis shrimp), which is able to absorb and transmit some of the highest forces in the animal kingdom [24, 47].

Specifically, the armoured tail segment of the stomatopod, known as the telson [53, 98, 99] (**Figure 4.1 A1-A2**) is an ideal model system to analyse multiscale material adaptations to resist high rate loading. The function of the telson is to withstand extremely high loading impacts from blows by the clubs (dactyl) of competitor stomatopods [63, 100]. While the dactyl has been the subject of recent studies demonstrating the importance of structural features such as a thin outer layer containing a different mineral type, and local sliding of mineral nanoparticles [104-106], very little comparable information is available on the telson. Morphological and mechanical analyses of the entire telson has shown that inelastic energy dissipation internal to the mineralized cuticle matrix in the telson is a crucial feature enabling this function [107], but the material origins of this phenomenon are not known. A main challenge in understanding how the material properties of mineralized cuticle lead to mechanical properties specialized to high impact resistance are the lack of quantitative structure-function relations which link the nanoscale fibrillar structure to mesoscale, tissue level variations.

The fibrillar structure of mineralized cuticle, poses a challenge to current experimental techniques not only because of the multiphase composition but significantly due its three-dimensional geometric complexity. While spectroscopic methods like energy-dispersive X-ray spectroscopy [108] and Raman microscopy [58] can determine local molecular composition in a surface-specific manner , obtaining local, spatially resolved three-dimensional characterization of the Bouligand structure (and variations therein) across lamellae (as well as fibre structure in pore canals) is challenging.
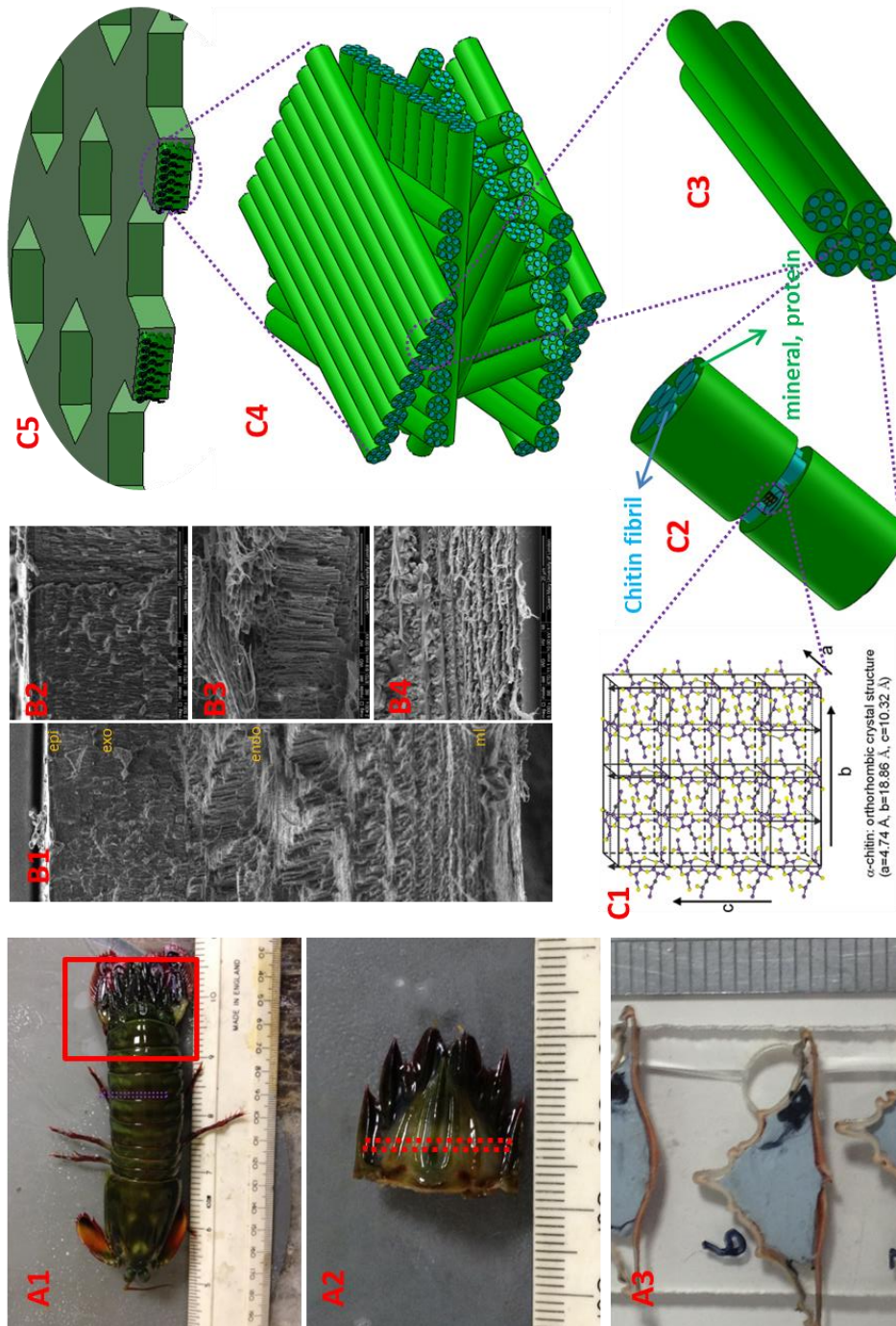
Figure 4.1: *Hierarchical structure of cuticle of stomatopod (mantis shrimp): A):*
Morphology of the stomatopod (A1). The red rectangle shows the telson sample
(A2) used as sample for synchrotron scanning-WAXD test after dissection; the
telson sample then was sectioned in to slices (A3) with a thickness around 1mm as
indicated by the red dash rectangle in (A2). B): SEM image (B1) from a cross
section of the cuticle shows the lamellar structure. The three high magnification

shows different fibre stack intensities across exocuticle (B2), endocuticle (B3) and membranous layer (B4); C): The hierarchical structure of cuticle.

X-ray diffraction techniques can determine both composition and structural orientation of the chitin and mineral phases, and have been applied to develop local structural models of cellulose [109], bone collagen [110] and the airflow sensors of insect cuticle [10]. However, due to the hierarchical structure of biological tissues like mineralized cuticle, their application to develop quantitative three-dimensional structural imaging of such systems has so far been limited. X-ray crystallographic texture measurements, for example with lab sources of ~100-500 micron beam size, can quantify variation of mineral crystal orientation across the entire exoskeleton [110] at the scale of millimetres to centimetres, but cannot resolve structure at the lamellar level. A second limitation of texture measurements is that due to the variation of fibre structure, orientation and packing at the scale of lamellae ~10 microns in width, direct combinations of X-ray texture measurements (which include sample rotation) with a smaller (micro) beam, such as those available at synchrotron sources, will not work because of the fact that structurally different micro volumes will be illuminated by the X-ray beam as the sample is rotated about its Euler angles. Lastly, for similar reasons, texture measurements are not suited to *in situ* deformation or temperature variation studies of nanoscale strain- and phase variation, which would be crucial to studying functional specialization[77]. New methodologies are therefore needed to determine micro- and nanoscale variation of three-dimensional fibre texture from the diffraction pattern for cuticle [115].

In this section, we demonstrate a new approach which circumvents these limitations by combining microbeam X-ray diffraction, three-

dimensional reconstruction of molecular and fibre orientation, and spatial mapping at the microscale. We construct at each point (a) the 3D orientation of the Bouligand plane (b) the main (or weighted average) direction of the fibres and (c) the angular distribution of the different sublamellae (equivalent to a width of the distribution). We further consider explicitly both the fibres in the pore canals (out-of-plane fibres (OP)) separately from the in-plane Bouligand layer fibres. We apply this methodology to quantitatively map for the first time the 3D mineralized fibrillar structure of telson cuticle across the entire tissue. By analysing the mesoscale variations in the Bouligand layers of fibres thus obtained, we propose a model linking the macroscopic impact resistance of telson to the spatial variations of its fibrillar architecture. We compare the 3D fibre architecture between the armoured telson and the non-armoured tergite from the same specimen, to identify ultrastructural material differences linked to function. The technique is scalable, general in principle and can be applied to analyse both natural biopolymer composites like the telson cuticle [116] as well as to bioinspired functional mimics of such materials (e.g. [117]).

4.2 Methods

4.2.1 Sample preparation

Specimens of *Odontodactylus scyllarus* from the tropical Indo-Pacific were purchased from a commercial supplier (Tropical Marine Centre, London) and stored at -20 °C till used for sample preparation. Before sample sectioning, the abdomen tergite and telson parts were dissected from defrosted mantis shrimps rinsed in fresh seawater to remove any loose organic debris, and briefly rinsed with deionized water to

remove any residual salt. For the synchrotron X-ray diffraction measurements, both abdomen tergite and telson parts were sectioned into 1 mm thickness specimens using a low-speed diamond saw (Buehler Isomet, Buehler, Germany). Sectioning was done under constant irrigation to minimize tissue damage. The samples were sectioned in the plane perpendicular to the long-axis of the animal (which is parallel to the medial axis of the telson (**Figure 4.1**)).

4.2.2 X-ray diffraction measurements

Synchrotron wide angle X-ray diffraction measurements were carried out at beamline I22 at the Diamond Synchrotron Light Source, using 14 keV X-rays with a beam spot focused to ca. 10 μm × 12 μm. Specimens with a 1mm thickness sliced with a diamond saw were then mounted onto the beamline sample holder in transmission geometry. Transmitted X-ray intensity was recorded using a photodiode detector fixed beyond the sample at the beam stop and normalized by incident intensity measured with an upstream ion chamber. Diffraction data were acquired with a PILATUS-2M detector. Calibration of beam centre and sample to detector distance was carried out with silicon powder and the CALIBRANT routine in Fit2D. Azimuthal intensity profiles of $I(\chi)$ for the (110) chitin peak were calculated using the CAKE and INTEGRATE routines in Fit2D. From the experimentally determined 2D WAXD spectrum, the azimuthal profile $I(\chi)$ of the (110) reflections is calculated using a wavelength of 0.6888 Å and detector-to-sample distance of 262.3 mm.

4.2.3 Scanning electron microscope (SEM)

SEM was used to examine the structural information of the dissected cuticle sample. Fracture surfaces of samples from telson and tergite

were obtained by gripping samples in a tensile tester and stretching to failure, gold coated and observed in the SEM (Inspect F, FEI, and Eindhoven, Netherlands).

4.2.4 X-ray microtomography measurements

X-ray microtomography measurements (denoted in the text as Micro-CT) were used to obtain tomograms and radiographs to examine the mineralisation degree at micro level across the whole telson and tergite sample. The intact telson and tergite were dried under room temperature and embedded in agarose gel (2mol/L) for scanning. A high-definition MuCat scanner was used, comprising an X-tek (Tring (Hertfordshire, UK), now part of Nikon Metrology (Leuven, Belgium)) ultrafocus X-ray generator and Spectral Instruments (Tucson, Arizona, USA) 800 series CCD camera in a time-delay integration readout mode. An accelerating voltage of 40 kV and voxel size of $12.5 \times 12.5 \times 12.5$ μm^3 was used for cuticle samples. After calibration for beam-hardening, microCT projection data were corrected to monochromatic equivalence at 25 keV. Subsequently, a cone-beam back-projection algorithm was used to reconstruct the 3D image. The tomograms were sliced into a series of 12.5 μm thick 2D bitmap stacks using Tomview software (in-house software of co-author G. R. Davis). The data stacks then were opened in ImageJ (U. S. National Institutes of Health, Bethesda, Maryland, USA) and grey-value line profiles were plotted.

4. 3 Modelling

As described in *Methods*, microbeam scanning X-ray diffraction maps were carried out across cross-sections of telson and tergite shells obtained from *Odontodactylus scyllarus* shrimp, complemented by

micro-computed tomography (micro CT) on intact shells and scanning electron microscopy of the ultrastructure. The 3D fibre orientation was obtained from the diffraction spectra as follows.

As proposed by Minke and Blackwell, the crystalline structure of α-chitin have an orthorhombic unit cell (a= 0.474 nm, b=1.886 nm, c = 1.032 nm). The previous X-ray diffraction experiments[59, 63] combined with high resolution transmission electron microscopy (HRTEM) test demonstrated that the c-axis of the orthorhombic unit cell for chitin molecules is coincides with the longitudinal axis of the chitin fibril[40, 162-164]. Therefore the orientation of the c-axis of the unit cell is used as a proxy for the chitin fibril orientation (**Figure 4.1 C1-C2**). Fibre symmetry of the unit cell of chitin around the c-axis in the fibril is assumed (**Figure 4.2 A1-A3**). In such a condition, the 3D reciprocal lattice of the chitin unit cell is rotated around the c-axis, leading to rings of equal intensity in reciprocal space rather than discrete spots, analogous to the case for cellulose microfibrils [1, 97]**. Figure 4.2 B** illustrates the fibre orientation distribution parameters (γ_0, $\Delta\gamma_0$) and fibre plane tilt angle in 3D ((α_0, β_0) need to be considered to construct 3D orientation distribution of a specific fibre plane. The yellow (colour online) arrow in **Figure 4.2 B** denotes the direction of the incident beam. The variation of fibre orientations will generate multiple intersected rings on *QS110*, and the rings from continuously distributed fibre plane then smear into a reflection band on the sphere (**Figure 4.2 C**).

4.3.1 3D model for 2D WAXD spectrum of chitin fibrils
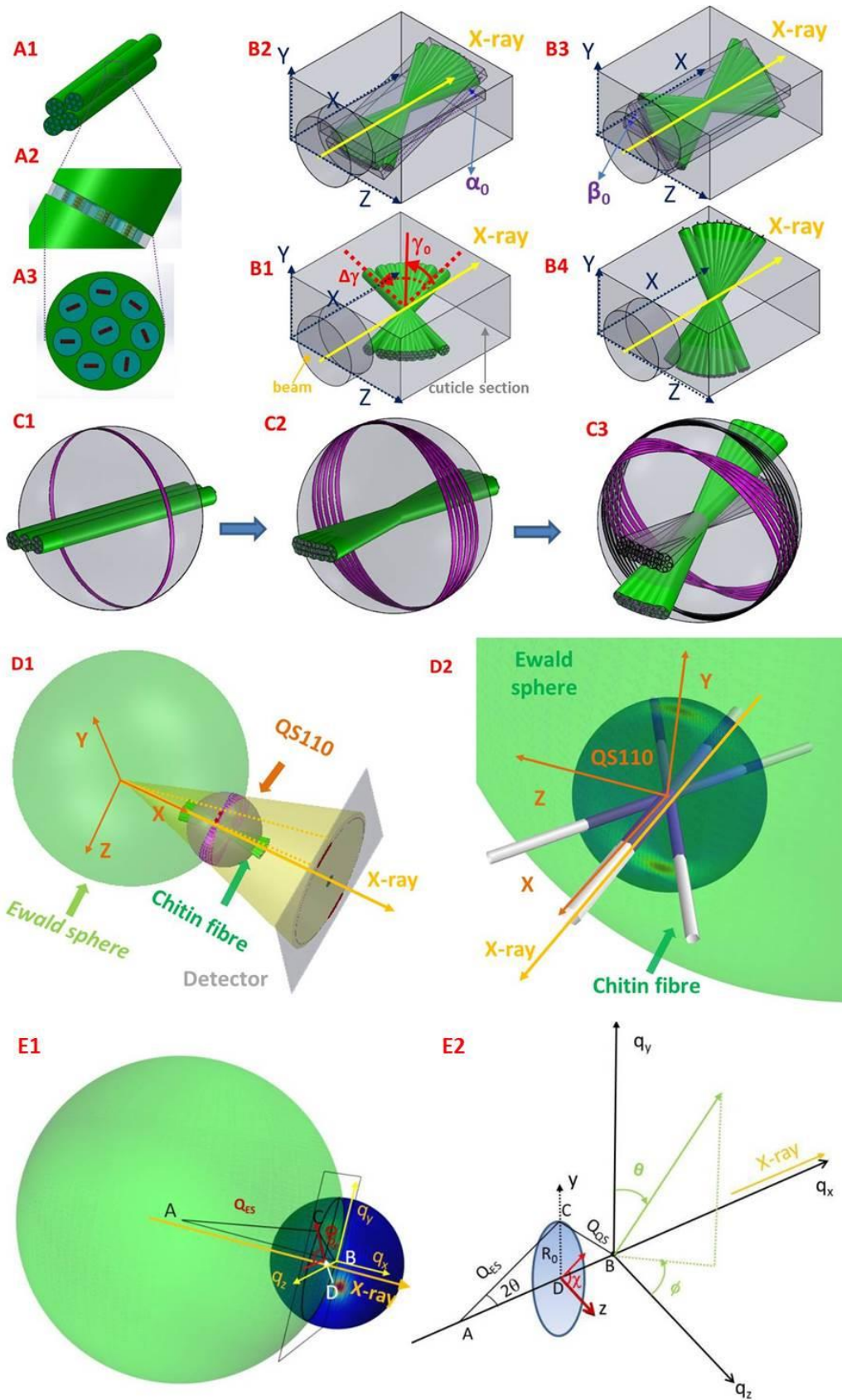
Figure 4.2. *Relation between chitin fibre arrays, fibre symmetry and the diffraction condition: A) Fibre symmetry result from the randomly oriented reciprocal 110 vectors from each single fibre around the mineralized chitin fibre axis. B): Schematics illustrating the fibre orientation distribution parameters (γ_0, $\Delta\gamma_0$) and fibre plane tilt angle in 3D ((α_0, β_0). C): Schematics show the intensity changes due to the fibre orientation distribution variations. D1): Sketch of the fibre diffraction geometry, with the Ewald sphere shown on left and QS110 on right. D2): The intersection of the Ewald sphere and QS110 plotted for a specific 3D fibre orientation. E1): Three dimensional representation, in detail, of the Ewald sphere (light green) intersecting QS110 (dark green), with the intersection circle shown as a dark ring. The rectangle represents the plane (at $q_x = -\lambda q^2_{(110)}/(4\pi)$) at which the intersection occurs. The X-ray beam is along the qi direction. The QS110 sphere is centred at the origin A and the Ewald sphere at B. Note that the radius of the QS110 sphere is enlarged 2.5 times for display purpose. E2): A detail view of A to show the definition of χ on the intersection plane of Ewald and QS110 sphere.*

The WAXD diffraction spectrum is the projection on a 2D detector of the intersection of the Ewald sphere with the collection of rings, as shown in **Figure 4.2 D1**. The intensity on the intersection ring of the Ewald sphere and *QS110* will contribute to the diffraction signal.

Standard texture measurements (rotating the sample about Euler axes) [44, 52] do not suffice to obtain the spatially resolved 3D intensity distribution for micro structurally heterogeneous materials like the telson, due to mixing WAXD spectra from adjacent regions during sample rotation. The following was inspired by Lichtenegger et al's work [22] on cellulose nanofibrils.

Consider initially a fibre oriented approximately along the q_x-axis (i.e. a fibre oriented parallel to the beam direction). The (110) reflection of

this fibre will form a ring with radius $q_{(110)}$ approximately in the q_y-q_z plane, and this ring is denoted hereafter as R110 (**Figure 4.2 C1**). Other chitin fibres which are oriented at varying angles to the q_x-axis will form rings which collectively all lie on the 3D sphere of radius $q_{(110)}$ (hereafter QS110) (**Figure 4.2 C2-C3**).

As the chitin nanofibres are packed into planar lamellae with a plywood architecture[27] , it is clear that instead of a single fibre orientation in the scattering volume, there are a range of fibre orientations corresponding to the different sub-lamellar orientations in the lamella (**Figure 4.2 B1-B4**). For simplicity, consider initially the principal fibre direction as along the q_x-axis. Denote the normalized fibre orientation distribution as w (γ, γ_0, $\Delta\gamma_0$), where γ is the angle (in the plane of the lamella q_x-q_z) of the fibre long axis with respect to the principal fibre direction, and γ_0 and $\Delta\gamma_0$ are the centre and width parameter of the distribution. This distribution leads, in reciprocal space, to a range of R110 rings distributed with the same orientation distribution w (γ, γ_0, $\Delta\gamma_0$). We fix w (γ, γ_0, $\Delta\gamma_0$) to a normalized Gaussian distribution:

$$w(\gamma; \gamma_0, \Delta\gamma_0) = \frac{1}{\sqrt{2\pi}\Delta\gamma_0} exp\left(-\frac{1}{2}\left(\frac{\gamma-\gamma_0}{\Delta\gamma_0}\right)^2\right) \; equation\; 4.1$$

Note that due the lamellar level fibre texture arising from w (γ, γ_0, $\Delta\gamma_0$), the continuous R110 reflections rings will sum into regions with higher intensity in the pole area of the QS110 sphere and lower intensity in the equatorial area. The intensities for the rings will constructively add along the vertical q_y-direction (**Figure 4.2 C2**).

To write down the intensity distribution on QS110, we need an expression for the intensity of the (110) ring on QS110, tilted in the

q_x-q_z plane. Considering the (untilted) single chitin fibril oriented along the horizontal q_x-direction as the reference state, the intensity of the ring will only depend on q_x, will be peaked at q_x=0, and will decrease rapidly on either side of q_x=0 with a width parameter a_x. We use the generalized δ-function expression:

$$r(q_x; a_x) = \frac{1}{\sqrt{\pi}a_x} \exp\left(-\left(\frac{q_x}{a_x}\right)^2\right) \; equation \; 4.2$$

Which approaches a sharp band as $a_x \rightarrow 0$. a_x is a parameter characterizing the degree of intrafibrillar alignment of chitin unit cells within a fibril; highly aligned unit cells correspond to small a_x. Similarly, the expression for a fibril oriented in the q_x-q_z plane at an angle γ is

$$r(q_x, q_z; \gamma, a_x) = \frac{1}{\sqrt{\pi}a_x} exp\left(-\left(\frac{q_x \cos\gamma - q_z \sin\gamma}{a_x}\right)^2\right) \; equation \; 4.3$$

To calculate the intensity at a specific (q_x, q_y, q_z) point on QS110, the weighted sum over all individual fibrils leads to

$$I(q_x, q_y, q_z) = \int_{-\frac{\pi}{2}}^{\frac{\pi}{2}} w(\gamma; \gamma_0, \Delta\gamma_0)\, r(q_x, q_z; \gamma, a_x) d\gamma \; equation \; 4.4$$

Incorporation of 3D tilts of fibre lamellar plane: So far our analysis has concerned a range of fibril orientations in a single plane (q_x-q_y) characterized by an average fibril direction in this plane given by γ_0 and a degree of dispersion of fibril angles given by $\Delta\gamma_0$. To represent the most general case, this plane of fibrils can itself tilt out of the (q_x-q_y) plane, and this tilt can be parameterized by two angles α and β. The expression Eq. 4 above still hold in the body-fixed frame of the fibril plane (denoted (q_x, q_y, q_z)), but in order to represent the

expression in the lab-fixed (q_x^L, q_y^L, q_z^L, superscript L denotes Lab coordinates) coordinates, the linear equations relating (q_x, q_y, q_z) to (q_x^L, q_y^L, q_z^L) is carried out. These relations are

$$
\begin{pmatrix} q_x \\ q_y \\ q_z \end{pmatrix} = \begin{pmatrix} cos(\alpha_0) & sin(\alpha_0) & 0 \\ -cos(\beta_0)sin(\alpha_0) & cos(\beta_0)cos(\alpha_0) & sin(\beta_0) \\ sin(\beta_0)sin(\alpha_0) & -sin(\beta_0)cos(\alpha_0) & cos(\beta_0) \end{pmatrix} \begin{pmatrix} q_x^L \\ q_y^L \\ q_z^L \end{pmatrix}
$$

equation 4.5

Substituting the Lab coordinate values into **equation 4.6** the final expression for the measured detector intensity is:

$$
I(q_x, q_y, q_z)
$$

$$
= \int_{-\pi/2}^{\pi/2} w(\gamma; \gamma_0, \Delta\gamma_0)\, r(q_x(\alpha_0, \beta_0, q_x^L, q_y^L, q_z^L), q_z(\alpha_0, \beta_0, q_x^L, q_y^L, q_z^L); \gamma, a_x)\, d\gamma
$$

equation 4.6

The spherical intensity distribution arising from such a general distribution of fibre orientations is shown in **Figure 4.2D2**, where the regions highlighted on the QS110 sphere have higher intensity than the rest, owing to constructive addition of intensity from rings. The fibre orientation is schematically shown as three white fibres plotted along the main fibre direction in **Figure 4.2D2** and at ± the half width at half maximum away from the main fibre direction. The incident beam directions are indicated in both (D1) and (D2) using yellow arrows. Here, the regions of high scattered intensity appear as distinct red streaks toward the upper and lower parts of *QS110*. The measured azimuthal intensity profile *I* (*χ*) corresponds to the intersection of the Ewald sphere with QS110, as shown schematically in **Figure 4.2 D1**.

4.3.2 2D intersection of QS110 and Ewald sphere

To relate the experimentally measured azimuthal intensity profile $I\,(\chi)$ to *Eq. (3)* above, we parameterize the wave vectors of the intersection circle located at the intersection of the Ewald sphere Q_{ES} and the QS110 sphere (**Figure 4.2D1**). The radius of the intersection circle is:

$$q_x^L = -\frac{Q_{QS110}^2}{2Q_{ES}}$$

equation 4.7

Hence, if the azimuthal angle on the detector is (in usual notation) denoted as χ, the wave vector components on the intersection circle are:

$$q_y^L = \frac{Q_{QS110}}{2Q_{ES}}\sqrt{(2Q_{ES}+Q_{QS110})(2Q_{ES}-Q_{QS110})}\,\sin\chi$$

equation 4.8

$$q_z^L = -\frac{Q_{QS110}}{2Q_{ES}}\sqrt{(2Q_{ES}+Q_{QS110})(2Q_{ES}-Q_{QS110})}\,\cos\chi$$

equation 4.9

Substituting into **Equation 4.6**, the intensity distribution $I\,(\chi)$ on the detector is:

$$I(\chi) =$$

$$\int_0^{2\pi} w(\gamma,\gamma_0,\Delta\gamma_0)\,\frac{1}{\sqrt{\pi}a_0}\,exp\left(-\left(\frac{q_x(\chi;\alpha_0,\beta_0)\cos\gamma-q_z\,(\chi;\alpha_0,\beta_0)\sin\gamma}{a_x}\right)^2\right)$$

equation 4.10

Lastly, our experimental observations show $I(\chi)$ to contain two sets of peaks corresponding to two sets of fibres (IP- and OP-fibres (**Figure 4.1 C5**), identified earlier in lobster cuticle [22, 27]). Both families of fibres (in-plane and out-of-plane) are characterized by the model in Eq. (5), although with different angular parameters and scaling factors (Φ_1 and Φ_2). The experimental data is hence fitted to the sum of two terms of the form of **equation 4.10**.

Figure 4.3 A1-A4 show the steps involved (for a single family of fibres) in going from a real-space representation of fibre orientation (**Figure 4.3 A1**) to the 2D azimuthal intensity profile $I(\chi)$. The beam direction is chosen along the $-q_x^L$ direction. The left centre image (**Figure 4.3 A2**) shows a side-view of the 3D intensity distribution on QS110. The intersection of the Ewald sphere (on the right) with QS110 leads to intersection with parts of the sphere near, but not at, the maxima, due to the curvature of the Ewald sphere. In **Figure 4.3 A3**, the vertical maxima along the color-coded intersection ring are clearly visible, and are shown as a 1D line profile in **Figure 4.3 A4** (which can be compared to experimental data).

Consider first the case where the fibrils are in the *xz* plane ($\alpha = 0, \beta = 0$), with the main fibril direction γ_0 aligned along the beam axis. The qualitative effect of increasing the width of the fibril distribution $\Delta\gamma_0$ is shown by comparing **Figure 4.3A** and **Figure 4.3B**. It is observed that increasing $\Delta\gamma_0$ will cause an increase in the width of the two peaks in $I(\chi)$. From the modelling results, we can see that increased $\Delta\gamma_0$ will cause a narrowed intensity distribution in the two pole areas of the Qaxis sphere as highlighted by the dashed rectangles in **Figure 4.3 A2** and **4.3 B2** while the in the equator area the intensity band is narrowed.
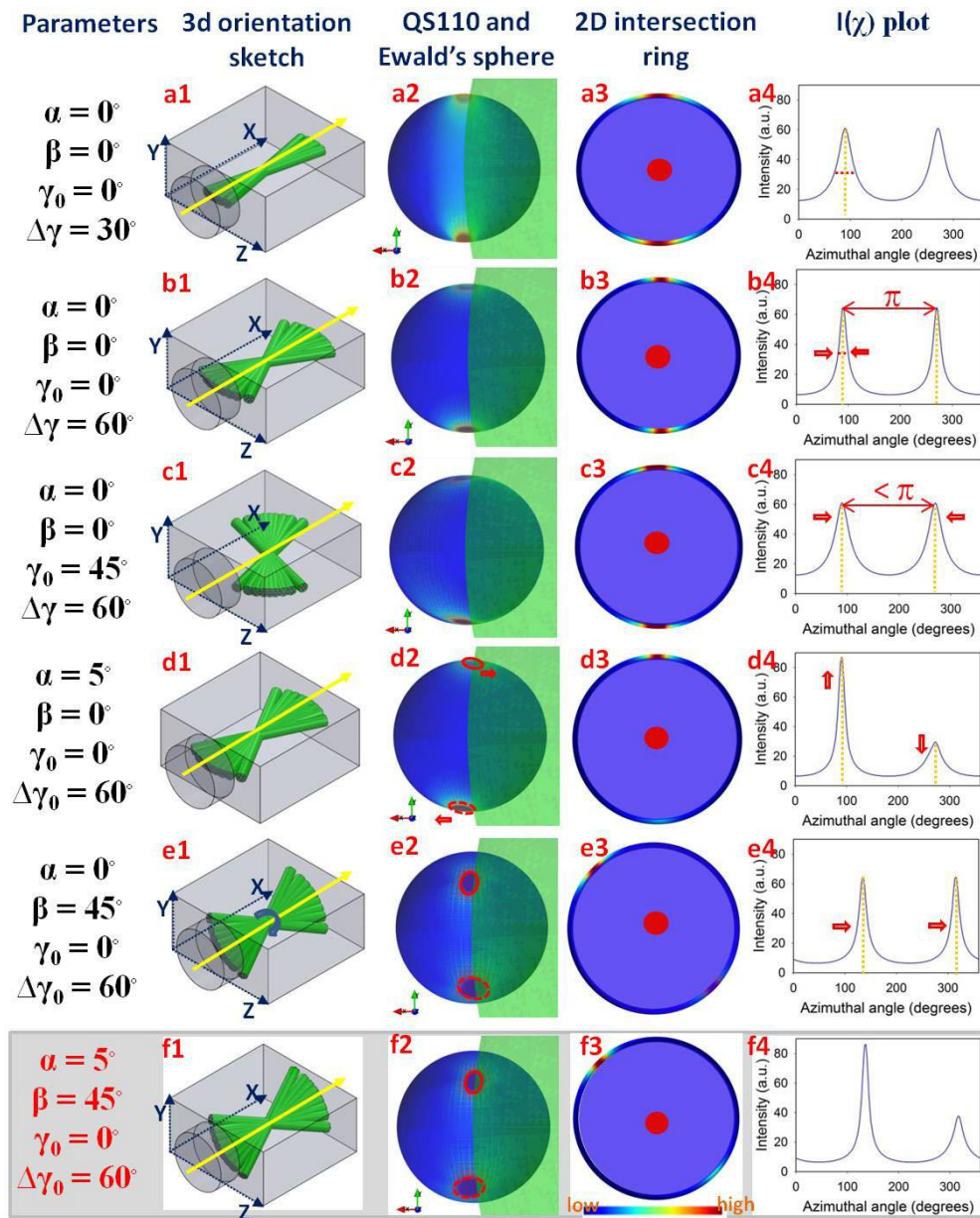
Figure 4.3. *Predicted 3D and 2D diffraction intensity profiles arising from a range of chitin fibre array geometries. A1-F1): Fibre plane in different 3D orientation; A2-F2): Intensity distribution in QS110 according to the variation of 3D orientation parameters; A3-F3): 2D intersection planes of QS110 and Ewald spheres; A4-F4): I(χ) results of different 3D orientation parameters form the model.*

Consider the next case where the principal fibre direction γ_0 is at an angle to the beam direction (**Figure 4C1**), with the fibrils still within the *xz* plane (i.e. $\alpha=0$, $\beta=0$), correspondingly the intensity band tilts around the x-axis, therefore the band strengthens in the two pore area and weakens in the equator area (**Figure 4C2**). However, because the central circle of intensity band is no longer parallel to the intersection circle of *QS110* and the Ewald sphere, which means the strongest central circle of the intensity band will not be captured in the detector. The shift between the central circle of the intensity band and the intersection circle of the two spheres will cause the two peaks in the I (χ) plot no longer separated by 180°.

We now consider the case where either α or β are nonzero. Consider a rotation about the *z*-axis in **Figure4.3 D1**. In this case, the two intensity maxima located at the polar zones of QS110 will shift, as indicated by the dashed line in **Figure4.3 D2**. It is clear from **Figure4.3 D2** that the intersection of the Ewald spheres with the intensity maxima will now be *unequal*: the upper intersection (arrow 1 in **Figure4.3 D2)** is closer to the maximum of the upper 2D intensity distribution, while the lower intersection (arrow 2 in **Figure4.3 D2**) is further from the maximum of the lower 2D intensity distribution. As a result, the 2 peaks in *I (χ)* are no longer equal. It is noted that the induced asymmetry of peaks is quite pronounced: a small tilt in α (5° in **Figure 4.3D**) will induce an asymmetry of a factor of ~3 between the two peaks (**Figure4.3 D4**).

Considering the complementary case when the lamella plane rotates around the *x*-axis (i.e. β is nonzero) as in **Figure 4.3E1**. In this case, as seen in **Figures 4.3E2** and **E3** the two polar intensity maxima

(solid and dashed ellipses) rotate about the *x*-axis, but the Ewald sphere intersection with both maxima is at symmetrical values (in contrast to the previous case in **Figure 4.3D**). Thus, in $I(\chi)$ the two peaks shift rigidly to the right (**Figure 4.3 E4**), with their peak intensities remaining equal.

Finally, we consider the most general case where the lamellar plane of chitin fibrils is tilted to the beam with γ_0, α and β nonzero (**Figure 4.3 F**). It can be readily seen that the azimuthal spectrum in such a case (**Figure 4.3 F4**) combines, qualitatively, the features of the previous three examples: specifically (a) separation of the peaks different from 180°, (b) unequal intensity of peaks and (c) peaks shifted from the north-south orientation (90°-270°) relative to **Figure 4.3 A4**. As will be seen by comparison with the experimental data, such features are characteristic of the $I(\chi)$ patterns obtained in chitin cuticle. Further examples of how the 3D intensity distribution and 2D integrated $I(\chi)$ profiles vary as a result of changing the tilt parameters are shown in **Figure 4.4**. One may notice that the intensity peaks of the $I(\chi)$ profiles are not necessarily to be Gaussian distributions even though a Gaussian distribution (equation 4.1) is assumed in our model for the fibre alignment. This is due to the fact that even though a Gaussian distributed chitin fibres in certain plane will lead to a Gaussian intensity distribution on the *QS110* sphere, but this intensity distribution may not be captured in the intersection plane (parallel to the yz plane) between the Ewald sphere and *QS110* sphere.
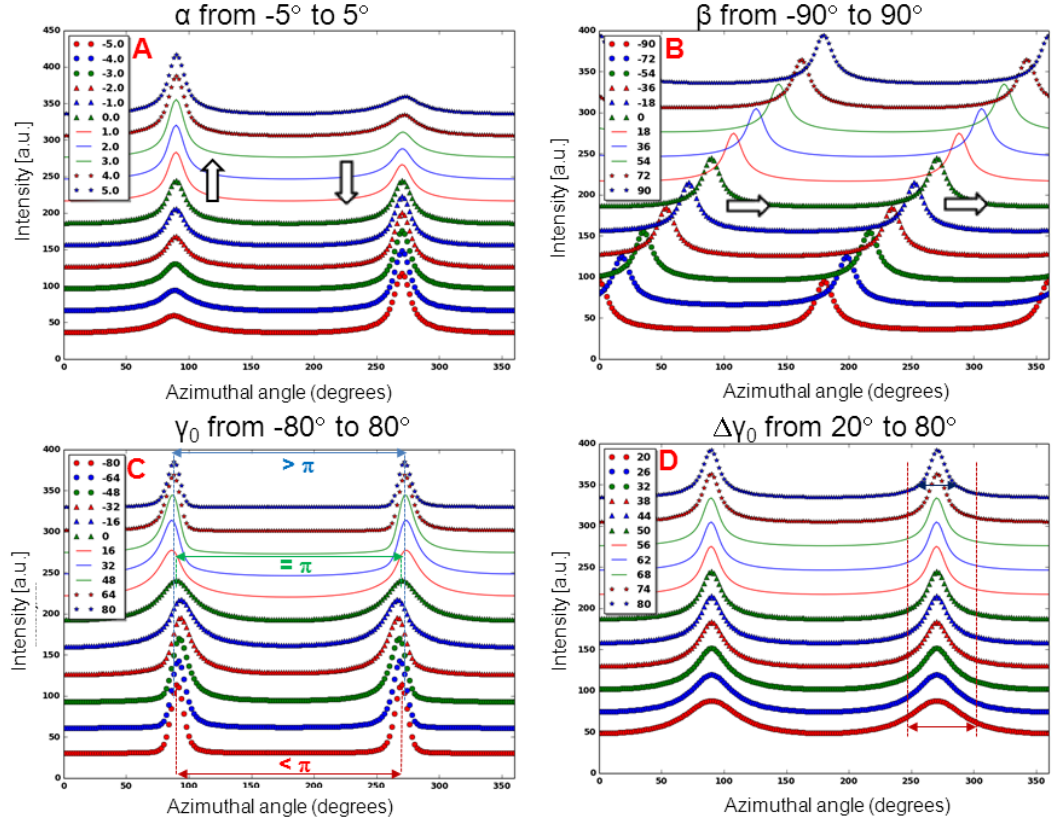
Figure 4.4. *1D plots of $I(\chi)$ for a range of parameter variations in α, β, γ_0, and $\Delta\gamma_0$, showing in greater detail the qualitative changes in azimuthal intensity profiles described in **Figure 4.3**. (A) Asymmetry in peak heights due to variation in α (B) shift of both peak positions due to change in β (c) peaks separation changing from 180° due to variation in γ_0 and (d) peak width variation due to change in $\Delta\gamma_0$.*

4.3.3 Fitting azimuthal intensity profiles

The experimentally derived $I(\chi)$ was fitted to the model above using customized fitting scripts written in Python (Enthought Canopy, Academic Non-commercial Use License) and using the Matplotlib and Mayavi Python libraries [23, 165]. The fitted parameters were (α_{01}, β_{01}, γ_{01}, $\Delta\gamma_{01}$, Φ_1) and (α_{02}, β_{02}, γ_{02}, $\Delta\gamma_{02}$, Φ_2) for a specific pair of 3D fibre orientations (with the '1' subscript denoting in-plane (IP) fibres and '2' subscript denoting out-of-plane (OP) fibres).

4.4 Experimental results

4.4.1 3D fibre orientation across the cuticle in telson and tergite
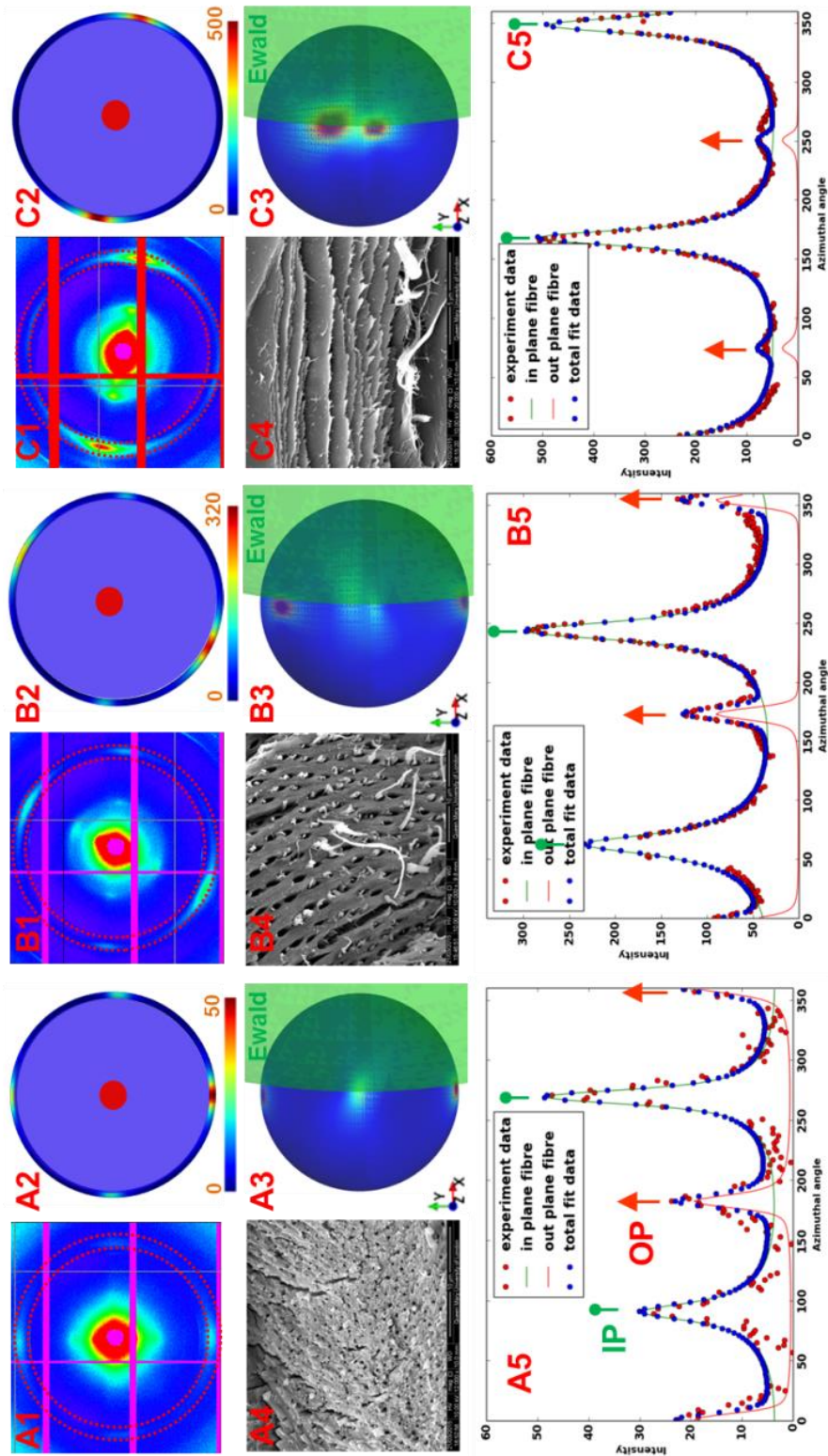
***Figure 4.5.** Comparison between experimental X-ray data and model predictions in different tissue locations. A1-C2): WAXD images collected in synchrotron experiments from exocuticle, endocuticle and membrane layer respectively; A3-C3): Intersection of QS110 and the Ewald sphere plotted using the fitted 3D orientation parameters; A4-C4): SEM images of the exocuticle, endocuticle and membrane layer show different pore canal size and densities; A5-C5): Comparison of experimental and fitting I (χ) curves for each WAXD pattern collected from exocuticle, endocuticle and membrane layer.*

Representative examples of WAXD spectra (obtained as part of the 2D map of WAXD spectra across the cross section of cuticle) in the three regions of the cuticle are shown in **Figure 4.4(A1, B1, C1)**. As described in the **Methods**, the 3D orientation parameters (α, β, γ_0 and $\Delta\gamma_0$) are obtained by fitting Eq. 5 to the azimuthal plot $I(\chi)$ collected from experimental values. Good fits of the data (red points; colour online) to the model (solid blue (colour online)) are observed in all cases. The 2D intersections Ewald and QS110 spheres **Figure 4.4(A2,B2,C2)** and the 3D intensity distributions in QS110 spheres **Figure 4.4(A3,B3,C3)** plotted using the fitted data were also shown to demonstrated the good match of the fitted pattern and the experiment pattern. Note the scale of the colour bar indicates considerable differences of the diffraction intensities in different region. The experimental I (χ) curves and the fitting results have demonstrated three important features **Figure 4.4(A4, B4, C4)**. The first feature to note is the presence and absence of an additional pair of peaks in the experimental I (χ) curves in different regions of cuticle (**Figure 4.4, A5-C5**). The peak corresponding to IP fibre indicated using green oval arrow and the OP fibre peak indicated using red arrow. These out-of-plane fibre intensity peaks represent a second family of fibres whose peak positions were separated nearly 90° within the in-plane

fibre peaks in $I(\chi)$ curves. From SEM images (**Figure 4.1 B5**) and prior work [119] on a related system (lobster cuticle) we identify these as the fibres aligned along the pore-canals which run perpendicular to the cuticle surface (out-of-plane (OP) fibres) in contrast to the dominant group of in-plane fibres (IP). The second feature is that the WAXD spectra differ in the azimuthal width of the IP-peaks between the exocuticle, endocuticle and membrane layer (**Figure 4.1 B1-B4**), which is due to variation of the fibre orientation distributions in the scanning volumes from different regions. Lastly we note that the proportion of OP fibres comparing to the IP fibres is higher in the exocuticle (**Figure 4.1 A5)** than in the endocuticle (**Figure 4.1 B5**) and is essentially absent in the membrane layer (**Figure 4.1 C5)**. In order to further understand the 3D fibre orientation distributions across exocuticle, endocuticle and membrane layers of telson and tergite cuticle, we mapped the 3D fibre orientations across telson and tergite and plotted in 3D. From the SEM image of cuticle (tergite), it can be seen that the expected exocuticle and endocuticle layer are accompanied with an interior layer with some morphological similarity to the exocuticle, which we denote the membrane layer.

Figure 4.6 shows a consolidated 3D mapping of the chitin fibre orientation, specifically comparing the apex of the telson (the point expected to bear maximum load during intraspecific combat) and the adjacent tergite segment. Results of 2D microfocus WAXD scans across the central carinae of telson and a selected portion of the region in tergite imaged in the SEM (**Figure 4.6 A1-B1**) are shown as WAXD pattern composite maps (**Figure 4.6 B1-B2**).
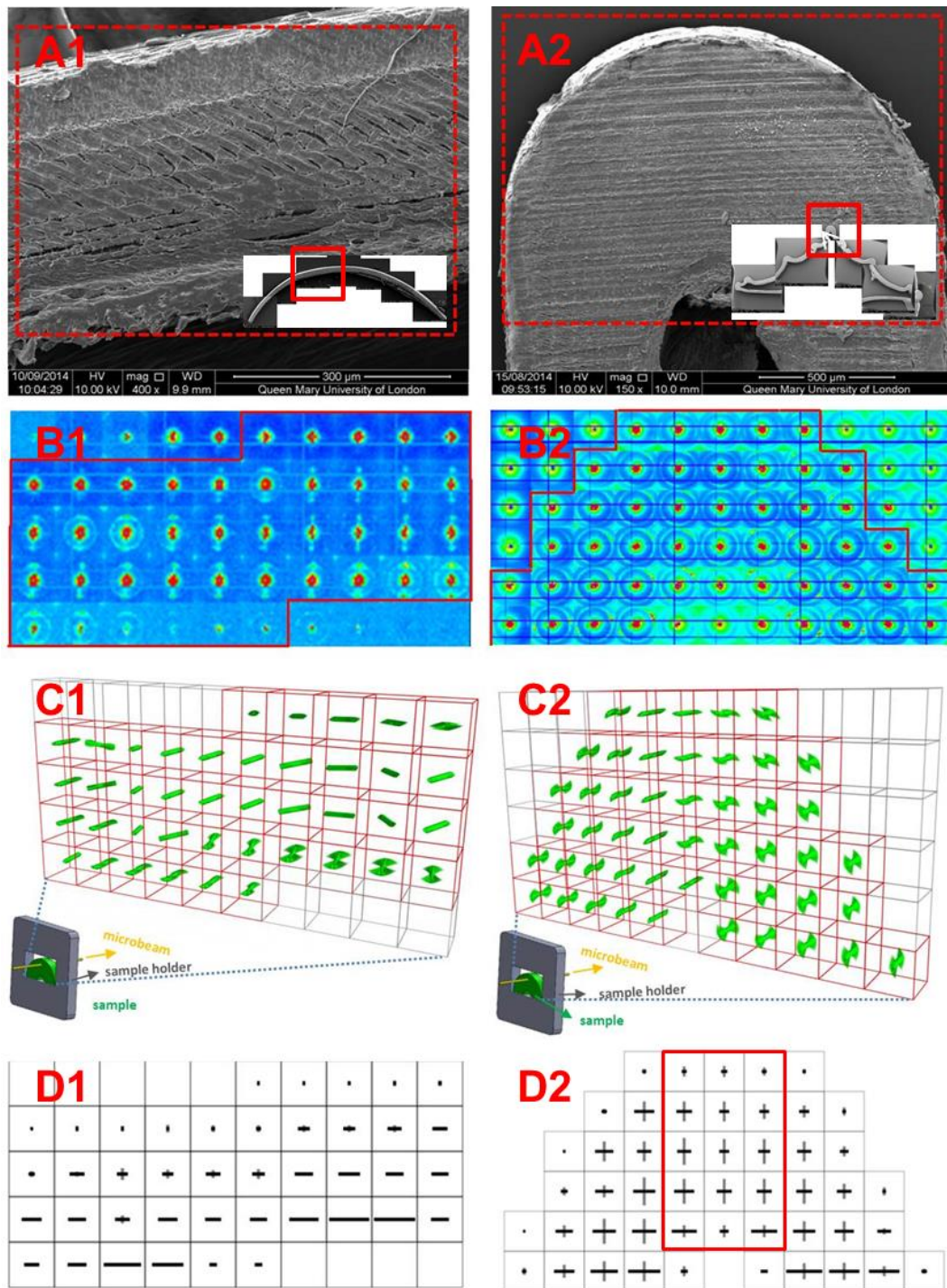
Figure 4.6. *Reconstruction of 3D fibrillar and lamellar orientation in telson and tergite. A: SEM images of the telson (A2) and the control abdominal tergite (A1) from the same animal. B: Microfocus WAXD composite maps of (B1) cuticle cross-section of abdominal tergite and (B2) cross-section of the central carina of the telson. C: 3D fibre orientation distribution across the scanned area. D: Quantitative comparison of the relative amount of in-plane and out of plane fibres.*

The inset images in **Figure 4.6 A1-B1** show low magnification images of the entire telson and tergite respectively. The regions used for the microfocus WAXD scan is outline by the red dashed rectangles, and is observed to cover the entire tissue; **Figure 4.6C** are three-dimensional representation figures of average fibre orientation for in-plane fibre planes. Each point is represented by a lamellar schematic (green; colour online). The mean direction of the lamella is given by the fitted parameters (α, β, γ_0) for that point. At each point, the width of the schematic fibre distribution is proportional to the fitted value of $\Delta\gamma_0$, according to a conversion factor. In both cases, it is seen that the plane of the schematic lamellae follow the macroscopic shape of the cuticle, which is coinciding the finding under SEM. The orientation of fibre planes are determined by the α, β parameters in **Equation 4.6**. Only the in-plane fibres are shown for clarity. A two-dimensional map of in-plane fibre (Φ_1, horizontal bar) and out-of-plane fibre (Φ_2, vertical bar) X-ray diffraction intensities across the scanned regions. Note the amount of out-of-plane fibres has been expanded by a factor of 3 relative to the in-plane fibres for display purposes. The red rectangle in D2 shows, as an example, the region chosen as the centre of the telson (as distinct from the side), used in the comparison of architectural parameters in **Figure 4.7**.

Figure 4.7 A-B show averaged values for the ratio of IP- to OP-fibres Φ_2/Φ_1 and the in-plane width of the fibre distribution $\Delta\gamma_0$ for the three telson and three tergite sections used in this study. The numerical values are sample averages, taken across all scan-points in the scanning-WAXD measurement for each sample. Three telson samples (black bars) and the three tergite samples (grey bars) were examined

for the data source of **Figure 4.7 A-B**. Error bars are standard deviations.
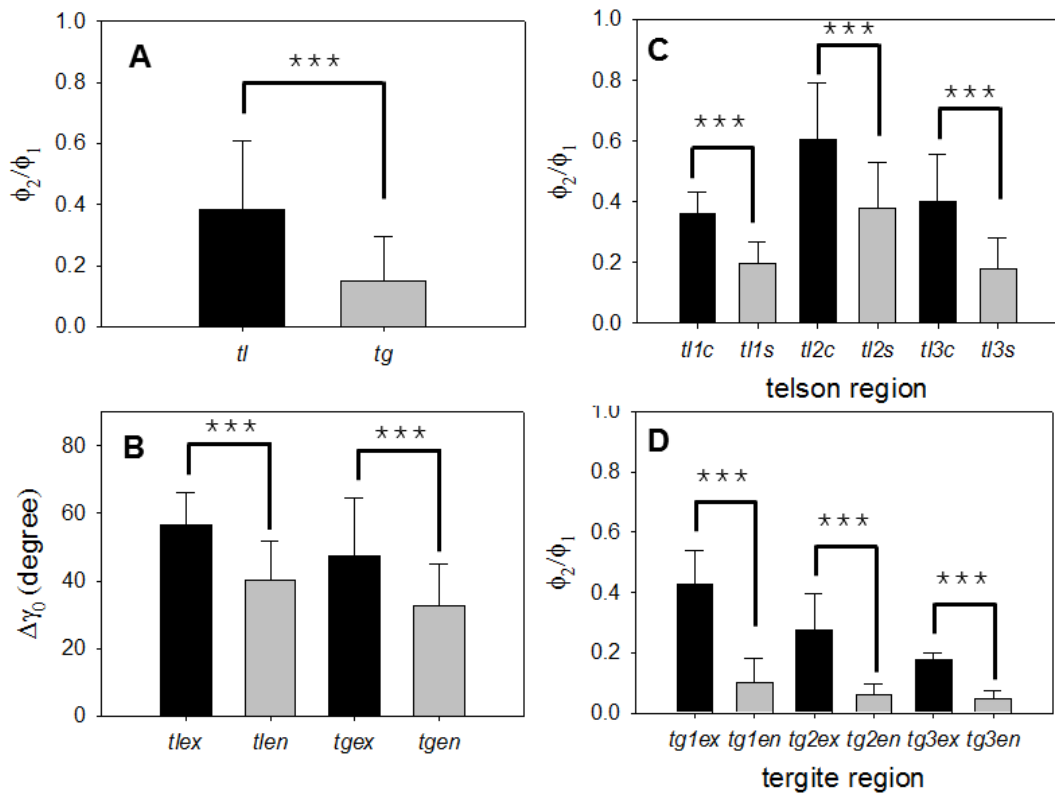
Figure 4.7. *Quantitative comparison of fibre architectural parameters between and within telson and tergite. A) Averaged values for the out-of-plane/in-plane (OP/IP) fibre ratio Φ_2/Φ_1 for telson and tergite samples. B) Averaged values for the angular width of the fibre distribution $\Delta\gamma_0$ in the exo and endo region of telson and tergite samples. C) Variation of Φ_2/Φ_1 between the central apical region of the telson (black bars; tl1c, tl2c and tl3c, tl means telson) and the adjacent side regions (grey bars; tl1s, tl2s and tl3s). D) Variation of Φ_2/Φ_1 between the exocuticle of the three tergite (black bars; tg1ex, tg2ex and tg3ex, tg means tergite) and the three endocuticle (grey bars; tg1en, tg2en and tg3en). The *** symbol indicates there is significant difference between the two sets of data.*

It is observed that the average of Φ_2/Φ_1 is larger in the telson (0.38) than the tergite (0.15), as can be seen qualitatively in **Figure 4.6D**. The equivalent volume fraction of OP fibres thus is on average about

27.5% in telson, and about 13.0% in tergite. However, there exist microscale gradients in these parameters within each tissue, which require closer examination (**Figure 4.7 C-D**). The $\Delta\gamma_0$ value ranges from ~20° to 70° across the different regions of both telson and tergite samples. On average, the $\Delta\gamma_0$ values in the exo region of the cuticle are higher than endo region in both cuticles (**Figure 4.7B**). Need to mention that parameters of the thinner membrane layers (**Figure 4.1 B4**) are not compared here due to limited data acquired. In terms of Φ_2/Φ_1 ratio distribution across different regions, **Figure 4.7C** compares Φ_2/Φ_1 in the centre of the telson carina with the adjacent tissue region (transitioning to the intermediate valleys between carina). To clarify which regions were selected as belonging to the centre versus the side regions, red rectangles (colour online) are drawn around the 2D WAXD parameter map in **Figure 4.6D**. It is observed that the ratio of OP-fibres to IP-fibres is larger in the central carina compared to the side regions, and t-tests show this difference is highly significant ($p < 0.001$) for both telson specimens. For the tergite, in an analogous manner, **Figure 4.6D** compares Φ_2/Φ_1 in the exocuticle to the endocuticle (again, the regions selected are highlighted in **Figure 4.6D**). The proportion of the OP-fibres to IP-fibres is higher in the exocuticle compared to the endocuticle, and t-tests again show this difference to be highly significant ($p < 0.001$). No significant difference exists in Φ_2/Φ_1 between the exo- to endocuticle in the telson (data not shown). Average values are plotted with standard deviations, and vertical/horizontal line pairs show comparisons using t-tests, resulting in highly significant (***; $p<0.001$) differences between the apical and side regions for both samples.

4.4.2 X-ray micro CT imaging of telson and tergite

As a complementary experimental probe to measure compositional variations instead of ultrastructural fibre orientations, the degree of mineralization in telson and tergite were also examined using micro-CT. **Figure 4.8A** shows the 3D structure of the entire telson, with the apical carina highlighted schematically. The mineralization is more concentrated in the central carinae of the telson than other areas of telson. Higher magnification images (**Figure 4.8B**) show the exocuticle region as much lighter than endocuticle and membrane layer, showing higher mineral content in the exocuticle. Besides, the visible vertical white streaks (**Figure 4.8B**) within the central carinae in telson indicate the presence of more pore canals running in this region since the pore canals are highly mineralized. The faint white streaks perpendicular to the surface inside **Figure 4.8B** indicate highly mineralized pore canals running through the cuticle. These are much harder to distinguish in micro-CT image than from the X-ray diffraction data in **Figure 4.6**. Those white mineralized pore canals are more clearly visible in a vertical perspective. Grey-scale line-scans across the horizontal direction (dash arrow in **Figure 4.8B**) show (**Figure 4.8 C1**) oscillations indicative of the presence of these mineralized pore canals. Analogously, a higher mineralization in the exo- versus endocuticle can be clearly visualized from a vertical scan (solid line in **Figure 4.8 B**) in **Figure 4.8 C2**. The mineralization discrepancy between different parts of crustacean exoskeleton have also been widely observed before [1, [52], which usually result in different mechanical function for the animals to adapt the different environments. In both C1 and C2, five successive 2D grayscale images (in the depth-direction) were averaged; starting from the 2D

images shown in Figure 4.8, and the line profile of grey levels was calculated on the averaged 2D images.
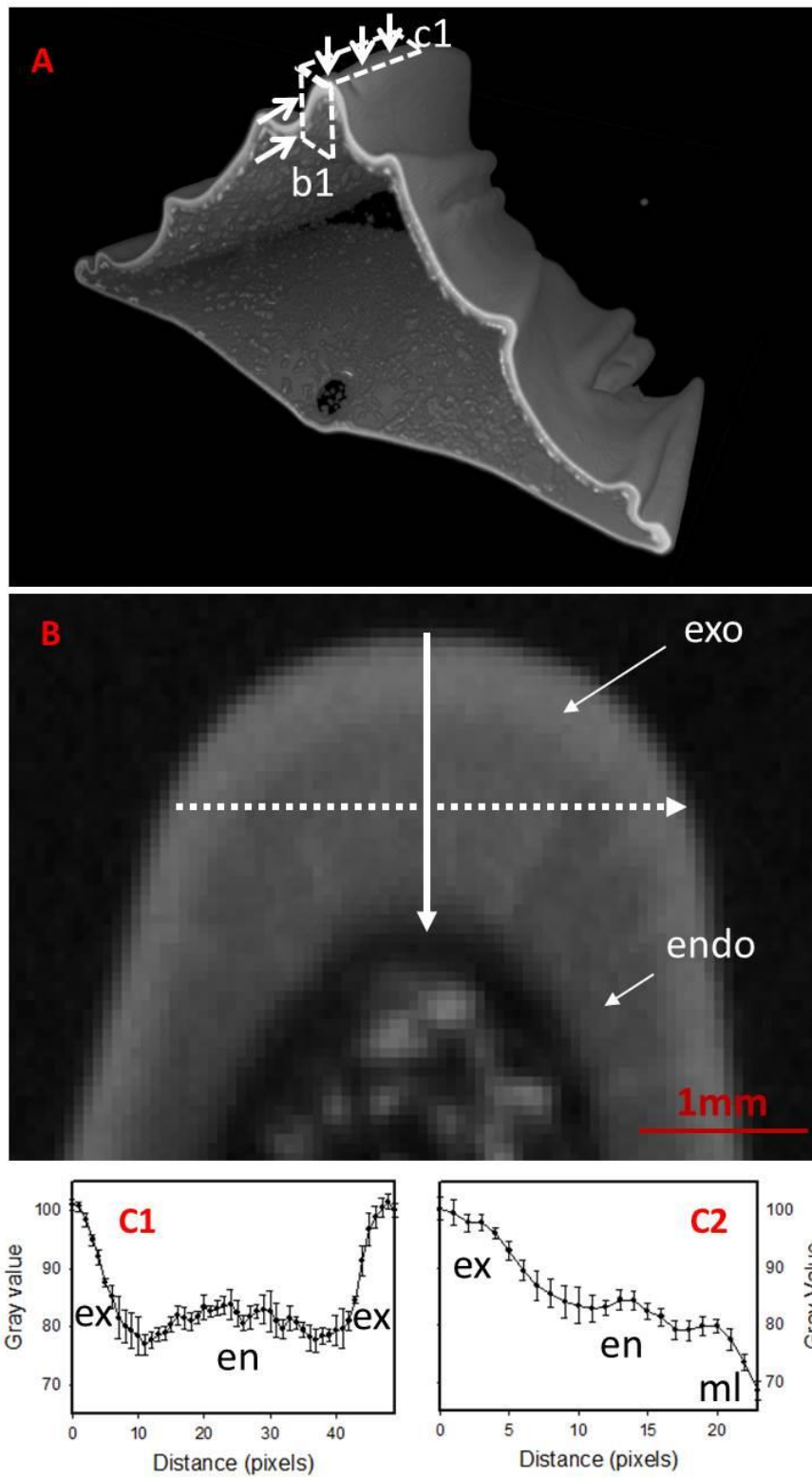
Figure 4.8. *3D X-ray microcomputed tomography of telson cuticle. A) 3D rendering of micro-CT from the stomatopod telson. B) A detailed 2D slice through the 3D reconstruction of the central carina (show in white rectangle b1 in **Figure 4.8A**). C) Greyscale line profile along the direction indicated by the horizontal dash (C1) arrow and solid arrow (C2) indicated in B.*

4.4.3 Correlating nanostructure to mechanical function
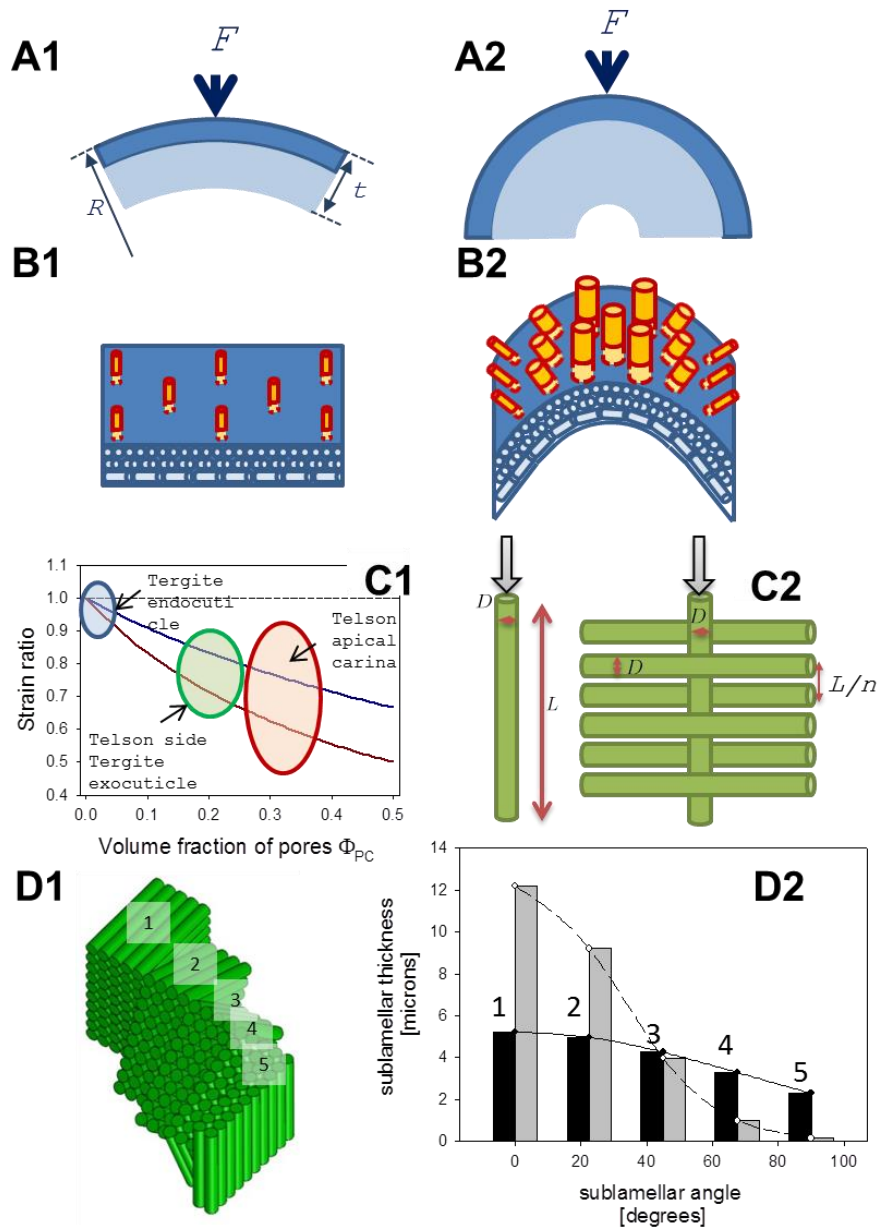
Figure 4.9. *Mechanisms for increased impact resistance of telson at the micro- and mesostructural level. A) Schematic of the apical carinal region of the telson (right) and an equivalent length of the tergite (left) at the macroscopic level,*

showing that they may be considered very approximately as shells with variable radii R and thickness t. B) Microstructural schematic of the intensity distribution of OP fibres on telson carina and the tergite. C1) Relative reduction in strain with increasing pore canal area fraction, assuming all pore canals are filled with OP-fibres. C2) Schematic picture shows the mechanism for increasing the critical Euler buckling load of the OP fibres by stabilizing the OP fibres with lateral IP fibres in the Bouligand layers [4, 5]. D1) Schematic of plywood structure with sublamellae of different thickness, with five sublamellae plotted. D2) Two examples of predicted sublamellar widths distribution for $\Delta\gamma_0 = 70°$ (black bars) and $\Delta\gamma_0 = 30°$ (grey bars) plotted.

From fitting the model to experimental maps of X-ray diffraction across the tissue, it is clear that the relative proportions, intensities, and architecture of the IP- and OP- fibre fractions vary across and between the cuticle types, and these results are supported by X-ray micro CT. Scanning X-ray diffraction maps of fibre orientation in tergite and telson (**Figure 4.6**) show the fibre orientation (γ_0) is parallel to the long axis of the animal for both tissue types, consistent with previous (larger-scale or lower spatial resolution) findings for lobster cuticle [63], while the in-plane lamellar tilt β mostly tracks parallel to the mesoscale shape of the cuticle. Our results of a wider degree of in-plane fibre orientation in the Bouligand layer in the denser exocuticle and membranous layer (relative to the endocuticle) may lead to increase in-plane mechanical isotropy in these layers.

Noticeable differences in telson and tergite lies in both the fraction of out-of-plane (OP) fibres and their spatial variation across the carina in the telson (**Figure 4.6**). Briefly, it can be seen from **Figure 4.6 D1-D2** and **Figure 4.7A** that the overall proportion of OP fibres is larger in telson compared to tergite, but considerable intra- and inter-tissue variations exist. In telson, the main difference is a larger proportion of

OP fibres in the centre of the apical carina, which is expected to be the site of first impact during intra- and inter-species combat[1, 23], when compared to the adjacent tissue sloping into the valleys. Supporting this finding, the X-ray micro CT results (**Figure 4.8**) show streaks of higher mineralization in the apical carina; the pore canals have a higher mineralization[24, 120]. SEM images also show qualitative differences in pore-canal density and size (**Figure 4.4 A4**, **B4**, and **C4**). In the tergite, the principal feature is the significantly larger proportion of OP fibres in the exocuticle compared to the endocuticle, a variation which is not observed at a significant level in telson.

The functional significance of the ultra-, micro- and meso-structural changes on the mechanics is illustrated schematically in **Figure 4.9**. At the mesoscale, by increasing local curvature of the cuticle on going from the tergite to the highly curved central carina of the telson (shown in **Figure 4.6A**) the resistance to deflection is increased (**Figure 4.9A**). The outer region with darker shading denotes the exocuticle and the inner region with lighter shading denotes the endocuticle. The deflection d can be simplistically estimated from the standard formulae for the elastic deflection of a shell [121] as $d \sim FR/Eh^2$, where F is the impact force, R the radius of curvature, E the elastic modulus of the shell, and h the shell thickness. In order to obtain an order of magnitude estimate of this effect, we neglect (for the moment) the elastic modulus difference between the tergite and telson and the specific details of the end-effects at the edges of the cuticle. Estimating the geometrical parameters R and h from the SEM images in **Figure 4.6**, the radius of the apical carina is $\sim 0.25/2.5 = 0.10$ the radius of the entire tergite, and the carinal thickness ~ 2 times the tergite thickness (**Figure 4.9A**). As a result, the deflection of the

central carina telson is reduced by a factor of ~20, for the same impact force. We note that this is an order-of-magnitude estimate only, as the carina (as well as the tergite) are quite thick and cannot be considered true elastic shells at the scale of ~1 mm considered in **Figure 4.6**.

Considering now the microstructural level, stiffness and buckling stability increases due to the higher volume fraction of OP fibres in the pore canal (**Figure 4.9B**). Following qualitatively our experimental results, the out-of-plane fibres (orange; colour online) are shown qualitatively to be having a larger volume fraction and be individually larger in the central apical region of the telson (**Figure 4.9 B1**), relative to the side regions. Further, the out-of-plane fibres in the tergite are shown schematically as fewer and smaller (**Figure 4.9 B2**). The horizontal light blue (colour online) circles, ellipses and fibres represent schematically the twisted plywood fibre structure of a Bouligand layer. An estimate of the increased stiffness may be made by using a standard Voigt model, where the elastic modulus in the direction parallel to the applied force for the IP fibres is E^{IP} and for the OP fibres E^{OP}. Estimates of these moduli can be taken from prior multiscale modelling results on lobster cuticle [52], with E^{IP} ~ 7 GPa, and E^{OP} ~14 GPa. The volume fraction of the OP fibre within pore canals is denoted by Φ_{OP}, and can be estimated from the OP-IP fibre ratio Φ_2/Φ_1 by $\Phi_{\text{OP}} = \Phi_2/ (\Phi_1 + \Phi_2)$. Comparing a homogeneous (*H*) plywood lamella with no (or few) pore canals or OP fibres (the tergite) with a honeycomb plywood lamella with large fraction of filled pore (*FP*) canals with OP fibres (the telson), the strain ratio is

$$\frac{\varepsilon_{FP}^{IP}}{\varepsilon_H^{IP}} = \frac{1}{\Phi_{PC}\left(\frac{E^{OP}}{E^{IP}}\right)+(1-\Phi_{PC})} \quad equation\ 4.11$$

In **Figure 4.9 C1**, we plot the decrease of strain ratio with increasing volume fraction, using an upper and lower estimate for the OP fibre axial stiffness of 14 GPa [52] and 21 GPa [166] respectively. The strain ratio decreases to ~55-60% of the nonporous (homogeneous) value for the high OP-fibre region of the apical carina in the telson, reducing impact deflection. Ellipses here denote approximately the area fractions corresponding to the experimentally observed OP/IP fibre ratios for the different regions of the telson and tergite.

While the OP fibres can increase the stiffness as described above, they may also be prone to lateral buckling instability. In this regard, the increase in buckling stability of the OP fibres due to the presence of the transverse IP fibres in the Bouligand structure can also be estimated (**Figure 4.9 C2**). If the OP fibres have a diameter D, an elastic modulus $E_A{}^{OP}$ (as above) and a length L, the Euler buckling load[167] $P_c{}^S$ is $\pi^2 ED^4/64L^2$ for isolated fibres. If, in contrast, the fibres are held in place in a repeating array of lamellae (IP fibres in the Bouligand structure), then the free length of the fibres is dramatically reduced, and the new critical buckling load is $P_c{}^H = \pi^2 ED^4/64((L/n)-D)^2$ (equation 4.12). In the case of telson (or tergite), the IP lamellae are in contact, for all practical purposes (as shown in **Figure 4.9 C2**), and L/n ~ D. As a result, the critical buckling load becomes very large, and the OP fibres are safe from buckling induced instability. Taken together, these relatively simple considerations, while not a complete explanation, identify some micro- and mesostructural mechanisms of relevance in giving telson its very high impact resistance.

4.5 Discussion and Conclusion

The stomatopod telson is a specialized exoskeleton segment used to resist impact [4], analogous to a shield, and from the perspective of advanced biologically inspired materials design [23], offers potential insights into the interplay between the tough and resilient material (chitin/protein fibres in a mineralized matrix) at the smallest (molecular) length scales and the gradients in fibre orientation and mineralization to achieve resistance to high rate loading. Prior work has shown that macroscopically, the telson absorbs and dissipates energy under impact, with an analogy drawn to a punching bag [122], but the micro- and nanostructural mechanisms within the mineralized fibrous matrix by which these occur are not well understood. These mechanisms will depend on parameters like deformation and shear in the organic/inorganic fibrous matrix at the scale of 1-10 nm, and (at the micron-length scale) on alterations in angular pitch and spacing of the Bouligand layers (lamellae), variation in the porosity of the honeycomb structure and the mechanical deformation and load-sharing between the lamellar (IP) fibres and the mineralized fibres in the pore canals. In order to emulate the function of the telson in synthetic or scaled-up versions of the system, in addition to precision synthesis at the molecular level, experimental input regarding the mesoscale gradients in nanostructure, and their functional relevance, is essential. The intrinsically three-dimensional architectural motifs at the material-level (the repeating Bouligand layers of mineralized fibres [122, 123], interpenetrated with the pore-canal/honeycomb pattern [50, 168], varying in size and orientation across the tissue, have to date made extracting such ultra structural information a challenge. Here, we have introduced a combination of synchrotron

microfocus X-ray diffraction with model-based reconstruction in mineralized cuticle, which provides a quantitative multiscale map of the three-dimensional mineralized fibrillar ultrastructure in telson across the entire tissue. We focussed on the apical carinal ridge, which is the first impact-site on the telson during intra- and interspecific conflict. The carina will clearly absorb and resist very high-frequency, high magnitude loading [169], and analysing fibre structure and orientation *in situ* at this site will give insight into local-structural optimizations for dynamic loading.

The conformation, orientation and strain in biomolecules *in situ* are challenging to determine experimentally. Techniques like single molecule force spectroscopy [170] or scanning probe microscopic probes of individual fibrils [52] can determine the molecular unfolding and internal energy landscape of single molecules or aggregates, but probe the molecule or fibril in an isolated state. Light microscopy (even super high resolution microscopy) cannot achieve the required resolution, while electron microscopic methods are surface-specific, and require the sample to be dehydrated. The X-ray diffraction reconstruction method circumvents the above issues, as it can be carried out for samples in a hydrated, close to native state and determines molecular conformation *in situ*. The method combines the intrinsic molecular resolution and statistical averaging power of X-ray diffraction with a method to circumvent the limited slice of reciprocal space obtained from a single X-ray pattern of an anisotropic nanotextured object. Further, by combining the model-based reconstruction with high brilliance microfocus synchrotron X-ray sources and scanning of sections [171], it is possible to produce, effectively, 3-dimensional maps of the ultra structural components *in situ*, in this case the alpha-chitin fibrils. In contrast to other 3D

imaging methods like X-ray micro-CT, the use of X-ray diffraction maps enables parameters like orientation, crystallinity and phase to be mapped at the same time, from the same scattering volumes, and with high statistical precision. Previous work on cellulose [172] determined a single parameter (the principal orientation of fibres) but did not consider the fibre angular distribution, a crucial parameter arising from the Bouligand-type plywood arrangement. More recently, a similar approach was used for spider sensilia [52], but without an explicitly specified model as we do in **equation 4.1** to **4.10**. In contrast, our model can be generalized to predict, quantitatively, the orientation, pre-strain and other parameters in multiple biological composites and biologically inspired materials [69], and the spatial resolution achievable of the molecular structure can be varied down to micron- and sub-micron scales with newer generation nanofocus setups [173]. While we considered only a single chitin diffraction peak here as an orientation marker, the analysis of reflections in multiple directions at the molecular level (like the c-axis (002) peak) will no doubt provide a more complete picture of the in-situ molecular and supramolecular architectures.

The principal assumption in our model is the existence of fibre symmetry, which from a practical viewpoint implies that the diffraction signal is averaged at least over a single fibre (~100 nm) (**Figure 4.1 C2**), and not the 3-5 nm individual fibrils. Current ultra structural data suggest that the alpha-chitin fibrils are, relative to each other, rotated around their axis of symmetry within a fibre, leading to effective fibre symmetry conditions. Given (a) typical dimensions of X-ray nanofocus beams (~100-300 nm) [97] combined with (b) the minimum thicknesses (~ 1-5 microns) possible for tissues like cuticle without inducing damage and (c) minimum scattering volumes of ~ 1

μm³ in order to obtain sufficient X-ray count statistics, it is therefore likely to remain a valid assumption for the wide majority of cases that may be considered.

The two local parameters characterizing the plywood (Bouligand) structure of the chitin fibres at each scan point are the principal fibre direction γ_0, and the angular width of the distribution $\Delta\gamma_0$. Our results show that the principal fibre direction is mainly oriented along the long axis of the animal (**Figure 4.1**), for both the telson as well as the tergite segment, although some small variations exist across the tissue. This result is consistent with larger scale X-ray texture measurements of the calcite texture reported in [69]. The second parameter, the angular width of the distribution $\Delta\gamma_0$, has not been explicitly calculated for cuticle, as far as we are aware, and limited quantitative data exists on the fibril orientation distribution in the literature. It is related to the full width at half maximum of the plywood distribution by:

$$FWHM = 2\sqrt{2\ln 2}\,\Delta\gamma_0 \ (equation\ 4.13)$$

way of comparison, the angular width estimated for other chitinous materials like squid beak [52] from two-dimensional plots increases with increase in the range of fibril orientations. In our case, due to the three-dimensional nature of our diffracting geometry combined with the use of the (110) reflection to determine fibre orientation, $\Delta\gamma_0$ decreases as the range of fibril orientations increases.

From experimentally measured $\Delta\gamma_0$, the twisted plywood architectures predicted by these values can be simulated. Plywood structures, found in arthropod [57] and bone [97] among others, are often considered as comprising of sublamellae, where each sublamellae has a specific principle fibre direction and thickness [52]. Electron- and light

microscopic studies on the chitin fibril arrangement in arthropod cuticle [57, 69] have suggested that the angular distribution of the fibrils inside lamellae is a continuous variable, implying a smooth twisting of the fibril principle axis. A quantitative model has been proposed for bone [52], where the twisted plywood structure of bone collagen has been represented as a 5 sublamellae model with fractional thicknesses/angles given by ([0.36/0°], [0.36/30°], [0.09/60°], [0.09/90°], [0.09/120°] (**Figure 4.5** in [69]). In order to predict the plywood structure from $\Delta\gamma_0$, either (a) the thickness of each sublamellae or (b) the angle of each sublamellae needs to be assumed. For illustration purposes, we will assume an n=5 sublamellae-structure with the sublamellae angles at $\gamma_i = 0°$, 22.5°, 45°, 67.5° and 90° to the principal fibre direction γ_0, but with the widths of the sublamellae variable. For an experimentally fitted distribution w (γ; γ_0, $\Delta\gamma_0$) and a lamellar thickness t, the thickness of each sublamellae is given by:

$$t_i(\gamma_i) = \frac{t\big(w(\gamma_i; \gamma_0, \Delta\gamma_0)\big)}{\big(\sum_{i=1}^{n=5} w(\gamma_i; \gamma_0, \Delta\gamma_0)\big)} \ (equation \ 4.14)$$

The predicted sublamellae widths are plotted in **Figure 4.9D2** using estimates of $\Delta\gamma_0$ for the telson from **Figure 4.7B**, assuming the same total lamellar thickness of 20 microns. For illustration purposes, from **Figure 4.7B** a high-end estimate of $\Delta\gamma_0 = 70°$ was taken for the telson exocuticle and a low-end estimate of $\Delta\gamma_0 = 30°$ was taken for the telson endocuticle. We see that the telson exocuticle has a fibril distribution closer to isotropic (all sublamellae have similar widths in the range of 3-5 microns), implying a wider range of fibril orientations. In contrast, the telson endocuticle has a more highly oriented distribution, with sublamellae ranging in size from 1 to 12 microns. Having a range of fibre orientations at the lamellar level can

be useful for mechanical toughening, as cracks can be diverted or deflected from their path to follow the direction which splits adjacent fibrils side-by-side instead of fracturing fibrils across their width. Such toughening mechanisms have been extensively documented for bone (e.g. [78, 92]) and are certain to play an important role in the micromechanical toughness and impact resistance of cuticle. From the computed values of $\Delta\gamma_0$ from our model, the variation of the plywood architecture can be determined across the tissue, and associated changes in mechanical properties like toughness can potentially be modelled.

As an example of the importance of microscale material gradients in enabling impact resistance, consider the division of the telson into protruding ridges (carinae) and adjoining sunken valley segments (**Figure 4.1 A2** and **Figure 4.6**). Simulated impact tests have previously shown that the carinae do not visibly deform (i.e. are highly stiff) during the macroscopic flexural deformation of the telson [174], which was ascribed to higher overall mineralization in the carinae relative to the valleys. Our results (**Figure 4.7 D2** and **4.6C**) shed light on this phenomenon, by determining an increased fraction of out-of-plane (OP) mineralized chitin fibres (in the pore canals) in the central carina, which increase resistance to vertical compression. The increased load sharing of vertically oriented OP fibres is especially pronounced at the centre of the carina. At the same time, due to the shape effect of the highly curved carina with a low radius of curvature, the carina is extremely resistant to bending. Considering the (non-ridged) tergite tissue, we observe that a greater density of OP fibres is visible in the exocuticle compared to the endocuticle, which would increase the outer-layer stiffness. These findings are consistent with nanoindentation measurements [1] showing more than 30%

higher stiffness in the exocuticle of lobster cuticle, although these authors ascribed the main material cause for the stiffness increase as a combination of increased mineralization and higher packing density of lamellae.

We note that the increased stiffness due to OP-fibre reinforcing in the exocuticle of the tergite is a different concept from the highly mineralized layer found on the surface of telson in [92] When comparing the material ultrastructural differences in the normal curved exocuticle segment like the tergite with the less deformable ridged telson of the stomatopod, the principal difference appears to be that lateral (side-to-side) gradients in OP/IP fibre fractions and increased isotropy in the centre of the carina exists in telson, while the tergite has mainly a gradient in fibrous ultrastructure from the outside to the inside. The mechanical benefits of the latter form of gradient have been previously discussed, enabling a flexion without failure.

In contrast, in the telson, the lateral gradient in fibre orientation and relative densities between the carina and valleys appears a significant factor enabling increased resistance to impacts. We contrast this approach with other natural shell-like structures, for example in the turtle shell, where a compliant superficial layer on top of a stiff underlying substrate was shown to increase energy absorption [24]. Indeed, the use of biological shell-like templates with variations or periodic modulations in shape [160], combined with modification of material parameters such as anisotropy, organic/inorganic ratio or fibre texture, is likely to be a promising route to develop a wide range of bio-inspired chitin-based structural and functional materials.

In terms of limitations of the current study, we focus on the chitin fibre network, and do not consider explicitly the diffraction signal from the mineral phase, largely because a considerable portion of the

mineral (especially in the endocuticle) is known to be amorphous[79, 80] with no significant X-ray diffraction signal. The mineral plays an important mechanical role, especially in the outer part of the exocuticle, where hard crystalline forms of calcium carbonate, calcium phosphate and fluorapatite based minerals (found in dactyl [23, 175, 176]) may be present. Further, it has been recently shown in the dactyl club that sliding and rotation of the mineral nanoparticles is an important energy dissipating mechanisms [1], and it would be thus interesting to explore the role of the equivalent mineral phase in telson. In order to fully understand the mechanical roles of the mineral phases, X-ray fluorescence (XRF) method together with tomography measurement can be used to determine the mineralization distribution within different length-levels. In addition, the in-situ mechanical test combined with WAXD measurements will also be sufficient to study the change of crystalline mineral phases in terms of mircotexture and strain. In conclusion, we have presented a novel 3D X-ray reconstruction method to experimentally measure, for the first time, the mesoscale variations of Bouligand and pore-canal chitin fibre orientation in a biomineralized chitinous composite optimized for high impact loading. The structural design of such evolutionarily optimized biomaterials can potentially be applied to the synthesis or fabrication of lightweight synthetic biologically inspired composites for applications in armour and defence, combining the superior properties of the nanoscale building blocks with spatial modulations in structure at higher length scales. Further, the quantitative approach can be applied readily to analyse the link between nano- and microscale fibrous architecture and function in biobased materials, whether the function is primarily structural, mechanical, photonic or electrical.

Chapter 5: Characterisation of fibril strain in mineralised chitin by *in situ* tensile testing

5.1 Synopsis

In the previous Chapter, we had developed a model to quantify the chitin fibril orientation in the telson, and had discussed possible ways in which the 3D orientation could play a mechanical role in enabling the high impact resistance. The complementary question of the deformation properties of the material comprising this fibre composite (the chitin/protein/mineral matrix) remained open. In the current Chapter, we take the first step toward answering this question by measuring the fibril-level deformation mechanisms of planar sections of stomatopod tergite. As discussed in the Chapter 2, the tergite is the generic exoskeleton element of stomatopod (and other shrimps) as shown in **Figure 5.1**. It can be considered as the "non-armoured" equivalent of the telson, which has macro-, micro- and possibly nano-level gradients in material- and property variation over and above that of the tergite. Because of its simpler geometry, the tergite is well suited to being used, in tensile testing, to obtain quantitative information on the *in situ* fibrillar strains in mineralized arthropod cuticle. Such experiments and their interpretation are the subject of this Chapter.
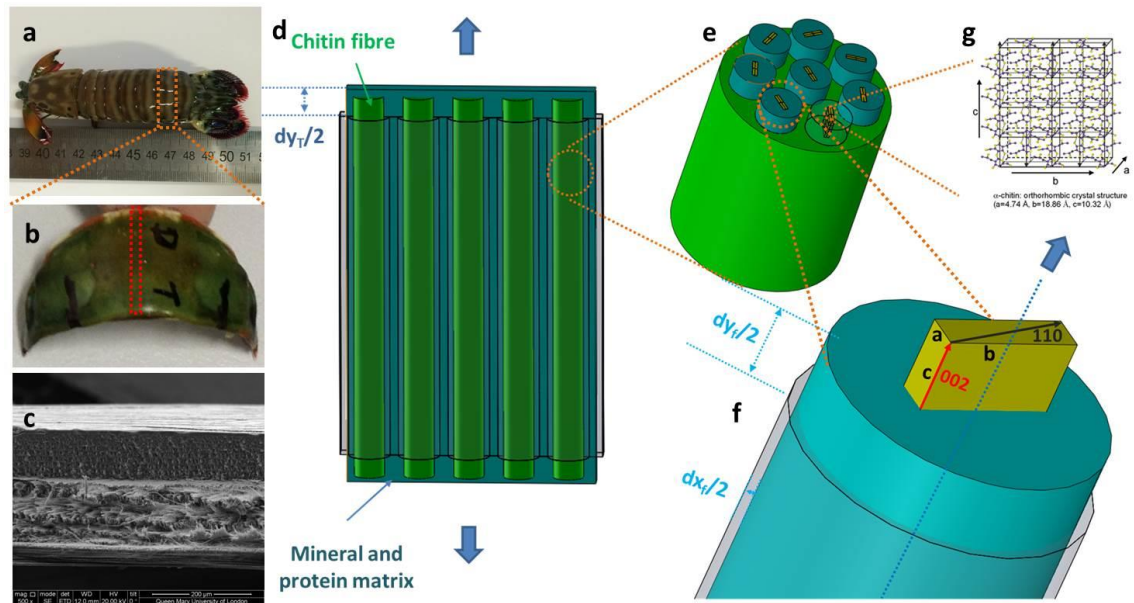
Figure 5.1. *Hierarchical structure of stomatopod cuticle. (a): Image of stomatopod. (b): Tergite sample obtained from the stomatopod shown in a. (c): SEM image showing the fracture surface of the specimen sectioned from the tergite after tensile test, the red rectangle indicates the region where the sample was obtained for tensile test (d) schematic image of one single mineralised chitin-protein fibre plane. (e): Chitin fibre which consists of crystalline chitin fibrils (blue) and protein (green). (f): Crystalline chitin fibril, one orthorhombic unit cell was added to indicate that the coincidence between fibril orientation and c-axis of unit cell. (g): Crystalline structure formed by chitin molecular chains.*

5.2 Materials and methods

5.2.1 Sample preparation

The mantis shrimp *Odontodactylus scyllarus* from the tropical Indo-Pacific were purchased from a commercial supplier (Tropical Marine Centre, London) and stored at -20°C till used for sample preparation. One day before synchrotron test, the abdomen tergite (**Figure 5.1b)** was dissected from defrosted mantis shrimp (**Figure 5.1a)**. Then the central region of tergite sample was cut into slices indicated by the dash rectangle in **Figure 5.2a** for tensile testing. Both ends of the

specimen were embedded in dental cement (Filtek^{TM} Supreme XT, 3M ESPE, USA.) as shown in the **Figure 5.2c** to grip the samples in the tensile testing device using customized moulds. The typical dimensions of specimens were approximately 0.5 mm (thickness), 0.6 mm (width) and 3.0 mm (length), note the parts which were embedded inside dental cement were not measured here. Then the embedded samples were placed into the custom sample holders of our lab developed tensile tester. After the tensile tests, all test specimens were air dried and prepared for scanning electron microscopy. The fractured surfaces were coated with gold and examined in SEM (Inspect F, FEI, Eindhoven, Netherlands).

Two different embedding configurations were used for the synchrotron tensile tests. As shown in **Figure 5.2d**, the L1 configuration is with the surface of tergite cuticle facing upwards so the incident X-ray beam will be perpendicular to the surface of the cuticle. While the L2 configuration is with the surface of tergite cuticle facing towards right or left so the incident X-ray beam will be parallel to the surface of the cuticle.
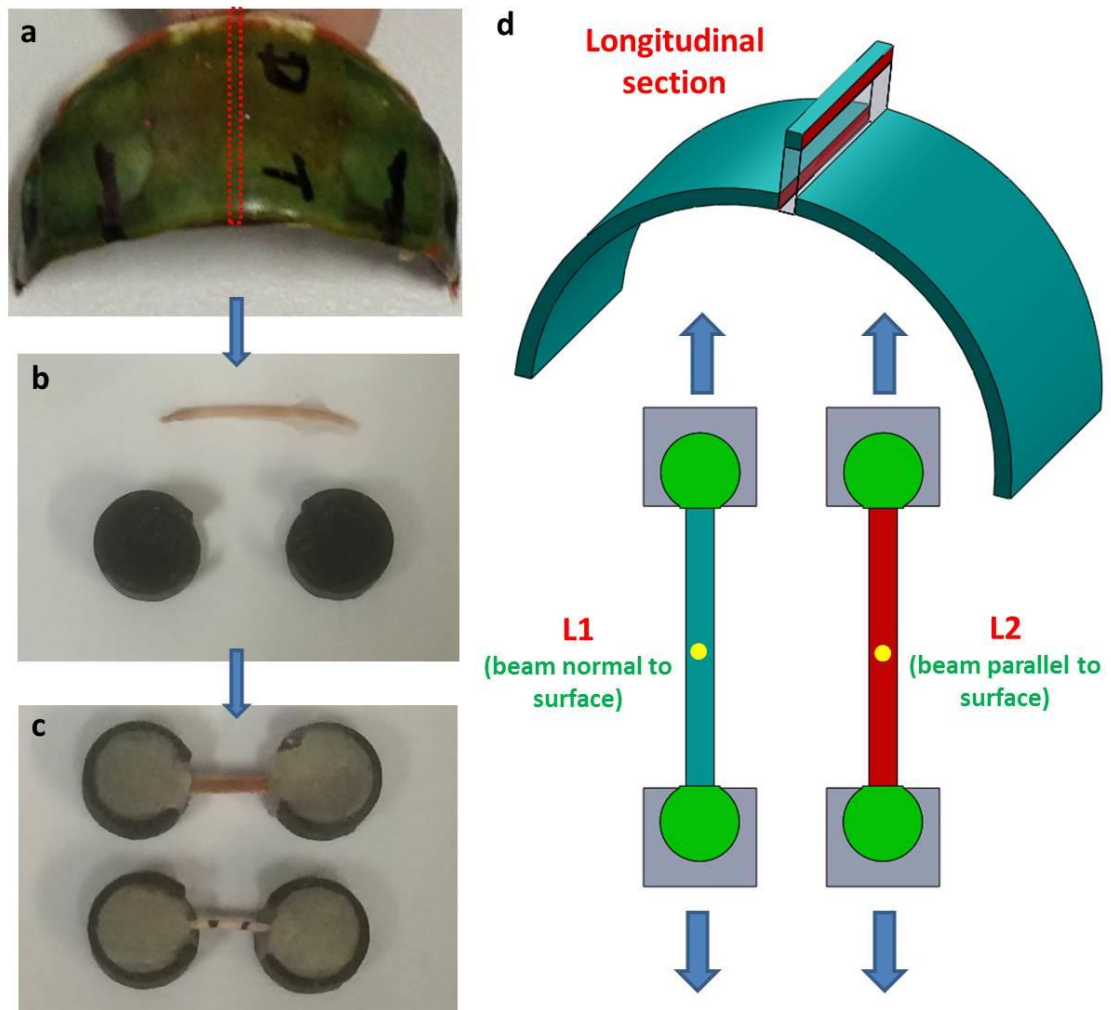
Figure 5.2. *Sample preparation. (a-c): The specimens were collected from the central region of the tergite cuticle. (d): Schematic plot for the L1 and L2 configurations in tensile test.*

5.2.2 Synchrotron tensile testing

The experiments were performed at the Diamond Light Source (DLS) in Oxfordshire, UK, using the imaging set-up at beamline I22. The embedded cuticle specimens (**Figure 5.2c**) were mounted in the micro-tensile tester (**Figure 5.3**) mounted on a 3-axis motorized stage in the beamline. In the customized micromechanical device the strain is applied by an M126.1DG motor which has a travel range of 25cm and a minimum incremental motion of 0.1 μm. Load was measured

with a 110 N tension/compression load cell. The loading rate was set to 0.002 mm/s for tensile test. During the test, WAXD images were collected every 0.5% motor strain increment from samples with initial length around 3mm. In order to reduce radiation, the samples were moved 10 μm vertically by moving the 3-axis motorized stage where the tensile tester was located to avoid the beam hit the same region throughout the test. Due to an initial slack-range in the grips, the stress-strain curve shows an initial toe-in region, which was not considered during the data evaluation.
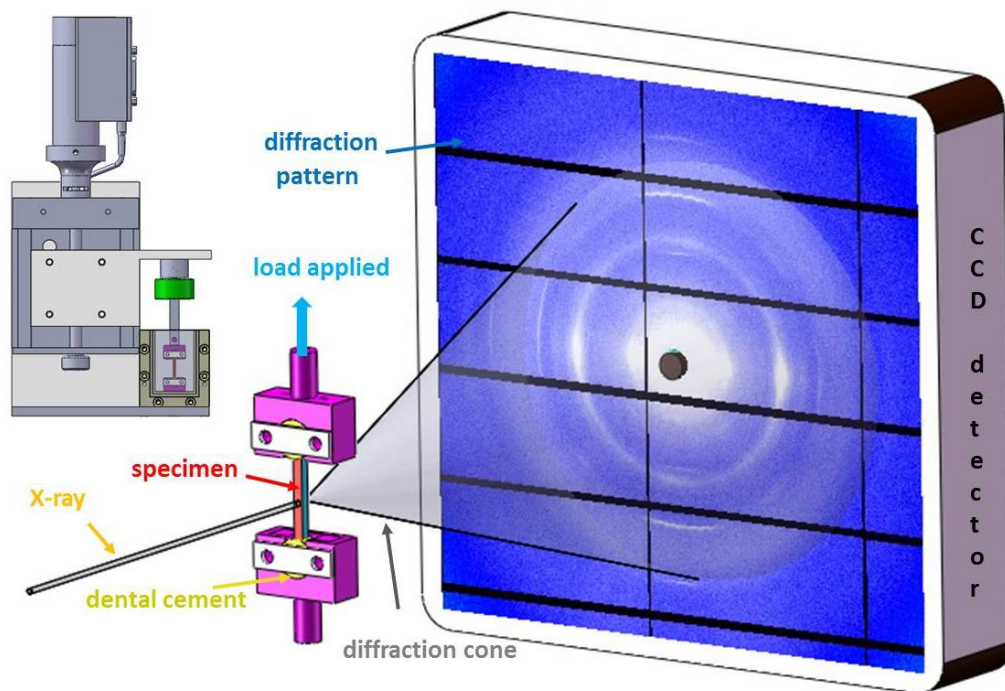
Figure 5.3. Experimental setup in synchrotron. (a) Mechanical tester design for tensile testing, the specimen can be immersed in fluid to mimic biological environment. (b) A narrow synchrotron X-ray beam impinges from the right to the cuticle specimen and the diffraction rings recorded on a 2D detector on the right, the tergite specimen was embedded in dental cement before test.

5.2.3 Tissue strain calibration
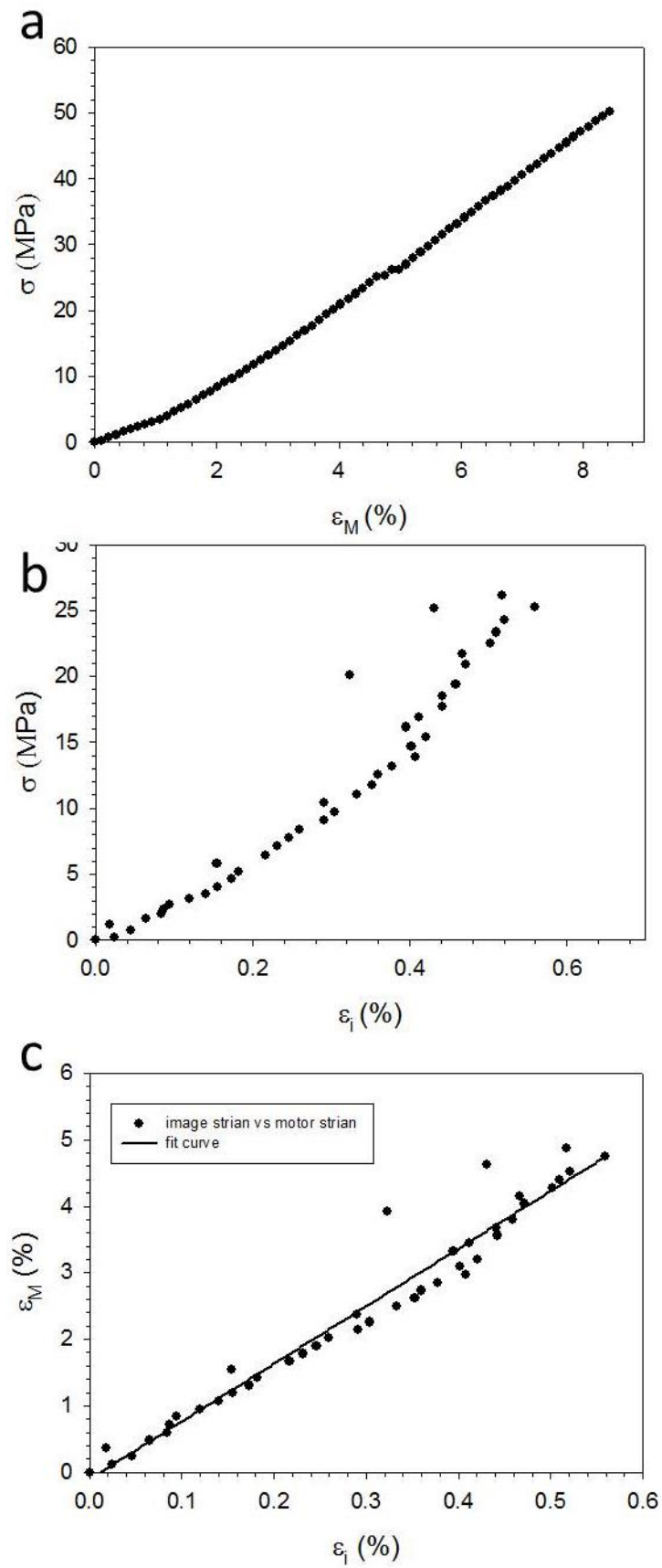
Figure 5.4. Tissue strain calibration. (a) The stress versus motor strain curve. (b) The stress versus tissue strain curve. (c) The motor strain verse tissue strain curve.

Due to the significant setup difficulties for mounting the GigE-standard camera which was integrated in the image correlation programme described in **Chapter 3**, we transfer the motor strains from synchrotron tensile tests to real tissue strain by multiplying a calibration coefficient between the motor strain and tissue strain which was acquired by multiple lab tests. The cuticle samples were marked with black marker pen in both ends to create black patterns to enhance grey scale contrast for digital image correlation. The series of digital images were analysed using in-house developed image correlation software which running in LabVIEW 2012 as described at **section 3.5**. After that, the motor strains (**Figure 5.4a**) and tissue strains (**Figure 5.4b**) were plotted together in SigmaPlot and the ratio between motor strains and tissue strains was obtained by fitting the curve using linear function (**Figure 5.4c**). During the sample movements during the tensile tests, the tissue strain analysis may not be able to go through all images till the sample fracture, therefore all the linear fitting were performed under the tissue strain of 0.55%. Seven tergite samples in total were calibrated and an average ratio value of 10.93±1.56 between the motor strains to tissue strains was obtained. This value (10.93) was used as calibration coefficient to calculate the tissue strains of those samples tested in synchrotron test by dividing the motor strains with the calibration coefficient value.

5.3 Results

5.3.1 Macro mechanical properties of stomatopod cuticle
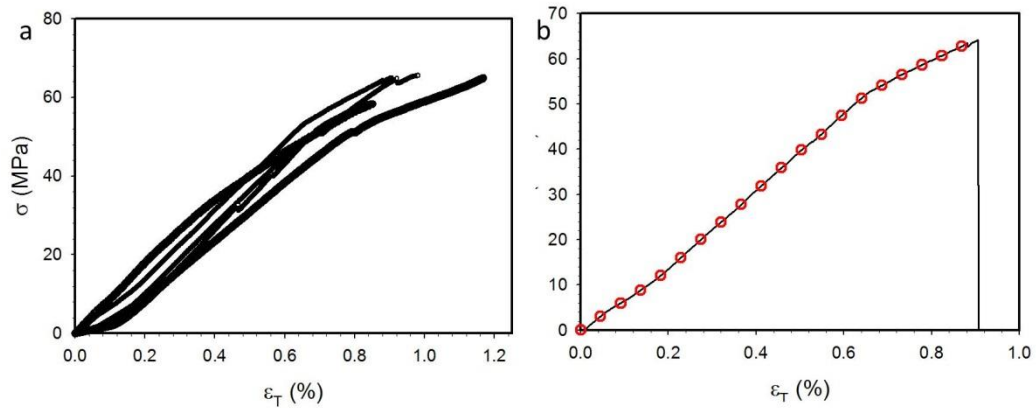
Figure 5.5. *Mechanical data. (a): Stress versus tissue strain data from L1 configuration. (b): One example stress and strain curve from L1. The red circles on top of the curve indicate the time points of which diffraction image acquired. The tissue strain (ε_T) was calibrated using image correlation.*

The representative stress–strain curves for L1 configurations were shown in **Figure 5.5a**. The stress values were obtained by dividing the load values with the cross-sectional area of the tergite samples before deformation. Note that the tissue strains (ε_T) for all the samples were calibrated from the motor strains (ε_m) using image correlation method described in the **section 5.2.3**. Both the stress to fracture (σ_f), average strain to fracture (ε_f) and Young's modulus (E) for the tergite samples in L1 and L2 tensile tests were listed in **Table 5.1**. The results were averaged from eight specimens each for L1 and L2 tensile tests. The mechanical properties acquired from L1 and L2 tensile tests shown no significant difference, which was expected. A representative stress and strain curve from L1 configuration was shown in Figure **5.5b**. The red circles on top of the curve indicate the respective time points of which

diffraction image acquired. The diffraction patterns then were analysed to study the strains in the nanoscale.

Table 5.1. The mechanical properties acquired from L1 and L2 tensile tests.

Configuration	Stress to fracture (σ_f) (MPa)	Strain to fracture (ε_f) (%)	Young's modulus (E) (GPa)
L1	55.51 ± 15.66	1.03 ± 0.23	0.68 ± 0.23
L2	48.34 ± 15.06	0.95 ± 0.14	0.55 ± 0.07

5.3.2 Deformation of chitin fibre under tensile testing

A typical 2D diffraction pattern from the tergite cuticle sample with the X-ray beam roughly perpendicular to the cuticle surface (L1 configuration) is shown in **Figure 5.6a**, and the corresponding 1D diffraction profile obtained by radially averaging the indicated 2D pattern region in **Figure 5.6a** is displayed in **Figure 5.6c**. The (110) and (002) reflections from alpha chitin were clearly discernible. Also, the 2D diffraction pattern from the tergite cuticle with the beam parallel to the cuticle surface (L2 configuration) was displayed in **Figure 5.6b**. The (002) and (110) reflections in L1 configuration exhibit as continuous rings while in L2 configuration the reflections only exist in arcs. These differences were even more clearly demonstrated by the azimuthally averaged 1D diffraction files (**Figure 5.4d**). The continuous (002) and (110) reflection rings confirmed that the chitin fibre planes arranged as continuous plywood structure with

fibre orientated in all directions. The orientation in the fibril is directly corresponding to the angle at (002) reflection ring.
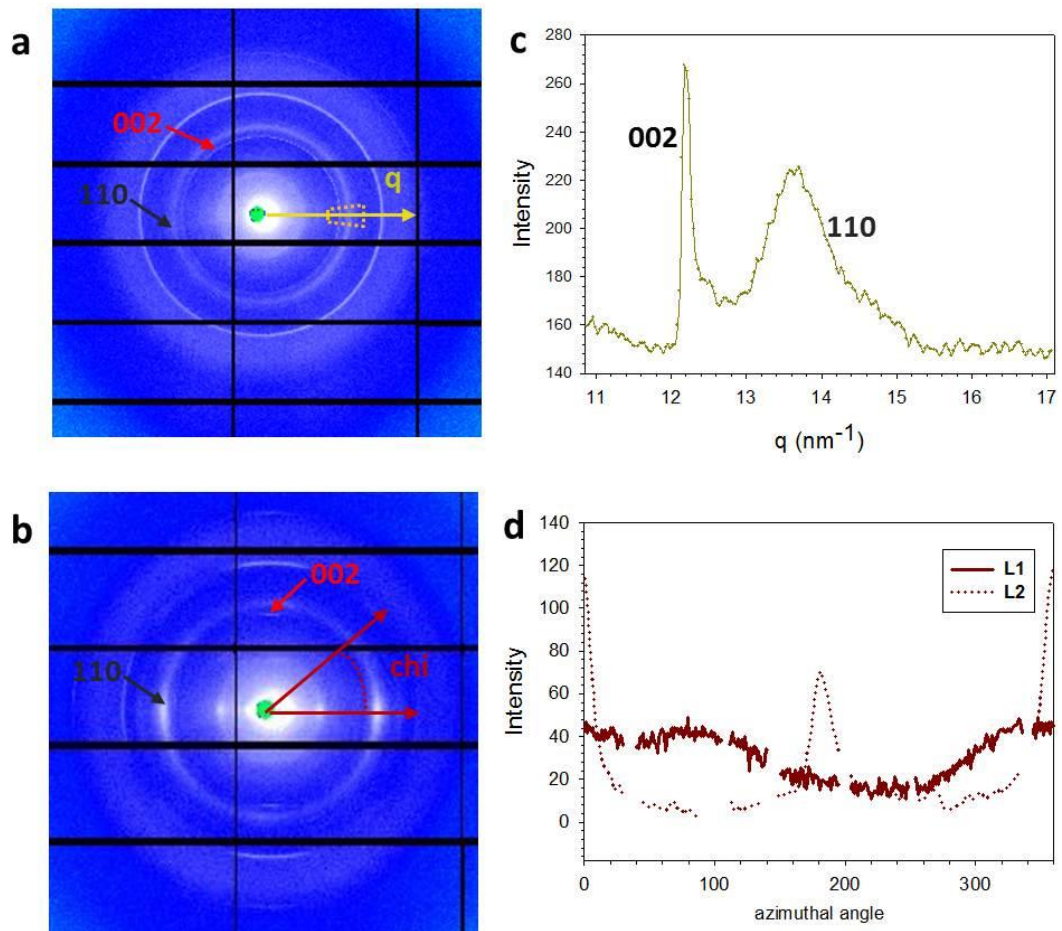
Figure 5.6. *Two different sample orientations for synchrotron tensile tests. (a-b): Representing WAXD patterns acquired from L1 (a) and L2 (b) configuration. The (002), (110) reflections are indicated in both cases. (c): The radial integration (c) for the dark yellow region in (a). The azimuthal integration (d) for (110) reflections from L1 (solid) and L2 (dash) configurations. The missed data here are due to the mask region of the CCD detector.*

When the cuticle is under tensile loading, the deformation of crystal lattice can be tracked by the peak positions of q value of different reflections. Since the c-axis of chitin crystals is parallel to the fibril and fibre axis, the q value change of (002) reflections will indicate whether the chitin fibre is under stretching or contracting.

Analogously, the q value variation of (110) reflections indicates the enlarging or compressing in the radial direction of chitin fibres. In addition, the orientation changes of chitin fibre can be obtained by tracking the azimuthal angle of the arcs of (110) and (002) reflections. Thus, a quantitative characterization of the fibre deformation can be performed simultaneously with the macroscopic deformation in the bulk sample. With the sample mechanically loaded in tension, diffraction patterns were collected *in situ* at regular intervals (indicate in **Figure 5.5b**) till the sample fractured. The patterns collected were used for quantitative analysis of fibre strain and reorientation.

Starting from the easier case, which is the fibres orientated along the tensile direction. In order to trace the deformation of fibres along the tensile direction, the (002) reflections here were integrated from 7 degrees sector which centred at 90 degrees while the (110) reflections were integrated from 7 degrees sector which centred at 0 degree in the diffraction pattern.

To demonstrate the strain calculation process, a set of 1D profile of (110) and (002) reflections and the fitting curves from a representative tensile test were shown in **Figure 5.7a** and **5.7c**. Note for clarity only parts of (002) and (110) reflection intensity curves were shown in **Figure 5.7a** and **5.7c**. The whole fitting results of q values for (002) and (110) reflections were plotted in Figure **5.7b** and **5.7d** respectively as a function of the tissue strain (ε_T). The Figure **5.7b** shows a clear q value increment for the 002 reflections as well as a distinctive q value decrement for the (110) reflections.
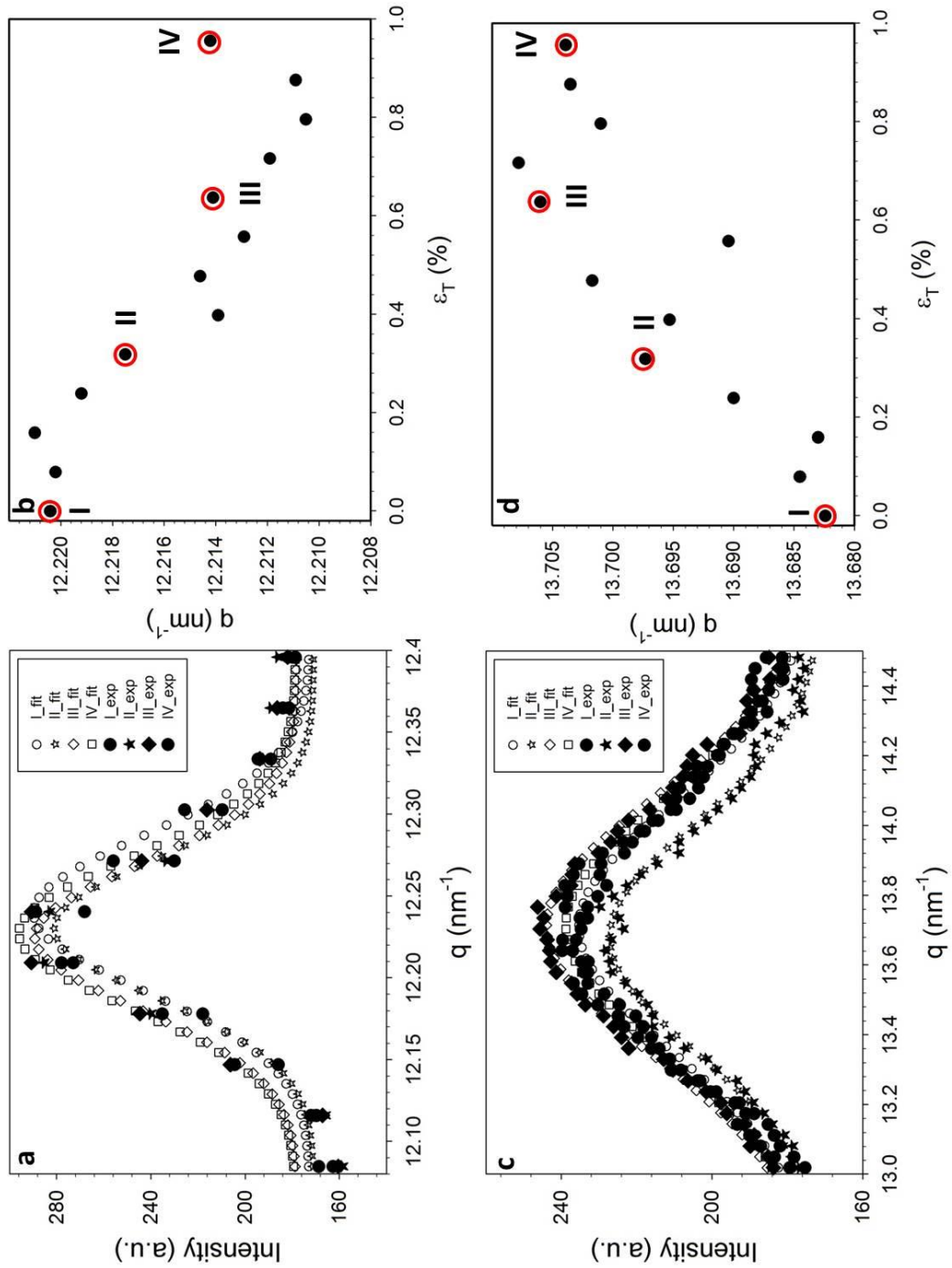
Figure 5.7. Quantified fibril strains as a function of tissue strains. (a, c): The 2D diffraction patterns were converted to 1D intensity versus q for (002) (a) and (110) (c) reflections. The peak positions of the (002) and (110) reflection reflect the deformation along the fibre axis and radial direction respectively. The curves with filled circles are experimental data while the curves with empty circles are the fitted data. (b, d): The quantified fibril strains calculated from (002) (b) and (110) (d) reflections as a function of tissue strains for an example tergite sample.

As the sample under tensile loading, the intensity peak positions of the (002) reflection shifted negatively and (110) reflection shifted positively till the point where tissue strain (ε_T) reach near 0.65%. The initial q value changes of (002) and (110) reflections demonstrated the chitin fibres were stretched along the fibre axis and contracted in the radial direction. The initial linear increase and decrease of q values indicate that the chitin fibril exhibit elastic deformation behaviour under loading. However, after the elastic deformation stage, the fibril strains began to level off even though the whole sample is still under elongation, which indicated the chitin fibril will yield before the whole tissue began to fail. In order to directly indicate the strain behaviour along the fibre axis and radial direction, we transfer the q values (q(002) and q(110)) into D values (D(002), D(110)), as the strain of D(002) and D(110) can be considered as equal to the fibril strain along chitin fibre axis as well as radial strain respectively. **Figure 5.8** shows the average strain increments for D (002) and D (110) as a function of tissue strains (along the tensile direction) from five specimens. The results demonstrated that the mineralised chitin fibril will yield earlier before the whole tissue fractured under tensile loading. The fact of that fibril strain is just a fraction of the overall tissue strain also exists in other biological tissues like collagen for bone[20] and cellulose for wood. By fitting the elastic region (ε_T less than 0.65%) of the strain curves, we found that the increment of D(002) value was 32.51% $\pm$ 1.61% of the elongation of whole tissue, while in the radial direction the chitin fibril contracted with a strain about 21.65% $\pm$ 6.46% of the whole tissue strain (ε_T). Therefore, by dividing the compression in the radial axis of the fibril with expansion along the fibril axis, we can acquire the poisson's ratio for the chitin fibril which is around 0.66.
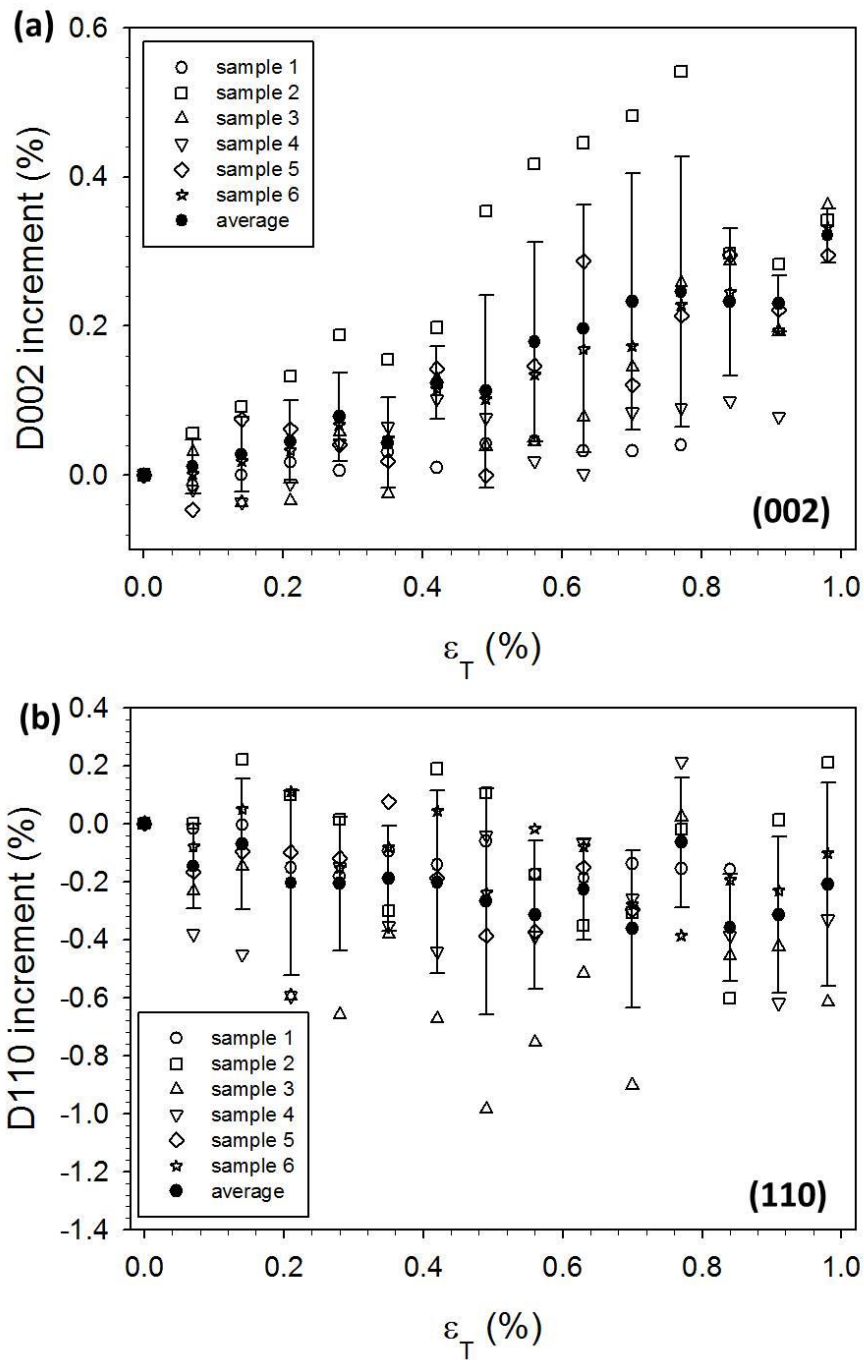
Figure 5.8. *D-spacing values increments for (002) (a) and (110) (b) reflections correspondingly as a function of tissue strain (εT).* The filled circles indicated the average values from 6 specimens. *Error bars represent the standard deviation.*

5.3.3 Fibre reorientation under tensile testing
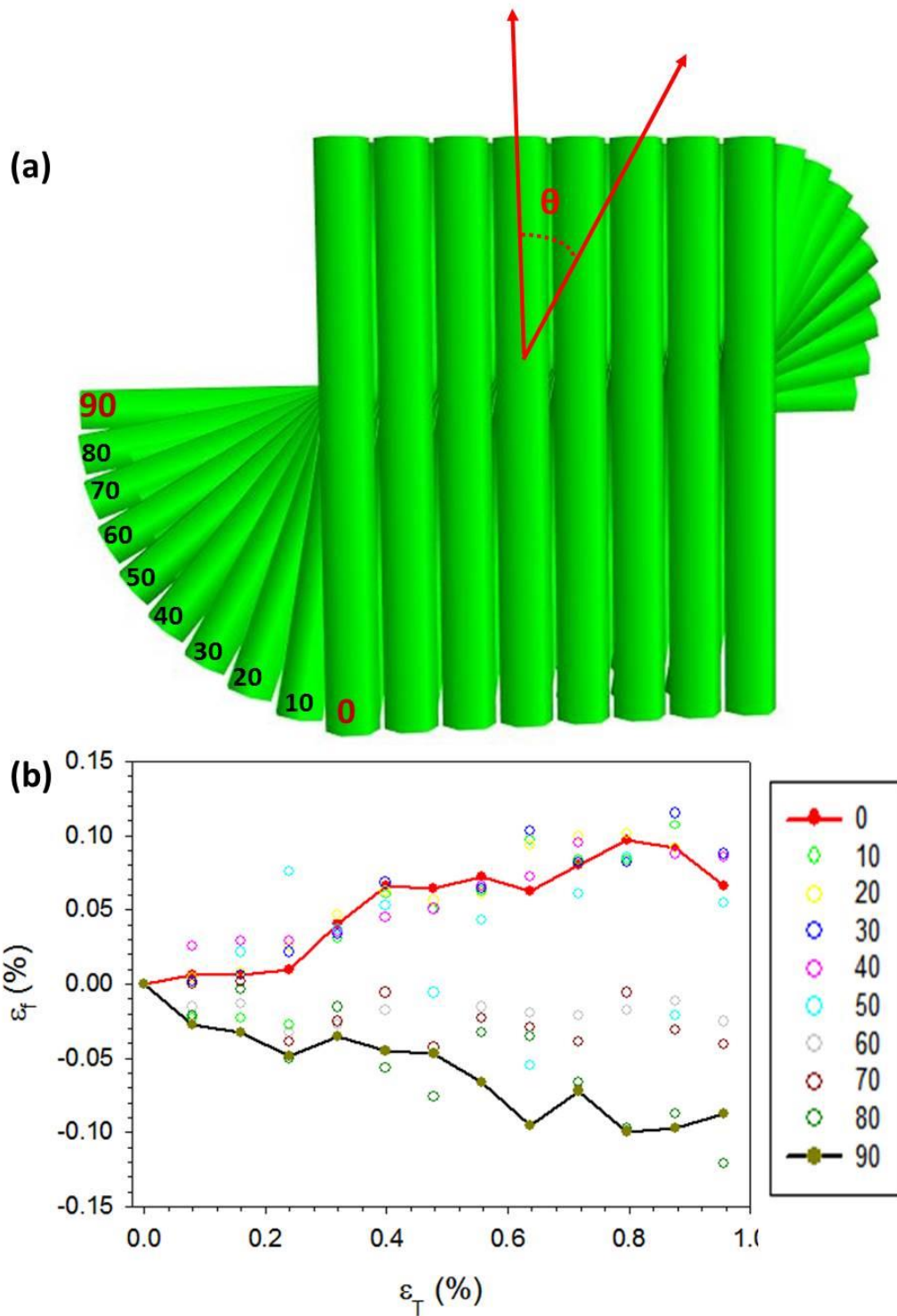
Figure 5.9. *Anisotropic fibril strain behaviour. (a) Schematic plot demonstrates 10 different sub-lamellas in one plywood lamella. Each sub-lamella represents a different fibre orientation (θ). (b) Quantified of fibril strains (ε_f) as a function of the tissue strains (ε_f) for different orientations. The results indicate significant*

differences in strain behaviour. Those sub-lamellas oriented between 0 – 40 degrees which is closer to the load direction deform in tension while those at 50 - 90 degrees which is away from load direction deform in compression.

We also investigated the strain increments off the tensile direction by comparing the D (002) value changes acquired from a series of similar azimuthal integration sectors which centred at θ = 10, 20, 30, 40, 50, 60, 70, 80, 90 degrees away from the tensile direction (**Figure 5.9a**). The strain increments exhibited different behaviours between those acquired from 0-40 degrees off tensile axis with those from 60 - 90 degrees off tensile axis with a transition zone between 40-60 degrees. The results indicated that the chitin fibres which orientated close to the tensile direction (0-40 degrees) show a positive strain till the fibril yielding as the load increasing, while fibres orientated further away from the tensile direction showed a negative strain till the fibril yielding at a tissue strain (ε_T) around 0.65% (**Figure 5.9b**). In the transition region (40 - 60 degrees) the chitin fibres showed no significant strain increments compared to the other regions.

Fibre reorientations within the lamella plane were analysed by tracking the fibre quantity changes in different azimuthal region (θ) away from the tensile direction by calculating the diffraction intensities of corresponding azimuthal sectors from the (002) reflection rings. During the synchrotron tests, the samples were shifted vertically with a step size equal to the beam size (10 μm) to avoid radiation damages which can affect the mechanical results. As a result, the diffraction intensity could be altered due to the scattering volume changes even without fibre reorientation change. However, by normalising the diffraction intensity across θ = 0 - 90 degrees, the scattering volume variation effect will be eliminated and therefore the

intensity change w (θ) will only determine by the fibre reorientation process.
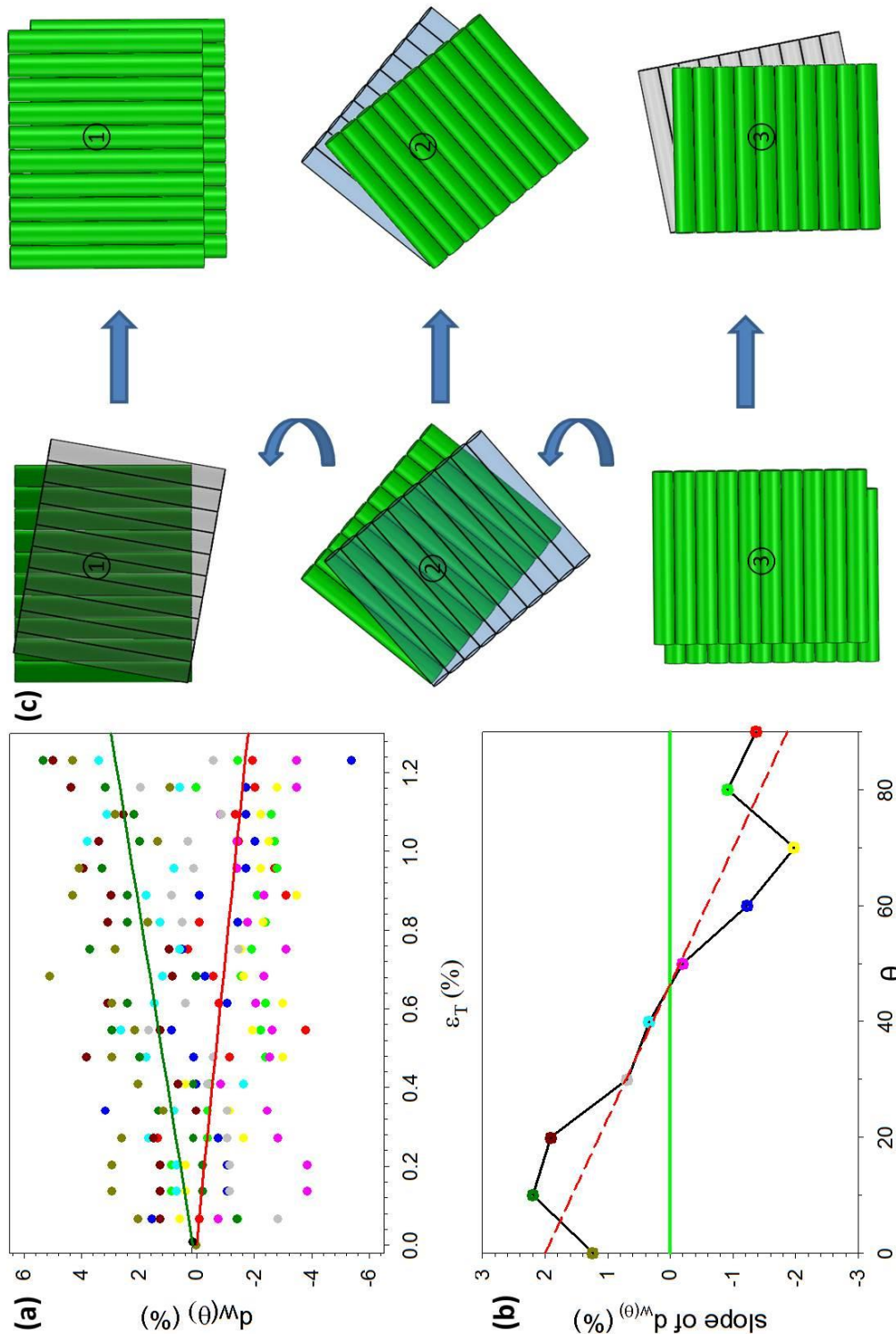
Figure 5.10. *In-plane fibre reorientation behaviour. (a) Quantification of fibre intensity percentage change for different orientations as a function of different*

tissue strains. Two fitted lines (θ = 10, red; θ = 80, dark green) were shown to indicate the trend. (b) The slope values by fitting the data from figure a. (c) Schematic plot showing the reorientation behaviour within one plywood lamella.

Figure 5.10a shows the increments of w (θ) as a function of tissue strains (ε_T). The diffraction intensities of the (002) reflection of WAXD patterns of L1 were integrated every 10 degrees. Therefore the w (θ) here actually represents an average value of all orientations within an azimuthal sector of ten degrees which cantered at θ. **Figure 5.10a** shows that under tensile loading the chitin fibre intensities increased within the 0 - 40 degrees region and the fibre intensities decreased in the region (50-90 degrees) away from the tensile directions. This tendency can even be more clearly viewed in **Figure 5.10b** which displays the slopes ($d_{w(\theta)}$) of the intensity percentage changes in different θ values. Positive slope values ($d_{w(\theta)}$) indicate the intensity in the corresponding azimuthal region was increasing while negative values show a decreasing in intensity. The schematic plot in **Figure 5.10c** explains why the intensity changes as the way shown in **Figure 5.10a**. The plywood lamella is divided into three regions by the orientation angle θ (① 0 – 30 degrees, ② 40 – 60 degrees and ③70 – 90 degrees). When the sample was under tensile loading, all fibres rotated towards the loading direction. As a result, the fibres in the region (60-90 degrees, ③) only moved out while new fibres kept moving into region ①. In the region ② the fibre intensity tends to be balanced with fibre moved in and out by the same amount. The transparent fibre planes in **Figure 5.10c** means the fibres is not belong to the current region.

5.4 Discussion

In this chapter, we have experimentally determined the molecular level strains in the planar tergite exoskeleton segment of the mantis shrimp, in response to tensile loading. The tergite was chosen in this initial study as a prototype mineralized cuticle, with a simpler geometry at the macro- and meso-scale compared to telson. Likewise, the simple tensile test protocol used was chosen for ease of experimentation and analysis, and not because it is the representative contact loading and bending scenario found in telson. In particular, the tensile tests were used to obtain some ideas about the nanoscale constitutive relation of the chitin fibrils in the mineralized protein matrix. Our main findings are:

- Using the (002) reflection along the fibre direction, we see there is an initial elastic tensile deformation of the chitin fibres parallel to the load direction (PLFs) up to tissue strains of ~0.4-0.6%, followed by a transition to inelastic deformation with a near-constant molecular strain.

- The Poisson's ratio of the chitin fibres was determined to be ~0.66 by measuring the relative radial contraction from the (110) reflection and comparing it to the along fibre (002) direction.

- Fibres are oriented at multiple angles (Bouligand structure), and an angle-dependent fibre strain response is observed for these fibres. There is tension in fibres between 0° and 45° to the loading axis, and compression for fibres at larger angles.

- All fibres, regardless of their initial angular position, reorient toward the loading axis upon increasing macroscopic load, but

the extent of the reorientation depends on the initial angular position.

- Both the angle-dependent fibre strain and reorientation can be explained from a composite laminate model of fibres in a mineralized protein matrix.

- Fibre strains, even along the loading axis, are lesser than tissue strains by a factor of ~0. 67.

Taken as a whole, these results are, to the best of our knowledge, the first fibre-level deformation studies of cuticle taking structural anisotropy into account and explicitly considering fibre reorientation. The second aspect is methodologically innovative as well, because while the methodology used: combination of *in situ* mechanical testing with high brilliance synchrotron SAXS or WAXD has been successfully used previously the supramolecular deformation of biological tissues like bone [14, 33, 141] and tendon [34, 177], these previous studies have largely assumed a principal fibre direction and calculated a single fibre strain along this direction. The justification for this has been that the tissues studied are either intrinsically parallel-fibred like tendon [178] , or near parallel-fibred variants thereof, such as fibro lamellar bone[19, 146], or chitinous locust tendon [47, 99] .

Previous static X-ray diffraction studies have already reported the chemical and crystal structure of alpha chitin [59, 80], and we use the findings of an orthorhombic structure, together with fibre symmetry, in our mechanical interpretation of the data. Also, *in-situ* synchrotron mechanical testing combined with WAXD on the chitin fibres isolated chemically from crab tendon Nishino et al [81] has reported the Young's modulus of alpha chitin to be 59.3 GPa. However, in nature,

the chitin fibres always co-existing with surrounding protein and mineral matrix, and more importantly, the orientations of chitin fibres exhibit complex 3D texture. Therefore, the characterization of mechanics of chitin fibres within natural tissue microenvironment is crucial to understand the biological structure function relations, which is an advantage of our approach

Our results on the angle-dependent strain and reorientation shed light on the mechanical function of the plywood (Bouligand) structure. Within stomatopod cuticle, the mineralised chitin fibres arrange in plywood style form into lamella structure across the exocuticle to endocuticle [1, 25]. The plywood architectures, which are widely found in natural body armours such as fish scales and exoskeleton of arthropods [10, 49, 179], have been considered playing a key role in contributing the mechanical properties of whole natural composites[49]. Nanoindentation testing can, in some extent, reveal gradients and anisotropy in the hardness and the elastic properties of such biological composites. However, due to the layered structure, the measured values are an integrated, weighted average of the Young's moduli of several layers of the chitin fibre planes [71], and cannot be related to individual elastic moduli of the lamellae. Therefore, the quantitative characterisation of the reorientation and deformation in the plywood lamella, of the type measured here, will be great importance to understanding the mechanisms of mechanical optimization at this level.

Under tensile testing, the wet stomatopod tergite sample usually yield or fractured at an average strain (ε_T) of 0.9%, which was smaller than the tissue strain to fracture found in the wet exoskeleton of other crustaceans like crab (6.4%) [180] and lobster (1.8%) [160] which

also have similar hierarchical structure design and chemical composition. The average fracture stress for stomatopod tergite cuticle (47.7 MPa) we obtained were slightly higher than crab exoskeleton (31.5 MPa)[180] and lobster cuticle (37.2 MPa) [160], while the Young's modulus of stomatopod tergite cuticle (604 MPa) were resemble crab exoskeleton (518 MPa) [180]. The Young's modulus of lobster cuticle obtained from tensile test was not reported before. The differences in obtained mechanical values including tissue strain to fracture (ε_T), Young's modulus (E), fracture stress (σ_f) mainly result from the chemical composition and structural differences between different animals, but also due to the locations where the sample were collected as well as the age of animals, and lastly the degree of accuracy in conversion from motor strain to tissue strain.

As mentioned before, the coincidence of c axis of alpha chitin crystal and the chitin fibre axis connect the orientation from molecular level to lamella level. We first quantified the deformation of chitin fibres in the tensile direction. Under tensile loading, the chitin fibres orientated along the tensile direction are exhibit elastic stretching along the tensile direction and compress in the radial direction of chitin fibre till the tissue strain (ε_T) reaches 0.6%. After that, the strain level starts to level off, this may due to the yielding of chitin fibrils. Similar yielding phenomenon has been observed from collagen fibrils in bone [14, 19, 20]. Also, we observed the fibril strains (ε_f) of chitin were less than half of the tissue strain, which demonstrated the stretching of chitin fibrils is hindered by the shear of mineral matrix. Interestingly, the chitin fibril to tissue strain ratio ($\varepsilon_f/\varepsilon_T$) of stomatopod tergite (0.45) is close to the collagen fibril to tissue train ratio ($\varepsilon_f/\varepsilon_T$) of bone which reported by Gupta et al [14, 19]. This coincidence indicates the

phenomenon may exist in all biological composites which constituent of organic fibrils and mineral matrix even though the material can vary.

In addition, by comparing the deformation in the radial direction and along the fibre axis we also obtained the Poisson's ratio of chitin fibril of 0.66, which has never been reported before. The Poisson's ratio of chitin fibril is higher than collagen fibril (0.28)[181], which is also an important fibrillar constituent for biological tissues like bone and cartilage. For other components, the Poisson's ratio of non-collagenous protein is 0.45[48], and the Poisson's ratio for amorphous calcium carbonate (ACC) are generally considered as the same as calcite (0.34) [182]. When it comes to the Poisson's ratio of tissue level, the value is anisotropic and the values varies a lot depending on the sample positions on bone (0.12-0.63) [183], cuticle as well as the method used to measure the Poisson's ratio. The Poisson's ratio of arthropod cuticle is believed to be around 0.3[184, 185]. The Poisson's ratio will be of great use in computational modelling for predict mechanical properties at different level as an important input value. Also, the observed positive strain for 002 reflections and negative strain for (110) reflections itself validates that the c axis of alpha chitin crystal is along the fibre axis.

Chitin fibril rotation towards the tensile axis was observed in the lamella of tergite. In this regard the group of Robert O. Ritchie[10] have recently observed that in fish scales the collagen fibrils to the tensile axis will rotate towards the tensile direction and those orientated close to perpendicular direction of tensile axis will rotate away from the tensile direction. However, though with similar Bouligand-type (twisted plywood) arrangement in the lamella

structure, all the chitin fibres in stomatopod cuticle are rotating towards the tensile axis. Those differences may due to the much higher stiffness of chitin than collagen fibril as well as the different surrounding matrix environments. The advantage of our method is we can track the fibre reorientation process upon loading of all fibre layers oriented at various angle in the chitin lamella by calculated the normalised intensity changes at different azimuthal angle of WAXD patterns. The quantitative reorientation calculation within plywood structure is a huge step forward compare the qualitative reorientation examination[10].

The anisotropic deformation behaviour we found within mineralised chitin lamella layer indicates an anisotropic stiffness in different fibre layers with different orientation angle. And those continuous stiffness oscillation is across the whole lamella is believed to be able to hinder crack propagation and thereby improve damage tolerance [1]. Also, upon loading, the chitin fibres will reorient to new direction which interrupt the original crack propagation path and increase the contact area of cracks and dissipate more energy[1, 26].

Chapter 6: The in-plane and out-of-plane chitin fibre deformation of stomatopod telson under in-situ bending test

6.1 Synopsis

In this **Chapter**, we turn to the experimental question of determining the full-field fibril-level deformation response of the telson to applied external macroscopic loading. In the previous two Chapters, we had considered the static 3D fibril structure of the telson (**Chapter 4**) and the fibril-level deformation of the Bouligand architecture of mineralized chitin fibrils (**Chapter 5**). In telson, the Bouligand architecture is combined with meso- and macro scale modulations of shape and structure (**Figure 4.6**). These structural variations at multiple length scales are expected to play a role in optimizing the telson for impact resistance, but the mechanisms (as stated earlier) are not known at the nanoscale. By progressing to more realistic deformation modes like 4-point bending, and combining the previous *in situ* loading approach with microfocus scanning to determine spatial variations of fibrillar-strain response to load across the meso- and macro scale structural levels, we take the first steps in determining the full-field nanoscale mechanical response of telson cuticle in response to loading.

6.2 Materials and Methods

6.2.1 Materials

Same with before, the mantis shrimp *Odontodactylus scyllarus* from the tropical Indo-Pacific were purchased from a commercial supplier

(Tropical Marine Centre, London) and stored at -20 °C till used for sample preparation. One day before synchrotron test, the abdomen tergite and telson was dissected from defrosted mantis shrimp. For bending test, the dissected tergite and telson were fully embedded in dental material and cut with diamond inner saw. For tergite, one transverse slice with thickness of 1mm in the central region was obtained for bending test, while for the telson, the transverse slice was collected form the highest point of central carina with thickness around 1mm.

6.2.2 Synchrotron bending test

Before the bending tests, telson samples were carefully placed in the region between the two loading pins and the holders as shown in **Figure 6.1**. No external force should be applied on the telson samples before the WAXD and transmission scans to collect the structural information in the native conditions (**Figure 6.1a**). The 2D transmission scans were collected before WAXD pattern scans from the area between the two loadings pins to help locate the different regions within the telson sample. The WAXD scans were then collected from the central carina and adjacent valley region of telson cuticle identified from the 2D transmission maps. The step size for both the transmission and WAXD scans were set to be 100 μm in both horizontal and vertical directions (**Figure 6.1**). The large step size for imaging was chosen in order to cover wider regions and reduce radiation damages at the same time. After the tests on the original status, the samples were deformed under bending with a motor velocity of 0.002mm/s till the displacement reached 2.1mm (**Figure 6.1b**). Then similar transmission and WAXD scans were performed to collect the information under bending. The bending force on the

cuticle samples was continuously measured along with displacement values. Need to mention that different regions of the telson sample will not necessarily under uniaxial deformation even though a uniaxial compression loading protocol was performed due to the complexity in sample geometry. As shown by the blue arrows in **Figure 6.1 b**, the telson sample compressed vertically as a whole under loading, while the carinae part which locates between the two loading pins was compressed horizontally. Therefore, the local stress and strain distributions over the telson sample are not straight forward to get. However, the local strains of chitin fibre acquired from *in-situ* WAXD test will be important to understand the mechanical responses in different hierarchical levels of the cuticle.
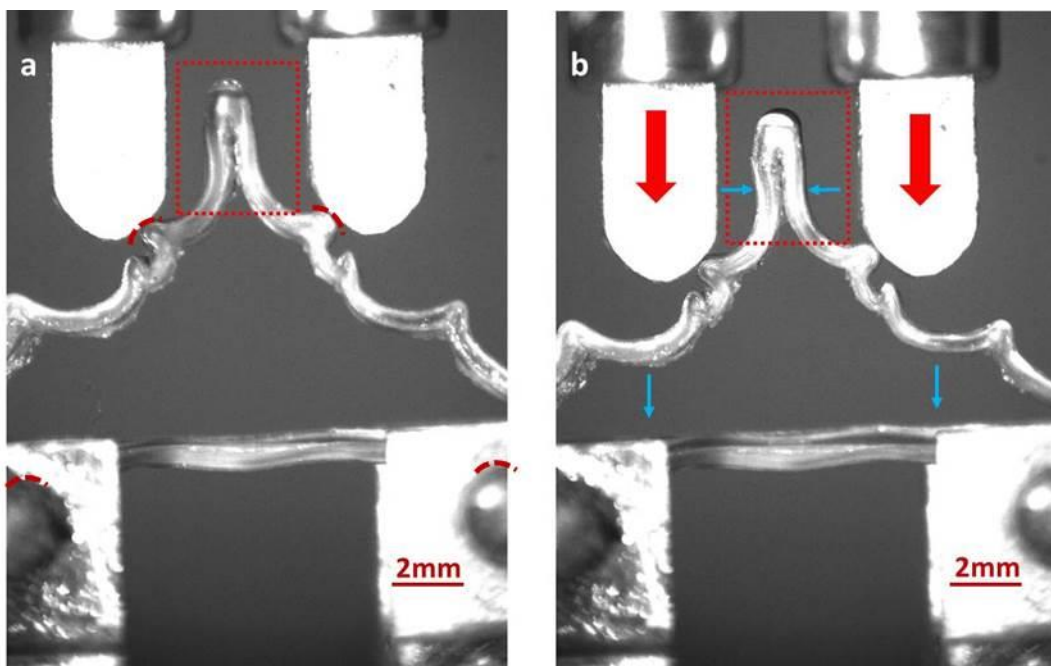
Figure 6.1. *The experimental setup for bending test. (a): before loading (b): under bending. Note the WAXD scans were performed between the two loading pins (areas are indicated with red dash rectangles) thereby both the central carina and valley region of the telson samples will be covered. The red arcs in (a) indicated the contact regions between the sample and the tester. The red arrows*

show the movements of the loading pins and the blue arrows indicate the resulting deformations of the telson in different regions.

6.3 Results

6.3.1 Load and displacement curve
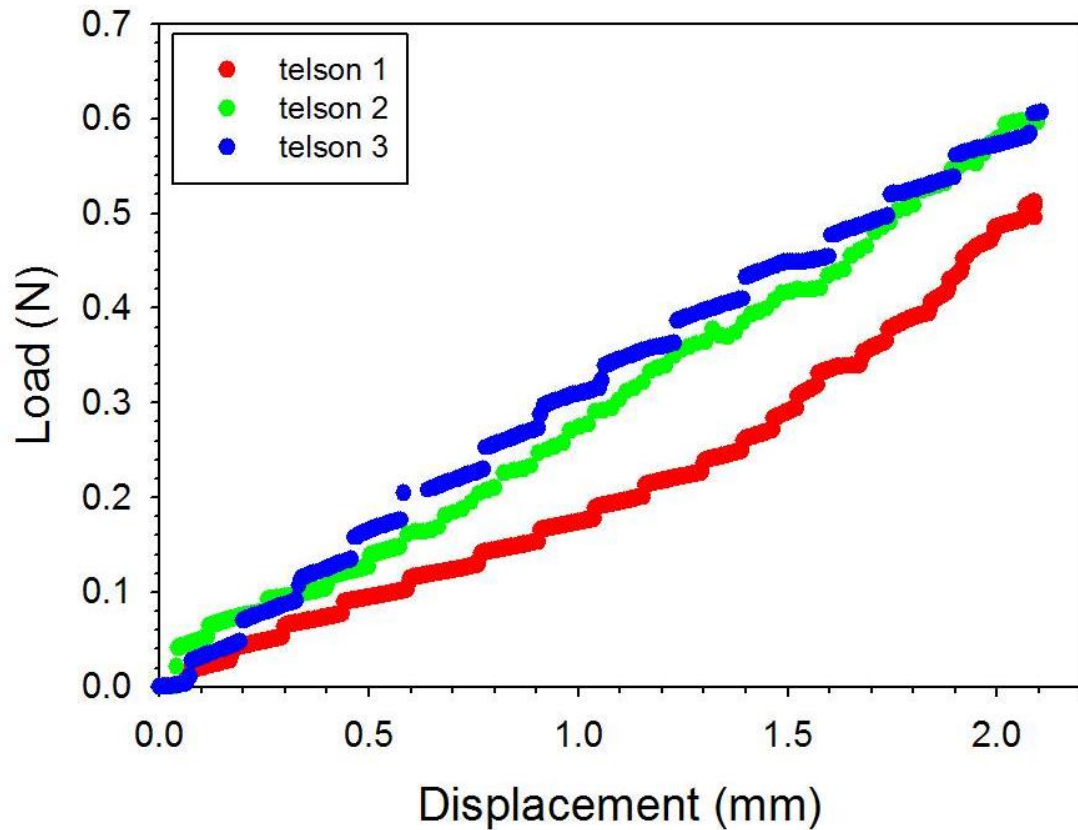
Figure 6.2. The load and displacement curves for telson under bending.

Three telson samples were tested in synchrotron and the corresponding displacement and load curves were displayed in **Figure 6.2**. The 2D transmission and WAXD scans were performed between the two loading pins prior loading and after the displacements reached 2.1mm. Due to the complicated sample shapes no further data analyses were done. However, the load and displacement values of macrostructural level collected here will be of great importance to be used as initial inputs in the future computational modelling analysis.

6.3.2 Transmission map
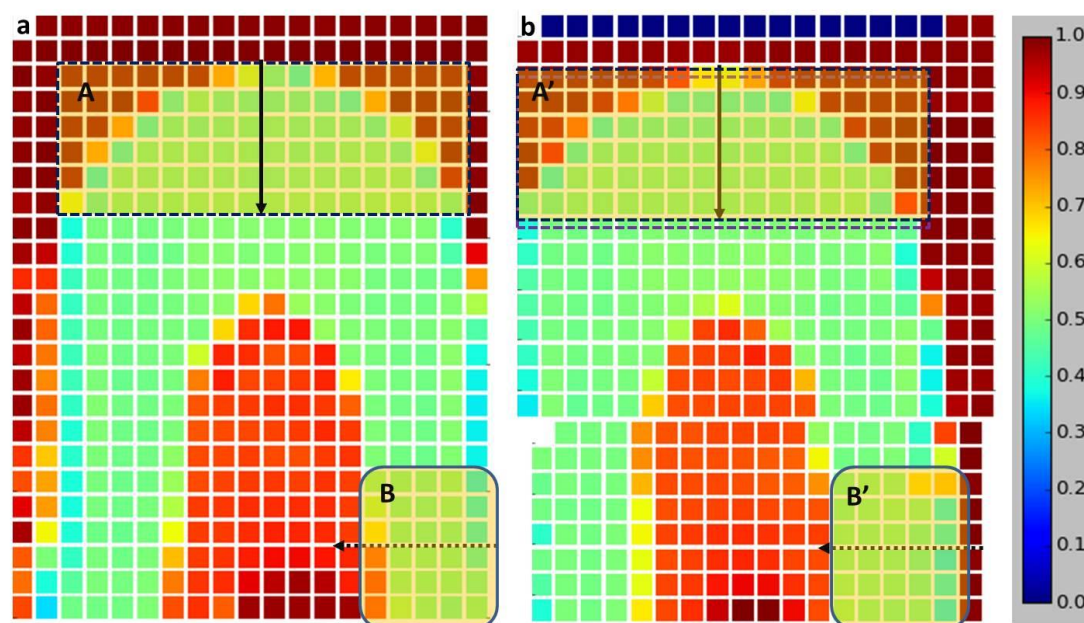
Figure 6.3. *X-ray absorption maps. (a): The transmission value map across the central carina region as well as part of the valley region between central carina and first side carina before loading. (b): The transmission value map collected from the same area when under loading.*

In order to locate the telson samples and more importantly the different regions of the samples, 2D *X-ray absorption* maps were obtained by normalising the diode readings from the sample regions with those from empty beam regions. As shown in **Figure 6.3**, the lower transmission values in telson sample pointed out the shapes of the sample very clearly compare to high values in empty regions. Also, we can clearly distinguish the exocuticle regions with transmission values less than 0.35 with the endocuticle region whose transmission values were ranging from 0.4-0.6. The transmission values for the inner membrane layer and the underlying organic tissue region can reach to 0.7 – 0.9. According to the transmission maps in **Figure 6.3**, two WAXD scanning regions were selected to represent the central

carina region and valley region of telson and were indicated with rectangles shown in **Figure 6.3.**

6.3.3 Data analysis of WAXD pattern
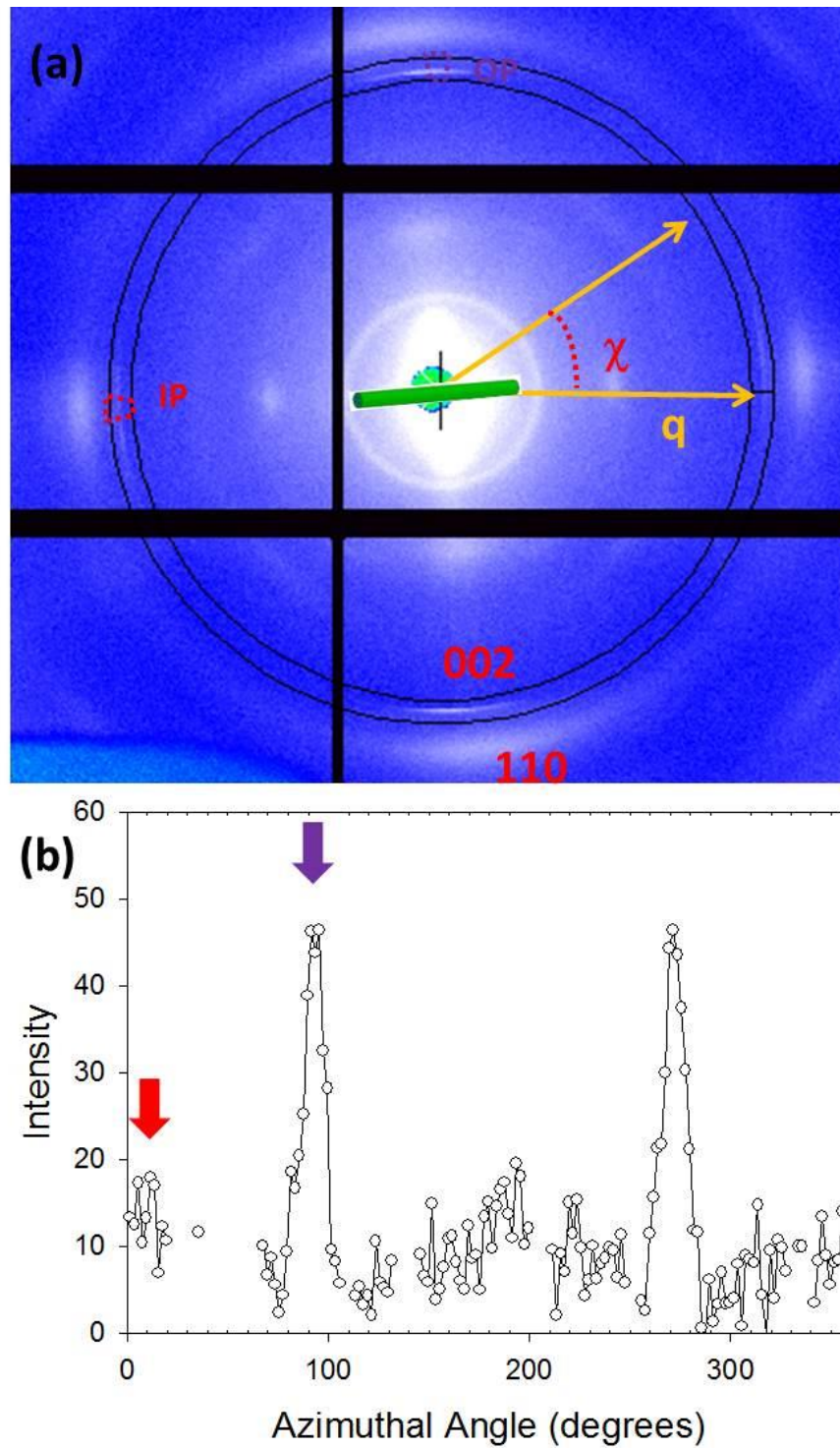
Figure 6.4. *WAXD patterns. a): Example WAXD pattern collected from central carina region. b): azimuthally integrated 1D profile for 002 reflections, the red arrow indicates the peak for in-plane fibre and the purple arrow indicates diffraction peak from out-of-plane fibre.*

The (002) reflections of the WAXD patterns (**Figure 6.4a**) collected from the telson sample were integrated azimuthally (**Figure 6.4b**) to find the peak positions for both in-plane and out-of-plane fibres. A peak fitting programme was developed using python programming to find the peak positions of IP and OP fibres of multiple WAXD frames at the same time. The full python script is displayed in **Appendix 3**. The fitted peak positions (for both IP and OP fibres) from the $I(\chi)$ curves of the (002) reflections were then used as a centre for a 7 degrees azimuthal sector of radial integrations to find the corresponding q (002) values. The fitting procedure for q (002) values of alpha chitin was the same as described in **chapter 5**. The q (002) values for all the scanning regions (**Figure 6.3**) were then transferred into D (002) values and plotted in **Figure 6.5 (**central carina) and **Figure 6.6** (valley). Different colours were used to represent the D (002) values variation across the sample with the scale bars shown in the side of each images. The D (002) values for both IP and OP fibres before and under bending were shown in **Figure 6.5 and Figure 6.6** and the differences between them will be discussed in detail below. You may notice some points in the exocuticle regions of the central carina (**Figure 6.5**) were missing, which was due to the large step size used in the 2D WAXD scans as well as the large curvature in the carina region.
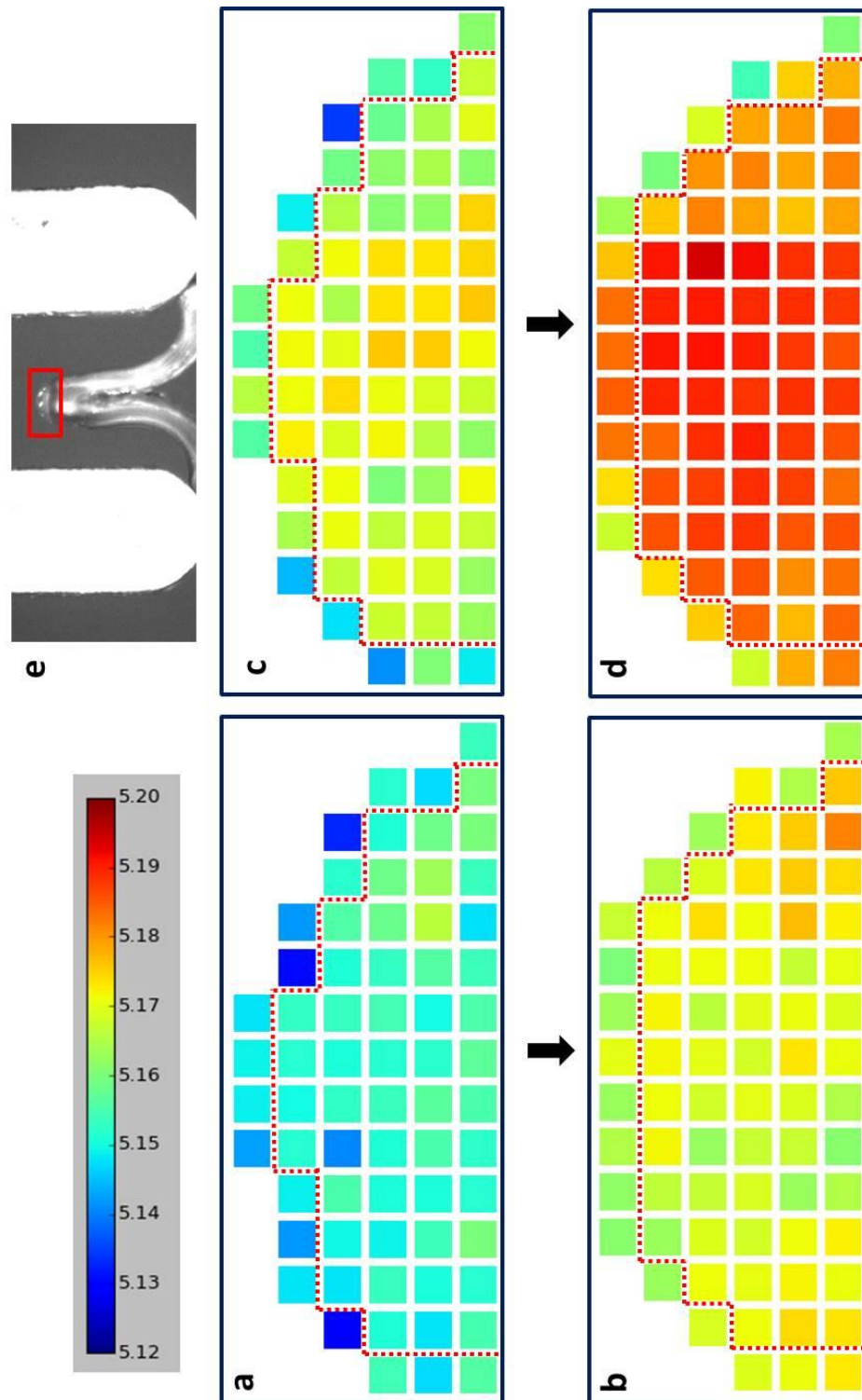
Figure 6.5. *D (002) value maps. (a-b): The D (002) value map of in-plane fibres across the central carina region before (a) and under bending (b). (c-d): The D (002) value map of out-of-plane fibres across the central carina region before (c) and under bending (d). WAXD scanning regions were indicated in the **Figure 6.3***

Figure 6.6*. D (002) value maps. (a-b): the D (002) value map of in-plane fibres across the valley region before (a) and under bending (b). (c-d): The D (002) value map of out-of-plane fibres across the valley region before (c) and under bending (d). WAXD scanning regions were indicated inside the **Figure 6.3** with symbol B (before loading) and B' (under loading). The unit for the scale bar is angstrom.*

In order to compare the mechanical functions of the central carina and valley region in the stomatopod telson, WAXD scans were also performed on valley region which indicated as rectangle in the **Figure 6.3 (B)** (before bending) and **Figure 6.3 (B')** (under bending). **Figure 6.5** and **Figure 6.6** displays the D(002) values distributions of IP and OP fibres across the centre region of central carina as well as valley region before and under bending. The different colours for each

scanning points represent different D (002) values ranging from 5.12 (A) to 5.20 (A). A first glance of **Figure 6.5** and **Figure 6.6** we found the D(002) values distributions were different in four different aspects: Firstly the D(002) values from central carina area showed clear difference from those in valley area; Secondly the D(002) values of exocuticle were generally smaller than the endocuticle for both central carina and valley region; Thirdly there were D(002) values differences for IP and OP fibres depend on the cuticle regions; Lastly the D(002) values for all IP and OP fibres were increased in different extents depending on the different cuticle regions when under bending. Below we will compare the above differences in more detail.

The D(002) values of IP and OP in the **Figure 6.5** and **Figure 6.6** were plotted as histograms in **Figure 6.7** and **Figure 6.8** correspondingly in order to view the difference quantitatively. The separations of exocuticle and endocuticle regions have been indicated using red dash lines in **Figure 6.5** and **Figure 6.6**.

The D (002) values for IP chitin fibres were analysed first which accounts for higher volume proportion compare to OP fibres as we learned from **Chapter 4**. As shown in **Figure 6.7 a**, The D (002) values of IP fibres in central carina region already exhibit a wide distribution even without any external loadings. There was a clear separation in D (002) value between exocuticle region (between 5.12 (A) to 5.135(A)) and endocuticle region (between 5.136 (A) to 5.170(A)). The smaller D (002) values for exocuticle indicated there were pre-strains exist within the in-plane chitin fibres even without any external forces. Similarly, the pre-strains was also been found in the exocuticle of the valley area as shown in **Figure 6.8 a**. The D(002) values of exocuticle in the valley area were found to be between

5.140(A) and 5.155(A), which were smaller than the D(002) values in endocuticle which ranging from 5.165(A) to 5.185(A). Another fact need to be noticed was that the valley region show higher D (002) values than the central carina region in total without bending.
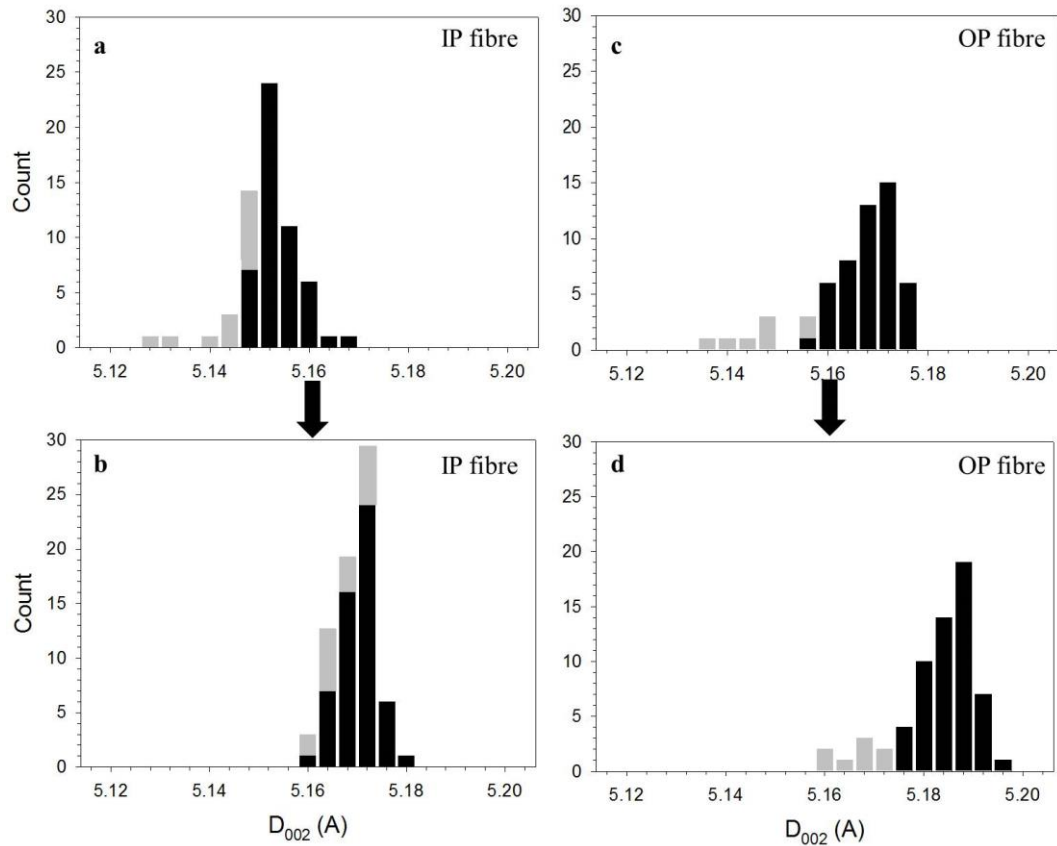
Figure 6.7. *Histogram of D (002) value for central carina. (a-b): the histogram plot of D (002) value for in-plane fibres across the central carina region before (a) and under bending (b). (c-d): the histogram plot of D (002) value for out-of-plane fibres across the central carina region before (c) and under bending (d). The grey bar indicates value from exocuticle while the black bar indicates value from endocuticle region. The map region were indicated in the figure 3 with A (before loading) and A' (under loading).*
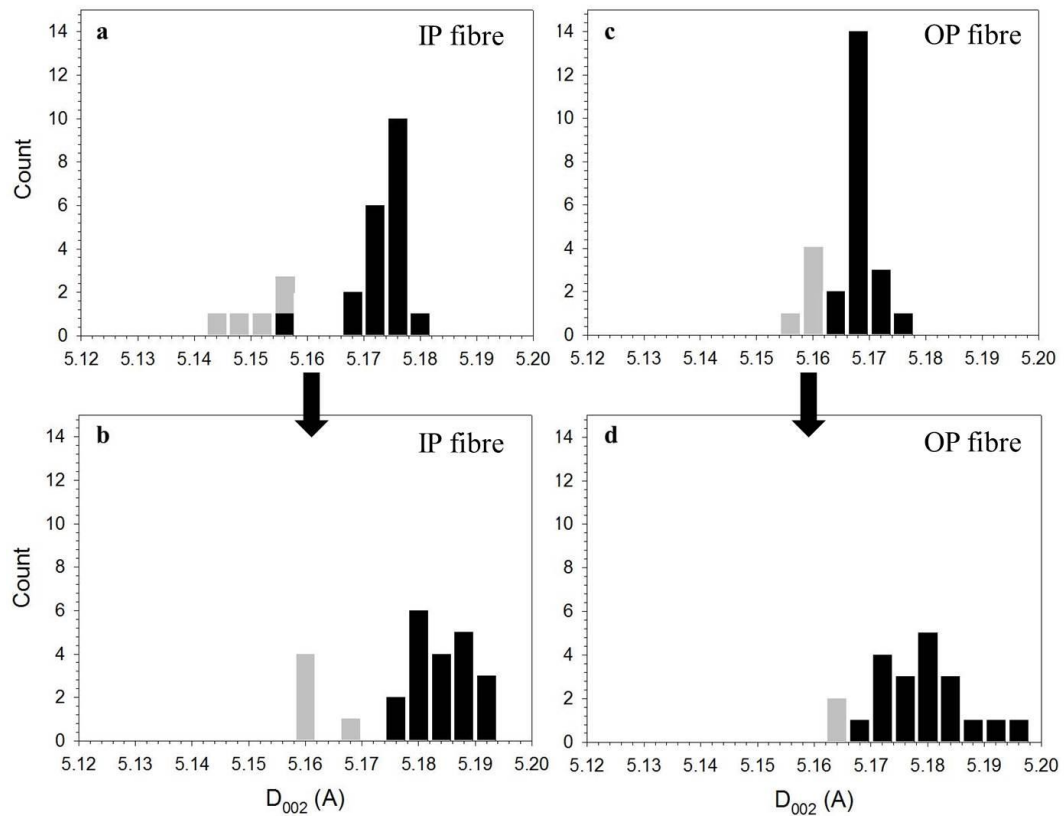
Figure 6.8. *Histogram of D (002) value of valley region. (a-b): The histogram plots of D (002) value for in-plane fibres across the valley region before (a) and under bending (b). (c-d): The histogram plots of D (002) value for out-of-plane fibres across the valley region before (c) and under bending (d). The mapping regions were indicated in the **Figure 6.3** with B (before loading) and B' (under loading).*

Figure 6.7b and **Figure 6.8b** show the D (002) values distributions for IP fibres when under bending. As we seen, the D(002) values in all the centre region of central carina have increased for all regions, which indicate the chitin fibrils within those regions were stretched along the fibre axis under bending. The D (002) values from Line scans which collected from central carina region (**Figure 6.9a**) and valley region (**Figure 6.9b**) respectively were plotted as an example to view the extent of IP fibre deformation. As shown in **Figure 6.9a** and **Figure 6.9b**, when under bending, the D (002) values along both the

scan lines increased which can transfer into a positive strain in the **Figure 6.9c**. Also, the strain increment was found higher in central carina region than the valley region.

However, one line is not statistically representative to demonstrate the mechanical response differences between the central carina region and valley region. In addition, due to the complex shape of telson sample, it was very difficult to do single point-to-point comparisons before and under bending. Therefore, we averaged the D(002) values of IP fibres for exocuticle and endocuticle from the 2D area scan shown in **Figure 6.5** and **Figure 6.6** and plotted the results in the **Figure 6.10**. Under bending the average D (002) value of exocuticle in the central carina increased from 5.146 ± 0.008 A to 5.166 ± 0.004 A with an increased strain of 0.38% and D (002) value of the endocuticle in the central carina increased from 5.153 ± 0.004A to 5.170 ± 0.004 A with an increased strain of 0.33%. While the D(002) value of exocuticle in the valley region increased from 5.161 ± 0.004 A to 5.171 ± 0.005 A with a strain of 0.21% whereas the D(002) value of endocuticle in the valley region increased from 5.168 ± 0.003A to 5.181 ± 0.009A with a strain of 0.24%. The results demonstrated that the strain increments were considerably depending on the morphological changes in the telson but showing no clear difference between exocuticle and endocuticle in the same region.
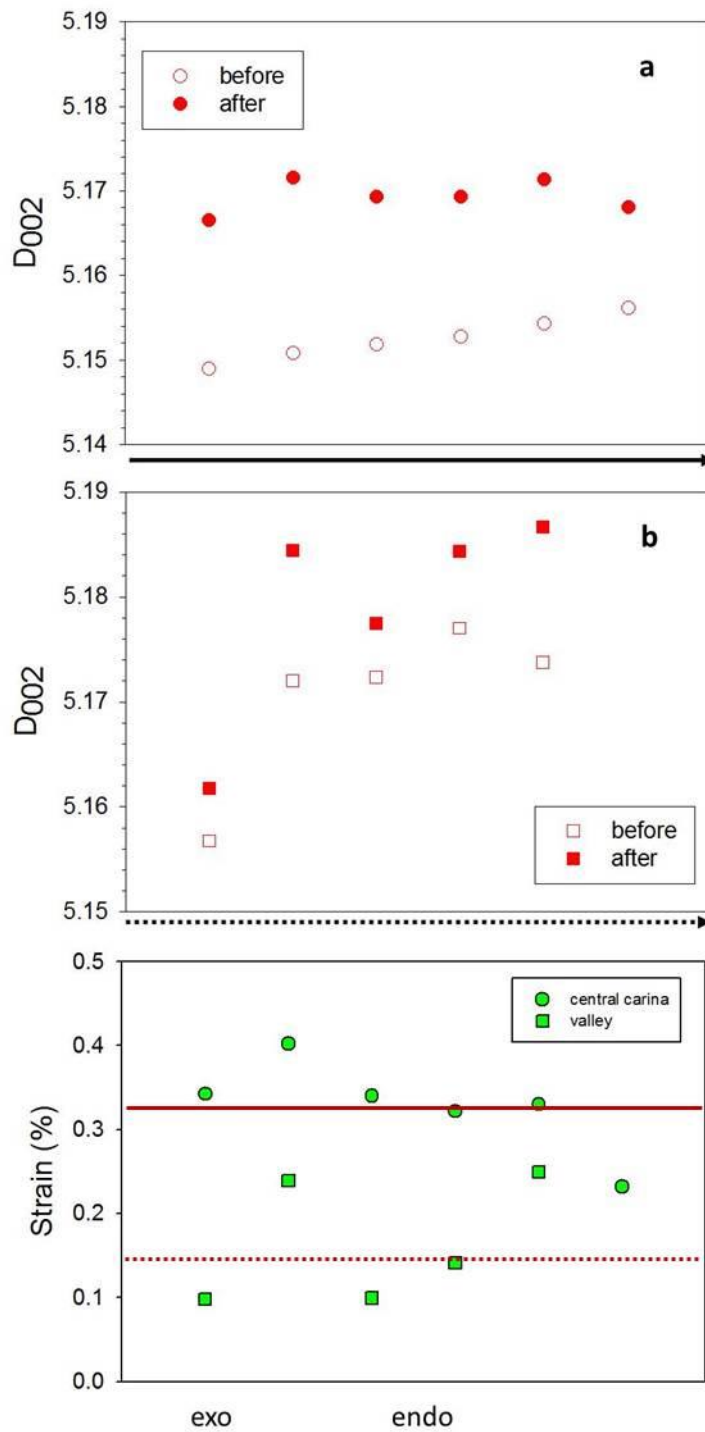
Figure 6.9. *D (002) value changes of in-plane fibre from line scans. (a): D (002) values along the line scan in central carina region before (empty circle) and under bending (filled circle). The scan line was indicated in **Figure 6.3** by solid black arrow (b): D (002) values along the line scan in valley region before (empty circle) and under bending (filled circle). The scan line was indicated by dash black arrow in **Figure 6.3**. (c): The corresponding strains of above line scans*
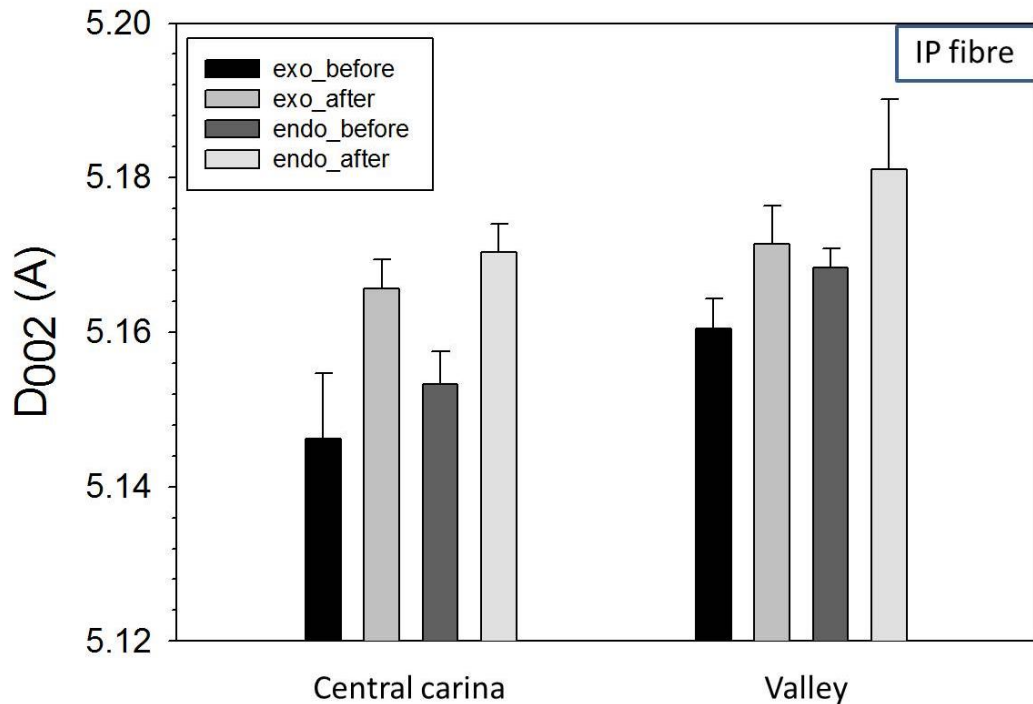
Figure 6.10. *The D (002) values of IP fibres changes in central carina and valley region.*

The D (002) value distributions for out-of-plane chitin fibres in the same region before bending were plotted in **Figure 6.5c** and **Figure 6.6c** as well as the corresponding histograms plots in **Figure 6.7c** and **Figure 6.8c**. From the 2D mapping (**Figure 6.5** and **Figure 6.6**) The D (002) values for out-of-plane fibres were found generally larger than in-plane fibres from the same scanning points. And similarly, the D (002) values for out-of-plane fibres in the exocuticle were smaller than those in the endocuticle for both central carina and valley region, which indicated the pre-strains were not only existing for in-plane fibres but also for out-of-plane fibres. When under bending, the average D (002) value for the exocuticle of the central carina

increased from $5.156 \pm 0.01A$ to $5.174 \pm 0.008A$ with a strain increase of 0.36% while in the endocuticle of the central carina increased from $5.168 \pm 0.005A$ to $5.186 \pm 0.005A$ with a strain of 0.33%. On the other hand, in the exocuticle of the valley region the average D (002) value increased from $5.151 \pm 0.005A$ to $5.162 \pm 0.003A$ with a strain of 0.21% while in the endocuticle of the valley region the average D (002) value increased from $5.173 \pm 0.005A$ to $5.185 \pm 0.005A$ with a strain of 0.23%. Similar strain increments for OP fibre and IP fibre were found in the same area of telson.

The D(002) value distributions for IP and OP fibre in exocuticle and endocuticle from central carina and valley region before and after loading were similar in the other examined telson samples which demonstrated the results we found from the first telson sample were repeatable (data not shown).

We are also interested in whether the pre-strain in exocuticle region also existing in the tergite sample. Due to the large geometrical differences between tergite and telson samples, the mechanical test were not comparable thereby we only show the D (002) value distributions here. Line scans were performed across the exocuticle to endocuticle for three tergite samples acquired from different animals without loading and the D (002) values were plotted in **Figure 6.11**. As a result, the differences of D (002) values between exocuticle and endocuticle were also found within the tergite samples. The chitin fibres in the exocuticle of tergite samples show higher pre-strains as the differences of D (002) values between exocuticle and endocuticle were larger.
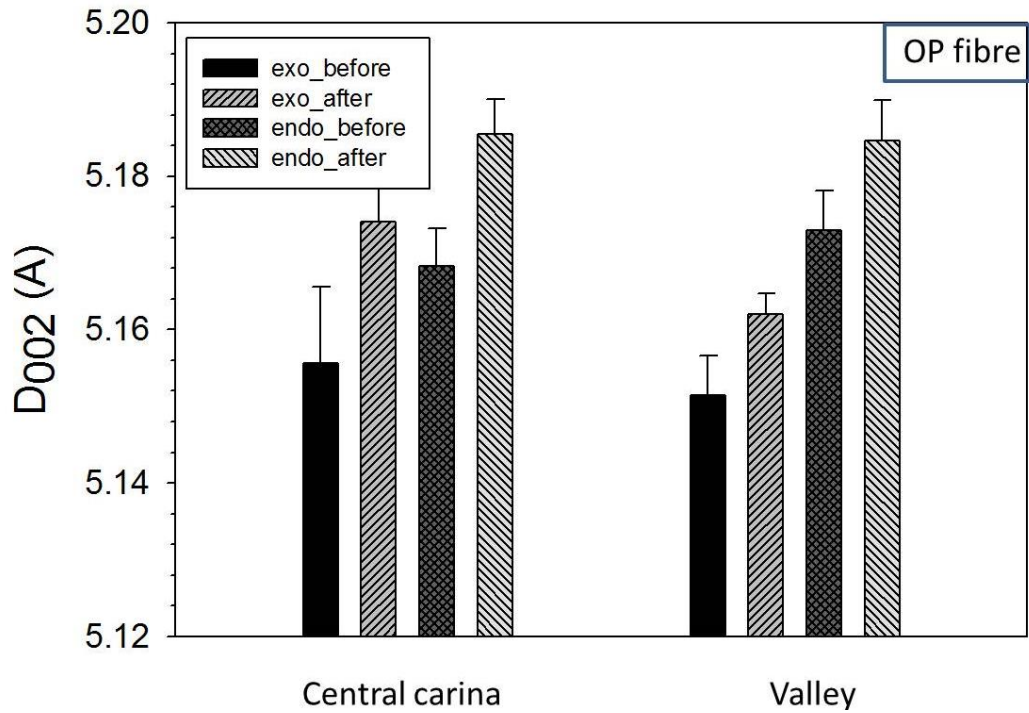
Figure 6.11. The D (002) values of OP fibres changes in central carina and valley region.
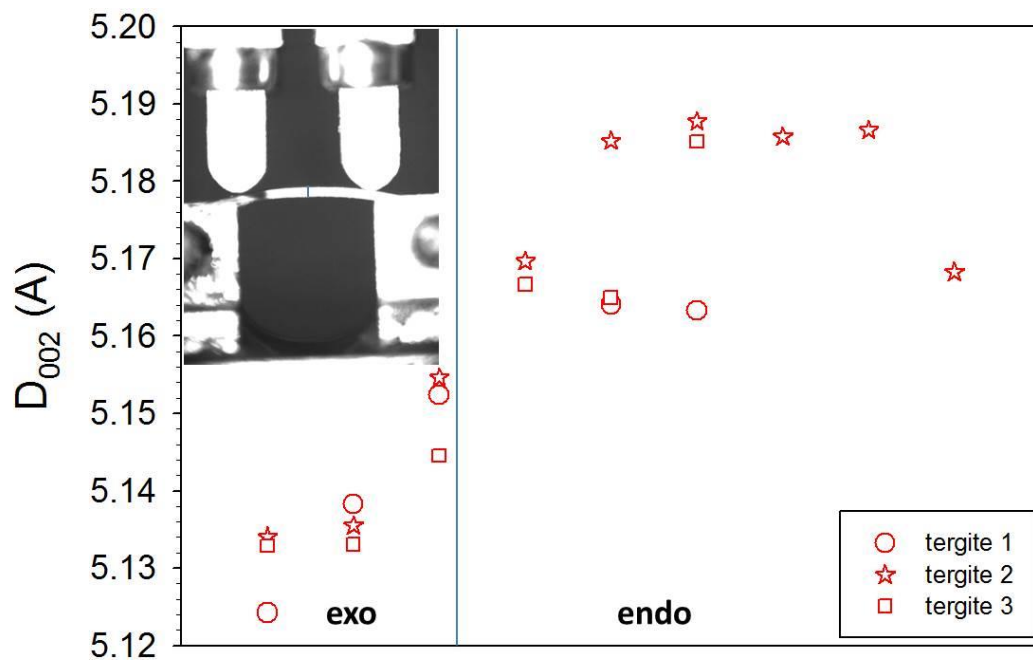
Figure 6.12. *D (002) values across tergite samples. The D (002) values of three tergite samples were calculated from exocuticle to endocuticle region. The line scan position was indicated at the inset picture of the tergite (blue line) without any loading added.*

6.3 Discussion

In this chapter, we have measured the spatially-resolved nanoscale mechanical deformation of our target system (the stomatopod telson) using *in situ* bending combined with time-resolved synchrotron WAXD. As discussed in **Chapter 1**(Section 2.2.3), it is known that the telson withstands high rate impact from the dactyl of competitor stomatopod during its lifetime, without structural damage. We were interested in the mechanical design of the stomatopod, especially its correlation to structure at multiple hierarchical levels. In **Chapter 5**, we focussed on the nanoscale mechanical response of the chitin fibre/mineralized matrix laminate. Here, we went to the next level of complexity, combining nanoscale mechanics with spatial mapping across both the micro-structural elements (~100 μm scale; exo- and endocuticle) as well as the meso-structural elements (~mm scale; central carina and adjacent valley region). In order to understand how the morphological differences between tergite to telson cuticle (at the meso-structural level) are crucial for the optimization for impact-resistant function of stomatopod cuticle, we carried out control measurements on the tergite segment adjacent to the telson, which shows no special shape corrugations. In the ideal situation, three-point bending will be more close to mimic the impact from the natural environment. However, for the synchrotron test, especially the WAXD test, the loading pin of three point bending tester will block part of the WAXD diffraction signal during test and complicate analysis of the peak shifts. Particularly, the central carina is the most interesting region since it is usually where the telson used to withstand the external impact, but its WAXD signal will be shadowed in the upper sector if a single pin load is applied at the carinal apex. As

showed in **Figure 6.1**, four-point bending tester were used in the *in situ* mechanical test in Diamond Light Source (DLS) so the diffraction X-ray beam from the central carina and valley area is not shadowed by the components of our sample environment, and the full signal can reach the detectors. The loading scenario simulated here is where the entire telson is under predatory impact by a larger animal, and thus has physiological relevance.

As we mentioned in **Chapter** 5, the variation of the D values for (002) reflections represent the stretch and compression of chitin fibres along the fibre axis. Therefore, by tracking the D values for (002) reflections in different regions of stomatopod cuticle, we can obtain the information of mechanical response along the fibre axis, from different regions of the whole cuticle under loading. In this initial work, we did not carry out a full three-dimensional fit, but made the approximation that as the 2θ angle for (002) is small (near $5°$), we take the peak shifts of the (002) peak along the principal direction as representative of the fibre-strain in the plane of the section of the sample.

Our main findings can be summarized as follows:

- Existence of compressive pre-strain in the chitin IP-fibres of exocuticle of tergite, compared to endocuticle (**Figure 6.12**), without any load applied.
- Disappearance of this pre-strain difference in the enlarged central carinal impact section of the telson, while the pre-strain difference is maintained in the adjacent valley region (**Figure 6.9. a** and **b**), without any load applied.

- The OP-fibres are elongated more, relative to the IP-fibres, in the central carina, in the undeformed state
- Upon deformation, both IP- and OP-fibres show positive (tensile) strain of ~0.3-0.5%, consistent with the overall macroscopic bending mode
- The range of strain-levels reached is different between the carina- and the valley.

These results are discussed in more detail in the following.

By fitting the D (002) values of IP chitin fibres in tergite and telson before any loading were added on the samples, we found that the D (002) values of IP chitin fibrils is generally smaller in exocuticle than endocuticle for both cuticle types. The D (002) values difference of the same material between different regions of cuticle has never been reported before. The smaller D (002) values in the exocuticle indicated that there were pre strains within those regions. Interestingly, the extent of pre strain in the exocuticle comparing to the corresponding endocuticle was found varied from tergite and telson in native state and also varied in different regions of stomatopod telson. Without loading, the differences between exocuticle and endocuticle are higher in the tergite cuticle than telson with larger D (002) values distribution. Within the telson cuticle, the differences between exocuticle and endocuticle are higher in the side region than the central carina, especially the centre region of the central carina. The reduced pre-strain in the central carina of telson then the other regions without any external mechanical loading demonstrated there are growth induced strain variation which matches the morphological differences of the stomatopod cuticle. We need to mention that the D (002) values of OP chitin fibres were also measured across the tergite

and telson cuticle, and the pre-strains were also found for OP fibres in the exocuticle. The higher compression in the exocuticle fibres without load may be related to the higher mineralized protein matrix in the exocuticle region which compresses densely packed chitin fibres, while in the less mineralized endocuticle the more loosely packed chitin fibres are less compressed. The changes of lattice parameter for biological materials according to its natural environment variation have been found in other biological tissues [186]. The axial molecular staggering D period of collagen can reduce from 67 nm in wet state to about 64 nm when it is in dry state [187], Further the lateral D period will reduce from 1.5 nm to 1.1 nm when the collagen turns from wet to dry [12, 188].

Till now we found there are spatial dependences for in the strain-levels of chitin fibres within the stomatopod cuticle in the static situation (prior to loading). We also mapped the D (002) values distribution for both IP and OP chitin fibres for telson under 4-point bending. Because of the significant morphological differences between tergite and telson samples, the macro-mechanical responses against four-point bending loads were not comparable, and hence we only consider telson here. We compare the D (002) values distribution of fibres between central carina and valley region of the same telson sample to find out how the different regions of telson functioned in withstand external loads. When under loading, the IP and OP fibres both the central carina and valley region between the loading pins were stretched according to the increased D (002) values than static states. From the D (002) values results, we also found that the OP chitin fibres are also bears significant loading. This finding is in contrast to the belief expressed in other works that the OP-fibres are

loosely bound to the pore canals and the in-plane fibre-sheets and do not contribute mechanically to the structure. The increased D (002) values of OP chitin fibres in all regions indicate that the OP chitin fibres play an important role to bear loads and dissipate energy. We note this supports the findings in **Chapter 4**, where we predicted that the OP/IP ratio distributions will affects the overall mechanical properties of stomatopod telson.

Due to the spatial heterogeneity of the sample, obtaining strains is only possible by averaging the D (002) values from different regions (like central carina and valley) and comparing before- and after-values. Using this approach, the IP-fibres and OP-fibres in central carina experience a strain of 0.35% and 0.33% respectively. In contrast in the side region, the increase is less, 0.21% and 0.23% for the IP and OP fibres respectively. This difference in response between the carina and valley may be related to the different pre-strains, as well as the overall shape-variations. The greater compressive pre-strain in the central carina may enable the fibres in this region to straighten more when under external (tensile) loading, and also absorb more energy than the valley region. However, macro scale mechanical results from Patek et al. suggested that the stiffer carina region deforms less than the more compliance valley region due to higher mineralisation in the carina[23]. The finding of opposite deformation mechanisms between macroscale to nanoscale in the same cuticle region is interesting, which confirmed that both chemical and mechanical approaches have been employed to optimize the impact resistance of telson cuticle. On the one side, higher mineralisation will increase the stiffness of the central carina region. On the other side, since high stiffness may lead to brittle fractions, pre-constrain are incorporated in the carina to

toughen the tissue without sacrifice of stiffness. Further, these differences occur within an anatomical site as well, across the exo- and endo-cuticle. By introduction of pre-strains in the location where the external impact first lands on the animal, it is possible to speculate that the mantis shrimp reduced the damage from external impact on the early stage of impact before the damage propagate into inner parts of telson. Also, the pre-stress on the chitin fibre will cause the surrounding matrix under compression residual forces, which impede the opening of cracks and thereby hinder the crack propagation at same time can balance the shear forces at the interface. In addition, the pre-strain for the collagen fibres within extracellular matrix is believed not only leading to better mechanical properties but also influence the mineralization processes in the biological tissues[189]. The stomatopod cuticle offers us a chance to understand the mechanism behind this kind of mechanical and chemical transduction process by further studying the strain arrangement for both the chitin fibres and the mineral phases in the different growth stage of the animal.

Pre-strain and pre-stress can also be found in other synthetic as well as synthetic composites. Usually it is the fibre phase under pre-stress with either compressive or tension strain[190]. In civil engineering pre-stressing is a well-developed method to overcome concrete's the natural weakness in tension. Also, pre-stress were also intentionally introduced into synthetic polymer-matrix composites to improve their mechanical performance. Previous works have demonstrated that the viscoelastically prestressed polymeric composites (VPPMCs) exhibit remarkable and lasting improvement in mechanical properties (cite) by introducing pre-stress on their fibre phase like nylon 6, 6 and

UHMWPE. Compared to the unstressed control counterparts, the tensile strength, modulus and toughness of VPPMCs can raise by over 15%, 30% and 40% respectively [191]. Moreover, the flexural stiffness can be increased by 50% at the same time [192]. Motahhari et al. managed to increase the young's modulus and strength of glass-epoxy composites by 33% by Introducing pre-stressing on the glass fibres during the curing process[193]. The recovery pre-stressed fibre either in tension or compression will induce compression on the matrix, which consequently impede the crack propagation. Also, the matrix compression will attenuate the dynamic overstress, which results in reduced fibre fracture outside the direct impact contact area. The pre-stress will also cancel out the shear stress between the interfaces as well as the external loads[190]. All those mechanisms leads to an higher toughness for prestressed composites compared to the control composites (unstressed), which also been experimentally verified by bending test on the UHMWPE fibres with a maximum 40% higher energy absorption than the control counterparts[194].

These data are some of the first, to the best of our knowledge, to experimentally map the spatial variation of nano-scale and molecular strains in biological composites. These initial findings provide intriguing glimpses into possible optimization mechanisms for impact, through alteration of pre-strains at the molecular level and spatial gradients in these strains. In the next steps in this project to elucidate the multi-scale mechanics of telson cuticle, it is planned to combine these experimental findings with finite element modelling, and to bring the loading protocols into the dynamic range, of high impact and cyclic loading, in order to replicate the physiological conditions during impact of telson.

Chapter 7: Conclusions and Future Work

7.1 Conclusions:

In chapter 4, we did 2D WAXD mapping across the central carina of stomatopod telson cuticle as well as the central region of tergite cuticle to investigate the structural differences between the two cuticle types. A novel 3D fibre orientation reconstruction method was presented to predict the orientation distribution within the cuticles. From the mathematical model we can obtain quantitative information about the main orientation of fibres inside the lamella plane (γ_0), the distribution width ($\Delta\gamma_0$), the 3D tilt angle of the lamella plane (α,β) as well as the ratio between in-plane fibre and out-of-plane fibres. Compare the 3D fibre architecture from the armoured telson to the non-armoured tergite from the same specimen, we found that the amount ratio between out-of-plane fibres (OP) and in-plane fibres (IP) decrease from exocuticle to endocuticle and inner membrane layers for both tergite and telson cuticle. We also found the gradient of OP/IP ratio was not only in the hierarchical level of different cuticle layers, the higher amount ratio between OP and IP fibre in the highly curved central carina region comparing to the less curved side valley region as well as tergite cuticle indicates the gradient of OP/IP ratio was also correlated to the morphological changes of cuticle in the highest hierarchical level. Beside, we also proposed a model linking the macroscopic impact resistance of telson to the spatial variations of its fibrous architecture. The 3D fibre reconstruction method developed in the chapter 4 is scalable, general in principle and can be applied to analyse both natural biopolymer composites like the telson cuticle as well as to bioinspired functional mimics of such materials.

In the next stage, we performed *in-situ* synchrotron tensile tests to investigate the mechanical responses of chitin at the nanoscale, also considering the Bouligand structural motif present at the microscale. From the results of chapter 4, the regular shaped tergite cuticle was used in the tensile test to eliminate the mechanical properties affect from morphological variation. During the tensile test, we not only obtained the mechanical properties of cuticle in the tissue level like, more importantly, we acquired the deformation of chitin crystals which can be lined to the fibril strain. As a result, we found the chitin fibril strain to yield was about 45% of the whole tissue strain to yield, also, the chitin fibril is yield around the strain of 0.6% which is earlier than the whole cuticle tissue (0.9%). In addition, from D value changes from (110) reflections and (002) reflections we obtained the compression and elongation strain of the chitin upon loading. By comparing the deformation in the radial direction and along the fibre axis we also obtained the Poisson's ratio of chitin fibril of 0.66, which has never been reported before. Need to mention the mechanical properties we measured about chitin is nearly in its native physiological states, which is already an improvement compare to the previous synchrotron test where the chitin fibre were separated from the tissues by removing minerals and proteins. Finally, we calculated the strain increments differences between differently orientated chitin fibres by D value fitting to the multiple azimuthal angles from the (002) reflections. Under tension, the cuticle exhibits anisotropic strain increments for fibres in different orientation. The fibres which orientated close to the tensile direction were stretched while those orientated away from tensile direction were compressed during the tensile test. The fibre reorientation process was also be quantitatively characterised, all the chitin fibres rotated towards the tensile test when

under loading. As far as we know, the ability to acquire both nanoscale strain increments for fibres in multiple orientations and the fibre reorientation from the same mechanically loaded sample has never been reported before. By measuring mechanical responses for fibres in all orientation will help us to understand the toughening mechanism of cuticle from the lamella hierarchical level.

By now, we had already acquired the structural differences between stomatopod tergite and telson cuticle by mapping the orientation and quantity distribution of IP and OP chitin fibres, and also we had learned the mechanical properties of the general stomatopod cuticle unit in different length scale by performing in-situ mechanical test on the stomatopod tergite cuticle. The next step was to consider the morphological features characteristic of telson, thereby to understand the mechanical significance from the evolution to regular shaped tergite to more sophisticated telson cuticle. A four-point bending tester was developed which can be used in the *in-situ* synchrotron mechanical test. The wide region between the two loading pins enables us to do 2D WAXD mapping which covers the central carina and valley regions of the telson cuticle before and under bending. By studying the D value distributions of 002 reflections in both central carina and valley region of telson as well as the tergite cuticle before bending. We found the D (002) values for exocuticle are generally smaller than in the endocuticle region for all cuticle types, which indicates the pre strains are exist within the exocuticle. Also, the valley area is less pre strained as a whole compared to the central carina region. In total, the chitin fibre exhibit higher pre strains in those cuticle regions where the impact load landed firstly. The pre strains in the composites are generally be considered to be beneficial for the total toughness as described in the discussion section in chapter

6. Under bending, the chitin fibre deform with a higher strain in the centre carina region than the valley region which make sure more energy can be dissipated in the central carina region so the impact damage can be delaminated in the initial stage.

Taken together, our results provide quantitative indications that the stomatopod telson cuticle has been structurally and mechanically optimized to withstand high rates of impact in its physiological state. These findings will provide the first useful guidelines for designing synthetic composite materials inspired by telson, which will be used to resist repetitive impact loading. However, there are several lines of future research which need to be investigated further in order to take full advantage of the potential for bioinspiration in telson, and in the following, these are briefly discussed.

7.2 Future Work:

Firstly, the 3D fibre orientation reconstruction model we proposed in the chapter 4 was still simplified by considering a single orientation of fibre plane in 3D. However, there is always a distribution of planes centred at the main orientation of fibre planes in 3D. A more detailed model needs to be developed to identify the 3D plane orientation distribution by incorporating the other reflections like 002 and 013 which captured the plane distribution information. Also, the fitting procedure for 3D orientation of chitin fibre can be optimized by introducing asymptotic analysis in the mathematical calculations in order to accommodate the extra structural information like the fibre plane distributions.

Secondly, our study has been focused on the characterization of the structural and mechanical properties of chitin. The other components

in the stomatopod cuticle including minerals and proteins are also play important roles to fulfil the mechanical and biological functions of the animal. Especially the chemical and texture variations of the mineral distribution which affect the stiffness and toughness of cuticle in large extent are regulated by a sophisticated biomineralization process during the growth and moulting process of the animal. Within the cuticle, the structural of mineral phase and chitin are closely related, examination and understanding the texture relationship between the chitin fibres and mineral crystals will help us deducing the biomineralization mechanism. Besides, it is also interesting to investigate the structural and chemical changes throughout the molting cycle or different growth stages of the animal. This will help us to understand the biological control of the biomineralization and the formation of strain arrangements for the chitin fibre network within the cuticle.

Thirdly, other techniques such as confocal microscopy，Raman and Infrared spectroscopy can be used to investigate the structural changes during the mechanical test for all the components of cuticle. The chemical and structural variation under loading will be important supplement for our synchrotron *in-situ* mechanical studies. However, the customized mechanical testers need to be further modified to accommodate the different requirements from those techniques.

Fourthly, all the mechanical tests performed in the thesis are quasi-static tests. In order to fully understand the structural optimization mechanisms of stomatopod cuticle to withstand repetitive loading from environments, dynamic mechanical testing need to be adopt to study the mechanical responses of cuticle for dynamic loadings. This requires an upgrade of the current in-situ mechanical tester. Fast

motors need to be integrated to perform high frequency loadings and more sensitive load cells is needed to record the fast load transformations. In addition, the experimental procedures in the synchrotron test need to be redesigned to satisfy more complicated requirements. Finally, the results of 3D fibre orientations in the stomatopod tergite and telson cuticle in chapter 4, together with the mechanical properties of chitin in different length scales acquired in chapter 5 and 6 can be used as inputs for finite element modelling (FEM). The structural and mechanical information inputs in nearly all hierarchical levels will considerably increase the modelling accuracy and makes the comparison of cuticle performance between different parts and species possible.

Because of the considerable technical development (both on the hardware side as well as, more significantly, on the data analysis aspect), these areas were not investigated during the course of the current PhD project. However, these avenues will be explored in future by my research group, to investigate the dynamic properties of Mantis shrimp across all the length scales.

References

1. Weaver, J.C., et al., *The Stomatopod Dactyl Club: A Formidable Damage-Tolerant Biological Hammer.* Science, 2012. **336**(6086): p. 1275-1280.
2. Helga, L., *PhD thesis*, 2002, University of Vienna.
3. Paris, O. and M. Muller, *Scanning X-ray microdiffraction of complex materials: Diffraction geometry considerations.* Nuclear Instruments & Methods in Physics Research Section B-Beam Interactions with Materials and Atoms, 2003. **200**: p. 390-396.
4. Taylor, J.R.A. and S.N. Patek, *Biological punching bags: impact analysis of a mantis shrimp telson.* Integrative and Comparative Biology, 2010. **50**: p. E173-E173.
5. Caldwell, R.L. and H. Dingle, *Ecology and Evolution of Agonistic Behavior in Stomatopods.* Naturwissenschaften, 1975. **62**(5): p. 214-222.
6. Chen, P.Y., J. McKittrick, and M.A. Meyers, *Biological materials: Functional adaptations and bioinspired designs.* Progress in Materials Science, 2012. **57**(8): p. 1492-1704.
7. Kosynkin, D.V., et al., *Longitudinal unzipping of carbon nanotubes to form graphene nanoribbons.* Nature, 2009. **458**(7240): p. 872-U5.
8. Baughman, R.H., A.A. Zakhidov, and W.A. de Heer, *Carbon nanotubes - the route toward applications.* Science, 2002. **297**(5582): p. 787-792.
9. Lee, C., et al., *Measurement of the elastic properties and intrinsic strength of monolayer graphene.* Science, 2008. **321**(5887): p. 385-388.
10. Zimmermann, E.A., et al., *Mechanical adaptability of the Bouligand-type structure in natural dermal armour.* Nat Commun, 2013. **4**.
11. Meyers, M.A., et al., *Mechanical strength of abalone nacre: Role of the soft organic layer.* Journal of the Mechanical Behavior of Biomedical Materials, 2008. **1**(1): p. 76-85.
12. Fratzl, P. and R. Weinkamer, *Nature's hierarchical materials.* Progress in Materials Science, 2007. **52**(8): p. 1263-1334.
13. Meyers, M.A., et al., *Structural biological composites: An overview.* Jom, 2006. **58**(7): p. 35-41.
14. Gupta, H.S., et al., *Cooperative deformation of mineral and collagen in bone at the nanoscale.* Proceedings of the National Academy of Sciences of the United States of America, 2006. **103**(47): p. 17741-17746.
15. Barthelat, F., *Nacre from mollusk shells: a model for high-performance structural materials.* Bioinspiration & Biomimetics, 2010. **5**(3).
16. Lin, A.Y.M., P.Y. Chen, and M.A. Meyers, *The growth of nacre in the abalone shell.* Acta Biomaterialia, 2008. **4**(1): p. 131-138.
17. Zhou, X.L., H.C. Miao, and F.X. Li, *Nanoscale structural and functional mapping of nacre by scanning probe microscopy techniques.* Nanoscale, 2013. **5**(23): p. 11885-11893.
18. Fratzl, P., et al., *Structure and mechanical quality of the collagen-mineral nano-composite in bone.* Journal of Materials Chemistry, 2004. **14**(14): p. 2115-2123.
19. Gupta, H.S., et al., *Nanoscale deformation mechanisms in bone.* Nano Letters, 2005. **5**(10): p. 2108-2111.
20. Gupta, H.S., et al., *Fibrillar level fracture in bone beyond the yield point.* International Journal of Fracture, 2006. **139**(3-4): p. 425-436.
21. Zack, T.I., T. Claverie, and S.N. Patek, *Elastic energy storage in the mantis shrimp's fast predatory strike.* Journal of Experimental Biology, 2009. **212**(24): p. 4002-4009.

22.   Patek, S.N. and R.L. Caldwell, *Extreme impact and cavitation forces of a biological hammer: strike forces of the peacock mantis shrimp Odontodactylus scyllarus.* Journal of Experimental Biology, 2005. **208**(Pt 19): p. 3655-64.

23.   Taylor, J.R.A. and S.N. Patek, *Ritualized fighting and biological armor: the impact mechanics of the mantis shrimp's telson.* Journal of Experimental Biology, 2010. **213**(20): p. 3496-3504.

24.   Amini, S., et al., *Textured fluorapatite bonded to calcium sulphate strengthen stomatopod raptorial appendages.* Nature Communications, 2014. **5**.

25.   Amini, S., et al., *The role of quasi-plasticity in the extreme contact damage tolerance of the stomatopod dactyl club.* Nature Materials, 2015. **14**(9): p. 943-+.

26.   Grunenfelder, L.K., et al., *Bio-inspired impact-resistant composites.* Acta Biomaterialia, 2014. **10**(9): p. 3997-4008.

27.   Patek, S.N., et al., *Linkage mechanics and power amplification of the mantis shrimp's strike.* Journal of Experimental Biology, 2007. **210**(Pt 20): p. 3677-88.

28.   Fratzl, P., S. Schreiber, and K. Klaushofer, *Bone mineralization as studied by small-angle x-ray scattering.* Connective Tissue Research, 1996. **35**(1-4): p. 9-16.

29.   Wagermaier, W., et al., *Scanning texture analysis of lamellar bone using microbeam synchrotron X-ray radiation.* Journal of Applied Crystallography, 2007. **40**: p. 115-120.

30.   Deymier-Black, A.C., et al., *Synchrotron X-ray diffraction study of load partitioning during elastic deformation of bovine dentin.* Acta Biomaterialia, 2010. **6**(6): p. 2172-2180.

31.   Svendsen, K.H., et al., *A Synchrotron Radiation X-Ray-Diffraction Study of the Crystallinity of Tendon Fibers.* International Journal of Biological Macromolecules, 1984. **6**(6): p. 298-302.

32.   Lichtenegger, H.C., et al., *Microfibril angles inside and outside crossfields of Norway spruce tracheids.* Holzforschung, 2003. **57**(1): p. 13-20.

33.   Almer, J.D. and S.R. Stock, *Micromechanical response of mineral and collagen phases in bone.* Journal of Structural Biology, 2007. **157**(2): p. 365-370.

34.   Gupta, H.S., et al., *Synchrotron diffraction study of deformation mechanisms in mineralized tendon.* Physical Review Letters, 2004. **93**(15).

35.   Puxkandl, R., et al., *Viscoelastic properties of collagen: synchrotron radiation investigations and structural model.* Philosophical Transactions of the Royal Society of London Series B-Biological Sciences, 2002. **357**(1418): p. 191-197.

36.   Paris, O., *From diffraction to imaging: New avenues in studying hierarchical biological tissues with x-ray microbeams (Review).* Biointerphases, 2008. **3**(2): p. Fb16-Fb26.

37.   Odegaard, F., *How many species of arthropods? Erwin's estimate revised.* Biological Journal of the Linnean Society, 2000. **71**(4): p. 583-597.

38.   Hegna, T.A., et al., *The correct authorship of the taxon name 'Arthropoda'.* Arthropod Systematics & Phylogeny, 2013. **71**(2): p. 71-74.

39.   Garcia-Bellido, D.C. and D.H. Collins, *Moulting arthropod caught in the act.* Nature, 2004. **429**(6987): p. 40-40.

40.   Hadley, N.F., *The Arthropod Cuticle.* Scientific American, 1986. **255**(1): p. 104-&.

41.   Cutler, B., *Arthropod Cuticle Features and Arthropod Monophyly.* Experientia, 1980. **36**(8): p. 953-953.

42.   Greenaway, P., *Calcium Balance and Molting in the Crustacea.* Biological Reviews of the Cambridge Philosophical Society, 1985. **60**(3): p. 425-454.

43.   Mann, S., *Biomineralization* 2001, Oxford,UK: Oxford University Press.

44. Al-Sawalmih, A., et al., *Microtexture and Chitin/Calcite Orientation Relationship in the Mineralized Exoskeleton of the American Lobster.* Advanced Functional Materials, 2008. **18**(20): p. 3307-3314.

45. Van de Velde, K. and P. Kiekens, *Structure analysis and degree of substitution of chitin, chitosan and dibutyrylchitin by FT-IR spectroscopy and solid state C-13 NMR.* Carbohydrate Polymers, 2004. **58**(4): p. 409-416.

46. Ashby, U.G.K.W.M.F., *The mechanical efficiency of natural materials*, in *Philosophical Magazine*2007.

47. Vincent, J.F.V. and U.G.K. Wegst, *Design and mechanical properties of insect cuticle.* Arthropod Structure & Development, 2004. **33**(3): p. 187-199.

48. François Barthelat, P.Z., Chad S. Korach, Barton C. Prorok, K. Jane Grande-Allen, *Mechanics of Biological Systems and Materials*. Vol. 4. 2013: Springer Science & Business Media. 189.

49. Giraud-Guille, M.M., *Plywood structures in nature.* Current Opinion in Solid State & Materials Science, 1998. **3**(3): p. 221-227.

50. Tanner, K.E., *Small But Extremely Tough.* Science, 2012. **336**(6086): p. 1237-1238.

51. Hepburn, H.R. and H.D. Chandler, *Material Properties of Arthropod Cuticles - Arthrodial Membranes.* Journal of Comparative Physiology, 1976. **109**(2): p. 177-198.

52. Nikolov, S., et al., *Revealing the Design Principles of High-Performance Biological Composites Using Ab initio and Multiscale Simulations: The Example of Lobster Cuticle.* Advanced Materials, 2010. **22**(4): p. 519-+.

53. Luquet, G., *Biomineralizations: insights and prospects from crustaceans.* Zookeys, 2012(176): p. 103-121.

54. *Materials Design Inspired by Nature: Function Through Inner Architecture*2013, London: Royal Society of Chemistry.

55. Roer, R. and R. Dillaman, *The Structure and Calcification of the Crustacean Cuticle.* American Zoologist, 1984. **24**(4): p. 893-909.

56. Longmuir, E., *Setal Development, Moult-Staging and Ecdysis in the Banana Prawn Penaeus-Merguiensis.* Marine Biology, 1983. **77**(2): p. 183-190.

57. Neville, A.C., *Biology of the Arthropod Cuticle*1975: Springer.

58. Hosokawa, J., et al., *Biodegradable Film Derived from Chitosan and Homogenized Cellulose.* Industrial & Engineering Chemistry Research, 1990. **29**(5): p. 800-805.

59. Minke, R. and J. Blackwell, *Structure of Alpha-Chitin.* Journal of Molecular Biology, 1978. **120**(2): p. 167-181.

60. Sikorski, P., R. Hori, and M. Wada, *Revisit of alpha-Chitin Crystal Structure Using High Resolution X-ray Diffraction Data.* Biomacromolecules, 2009. **10**(5): p. 1100-1105.

61. Younes, I. and M. Rinaudo, *Chitin and Chitosan Preparation from Marine Sources. Structure, Properties and Applications.* Marine Drugs, 2015. **13**(3): p. 1133-1174.

62. Gardner, K.H. and J. Blackwell, *Refinement of Structure of Beta-Chitin.* Biopolymers, 1975. **14**(8): p. 1581-1595.

63. Raabe, D., et al., *Preferred crystallographic texture of alpha-chitin as a microscopic and macroscopic design principle of the exoskeleton of the lobster Homarus americanus.* Acta Biomaterialia, 2007. **3**(6): p. 882-895.

64. Wharton, D.A., *Trichurid Eggshell - Evidence in Support of the Bouligand Hypothesis of Helicoidal Architecture.* Tissue & Cell, 1978. **10**(4): p. 647-658.

65. Bouligan.Y, *Twisted Fibrous Arrangements in Biological-Materials and Cholesteric Mesophases.* Tissue & Cell, 1972. **4**(2): p. 189-&.

66. Dennell, R., *Cuticle of Crabs Cancer-Pagurus L and Carcinus-Maenas (L).* Zoological Journal of the Linnean Society, 1974. **54**(3): p. 241-&.

67. Dalingwater, J.E., *Reality of Arthropod Cuticular Laminae.* Cell and Tissue Research, 1975. **163**(3): p. 411-413.

68. Weiner, S., W. Traub, and H.D. Wagner, *Lamellar bone: Structure-function relations.* Journal of Structural Biology, 1999. **126**(3): p. 241-255.

69. Raabe, D., C. Sachs, and P. Romano, *The crustacean exoskeleton as an example of a structurally and mechanically graded biological nanocomposite material.* Acta Materialia, 2005. **53**(15): p. 4281-4292.

70. Hild, S., et al., *Ultrastructure and mineral distribution in the tergal cuticle of the terrestrial isopod Titanethes albus. Adaptations to a karst cave biotope.* Journal of Structural Biology, 2009. **168**(3): p. 426-436.

71. Sachs, C., H. Fabritius, and D. Raabe, *Hardness and elastic properties of dehydrated cuticle from the lobster Homarus americanus obtained by nanoindentation.* Journal of Materials Research, 2006. **21**(8): p. 1987-1995.

72. Pelletier, A., et al., *Chitin Chitosan Transformation by Thermomechanochemical Treatment Including Characterization by Enzymatic Depolymerization.* Biotechnology and Bioengineering, 1990. **36**(3): p. 310-315.

73. Ifuku, S., *Chitin and Chitosan Nanofibers: Preparation and Chemical Modifications.* Molecules, 2014. **19**(11): p. 18367-18380.

74. Ianiro, A., et al., *Customizing Properties of beta-Chitin in Squid Pen (Gladius) by Chemical Treatments.* Marine Drugs, 2014. **12**(12): p. 5979-5992.

75. Focher, B., et al., *Structural Differences between Chitin Polymorphs and Their Precipitates from Solutions - Evidence from Cp-Mas C-13-Nmr, Ft-Ir and Ft-Raman Spectroscopy.* Carbohydrate Polymers, 1992. **17**(2): p. 97-102.

76. Yamaguchi, I., et al., *The chitosan prepared from crab tendon I: the characterization and the mechanical properties.* Biomaterials, 2003. **24**(12): p. 2031-2036.

77. Nishino, T., R. Matsui, and K. Nakamae, *Elastic modulus of the crystalline regions of chitin and chitosan.* Journal of Polymer Science Part B-Polymer Physics, 1999. **37**(11): p. 1191-1196.

78. Politi, Y., et al., *A Spider's Fang: How to Design an Injection Needle Using Chitin-Based Composite Material.* Advanced Functional Materials, 2012. **22**(12): p. 2519-2528.

79. Erko, M., et al., *Micro- and nano-structural details of a spider's filter for substrate vibrations: relevance for low-frequency signal transmission.* Journal of the Royal Society Interface, 2015. **12**(104).

80. Blackwell, J. and M.A. Weih, *Structure of chitin-protein complexes: ovipositor of the ichneumon fly Megarhyssa.* Journal of Molecular Biology, 1980. **137**(1): p. 49-60.

81. Ogawa, Y., et al., *Elastic modulus in the crystalline region and the thermal expansion coefficients of alpha-chitin determined using synchrotron radiated X-ray diffraction.* Carbohydrate Polymers, 2011. **83**(3): p. 1213-1217.

82. Wada, M., T. Okano, and J. Sugiyama, *Synchrotron-radiated X-ray and neutron diffraction study of native cellulose.* Cellulose, 1997. **4**(3): p. 221-232.

83. Dorozhkin, S.V. and M. Epple, *Biological and medical significance of calcium phosphates.* Angewandte Chemie-International Edition, 2002. **41**(17): p. 3130-3146.

84. Arakaki, A., et al., *Biomineralization-inspired synthesis of functional organic/inorganic hybrid materials: organic molecular control of self-*

organization of hybrids. Organic & Biomolecular Chemistry, 2015. **13**(4): p. 974-989.

85.   Weiner, S. and L. Addadi, *Design strategies in mineralized biological materials.* Journal of Materials Chemistry, 1997. **7**(5): p. 689-702.

86.   Neues, F., A. Ziegler, and M. Epple, *The composition of the mineralized cuticle in marine and terrestrial isopods: A comparative study.* Crystengcomm, 2007. **9**(12): p. 1245-1251.

87.   Iconomidou, V.A., et al., *"Soft"-cuticle protein secondary structure as revealed by FT-Raman, ATR FT-IR and CD spectroscopy.* Insect Biochemistry and Molecular Biology, 2001. **31**(9): p. 877-885.

88.   Weiner, S. and P.M. Dove, *An overview of biomineralization processes and the problem of the vital effect.* Biomineralization, 2003. **54**: p. 1-29.

89.   Weiner, H.A.L.S., *On Biomineralization*1989: Oxford University Press

90.   Lyandres, O., et al., *Preferred Orientation in Sputtered TiO2 Thin Films and Its Effect on the Photo-Oxidation of Acetaldehyde.* Chemistry of Materials, 2012. **24**(17): p. 3355-3362.

91.   Wagner, D.W., D.P. Lindsey, and G.S. Beaupre, *Deriving tissue density and elastic modulus from microCT bone scans.* Bone, 2011. **49**(5): p. 931-938.

92.   Bobelmann, F., et al., *The composition of the exoskeleton of two crustacea: The American lobster Homarus americanus and the edible crab Cancer pagurus.* Thermochimica Acta, 2007. **463**(1-2): p. 65-68.

93.   Diaz-Rojas, E.I., et al., *Determination of chitin and protein contents during the isolation of chitin from shrimp waste.* Macromolecular Bioscience, 2006. **6**(5): p. 340-347.

94.   Andersen, S.O., P. Hojrup, and P. Roepstorff, *Insect Cuticular Proteins.* Insect Biochemistry and Molecular Biology, 1995. **25**(2): p. 153-176.

95.   Kumari, S.S. and D.M. Skinner, *Proteins of Crustacean Exoskeleton .2. Immunological Evidence for Their Relatedness to Cuticular Proteins of 2 Insects.* Journal of Experimental Zoology, 1993. **265**(3): p. 195-210.

96.   Obrien, J.J., S.S. Kumari, and D.M. Skinner, *Proteins of Crustacean Exoskeletons .1. Similarities and Differences among Proteins of the 4 Exoskeletal Layers of 4 Brachyurans.* Biological Bulletin, 1991. **181**(3): p. 427-441.

97.   Nikolov, S., et al., *Robustness and optimal use of design principles of arthropod exoskeletons studied by ab initio-based multiscale simulations.* Journal of the Mechanical Behavior of Biomedical Materials, 2011. **4**(2): p. 129-145.

98.   Blackwell, J. and M.A. Weih, *Structure of Chitin-Protein Complexes - Ovipositor of the Ichneumon Fly Megarhyssa.* Journal of Molecular Biology, 1980. **137**(1): p. 49-60.

99.   Neville, A.C., *Biology of fibrous composites: Development beyond the cell membrane*1993, New York, NY: Cambridge University Press.

100.   Raikhel, N.V., H.I. Lee, and W.F. Broekaert, *Structure and Function of Chitin-Binding Proteins.* Annual Review of Plant Physiology and Plant Molecular Biology, 1993. **44**: p. 591-615.

101.   Rebers, J.E. and J.H. Willis, *A conserved domain in arthropod cuticular proteins binds chitin.* Insect Biochemistry and Molecular Biology, 2001. **31**(11): p. 1083-1093.

102.   Reynolds, S.E., *Mechanical-Properties of Abdominal Cuticle of Rhodnius Larvae.* Journal of Experimental Biology, 1975. **62**(1): p. 69-80.

103.   Nissan, A.H., *H-Bond Dissociation in Hydrogen-Bond Dominated Solids.* Macromolecules, 1976. **9**(5): p. 840-850.

104.   Fabritius, H.O., et al., *Influence of Structural Principles on the Mechanics of a Biological Fiber-Based Composite Material with Hierarchical Organization: The Exoskeleton of the Lobster Homarus americanus.* Advanced Materials, 2009. **21**(4): p. 391-400.

105.   Lee, J.Y., et al., *Customized biomimetic scaffolds created by indirect three-dimensional printing for tissue engineering.* Biofabrication, 2013. **5**(4).

106.   Jayakumar, R., et al., *Biomaterials based on chitin and chitosan in wound dressing applications.* Biotechnology Advances, 2011. **29**(3): p. 322-337.

107.   Morganti, P., et al., *New chitin complexes and their anti-aging activity from inside out.* Journal of Nutrition Health & Aging, 2012. **16**(3): p. 242-245.

108.   Rejinold, N.S., et al., *Multifunctional Chitin Nanogels for Simultaneous Drug Delivery, Bioimaging, and Biosensing.* Acs Applied Materials & Interfaces, 2011. **3**(9): p. 3654-3665.

109.   Mushi, N.E., et al., *Nanostructured membranes based on native chitin nanofibers prepared by mild process.* Carbohydrate Polymers, 2014. **112**: p. 255-263.

110.   Ifuku, S., et al., *Preparation of zwitterionically charged nanocrystals by surface TEMPO-mediated oxidation and partial deacetylation of alpha-chitin.* Carbohydrate Polymers, 2015. **122**: p. 1-4.

111.   Xu, H., et al., *Mechanical properties of plywood reinforced by bamboo or jute.* Forest Products Journal, 1998. **48**(1): p. 81-85.

112.   Chen, B., et al., *Hole-pin joining structure with fiber-round-hole distribution of lobster cuticle and biomimetic study.* Journal of the Mechanical Behavior of Biomedical Materials, 2014. **40**: p. 161-167.

113.   Kuballa, A.V., D.J. Merritt, and A. Elizur, *Gene expression profiling of cuticular proteins across the moult cycle of the crab Portunus pelagicus.* Bmc Biology, 2007. **5**.

114.   Sun, J.Y., et al., *Quantitative Nanomechanical Properties of the Cuticle of the Multicolored Asian Lady Beetle Using the Modulus Mapping Technique.* Current Nanoscience, 2015. **11**(2): p. 245-252.

115.   Ogawa, Y., et al., *Crystal analysis and high-resolution imaging of microfibrillar alpha-chitin from Phaeocystis.* Journal of Structural Biology, 2010. **171**(1): p. 111-116.

116.   Ker, R.F., *Investigation of Locust Cuticle Using Insecticide Diflubenzuron.* Journal of Insect Physiology, 1977. **23**(1): p. 39-&.

117.   Yamaguchi, I., et al., *The chitosan prepared from crab tendons: II. The chitosan/apatite composites and their application to nerve regeneration.* Biomaterials, 2003. **24**(19): p. 3285-3292.

118.   Parr, R.G.C.D.P.R., I. G, *Molecular Orbital Calculations of the Lower Excited Electronic Levels of Benzene, Configuration Interaction included.* Journal of Chemical Physics, 1950. **18**(12).

119.   Tavares, M., *Stomatopods.* The living marine resources of the western central Atlantic. FAO, Roma, 2002. **1**: p. 245-250.

120.   Currey, J.D., A. Nash, and W. Bonfield, *Calcified cuticle in the stomatopod smashing limb.* Journal of Materials Science, 1982. **17**(7): p. 1939-1944.

121.   Ooi, C., M. Hamdi, and S. Ramesh, *Properties of hydroxyapatite produced by annealing of bovine bone.* Ceramics international, 2007. **33**(7): p. 1171-1177.

122.   Taylor, J.R. and S.N. Patek, *Ritualized fighting and biological armor: the impact mechanics of the mantis shrimp's telson.* Journal of Experimental Biology, 2010. **213**(Pt 20): p. 3496-504.

123.   Felts, J., et al., *Conference 8031: Micro-and Nanotechnology Sensors, Systems, and Applications III.* Connecting minds for global solutions. **14**: p. 212.

124. Keene, D.R. and S.F. Tufa, *Transmission Electron Microscopy of Cartilage and Bone.* Electron Microscopy of Model Systems, 2010. **96**: p. 443-473.

125. *Scanning Probe Microscopy in Nanoscience and Nanotechnology* Vol. 3. 2013.

126. Boyde, A., et al., *Vital Confocal Microscopy in Bone.* Scanning, 1995. **17**(2): p. 72-85.

127. Smolla, M., et al., *Clearing pigmented insect cuticle to investigate small insects' organs in situ using confocal laser-scanning microscopy (CLSM).* Arthropod Structure & Development, 2014. **43**(2): p. 175-181.

128. Butzloff, P.R., *Micro-CT Imaging of Denatured Chitin by Silver to Explore Honey Bee and Insect Pathologies.* Plos One, 2011. **6**(11).

129. Lichtenegger, H., et al., *Imaging of the helical arrangement of cellulose fibrils in wood by synchrotron X-ray microdiffraction.* Journal of Applied Crystallography, 1999. **32**: p. 1127-1133.

130. Lichtenegger, H., et al., *Variation of cellulose microfibril angles in softwoods and hardwoods - A possible strategy of mechanical optimization.* Journal of Structural Biology, 1999. **128**(3): p. 257-269.

131. Fratzl, P., et al., *Mineral Crystals in Calcified Tissues - a Comparative-Study by Saxs.* Journal of Bone and Mineral Research, 1992. **7**(3): p. 329-334.

132. Guinier, A., *X-ray Diffraction in Crystals, Imperfect Crystals, and Amorphous Bodies*1994: Courier Corporation. 378.

133. Warren, B.E., *X-Ray Diffraction*1969, Massachusetts: Addison-Wesley Publishing Company.

134. Borisov, S.V. and N.V. Podberezskaya, *X-ray diffraction analysis: A brief history and achievements of the first century.* Journal of Structural Chemistry, 2012. **53**: p. S1-S3.

135. Dingley, D.J. and V. Randle, *Microtexture Determination by Electron Back-Scatter Diffraction.* Journal of Materials Science, 1992. **27**(17): p. 4545-4566.

136. Kalidindi, S.R., C.A. Bronkhorst, and L. Anand, *Crystallographic Texture Evolution in Bulk Deformation Processing of Fcc Metals.* Journal of the Mechanics and Physics of Solids, 1992. **40**(3): p. 537-569.

137. Vaudin, M.D., et al., *A method for crystallographic texture investigations using standard x-ray equipment.* Journal of Materials Research, 1998. **13**(10): p. 2910-2919.

138. Marrison, J., et al., *Ptychography - a label free, high-contrast imaging technique for live cells using quantitative phase information.* Scientific Reports, 2013. **3**.

139. Holler, M., et al., *X-ray ptychographic computed tomography at 16 nm isotropic 3D resolution.* Scientific Reports, 2014. **4**.

140. Wise, A.M., et al., *Nanoscale Chemical Imaging of an Individual Catalyst Particle with Soft X-ray Ptychography.* Acs Catalysis, 2016. **6**(4): p. 2178-2181.

141. Gourrier, A., et al., *Scanning X-ray imaging with small-angle scattering contrast.* Journal of Applied Crystallography, 2007. **40**: p. S78-S82.

142. Burger, C., et al., *Lateral packing of mineral crystals in bone collagen fibrils.* Biophysical Journal, 2008. **95**(4): p. 1985-1992.

143. Vaĭnshteĭn, B.K., *Modern Crystallography I: Fundamentals of Crystals: Symmetry, and Methods of Structural Crystallography*, 1996, Springer. p. 482.

144. Chernov, A.A., *Modern Crystallography III*, 1984, Springer.

145. Schaff, F., et al., *Six-dimensional real and reciprocal space small-angle X-ray scattering tomography.* Nature, 2015. **527**(7578): p. 353-+.

146. Wagermaier, W., et al., *Spiral twisting of fiber orientation inside bone lamellae.* Biointerphases, 2006. **1**(1): p. 1-5.

147.   Farber, J., et al., *Cellulose microfibril angles in a spruce branch and mechanical implications.* Journal of Materials Science, 2001. **36**(21): p. 5087-5092.

148.   Ogurreck, M., H.C. Lichtenegger, and M. Muler, *Analytical description of the scattering of cellulose nanocrystals in tracheid wood cells (vol 43, pg 256, 2010).* Journal of Applied Crystallography, 2013. **46**: p. 1907-1907.

149.   Reiterer, A., et al., *Experimental evidence for a mechanical function of the cellulose microfibril angle in wood cell walls.* Philosophical Magazine a-Physics of Condensed Matter Structure Defects and Mechanical Properties, 1999. **79**(9): p. 2173-2184.

150.   Hammersley, A.P., et al., *Calibration and application of an X-ray image intensifier/charge-coupled device detector for monochromatic macromolecular crystallography.* Journal of Synchrotron Radiation, 1997. **4**: p. 67-77.

151.   Hammersley, A.P., *FIT2D: An Introduction and Overview*, 1997, ESRF: Grenoble, France.

152.   Rose-Petruck, C., et al., *Picosecond-milliangstrom lattice dynamics measured by ultrafast X-ray diffraction.* Nature, 1999. **398**(6725): p. 310-312.

153.   Chung, J.S. and G.E. Ice, *Automated indexing for texture and strain measurement with broad-bandpass x-ray microbeams.* Journal of Applied Physics, 1999. **86**(9): p. 5249-5255.

154.   Robinson, I. and R. Harder, *Coherent X-ray diffraction imaging of strain at the nanoscale.* Nature Materials, 2009. **8**(4): p. 291-298.

155.   Margaritondo, G., *The evolution of a dedicated synchrotron light source.* Physics Today, 2008. **61**(5): p. 37-43.

156.   Mujika, F., *On the difference between flexural moduli obtained by three-point and four-point bending tests.* Polymer Testing, 2006. **25**(2): p. 7.

157.   Raabe, D., et al., *Micromechanical and macromechanical effects in grain scale polycrystal plasticity experimentation and simulation.* Acta Materialia, 2001. **49**(17): p. 3433-3441.

158.   Raabe, D., et al., *Grain-scale micromechanics of polycrystal surfaces during plastic straining.* Acta Materialia, 2003. **51**(6): p. 1539-1560.

159.   Zaefferer, S., et al., *On the influence of the grain boundary misorientation on the plastic deformation of aluminum bicrystals.* Acta Materialia, 2003. **51**(16): p. 4719-4735.

160.   Sachs, C., H. Fabritius, and D. Raabe, *Experimental investigation of the elastic-plastic deformation of mineralized lobster cuticle by digital image correlation.* Journal of Structural Biology, 2006. **155**(3): p. 409-25.

161.   Benecke G, K.M., Fratzl P, Gupta HS, *Digital image correlation shows localized deformation bands in inelastic loading of fibrolamellar bone.* Journal of Materials Research, 2009. **24**(02): p. 421-429.

162.   Raabe, D., et al., *Microstructure and crystallographic texture of the chitin-protein network in the biological composite material of the exoskeleton of the lobster Homarus americanus.* Materials Science and Engineering a-Structural Materials Properties Microstructure and Processing, 2006. **421**(1-2): p. 143-153.

163.   Vincent, J.F.V., *Arthropod cuticle: a natural composite shell system.* Composites Part a-Applied Science and Manufacturing, 2002. **33**(10): p. 1311-1315.

164.   Giraudguille, M.M., H. Chanzy, and R. Vuong, *Chitin Crystals in Arthropod Cuticles Revealed by Diffraction Contrast Transmission Electron-Microscopy.* Journal of Structural Biology, 1990. **103**(3): p. 232-240.

165.   Hunter, J.D., *Matplotlib: A 2D graphics environment.* Computing In Science & Engineering, 2007. **9**(3): p. 90-95.

166.   Lhadi, S., et al., *Effects of homogenization technique and introduction of interfaces in a multiscale approach to predict the elastic properties of arthropod cuticle.* Journal of the Mechanical Behavior of Biomedical Materials, 2013. **23**: p. 103-116.

167.   Jones, R.M., *Buckling of Bars, Plates, and Shells*2007: Bull Ridge Corporation. 824.

168.   Wu, C.N., et al., *Highly tough and transparent layered composites of nanocellulose and synthetic silicate.* Nanoscale, 2014. **6**(1): p. 392-399.

169.   Wang, Y., et al., *The predominant role of collagen in the nucleation, growth, structure and orientation of bone apatite.* Nature Materials, 2012. **11**(8): p. 724-33.

170.   Mushi, N.E., et al., *Nanopaper Membranes from Chitin-Protein Composite Nanofibers-Structure and Mechanical Properties.* Journal of Applied Polymer Science, 2014. **131**(7).

171.   Paris, O., M.A. Hartmann, and G. Fritzi-Popovski, *The Mineralized Crustacean Cuticle: Hierarchical Structure and Mechanical Properties*, in *Materials Design Inspired by Nature: Function through Inner Architecture*, P. Fratzl, J.W.C. Dunlop, and R. Weinkamer, Editors. 2013.

172.   Bouligand, Y., *Twisted fibrous arrangements in biological materials and cholesteric mesophases.* Tissue and Cell, 1972. **4**.

173.   Seidl, B.H.M. and A. Ziegler, *Electron microscopic and preparative methods for the analysis of isopod cuticle.* Zookeys, 2012(176): p. 73-85.

174.   Bar-On, B., et al., *Multiscale structural gradients enhance the biomechanical functionality of the spider fang.* Nature Communications, 2014. **5**.

175.   Hitchner, E.M., et al., *Host plant choice experiments of Colorado potato beetle (Coleoptera : Chrysomelidae) in Virginia.* Journal of Economic Entomology, 2008. **101**(3): p. 859-865.

176.   Currey, J.D., A. Nash, and W. Bonfield, *Calcified cuticle in the stomatopod smashing limb.* Journal of Materials Science, 1982. **17**: p. 1939-1944.

177.   Fratzl, P., N. Fratzlzelman, and K. Klaushofer, *Collagen Packing and Mineralization - an X-Ray-Scattering Investigation of Turkey Leg Tendon.* Biophysical Journal, 1993. **64**(1): p. 260-266.

178.   Maffulli, N., K.M. Khan, and G. Puddu, *Overuse tendon conditions: Time to change a confusing terminology.* Arthroscopy, 1998. **14**(8): p. 840-843.

179.   Yang, W., et al., *Flexible Dermal Armor in Nature.* Jom, 2012. **64**(4): p. 475-485.

180.   Chen, P.Y., et al., *Structure and mechanical properties of crab exoskeletons.* Acta Biomaterialia, 2008. **4**(3): p. 587-596.

181.   Barkaoui, A. and R. Hambli, *Finite element 3D modeling of mechanical behavior of mineralized collagen microfibrils.* Journal of Applied Biomaterials & Biomechanics, 2011. **9**(3): p. 199-206.

182.   H.Fabritius, *Chitin: Formation and Diagenesis*2010: Springer Science & Business Media. 176.

183.   Shahar, R., et al., *Anisotropic Poisson's ratio and compression modulus of cortical bone determined by speckle interferometry.* J Biomech, 2007. **40**(2): p. 252-264.

184.   Hornschemeyer, T., J. Bond, and P.G. Young, *Analysis of the functional morphology of mouthparts of the beetle Priacma serrata, and a discussion of possible food sources.* Journal of Insect Science, 2013. **13**.

185.   Flannigan, W.C., *Finite Element Modeling of Arthropod Exoskeleton*, in *Department of Mechanical and Aerospace Engineering*1998, Case Western Reserve University.

186.   Masic, A., et al., *Osmotic pressure induced tensile forces in tendon collagen.* Nature Communications, 2015. **6**.

187.   Wess, T.J. and J.P. Orgel, *Changes in collagen structure: drying, dehydrothermal treatment and relation to long term deterioration.* Thermochimica Acta, 2000. **365**(1-2): p. 119-128.

188.   Price, R.I., S. Lees, and D.A. Kirschner, *X-ray diffraction analysis of tendon collagen at ambient and cryogenic temperatures: Role of hydration.* International Journal of Biological Macromolecules, 1997. **20**(1): p. 23-33.

189.   Freeman, J.W. and F.H. Silver, *The effects of prestrain and collagen fibril alignment on in vitro mineralization of self-assembled collagen fibers.* Connective Tissue Research, 2005. **46**(2): p. 107-115.

190.   Zaidi, B.M., K. Magniez, and M.H. Miao, *Prestressed natural fibre spun yarn reinforced polymer-matrix composites.* Composites Part a-Applied Science and Manufacturing, 2015. **75**: p. 68-76.

191.   Pang, J.W.C. and K.S. Fancey, *Analysis of the tensile behaviour of viscoelastically prestressed polymeric matrix composites.* Composites Science and Technology, 2008. **68**(7-8): p. 1903-1910.

192.   Pang, J.W.C. and K.S. Fancey, *The flexural stiffness characteristics of viscoelastically prestressed polymeric matrix composites.* Composites Part a-Applied Science and Manufacturing, 2009. **40**(6-7): p. 784-790.

193.   Motahhari, S. and J. Cameron, *Fibre prestressed composites: Improvement of flexural properties through fibre prestressing.* Journal of Reinforced Plastics and Composites, 1999. **18**(3): p. 279-288.

194.   Fazal, A. and K.S. Fancey, *UHMWPE fibre-based composites: Prestress-induced enhancement of impact properties.* Composites Part B-Engineering, 2014. **66**: p. 1-6.

Appendix 1: Python script for fitting I (χ) curve

Here, we show some examples of the Python scripts developed for the WAXD scanning and *in situ* data evaluation as part of this PhD project.

The following script (**Script Listing 1**) is one of the several peak fitting programmes developed to find the peak position, peak width, peak amplitude for the I (χ) curve which will be used as initial guess parameters for the 3D orientation fitting process in **Chapter 4** and also to find the peak positions of IP and OP fibre for further data analysis in **Chapter 6**. For this particular script, the goal is to find and fit the two main peaks (usually belongs to the IP fibres) from the I (χ) curves for each WAXD frames as a batch.

For presentation purposes, the font for important function names in the script were kept in bold compare to the other regular text. The texts in italic font were the comments which do not belong to the programme. Due to the limited page width, those lines which were over the width were divided into several lines and highlighted by underlines. This presentation standard was used in all the python scripts presented here.

Script Listing 1:

```
import os

os.chdir("C:\Users\exw466\Dropbox\yizhang1\Diamond")    ### define working
directory###
from mayavi import mlab
import pylab
import numpy as np
import matplotlib.pyplot as plt
from scipy import integrate, array
```

```python
from scipy.optimize import leastsq ### Levenberg-Marquadt Algorithm ###
import savitzky_golay as sg
from scipy.interpolate import interp1d
import scipy as sp
from scipy import optimize
from pandas import read_csv
#################################################################
#################################################################
### zero crossing to find the mask peak1 region ###
def zero(xe,ye):  ###find all the zero crossing points for the vector ye, xe###
    for xvalue in xe:
        if ye[findxindex(xe,xvalue)]<0 and ye[findxindex(xe,xvalue)+1] > 0:
            print xvalue
            result = xvalue
            return result
#################################################################
### returns the x-index in xdata corresponding to xval ###
def findxindex(xdata,xval):
    rval = -1        ### if the function returns -1 (no value in xdata equal to xval)
###
    for i in xrange(len(xdata)):
        if xdata[i] == xval:
            rval = i
    return rval


def findyindex(ydata,yval):   ### find index of a yexp value which equals
localmin###
    rval = -1   ### if the function returns -1, no value in ydata equal to yval ###
    for i in xrange(len(ydata)):
        if ydata[i] == yval:
            rval = i
    return rval


def zerocross(xarray,yarray):
    ### find all the zero crossing points for the array ###
    xcross_values =  []
    xcross_indices = []
    for i in range(len(xarray)-1):
        if yarray[i]*yarray[i+1] < 0:
            ### for every value where the sign of the product is negative ###
            ###  we know that the value is crossing the x-axis ###
            xcross_values  = np.append(xcross_values,xarray[i])
            xcross_indices = np.append(xcross_indices,i)
            ### append the xvalue x to the array of xcross_values ###
            ### append the index  i to the array of xcross_indices ###
    return xcross_values, xcross_indices

def find_xindex_list(xe,xr):
    result = []
    indexlist = []
```

```python
    xval = []
    for xval in xr:
      xval_index = findxindex(xe,xval)
      indexlist = np.append(indexlist,xval_index)
      result = indexlist
    return result


def nearestzero_right(xpeak1,x_zc,x_zci,xdata,index_in_xdata):
    ### find the nearest zero crossing points above peak1 (highest peak) ###
    alllarger = []
    alllarger_index = []
    if index_in_xdata>x_zci[len(x_zci)-1]:
        ###  if the index of the peak is larger than the right-most zero crossing ###
        return xpeak1,len(xdata)-1
    else:
        for x_zeroval in x_zc:
          if  xpeak1 < x_zeroval:
              alllarger      = np.append(alllarger,x_zeroval)
              alllarger_index =
np.append(alllarger_index,findxindex(xdata,x_zeroval))
        result      = alllarger[0]
        result_index = alllarger_index[0]
    return result,result_index


def nearestzero_left(xpeak1,x_zc,x_zci,xdata,index_in_xdata):
    ### find the nearest zero crossing points below peak1 (highest peak) ###
    allsmaller = []
    allsmaller_index = []
    if index_in_xdata<x_zci[0]:
        ### if the index of the peak is smaller than the left-most zero crossing ###
        return xpeak1,0
    else:
        for x_zeroval in x_zc:
          if  xpeak1 > x_zeroval:
              allsmaller = np.append(allsmaller,x_zeroval)
                            allsmaller_index =
              np.append(allsmaller_index,findxindex(xdata,x_zeroval))
        result = allsmaller[-1]
        result_index = allsmaller_index[-1]
    return result, result_index


def mask_a_region(total,mask):
    itemsToRemove = set(mask)
    b = filter(lambda x: x not in itemsToRemove, total)
    return b


def find_two_main_peaks(xe,ye,threshold):
    ### initialize the following: ###
    ###   1) peak positions: xpeak_positions ###
    ###   2) peak values   : xpeak_values ###
```

```python
### 3) peak indices : xpeak_indices ###
xpeak_positions    = np.empty(0)
xpeak_values       = np.empty(0)
xpeak_indices      = np.empty(0)
ydata = ye       ### initializes y_sg_d2 to the experimental array ye ###
xnew  = xe       ### initializes xnew to the experimental array xe ###
i = 1
edgepeak = 1
limit    = threshold
while True:
    localmin = min(ydata)
    pindex = 0
    if localmin > limit:
        print "there are no more peaks"
        break
    else :
        xpeak = xnew[findyindex(ydata,localmin)]
        ### reports the index location of the localmin value in the ORIGINAL ye
array ###
        index_in_original = findyindex(ye,localmin)
        index_in_current  = findyindex(ydata,localmin)
        xcv, xci = zerocross(xnew,ydata)
        ### find the closest zero crossing on RIGHT ###
        xzeroval_closest_right, xzeroval_closest_index_right =
        nearestzero_right(xpeak,xcv,xci,xnew,index_in_current)
        xzeroval_closest_left,  xzeroval_closest_index_left  =
        nearestzero_left(xpeak,xcv,xci,xnew,index_in_current)
        ### now remove all the x- and y-values in index-range: ###
        ### [xzeroval_closest_index_left, xzeroval_closest_index_right] ###
        xnew_tmp = xnew
        pindex = 1
        if xzeroval_closest_index_left == 0:
            xnew = xnew[xzeroval_closest_index_right+1:len(xnew)]
            ydata = ydata[xzeroval_closest_index_right+1:len(xnew_tmp)]
            edgepeak = 2
            pindex = i
        elif xzeroval_closest_index_right == len(xnew)-1:
            xnew  = xnew[0:xzeroval_closest_index_left+1]
            ydata = ydata[0:xzeroval_closest_index_left+1]
            edgepeak = 3
            pindex = i
        else:
            xnew =
np.concatenate((xnew[0:xzeroval_closest_index_left+1],xnew[xzeroval_closest_i
ndex_right+1:len(xnew)]))
            ydata =
np.concatenate((ydata[0:xzeroval_closest_index_left+1],ydata[xzeroval_closest_i
ndex_right+1:len(xnew_tmp)]))
        i = i+1
        xpeak_positions = np.append(xpeak_positions,xpeak)
```

```python
        xpeak_values   = np.append(xpeak_values,localmin)
        xpeak_indices  = np.append(xpeak_indices,index_in_original)
        if i >= 3:
            break
    return xpeak_positions, xpeak_values,
xpeak_indices,len(xpeak_positions),edgepeak,pindex


####################################################################

def fitfunc_lorentzian_2peaks_normal(x,p0,p1,p2,p3,sp):
    p = (p0,p1,p2,p3)
    return p3+(p0/(1+((x-xpp[0])/p2)**2))+(p1/(1+((x-xpp[1])/p2)**2))


def fitfunc_lorentzian_2peaks_normal_zb(x,p0,p1,p2,p3,sp):
    p = (p0,p1,p2,p3)
    return (p0/(1+((x-xpp[0])/p2)**2))+(p1/(1+((x-xpp[1])/p2)**2))


def fitfunc_lorentzian_2peaks_left(x,p0,p1,p2,p3,sp):
    p = (p0,p1,p2,p3)
    sp=int(sp)
    pextra = p[sp-1]
    return p3+(p0/(1+((x-xpp[0])/p2)**2))+(p1/(1+((x-
xpp[1])/p2)**2))+(pextra/(1+((x-xpp[sp-1]-360)/p2)**2))


def fitfunc_lorentzian_2peaks_left_zb(x,p0,p1,p2,p3,sp):
    p = (p0,p1,p2,p3)
    sp=int(sp)
    pextra = p[sp-1]
    return (p0/(1+((x-xpp[0])/p2)**2))+(p1/(1+((x-
xpp[1])/p2)**2))+(pextra/(1+((x-xpp[sp-1]-360)/p2)**2))


def fitfunc_lorentzian_2peaks_right(x,p0,p1,p2,p3,sp):
    p = (p0,p1,p2,p3)
    sp=int(sp)
    pextra = p[sp-1]
    return p3+(p0/(1+((x-xpp[0])/p2)**2))+(p1/(1+((x-
xpp[1])/p2)**2))+(pextra/(1+((x-xpp[sp-1]+360)/p2)**2))


def fitfunc_lorentzian_2peaks_right_zb(x,p0,p1,p2,p3,sp):
    p = (p0,p1,p2,p3,p4,p5,p6)
    p = (p0,p1,p2,p3)
    sp=int(sp)
    pextra = p[sp-1]
    return (p0/(1+((x-xpp[0])/p2)**2))+(p1/(1+((x-
xpp[1])/p2)**2))+(pextra/(1+((x-xpp[sp-1]+360)/p2)**2))


####################################################################
###  checking whether there is a right side or left side sidepeak ###
#############################################
def choose_fitfunc_2peaks(peak_indices,xdata,ydata,ept,params,xi,spi,bzz):
```

```python
        yfit = np.ones_like(xi)
        parvals = np.append(params,spi)
        if ept == 1:
            if bzz==0:
                popt1, pcov1 =
sp.optimize.curve_fit(fitfunc_lorentzian_2peaks_normal,xdata,ydata,parvals)
                yfit =
fitfunc_lorentzian_2peaks_normal(xi,popt1[0],popt1[1],popt1[2],popt1[3],spi)
                plt.subplot(3, 2, str(subplot_index))
                plt.plot(xdata,ydata, "bo", xi, yfit, "r-")
                plt.title(filehead)
                plt.ylabel('intensity')
                plt.xlim([0,360])
                plt.show()
                plt.tight_layout()
                plt.savefig('fitting_2peaks_'+ str(pageindex), format = 'pdf')
                if subplot_index == nplots:
                    plt.clf()
            else:
                popt1, pcov1 =
sp.optimize.curve_fit(fitfunc_lorentzian_2peaks_normal_zb,xdata,ydata,parvals)
                yfit =
fitfunc_lorentzian_2peaks_normal_zb(xi,popt1[0],popt1[1],popt1[2],popt1[3],s
pi)
                plt.subplot(3, 2, str(subplot_index))
                plt.plot(xdata,ydata, "bo", xi, yfit, "r-")
                plt.title(filehead)
                plt.ylabel('intensity')
                plt.xlim([0,360])
                plt.show()
                plt.tight_layout()
                plt.savefig('fitting_2peaks_'+ str(pageindex), format = 'pdf')
                if subplot_index == nplots:
                    plt.clf()
        if ept == 2:
            if bzz==0:
                popt1, pcov1 =
sp.optimize.curve_fit(fitfunc_lorentzian_2peaks_left,xdata,ydata,parvals)
                yfit =
fitfunc_lorentzian_2peaks_left(xi,popt1[0],popt1[1],popt1[2],popt1[3],spi)
                plt.subplot(3, 2, str(subplot_index))
                plt.plot(xdata,ydata, "bo", xi, yfit, "r-")
                plt.title(filehead)
                plt.ylabel('intensity')
                plt.xlim([0,360])
                plt.show()
                plt.tight_layout()
                plt.savefig('fitting_2peaks_'+ str(pageindex), format = 'pdf')
                if subplot_index == nplots:
                    plt.clf()
```

```python
        else:
                              popt1, pcov1 =
    sp.optimize.curve_fit(fitfunc_lorentzian_2peaks_left_zb,xdata,ydata,parvals)
                              yfit =
    fitfunc_lorentzian_2peaks_left_zb(xi,popt1[0],popt1[1],popt1[2],popt1[3],spi)
                         plt.subplot(3, 2, str(subplot_index))
            plt.plot(xdata,ydata, "bo", xi, yfit, "r-")
            plt.title(filehead)
            plt.ylabel('intensity')
            plt.xlim([0,360])
            plt.show()
            plt.savefig('fitting_2peaks_'+ str(pageindex), format = 'pdf')
            plt.tight_layout()
            if subplot_index == nplots:
                plt.clf()
    if ept == 3:
        if bzz==0:
                              popt1, pcov1 =
    sp.optimize.curve_fit(fitfunc_lorentzian_2peaks_right,xdata,ydata,parvals)
                              yfit =
    fitfunc_lorentzian_2peaks_right(xi,popt1[0],popt1[1],popt1[2],popt1[3],spi)
                         plt.subplot(3, 2, str(subplot_index))
            plt.plot(xdata,ydata, "bo", xi, yfit, "r-")
            plt.title(filehead)
            plt.ylabel('intensity')
            plt.xlim([0,360])
            plt.show()
            plt.tight_layout()
            plt.savefig('fitting_2peaks_'+ str(pageindex), format = 'pdf')
            if subplot_index == nplots:
                plt.clf()
        else:
            popt1, pcov1 =
sp.optimize.curve_fit(fitfunc_lorentzian_2peaks_right_zb,xdata,ydata,parvals)
            yfit =
fitfunc_lorentzian_2peaks_right_zb(xi,popt1[0],popt1[1],popt1[2],popt1[3],spi)
            plt.subplot(3, 2, str(subplot_index))
            plt.plot(xdata,ydata, "bo", xi, yfit, "r-")
            plt.title(filehead)
            plt.ylabel('intensity')
            plt.xlim([0,360])
            plt.show()
            plt.tight_layout()
            plt.savefig('fitting_2peaks_'+ str(pageindex), format = 'pdf')
            if subplot_index == nplots:
                plt.clf()# Plot of the data and the fit


    #################################################################
```

```python
def
totalfitting_2peaks(n,pindex,x,y,edge_peak_type,p2,x_interpolated,f_cub,side_peak_index,bz,np):
    if n == 2:

choose_fitfunc_2peaks(pindex,x,y,edge_peak_type,p2,x_interpolated,side_peak_index,bz)
        print "2peaks"
        return
    else:
        print "this frame is special"
        plt.subplot(3, 2, str(subplot_index))
        plt.plot(x,y, "bo", x_interpolated,f_cub, "r-")
        plt.title(filehead)
        plt.ylabel('intensity')
        plt.xlim([0,360])
        plt.show()
        plt.tight_layout()
        plt.savefig('fitting_2peaks_'+ str(pageindex), format = 'pdf')
        if subplot_index == np:
            plt.clf()
        return


###########################################################################
filelist = read_csv("file1_mainpeaks.csv")
### the sourse file for fitting which contain multiple I(chi) files  ###
flist = []
findex = []
maskindex = []
for i, row in enumerate(filelist.values):
    myk,myfile,mymask=row
    flist.append(myfile)
    findex.append(myk)
    maskindex.append(mymask)
######################################################################
def findindex(data,val):
 ### find index of a yexp value which equals localmin ###
    rval = -1
    for i in xrange(len(data)):
        if data[i] == val:
            rval = i
    return rval
######################################################################
### define page index ###
############################
def find_pageindex(finx,nval):
    constant = (finx-1)/nval
    pval = int(constant) + 1
    return pval
```

```python
def find_subplot_index(finx,nval):
    remainder = (finx) % nval +1
    return remainder


####################################
p0 = 150
p1 = 150
p2 = 10
p3 = 0
baseline_zero = 0
p02 = [p0,p1,p2,p3]
### read experimental data ###
for fname in flist:
    nplots = 6    ### define how many frames in one page ###
    fname_index = findindex(flist,fname)
    fname_index = int(fname_index)
    filehead, fileext = fname.split("bend5_")
    pageindex = find_pageindex(fname_index+1,nplots)
    pageindex = int(pageindex)
    subplot_index = find_subplot_index(fname_index,nplots)
    subplot_index = int(subplot_index)
    print fname_index,pageindex,subplot_index
    xexp, yexp = np.loadtxt(fname, unpack = True)
    xnew = np.linspace(1,359,180)
    xnew_integers = [int(x) for x in xnew]
    sg_window_size = 31
    sg_order = 4
        y_sg_1 = sg.savitzky_golay(yexp, window_size=sg_window_size,
                                order=sg_order)
      y_sg_d1 = sg.savitzky_golay(yexp, window_size=sg_window_size,
                            order=sg_order, deriv=1)
      y_sg_d2 = sg.savitzky_golay(yexp, window_size=sg_window_size,
                            order=sg_order, deriv=2)
    if maskindex[fname_index] == 0:
        plt.subplot(3, 2, str(subplot_index))
        plt.plot(xexp, yexp, 'ro')
        plt.title(filehead)
        plt.ylabel('intensity')
        plt.xlim([0,360])
        plt.show()
        plt.tight_layout()
        plt.savefig('fitting_2peaks_'+ str(pageindex), format = 'pdf')
        if subplot_index == nplots:
            plt.clf()
    if maskindex[fname_index] == 1:
        threshold=-.05
                    xpp, xpv, xpi, npeaks, edgepeak,pindex =
                find_two_main_peaks(xnew,y_sg_d2,threshold)
                            totalfitting_2peaks
(npeaks,pindex,xexp,yexp,edgepeak,p02,xnew,yexp,pindex,baseline_zero,nplots)
```

Appendix 2: Python script for 3D fibre orientation fitting

This script was developed to extract from the $I(\chi)$ curve generated from a single WAXD pattern, the full 3D orientation using the mathematic functions which are presented in **Chapter 4.** Both the 3D orientation of IP and OP fibre will be acquired during from this fitting procedure.

Script Listing 2:

```
######################################################################
import os
os.chdir("C:\Users\exw466\Dropbox\yizhang1\modelling_and_plotting\\new_wax
d_83744")
import numpy as np
import matplotlib.pyplot as plt
import time
from matplotlib.pyplot import figure, show, savefig
from matplotlib import cm, colors
from numpy import ma
import scipy.special as ssp
import savitzky_golay as sg
from scipy.interpolate import interp1d
import sys
import pandas as pd
from scipy import integrate, array


######################################################################
########
def weight_func(gamma, gamma0, dgamma0):
                prefac = (1.0/(dgamma0*np.sqrt(2*np.pi)))
        expterm = np.exp(-((gamma-gamma0)**2/(2*(dgamma0**2))))
    return prefac * expterm

def Gaussian2Peak(chi,chi01,chi02,Dchi0,A1,A2,A0):
### dummy 2 Gaussian function ###
    fval = A1*np.exp(-((chi-chi01)**2)/(2*(Dchi0**2)))+A2*np.exp(-((chi-
                        chi02)**2)/(2*(Dchi0**2)))+A0
    return fval

def Chisquare(model_data,experimental_data, variance_array):
    diffvar = np.sum(((model_data-experimental_data)/variance_array)**2)
    return diffvar
```

```python
def delta_ax(x,z,gamma,ax):
    delta_val = (1./(ax*np.sqrt(np.pi)))*np.exp(-((x*np.cos(gamma)-
z*np.sin(gamma))**2/(ax**2)))
    return delta_val

def weight_function(gamma, gamma0, sigma_gamma):
  w_gamma = (1.0/(2*sigma_gamma*np.sqrt(2*np.pi)))*(np.exp(-0.5*(((gamma-
            gamma0)**2)/(sigma_gamma**2)))+np.exp(-0.5*(((gamma-
                (gamma0+np.pi))**2)/(sigma_gamma**2))))
    return w_gamma


def IntegratedIntensity(x,y,z,gamma0,sigma_gamma,ax):
            IntegIntensity = integrate.quad(IntensityIntegrand,-
            np.pi/2.0,np.pi/2.0,args=(x,z,gamma0,sigma_gamma,ax))
    return IntegIntensity

def IntensityIntegrand(gamma,x,z,gamma0,sigma_gamma,ax):
IntIntegrand = weight_function(gamma, gamma0,
sigma_gamma)*delta_ax(x,z,gamma,ax)
return IntIntegrand

vIntegratedIntensity = np.vectorize(IntegratedIntensity)

def chi_intensity_pe(Alpha_pe,Beta_pe,Gamma_pe,dgamma_pe,scale_pe):
    R_qaxis = 0.1479
    ax = R_qaxis/10.0
    R_Ewald = 1
    nchi =180
    dchi = 2*np.pi/nchi
    chi = np.arange(1*np.pi/180,2*np.pi,dchi)
    Gamma_pe = np.deg2rad(Gamma_pe)
    Beta_pe = np.deg2rad(Beta_pe)
    Alpha_pe = np.deg2rad(Alpha_pe)
    dgamma_pe = np.deg2rad(dgamma_pe)
    y_lab_pe =
(R_qaxis/2*R_Ewald)*np.sqrt((2*R_Ewald+R_qaxis)*(2*R_Ewald-
R_qaxis))*np.sin(chi)
    z_lab_pe = -
(R_qaxis/2*R_Ewald)*np.sqrt((2*R_Ewald+R_qaxis)*(2*R_Ewald-
R_qaxis))*np.cos(chi)
    x_lab_pe = -((R_qaxis*R_qaxis)/(2*R_Ewald))*np.ones_like(chi)
    x_bcs_pe = np.cos(Beta_pe)*x_lab_pe - np.sin(Beta_pe)*y_lab_pe
    y_bcs_pe = -np.sin(Beta_pe)*np.cos(Alpha_pe)*x_lab_pe +
np.cos(Beta_pe)*np.cos(Alpha_pe)*y_lab_pe + np.sin(Alpha_pe)*z_lab_pe
    z_bcs_pe = np.sin(Beta_pe)*np.sin(Alpha_pe)*x_lab_pe -
np.sin(Alpha_pe)*np.cos(Beta_pe)*y_lab_pe + np.cos(Alpha_pe)*z_lab_pe
    u_pe,du_pe =
vIntegratedIntensity(x_bcs_pe,y_bcs_pe,z_bcs_pe,Gamma_pe,dgamma_pe,ax)
    chi = np.rad2deg(chi)
```

```python
    u_pe = scale_pe * u_pe
    return chi,u_pe
###################################################
### define fitting parameter for IP fibres###
Alpha_min = -4
Alpha_max = 100
dAlpha = 300
Beta_min = -0.15
Beta_max = 40
dBeta = 200
Gamma0_min = 27
Gamma0_max = 80
dGamma = 100
dgamma0_min = 5
dgamma0_max = 80
ddgamma = 100
scale_min = 12
scale_max = 30
dscale = 266
Beta_range1 = np.arange(Beta_min, Beta_max, dBeta)
Alpha_range1 = np.arange(Alpha_min, Alpha_max, dAlpha)
Gamma0_range1 = np.arange(Gamma0_min, Gamma0_max, dGamma)
dgamma0_range1 = np.arange(dgamma0_min, dgamma0_max, ddgamma)
scale_range1 = np.arange(scale_min, scale_max, dscale)
###################################################
### define fitting parameter for OP fibres###
Alpha_min = -92.5
Alpha_max = 3.5
dAlpha = 200
Beta_min = 0
Beta_max = 60
dBeta = 120
Gamma0_min = -75
Gamma0_max = 85
dGamma = 5
dgamma0_min = 10
dgamma0_max = 80
ddgamma = 10
scale_min =4.5
scale_max = 5
dscale = 100
Beta_range2 = np.arange(Beta_min, Beta_max, dBeta)
Alpha_range2 = np.arange(Alpha_min, Alpha_max, dAlpha)
Gamma0_range2 = np.arange(Gamma0_min, Gamma0_max, dGamma)
dgamma0_range2 = np.arange(dgamma0_min, dgamma0_max, ddgamma)
scale_range2 = np.arange(scale_min, scale_max, dscale)
##########################################################
VGaussian2Peak = np.vectorize(Gaussian2Peak)
chi1=0
chi2=360
```

```python
nchi = 180
chi = np.linspace(chi1,chi2,nchi)
Alpha_pe = 0.4
Beta_pe = -7
gamma0_pe = -15
dgamma0_pe = 70
scale_pe = -0.15
##########################################################
### read experimental data ###
fname = "i22-83744_BSL_030.c0T"
xexp, yexp = np.loadtxt(fname, unpack = True)
f_cub = interp1d(xexp, yexp, kind='cubic')
xnew = np.linspace(1,359,180)
xnew_integers = [int(x) for x in xnew]
sg_window_size = 31
sg_order = 4
y_sg_1 = sg.savitzky_golay(f_cub(xnew), window_size=sg_window_size,
order=sg_order)
experimental_data = y_sg_1
print len(experimental_data)
error_array = np.ones_like(experimental_data)
NEG_DUMMY_VALUE = -10
chisquare = NEG_DUMMY_VALUE

df =
pd.DataFrame(columns=["Alpha1","Beta1","gamma01","dgamma01","scale1","
Alpha2","Beta2","gamma02","dgamma02","scale2","Alpha_tmp2", "chisquare"])
                                      data =
[{"Alpha_tmp1":Alpha_pe,"Beta_tmp1":Beta_pe,"gamma0_tmp1":gamma0_pe,"
dgamma0_tmp1":dgamma0_pe,"scale_tmp1":scale_pe,"Alpha_tmp2":Alpha_pe,"
Beta_tmp2":Beta_pe,"gamma0_tmp2":gamma0_pe,"dgamma0_tmp2":dgamma0_
    pe,"scale_tmp2":scale_pe,"chisquare": chisquare} for i in np.arange(1)]
df = pd.DataFrame(data)
print "dataframe = ", df
f = open("workfile.txt", "w")
#####################################################################
################
### start to fitting process ###
for Alpha_tmp1 in Alpha_range1:
    for Beta_tmp1 in Beta_range1:
        for dgamma0_tmp1 in dgamma0_range1:
            for gamma0_tmp1 in Gamma0_range1:
                for scale_tmp1 in scale_range1:
                    for Alpha_tmp2 in Alpha_range2:
                        for Beta_tmp2 in Beta_range2:
                            for dgamma0_tmp2 in dgamma0_range2:
                                for gamma0_tmp2 in Gamma0_range2:
                                    for scale_tmp2 in scale_range2:
                                        R_qaxis = 0.1479
                                        ax = R_qaxis/10.0
                                        R_Ewald = 1
```

$$u31,du31 =$$
chi_intensity_pe(Alpha_tmp1,Beta_tmp1,gamma0_tmp1,dgamma0_tmp1,scale_tmp1)

u32,du32 =
chi_intensity_pe(Alpha_tmp2,Beta_tmp2,gamma0_tmp2,dgamma0_tmp2,scale_tmp2)

Xplt = chi
Yplt = du31+du32
synthetic_data = (Yplt)
synthetic_chisquare = **Chisquare**(synthetic_data,experimental_data,error_array)
f.write(strline)

data =
[{"Alpha_tmp1":Alpha_tmp1,"Beta_tmp1":Beta_tmp1,"gamma0_tmp1":gamma0_tmp1,"dgamma0_tmp1":dgamma0_tmp1,"scale_tmp1":scale_tmp1,"Alpha_tmp2":Alpha_tmp2,"Beta_tmp":Beta_tmp2,"gamma0_tmp2":gamma0_tmp2,"dgamma0_tmp2":dgamma0_tmp2,"scale_tmp2":scale_tmp2,"chisquare": synthetic_chisquare} for i in np.arange(1)]

df=df.append(data)
df = df[df.chisquare != NEG_DUMMY_VALUE]
print df.sort("chisquare",
ascending=True).head(3)[["Alpha_tmp1","Beta_tmp1","gamma0_tmp1","dgamma0_tmp1","scale_tmp1","Alpha_tmp2","Beta_tmp2","gamma0_tmp2","dgamma0_tmp2","scale_tmp2", "chisquare"]]

###
###

Examples of the fitting results (also shown in Figure 4.5 B5):

###
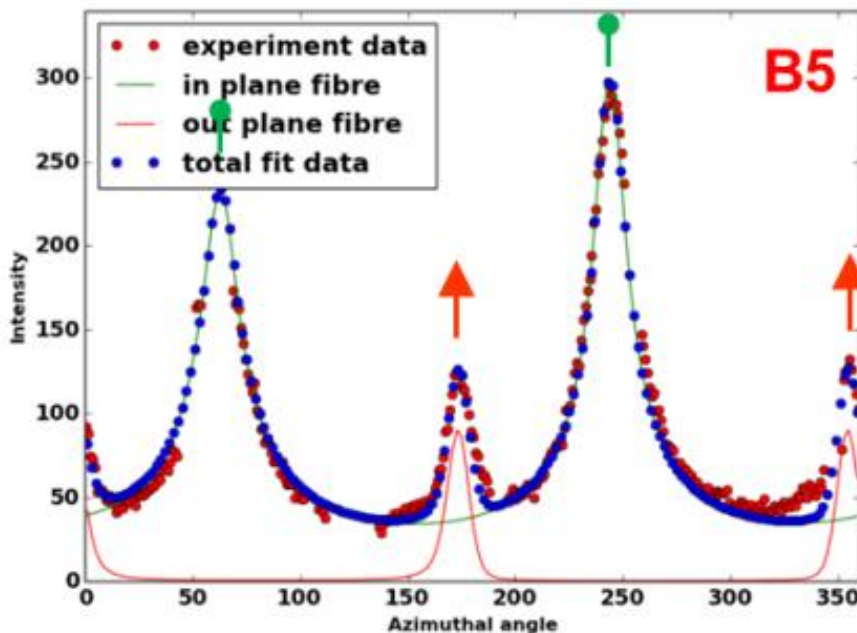
Appendix 3: Python script for Qaxis sphere visualization

This script is primarily a display-oriented routine, developed to display the 3D intensity distribution on the QS110 and QS013 sphere corresponding to a set of fibre orientation parameters (fitted from the script shown in **Script Listing 2**. The result will help us to view the diffraction distribution changes according to the fibre orientation changes directly, also, it can helps to verify the mathematic model for (110) reflections we presented in **Chapter 4** and (unreported) (013) reflections.

Script Listing 3:

```python
###########################################################################
import os
os.chdir("C:\Users\exw466\Dropbox\data_analysis\\test\Text_for_WAXD\83744")
import numpy as np
import matplotlib.pyplot as plt
import time
from matplotlib.pyplot import figure, show, savefig
from matplotlib import cm, colors
from numpy import ma
import scipy.special as ssp
import savitzky_golay as sg
from scipy.interpolate import interp1d
import sys
import pandas as pd
from scipy import integrate, array
from mayavi import mlab
from tvtk.tools import visual
#####################################################################
def weight_func(gamma, gamma0, dgamma0):
    prefac = (1.0/(dgamma0*np.sqrt(2*np.pi)))
    expterm = np.exp(-((gamma-gamma0)**2/(2*(dgamma0**2))))
    return prefac * expterm

def axes():
    xaxis_len = 1.6
    xaxis = [[0,xaxis_len],[0,0],[0,0]]
    xaxis_line = mlab.quiver3d(0,0,0,0.8,0,0,line_width=0.02,color=(1,1,0),mode
                = "2darrow",scale_factor=1,opacity = 0.5)
    yaxis_len = 1.6
    yaxis = [[0,0],[0,yaxis_len],[0,0]]
```

```python
        yaxis_line = mlab.quiver3d(0,0,0,0,0.8,0,line_width=0.02,color=(1,1,0),mode
                    = "2darrow",scale_factor=1,opacity = 0.5)
        zaxis_len = 1.6
        zaxis = [[0,0],[0,0],[0,zaxis_len]]
        zaxis_line = mlab.quiver3d(0,0,0,0,0,0.8,line_width=0.02,color=(1,1,0),mode
                    = "2darrow",scale_factor=1,opacity = 0.5)
        x_axis_x = 1.0
        x_axis_y = 0
        x_axis_z = -0.2
                xtxt_label = mlab.text3d(x_axis_x, x_axis_y, x_axis_z,
                        "q_x",scale=0.1,color=(1,0,0))
        y_axis_x = 0.2
        y_axis_y = 0.8
        y_axis_z = 0
                ytxt_label = mlab.text3d(y_axis_x, y_axis_y, y_axis_z,
                        "q_y",scale=0.1,color=(1,0,0))
        z_axis_x = 0.4
        z_axis_y = 0
        z_axis_z = 0.8
                ztxt_label = mlab.text3d(z_axis_x, z_axis_y, z_axis_z,
                        "q_z",scale=0.1,color=(1,0,0))
    return


def Arrow_From_A_to_B(x1, y1, z1, x2, y2, z2):
    ar1=visual.arrow(x=x1, y=y1, z=z1)
    ar1.length_cone=0.4
    arrow_length=np.sqrt((x2-x1)**2+(y2-y1)**2+(z2-z1)**2)
    ar1.actor.scale=[arrow_length, arrow_length, arrow_length]
    ar1.pos = ar1.pos/arrow_length
    ar1.axis = [x2-x1, y2-y1, z2-z1]
    return ar1


def Gaussian2Peak(chi,chi01,chi02,Dchi0,A1,A2,A0):
    fval = A1*np.exp(-((chi-chi01)**2)/(2*(Dchi0**2)))+A2*np.exp(-((chi-
                    chi02)**2)/(2*(Dchi0**2)))+A0
    return fval


def Chisquare(model_data,experimental_data, variance_array):
diffvar = np.sum(((model_data-experimental_data)/variance_array)**2)
    return diffvar


def delta_ax110(x,y,gamma,ax):
        delta_val = (1./(ax*np.sqrt(np.pi)))*np.exp(-((x*np.sin(gamma)-
                    y*np.cos(gamma))**2/(ax**2)))
    return delta_val


def delta_ay013(x,y,gamma,ay):
    q_013 = 0.262
    tan_mu = 10.32/(3*18.86)
    mu_013 = np.cos(np.arctan(tan_mu))
```

```python
    mu_013 = 10.337
    mu_013 = np.deg2rad(mu_013)
        delta_val = (1./(ay*np.sqrt(np.pi)))*(np.exp(-(((y*np.cos(gamma)-
        x*np.sin(gamma))-q_013*np.cos(mu_013))**2/(ay**2)))+np.exp(-
 (((y*np.cos(gamma)-x*np.sin(gamma))+q_013*np.cos(mu_013))**2/(ay**2))))
    return delta_val


def weight_function(gamma, gamma0, sigma_gamma):
        w_gamma = (1.0/(2*sigma_gamma*np.sqrt(2*np.pi)))*(np.exp(-
    0.5*(((gamma-gamma0)**2)/(sigma_gamma**2)))+np.exp(-0.5*(((gamma-
                (gamma0+np.pi))**2)/(sigma_gamma**2))))
    return w_gamma


def IntegratedIntensity_110(x,y,z,gamma0,sigma_gamma,ax):
            IntegIntensity = integrate.quad(IntensityIntegrand_110,-
            np.pi/2.0,np.pi/2.0,args=(x,y,gamma0,sigma_gamma,ax))
    return IntegIntensity


def IntensityIntegrand_110(gamma,x,y,gamma0,sigma_gamma,ax):
            IntIntegrand = weight_function(gamma, gamma0,
            sigma_gamma)*delta_ax110(x,y,gamma,ax)
    return IntIntegrand


vIntegratedIntensity_110 = np.vectorize(IntegratedIntensity_110)


def IntegratedIntensity_013(x,y,z,gamma0,sigma_gamma,ay):
            IntegIntensity = integrate.quad(IntensityIntegrand_013,-
            np.pi/2.0,np.pi/2.0,args=(x,y,gamma0,sigma_gamma,ay))
    return IntegIntensity


def IntensityIntegrand_013(gamma,x,y,gamma0,sigma_gamma,ay):
IntIntegrand = weight_function(gamma, gamma0,
sigma_gamma)*delta_ay013(x,y,gamma,ay)
    return IntIntegrand


vIntegratedIntensity_013 = np.vectorize(IntegratedIntensity_013)


def Ewald(R_EwaldE,phiE, thetaE, r00E):
    r2 = R_EwaldE*np.ones_like(r00E)
    x2 = r2*np.sin(phiE)*np.sin(thetaE)+1
    y2 = r2*np.cos(thetaE)
    z2 = r2*np.cos(phiE)*np.sin(thetaE)
    return mlab.mesh(x2,y2,z2,opacity=0.3,color=(0,1,0))


def QS013(R_013,phiE, thetaE, r00E):
    r2 = R_013*np.ones_like(r00E)
    x2 = r2*np.sin(phiE)*np.sin(thetaE)
    y2 = r2*np.cos(thetaE)
    z2 = r2*np.cos(phiE)*np.sin(thetaE)
    return mlab.mesh(x2,y2,z2,opacity=0.3,color=(1,0.75,0.8))
```

```python
def QS013ring(R_013,phiE, thetaE, r00E):
    r2 = R_013*np.ones_like(r00E)
    x2 = r2*np.sin(phiE)*np.sin(thetaE)
    y2 = r2*np.cos(thetaE)*(10.32/3*18.86)
    z2 = r2*np.cos(thetaE)
    return mlab.plot3d(x2,y2,z2,color=(0,0,0), tube_radius = 0.004,opacity = 0.5)

def xyz_axes(x,y,z,u,v,w):
    obj = mlab.quiver3d (x,y,z,u,v,w,line_width=3, mode='arrow', scale_factor=1)
    return obj

def chi_intensity_110(Alpha_pe,Beta_pe,Gamma_pe,dgamma_pe,scale_pe):
    R_110 = 0.1925
    ax = R_110/10.0
    R_Ewald = 1
    nchi =180
    dchi = 2*np.pi/nchi
    chi = np.arange(0*np.pi/180,2*np.pi+dchi,dchi)
    Gamma_pe = np.deg2rad(Gamma_pe)
    Beta_pe = np.deg2rad(Beta_pe)
    Alpha_pe = np.deg2rad(Alpha_pe)
    dgamma_pe = np.deg2rad(dgamma_pe)
    y_lab_pe = (R_110/2*R_Ewald)*np.sqrt((2*R_Ewald+R_110)*(2*R_Ewald-
                           R_110))*np.sin(chi)
    z_lab_pe = -(R_110/2*R_Ewald)*np.sqrt((2*R_Ewald+R_110)*(2*R_Ewald-
                           R_110))*np.cos(chi)
    x_lab_pe = ((R_110*R_110)/(2*R_Ewald))*np.ones_like(chi)
    x_bcs_pe = np.cos(Alpha_pe)*x_lab_pe - np.sin(Alpha_pe)*z_lab_pe
           y_bcs_pe = np.sin(Alpha_pe)*np.sin(Beta_pe)*x_lab_pe +
    np.cos(Beta_pe)*y_lab_pe + np.cos(Alpha_pe)*np.sin(Beta_pe)*z_lab_pe
           z_bcs_pe = np.sin(Alpha_pe)*np.cos(Beta_pe)*x_lab_pe -
    np.sin(Beta_pe)*y_lab_pe + np.cos(Alpha_pe)*np.cos(Beta_pe)*z_lab_pe
                           u_pe,du_pe =
vIntegratedIntensity_110(x_bcs_pe,y_bcs_pe,z_bcs_pe,Gamma_pe,dgamma_pe
                           ,ax)
    chi = np.rad2deg(chi)
    u_pe = scale_pe * u_pe
    return chi,u_pe

def coordinates_trans(x_in,y_in,z_in,Alpha_pe,Beta_pe):
    x_out= np.cos(Alpha_pe)*x_in - np.sin(Alpha_pe)*z_in
    y_out = np.sin(Alpha_pe)*np.sin(Beta_pe)*x_in + np.cos(Beta_pe)*y_in +
                   np.cos(Alpha_pe)*np.sin(Beta_pe)*z_in
    z_out = np.sin(Alpha_pe)*np.cos(Beta_pe)*x_in - np.sin(Beta_pe)*y_in +
                   np.cos(Alpha_pe)*np.cos(Beta_pe)*z_in
    return x_out,y_out,z_out

def chi_intensity_013(Alpha_pe,Beta_pe,Gamma_pe,dgamma_pe,scale_pe):
    R_013 = 0.262
```

```
    ay = R_013/10.0
    R_Ewald = 1
    nchi =180
    dchi = 2*np.pi/nchi
    chi = np.arange(0*np.pi/180,2*np.pi+dchi,dchi)
    Gamma_pe = np.deg2rad(Gamma_pe)
    Beta_pe = np.deg2rad(Beta_pe)
    Alpha_pe = np.deg2rad(Alpha_pe)
    dgamma_pe = np.deg2rad(dgamma_pe)
#############################
    y_lab_pe = (R_013/2*R_Ewald)*np.sqrt((2*R_Ewald+R_013)*(2*R_Ewald-
                          R_013))*np.sin(chi)
    z_lab_pe = -(R_013/2*R_Ewald)*np.sqrt((2*R_Ewald+R_013)*(2*R_Ewald-
                          R_013))*np.cos(chi)
    x_lab_pe = ((R_013*R_013)/(2*R_Ewald))*np.ones_like(chi)
####################################################
    x_bcs_pe = np.cos(Alpha_pe)*x_lab_pe - np.sin(Alpha_pe)*z_lab_pe
    y_bcs_pe = np.sin(Alpha_pe)*np.sin(Beta_pe)*x_lab_pe +
np.cos(Beta_pe)*y_lab_pe + np.cos(Alpha_pe)*np.sin(Beta_pe)*z_lab_pe
    z_bcs_pe = np.sin(Alpha_pe)*np.cos(Beta_pe)*x_lab_pe -
np.sin(Beta_pe)*y_lab_pe + np.cos(Alpha_pe)*np.cos(Beta_pe)*z_lab_pe
                      u_pe,du_pe =
vIntegratedIntensity_013(x_bcs_pe,y_bcs_pe,z_bcs_pe,Gamma_pe,dgamma_pe,a
                          y)
    chi = np.rad2deg(chi)
    u_pe = scale_pe * u_pe
    return chi,u_pe


mlab.clf()

def fiber_3d1(x0,y0,z0,psi0,xi0,dgamma0,gamma0,rscale):
    gamma0 = np.deg2rad(gamma0)
    psi0 = np.deg2rad(psi0)
    xi0 = np.deg2rad(xi0)
    psi0 = -psi0
    xi0 = -xi0
    v0pp = np.array([0,rscale,0])
            rot_matrix_gamma = np.array([[np.cos(gamma0),-
       np.sin(gamma0),0],[np.sin(gamma0),np.cos(gamma0),0],[0,0,1]])
    v0 = rot_matrix_gamma.dot(v0pp.T)
    dgamma0_origin = dgamma0
    dgamma0_min = 0
    dgamma0_max = dgamma0
    ddgamma = 5
    dgamma_range = np.arange(dgamma0_min, dgamma0_max, ddgamma)
    if dgamma0_origin != 0:
    dgamma0_origin = np.deg2rad(dgamma0_origin)
    for dgamma0 in dgamma_range:
    dgamma0 = np.deg2rad(dgamma0)
```

rot_matrix_3dimensional = np.array([[np.cos(psi0), 0,-np.sin(psi0)],[np.sin(xi0)*np.sin(psi0),np.cos(xi0),np.sin(xi0)*np.cos(psi0)],[np.cos(xi0)*np.sin(psi0),-np.sin(xi0),np.cos(xi0)*np.cos(psi0)]])

v_gamma0 = rot_matrix_3dimensional.dot(v0.T)

fibre distribution weight function

w_gamma0 = **weight_function**(gamma0, gamma0, dgamma0)

fibre at +/- dgamma angles

 ### + angles ###

rot_matrix_plusdgamma = np.array([[np.cos(dgamma0),np.sin(dgamma0),0],[-np.sin(dgamma0),np.cos(dgamma0),0],[0,0,1]])

v0_plus = rot_matrix_plusdgamma.dot(v0.T)

v_gamma0_plusdgamma = rot_matrix_3dimensional.dot(v0_plus.T)

w_gamma0_plusdgamma = weight_function(gamma0+dgamma0, gamma0, dgamma0)

- angles

rot_matrix_minusdgamma = np.array([[np.cos(-dgamma0),np.sin(-dgamma0),0],[-np.sin(-dgamma0),np.cos(-dgamma0),0],[0,0,1]])

v0_minus = rot_matrix_minusdgamma.dot(v0.T)

v_gamma0_minusdgamma = rot_matrix_3dimensional.dot(v0_minus.T)

w_gamma0_minusdgamma = weight_function(gamma0-dgamma0, gamma0, dgamma0)

vn_gamma0 = -v_gamma0

vn_gamma0_plusdgamma = -v_gamma0_plusdgamma

vn_gamma0_minusdgamma = -v_gamma0_minusdgamma

v_place = np.array([x0,y0,z0])

v_gamma0_pm = np.concatenate((np.array([v_gamma0]+v_place),np.array([vn_gamma0+v_place])),axis=0).T

v_gamma0_plusdgamma_pm = np.concatenate((np.array([v_gamma0_plusdgamma+v_place]),np.array([vn_gamma0_plusdgamma+v_place])),axis=0).T

v_gamma0_minusdgamma_pm = np.concatenate((np.array([v_gamma0_minusdgamma+v_place]),np.array([vn_gamma0_minusdgamma+v_place])),axis=0).T

tube_radius_max = 0.015

tr_0 = tube_radius_max

tr_plus = tube_radius_max-(dgamma0/dgamma0_origin)*tube_radius_max

tr_minus = tube_radius_max-(dgamma0/dgamma0_origin)*tube_radius_max

opanum = 1-1*(dgamma0/dgamma0_origin)

vector_vgamma0 = mlab.plot3d(v_gamma0_pm[0],v_gamma0_pm[1],v_gamma0_pm[2],tube_radius=tr_0, color=(0,1,0),opacity=1)

vector_vgamma0_plusdgamma = mlab.plot3d(v_gamma0_plusdgamma_pm[0], v_gamma0_plusdgamma_pm[1], v_gamma0_plusdgamma_pm[2], tube_radius=tr_plus, color=(0,0.9,0),opacity=opanum)

vector_vgamma0_minusdgamma = mlab.plot3d(v_gamma0_minusdgamma_pm[0], v_gamma0_minusdgamma_pm[1], v_gamma0_minusdgamma_pm[2], tube_radius=tr_minus, color=(0,0.9,0),opacity=opanum)

```python
        else:
            return
    return


def detectorplane(x_constant,square_len,color_pe):
    color = color_pe
            side1 = [[x_constant,x_constant],[square_len,square_len],[-
                        square_len,square_len]]
            side2 = [[x_constant,x_constant],[-square_len,-square_len],[-
                        square_len,square_len]]
        side3 = [[x_constant,x_constant],[-square_len,square_len],[-square_len,-
                        square_len]]
            side4 = [[x_constant,x_constant],[-
                square_len,square_len],[square_len,square_len]]
        mlab.plot3d(side1[0], side1[1], side1[2], tube_radius=0.002, color =
                        color,opacity = 0.5)
        mlab.plot3d(side2[0], side2[1], side2[2], tube_radius=0.002, color =
                        color,opacity = 0.5)
        mlab.plot3d(side3[0], side3[1], side3[2], tube_radius=0.002, color =
                        color,opacity = 0.5)
        mlab.plot3d(side4[0], side4[1], side4[2], tube_radius=0.002, color =
                        color,opacity = 0.5)
    return
#######################################################

###  define the 3D fibre orientation parameters ###
###########
Alpha_1 = 0
Beta_1 = 0
dgamma0_1 = 60
gamma0_1 = 20
scale_1 = 24
#######################################################
############################################################
nchi =180
dchi = 2*np.pi/nchi
chi = np.arange(0*np.pi/180,2*np.pi+dchi,dchi)
print len(chi)
R_Ewald = 1
nphi = 100
ntheta = 100
dphi, dtheta = 2*np.pi/nphi, np.pi/ntheta
[theta,phi] = np.mgrid[0:np.pi+dtheta*1.0:dtheta,0:2*np.pi+dphi*1.0:dphi]
r00 = np.sin(phi) + np.cos(phi) + np.sin(theta) + np.cos(theta)
Ewald(R_Ewald,phi, theta, r00)
############################################################
############################################################
### plot the intensity distributions on QS110 sphere ###
R_110 = 0.1925 #radius of qaxis sphere0 in units of Ewald sphere radius
gamma0_1 = np.deg2rad(gamma0_1)
```

```
Beta_1 = np.deg2rad(Beta_1)
Alpha_1 = np.deg2rad(Alpha_1)
dgamma0_1 = np.deg2rad(dgamma0_1)
gamma0_2 = np.deg2rad(gamma0_2)
Beta_2 = np.deg2rad(Beta_2)
Alpha_2 = np.deg2rad(Alpha_2)
dgamma0_2 = np.deg2rad(dgamma0_2)
r0 = R_110*np.ones_like(r00)
x_l110 = r0*np.sin(phi)*np.sin(theta)
y_l110 = r0*np.cos(theta)
z_l110 = r0*np.cos(phi)*np.sin(theta);
ax = R_110/10.0
                       x_bcs_1,y_bcs_1,z_bcs_1 =
        coordinates_trans(x_l110,y_l110,z_l110,Alpha_1,Beta_1)
                       x_bcs_2,y_bcs_2,z_bcs_2 =
        coordinates_trans(x_l110,y_l110,z_l110,Alpha_2,Beta_2)
                              u21,du21 =
vIntegratedIntensity_110(x_bcs_1,y_bcs_1,z_bcs_1,gamma0_1,dgamma0_1,ax)
                              u22,du22 =
vIntegratedIntensity_110(x_bcs_2,y_bcs_2,z_bcs_2,gamma0_2,dgamma0_2,ax)
 qaxis_opacity = 0.7
 scalearray = scale_1*u21+scale_2*u22
 vmax110 = np.amax(scalearray)
 vmin110 = np.amin(scalearray)
 QS110 = mlab.mesh(x_l110, y_l110, z_l110, scalars=scale_1*u21+scale_2*u22,
    colormap="jet",opacity=qaxis_opacity,vmax =vmax110,vmin=vmin110 )
                       ### plot the QS110 sphere ###
   yi_lab = (R_110/2*R_Ewald)*np.sqrt((2*R_Ewald+R_110)*(2*R_Ewald-
                              R_110))*np.sin(chi)
   zi_lab = -(R_110/2*R_Ewald)*np.sqrt((2*R_Ewald+R_110)*(2*R_Ewald-
                              R_110))*np.cos(chi)
   xi_lab = ((R_110*R_110)/(2*R_Ewald))*np.ones_like(chi)
gamma0_1 = np.rad2deg(gamma0_1)
Beta_1 = np.rad2deg(Beta_1)
Alpha_1 = np.rad2deg(Alpha_1)
dgamma0_1 = np.rad2deg(dgamma0_1)
gamma0_2 = np.rad2deg(gamma0_2)
Beta_2 = np.rad2deg(Beta_2)
Alpha_2 = np.rad2deg(Alpha_2)
dgamma0_2 = np.rad2deg(dgamma0_2)
chi,u31_110 =
chi_intensity_110(Alpha_1,Beta_1,gamma0_1,dgamma0_1,scale_1)
     circle_line = mlab.plot3d(xi_lab,yi_lab,zi_lab,u31_110,colormap='jet',
                              tube_radius = 0.005)
#######################################################################
#### plot the intensity distributions on QS013 sphere ###
#######################################################################
nphi = 100
ntheta = 100
dphi, dtheta = 2*np.pi/nphi, np.pi/ntheta
```

```python
[theta,phi] = np.mgrid[0:np.pi+dtheta*1.0:dtheta,0:2*np.pi+dphi*1.0:dphi]
R_013 = 0.262
gamma0_1 = np.deg2rad(gamma0_1)
Beta_1 = np.deg2rad(Beta_1)
Alpha_1 = np.deg2rad(Alpha_1)
dgamma0_1 = np.deg2rad(dgamma0_1)
gamma0_2 = np.deg2rad(gamma0_2)
Beta_2 = np.deg2rad(Beta_2)
Alpha_2 = np.deg2rad(Alpha_2)
dgamma0_2 = np.deg2rad(dgamma0_2)
r00 = np.sin(phi) + np.cos(phi) + np.sin(theta) + np.cos(theta)
r0 = R_013*np.ones_like(r00)
xi_013 = r0*np.sin(phi)*np.sin(theta)
yi_013= r0*np.cos(theta)
zi_013 = r0*np.cos(phi)*np.sin(theta);
ay = R_013/10
x_b013_1,y_b013_1,z_b013_1 =
coordinates_trans(x_l013,y_l013,z_l013,Alpha_1,Beta_1)
x_b013_2,y_b013_2,z_b013_2 =
coordinates_trans(x_l013,y_l013,z_l013,Alpha_2,Beta_2)
u21,du21 =
vIntegratedIntensity_013(x_b013_1,y_b013_1,z_b013_1,gamma0_1,dgamma0_1,
ay)
print u21
qaxis_opacity = 0.3
chi = np.arange(0*np.pi/180,2*np.pi+dchi,dchi)
print "chi =",chi
scalearray = scale_1*u21
vmax013 = np.amax(scalearray)
vmin013 = np.amin(scalearray )
QS013 = mlab.mesh(x_l013, y_l013, z_l013, scalars=scale_1*u21,
colormap="jet",opacity=qaxis_opacity,vmax =vmax013,vmin=vmin013 )
                ### plot the QS013 sphere ###
   yi_013 = (R_013/2*R_Ewald)*np.sqrt((2*R_Ewald+R_013)*(2*R_Ewald-
                        R_013))*np.sin(chi)
   zi_013 = -(R_013/2*R_Ewald)*np.sqrt((2*R_Ewald+R_013)*(2*R_Ewald-
                        R_013))*np.cos(chi)
          xi_013 = ((R_013*R_013)/(2*R_Ewald))*np.ones_like(chi)
                            ###
                xi_b013_1,yi_b013_1,zi_b013_1 =
            coordinates_trans(xi_013,yi_013,zi_013,Alpha_1,Beta_1)
                        u31_013,du31 =
 vIntegratedIntensity_013(xi_b013_1,yi_b013_1,zi_b013_1,gamma0_1,dgamma
                            0_1,ay)
circle_line2 = mlab.plot3d(xi_013,yi_013,zi_013,u31_013,colormap='jet',
tube_radius = 0.005)      ### the intersection ring between Ewald and QS013###
###################################################################
###################################################################
#########################
R_110 = 0.1925
```
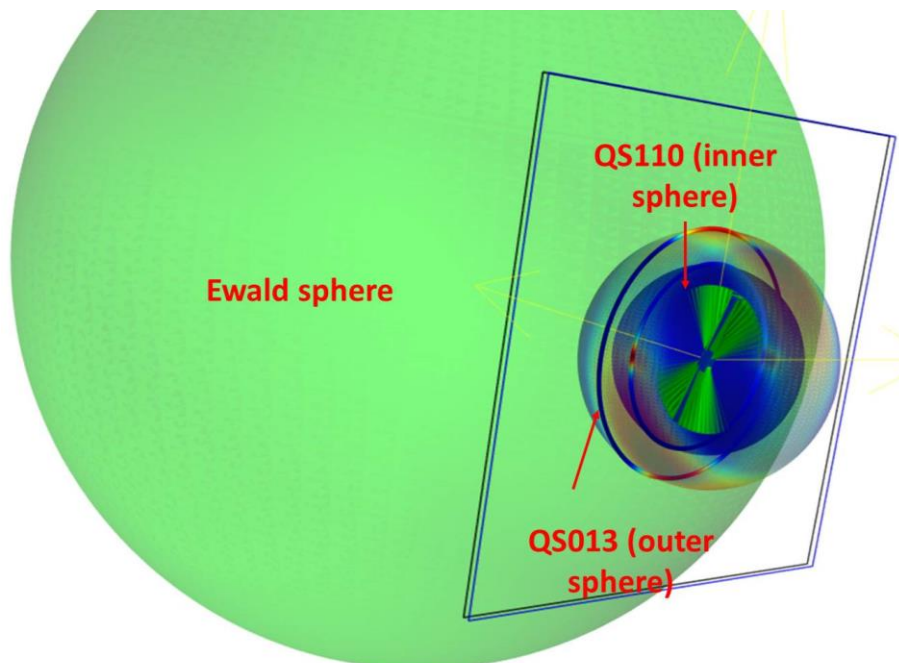
```
ax = R_110/10.0
R_Ewald = 1
gamma0_1 = np.rad2deg(gamma0_1)
Beta_1 = np.rad2deg(Beta_1)
Alpha_1 = np.rad2deg(Alpha_1)
dgamma0_1 = np.rad2deg(dgamma0_1)
gamma0_2 = np.rad2deg(gamma0_2)
Beta_2 = np.rad2deg(Beta_2)
Alpha_2 = np.rad2deg(Alpha_2)
dgamma0_2 = np.rad2deg(dgamma0_2)
###############################################
square_len = 0.5
x_constant1 = xi_013[0]
x_constant2 = xi_lab[0]
color1 = (0,0,0)
color2 = (0,0,1)
detectorplane(x_constant1,square_len,color1)
detectorplane(x_constant2,square_len,color2)
axes()
fiber_3d1(0,0,0,0,0,60,20,0.15)
#######################################################################
#######################################################################
```

From the script, we can obtain 3D intensity distributions on QS110 and QS013, as in the picture below:


```
###############################################################
```